UNIVERSITY OF VAASA

SCHOOL OF TECHNOLOGY AND INNOVATIONS

COMMUNICATION AND SYSTEMS ENGINEERING

DALBERT ZIMUZOCHUKWU ONYEBUCHI

PERFORMANCE EVALUATION OF LOW-COST PRECISION POSITIONING METHODS FOR FUTURE PORT APPLICATIONS

Master's thesis for the degree of Master of Science in Technology submitted for assessment.

Vaasa, August 25, 2021.

Supervisor	Professor Heidi Kuusniemi
Co-Supervisor	Professor Mohammed Elmusrati
Instructor	Dr. Mohammad Zahidul Hassan Bhuiyan Research Manager, Department of Navigation and Positioning, National Land Survey of Finland

UNIVERSITY OF VAASA
SCHOOL OF TECHNOLOGY AND INNOVATION

Author: Dalbert Zimuzochukwu Onyebuchi
Student Number z109554
Thesis Title: Performance evaluation of low-cost precision positioning methods for future port applications

Degree: Master of Science in Technology
Major of Subject: Communication and Systems Engineering
Supervisor: Professor Heidi Kuusniemi
Co-Supervisor: Professor Mohammed Elmusrati
Instructor: Dr. Mohammad Zahidul Hasan Bhuiyan
Research Manager, Department of Navigation and Positioning, National Land Survey of Finland

Year of Entering the University: 2016
Year of Completing the Thesis: 2021 **Number of pages:** 215

ABSTRACT:

In recent times, a lot of research has been conducted to improve the accuracy of various positioning systems. The motivation behind this trend is to ensure high quality GNSS services for various applications. In particular, emphasis has been placed on improving the level of accuracy of consumer grade GNSS receivers. Significant improvements in the quality of signal reception of these receivers would enable low-cost solutions for asset management in for example, harbor areas. Research in Receiver Autonomous Integrity Monitoring - Fault Detection and Exclusion (RAIM-FDE) algorithms give users the ability to exclude satellites with degraded signals, hereby improving the performance of the GNSS solution. This research investigates and evaluates the performance of various customer grade GNSS positioning systems intended for port applications. Various high precision techniques such as Precise Point Positioning and Real-Time Kinematic were conducted and accuracy levels were noted on Multi-band receivers, Single frequency receivers, and GNSS-enabled smartphone. Our final conclusion suggests optimal low-cost GNSS solutions for asset monitoring and management.

KEYWORDS: GNSS, PPP, RTK, low-cost, precision navigation, DGNSS/DGPS, SBAS/EGNOS/WAAS, RAIM-FDE, port operations, position determination, navigation algorithms.

ACKNOWLEDGEMENTS

To my one true King, The Principal Architect of the Universe. You make all things beautiful.

My deepest gratitude to my supervisor, Professor Heidi Kuusniemi for her guidance and support throughout my thesis work. Profound regards to Dr. Mohammad Zahidul Hasan Bhuiyan for his counsel throughout this work.

Special thanks to Professor Mohammed Elmusrati for providing general counsel.

Immense gratitude to Lector Sem Timmerbacka from Novia University of Applied Sciences for providing the Topcon GNSS Reference System.

To my Dad, Dr. Uwaezuoke Onyebuchi. You instilled discipline in me.

To my Mom, Irene Onyebuchi. You inspired me to pursue my dreams.

To Ella, David, Chinua, Alswell and Sharon. Your support, and words of encouragement were profoundly helpful in my darkest moments.

To the entire community at the University of Vaasa, City Church Vaasa, Grace Church Vaasa, Vaasa Toastmasters, and Rotaract Vaasa. Your support made this thesis happen. Thank you so much.

TABLE OF CONTENT

LIST OF FIGURES

LIST OF TABLES

LIST OF ABBREVIATIONS

DGNSS	Differential Global Navigation Satellite Systems
DOP	Dilution of Precision
EKF	Extended Kalman Filter
FDE	Fault Detection and Exclusion
GDOP	Geometric Dilution of Precision
GBAS	Ground-based Augmentation System
HDOP	Horizontal Dilution of Precision
NMEA	National Marine Electronics Association
PPP	Precise point positioning
RAIM	Receiver Autonomous Integrity Monitoring
RINEX	Receiver Independent Exchange Format
RTCM	Radio Technical Commission for Maritime Services
RTK	Real time kinematics
SBAS	Satellite-based Augmentation System
SPP	Single point positioning
VDOP	Vertical Dilution of Precision

1. INTRODUCTION

Global Navigation Satellite Systems (GNSS) are a system of satellites in the medium earth orbit that provides global autonomous geo-spatial positioning coverage and uses line-of-sight time signals to deliver location (longitude, latitude, and altitude/elevation) to small earth bound receivers. They are used for navigation and position determination. This term includes e.g. the GPS, GLONASS, Galileo, Beidou and other regional systems. GNSSs are designed in such a way to allow for redundancy to ensure 100% availability. This design feature makes them suitable for applications that required remote continuous monitoring such as pedestrian/ air navigation, land surveying, and autonomous driving.

1.1 Background

In recent times, there is a high demand to use GNSS for freight asset management. This trend is precipitated by the miniaturization of radio frequency electronics, an increase of computing power in small devices, and increased accuracy in both standard point positioning (SPP) and precise point positioning (PPP) GNSS related technology. Besides, 100% availability of GNSSs makes them suitable for this application.

Furthermore, the rise of Internet of things (IOT) technology necessitates that freight assets such as ships, and shipping containers be remotely monitored to deliver favourable return on investments (ROI). With IOT systems, stakeholders can glean useful insights to optimize supply chain processes and reduce carbon footprint. This also allows for port automation, herby improving process efficiency and reducing lead times. Besides, portability, adaptability, low price and low energy consumption of consumer grade GNSS receivers make it suitable for use in various environments, and for various purposes. In addition, the improved Carrier to Noise ratio (C/No) of consumer-grade GNSS receivers makes them suitable for use in industrial applications. These devices can deliver sub meter level precise point positioning (PPP) and allow for selective receiver tuning. For example, it is possible to select a

specific satellite constellation depending on the user location. Nevertheless, GNSS signals suffer from interference due to reflections, natural obstacles in port areas necessitating the need for backup navigation system, as well as terrestrial systems (for example e-Loran) and augmentation systems (like DGPS or SBAS). Other practical maritime uses include applications for search and rescue, inland waterways, environmental protection and sailing (European GNSS Agency, 2015).

In addition, GNSS-enabled smartphones have been used for PPP and SPP evaluation and analysis yielding a coordinate accuracy of the order of 1 m (2-sigmas) using 30 minutes of data while retaining code noise and multipath effects due to antenna design restrictions (Lachapelle et al., 2019).

1.2 Thesis Statement

The main task in this thesis is to evaluate the performance level of low-cost consumer grade GNSS receivers for port operations to assess their feasibility and suitability. Analysis is performed via collecting RINEX observations and navigation data from a single frequency and double frequency low-cost GNSS receivers, as well as a smartphone for Standard Point Positioning (SPP), Real-time Kinematics (RTK), and Precise Point Positioning (PPP) evaluations in RTKLib with EUREF Reference RINEX data for error corrections. These devices are categorized into single frequency, and double frequency low-cost GNSS receivers. Data subject to evaluation was collected at the University of Vaasa GNSS research lab, and the Kvarken Ports harbour area in the Vaasa Region. Various statistics are conducted and analysed such as Horizontal and Vertical errors (2-sigma: 95% confidence level). Comparisons such as analysis of accuracy, precision, and availability will be made for GNSS solutions with RAIM-FDE (Receiver Autonomous Integrity Monitoring- Fault Detection and Exclusion), and without RAIM-FDE settings.

1.3 Motivation

In recent times, GNSS has largely been considered a maritime navigation technique. A set of set operational performance requirements for GNSS has been set by the International Maritime Organization (IMO) for World-Wide Radio Navigation Systems (WWRNS) recognition (IMO Resolution A. 915(22), 2002). The data shows a growth trend for the installed base of GNSS devices across the world. This rise is expected to reach 100% by 2023 (GNSS Market Report, 2015). Moreover, GNSS penetration, a metric that shows the proportion of all possible vessels equipped by GNSS indicates an upward trend. Core regional revenue of GNSS device sale, and amount of GNSS sales when considering use-cases has also increased. Besides, there exist emerging opportunities for GNSS applications such as marine engineering for example cable or pipe laying, search and rescue, and traffic management/ surveillance. These could serve as avenues for future growth. Furthermore, the availability of various types of receivers and frequency configurations enable various applications. There is therefore motivation to embark on a GNSS port application pilot study also for the Vaasa Region. Research findings would shorten future research efforts and deployments with increased automation needs.

1.4 Maritime user needs and requirements

Major GNSS regulatory bodies such as International Maritime Organization (IMO), US Federal Radionavigation Plan (FRP), Europe's MARUSE project (MAR), and the International Hydrographic Organization (IHO) specify performance parameters for different phases of navigation as shown in Table 1:

Table 1. Comparison of IMO, FRP and IHO main performance parameters.

Phase of Navigation	ACCURACY (meters, 2 drms)				AVAILABILITY % / period		CONTINUITY (over 15 min)		INTEGRITY (Alert Limit / risk per 3 hours)			TIME TO ALARM (s)	
	IMO	MAR	FRP	IHO	IMO	FRP	IMO	FRP	IMO	MAR	FRP	IMO	FRP
Ocean	10 - 100	10	1800 – 3700	30 - 420	99.8 30 days	99 12 h	N/A	*	25 / 10^{-5}	25 / 10^{-5}	TBD	10	TBD
Coastal	10	10	460	5 - 10	99.8 30 days	99.7	N/A	*	25 / 10^{-5}	25 / 10^{-5}	TBD	10	TBD
Port Approach & Restricted waters	10	10	8 - 20**	5 - 10	99.8 30 days	99.7	99.97	*	25 / 10^{-5}	25 / 10-5	TBD	10	TBD
Port	1	1	-	2	99.8 30 days	-	99.97	-	2.5 / 10^{-5}	2.5 / 10^{-5}	-	10	-
Inland waterways (IWW)	10	3	2 – 5	2	99.8 30 days	99.9	99.97	*	25 / 10^{-5}	7.5 / 10^{-5}	TBD	10	TBD

TBD – To be discussed

* Dependent upon mission time

** Varies from one harbour to another

IHO quoted accuracy is “Maximum allowable Total Horizontal Uncertainty” at 95%

(Source: European GNSS Agency, 2019).

The table above shows accuracy, integrity and availability requirements for various phases of navigation.

The European Global Navigation Satellite Systems Agency (GSA) defines port operations as activities directly associated with vessels (European GNSS Agency, 2019). They are:

a. Local Traffic Management
b. Container and cargo tracking and asset management
c. Law enforcement activities
d. Cargo handling

Other broad definitions of port operations include: port navigation, tugs and pushers operations, navigation aids management, casualty analysis, leisure/recreation, automatic collision avoidance and track control. Accuracy and coverage requirements differ for each of these port operation category.

Furthermore, Maritime and Inland Waterways (IWW) user requirements for port operations are placed into categories as shown in Table 2:

Table 2. Consolidated maritime and IWW users' requirements for port applications.

Category	Applications	Main User requirements
Category 2 (1m horizontal accuracy requirement)	Port Operations: Local vessel traffic services (VTS) Casualty Analysis: Port approach, restricted waters and inland waterways Leisure boat applications in congested areas (geofencing, boat inspections, docking assistance)	1m horizontal accuracy 95% 99.8% availability over any 30 day, 2.5m horizontal alert limit, Time to alarm smaller than 10 s, Integrity risk smaller than 10-5 per 3 hours, Regional coverage (local for VTS) Position fixes at least once per second
Category 2+ (same as 2 + local continuity requirement)	General Navigation (SOLAS): Ports and restricted waters. General navigation (recreation and leisure): Ports and restricted waters Operations of Locks, Tugs, Pushers and Icebreakers	Identical to category 2, with the addition of a local coverage and a continuity of 99,97 % over 15 minutes
Category 2++ (same as 2 + local 1m vertical accuracy requirement)	Ports operations: Container / Cargo management & Law enforcement	Identical to category 2, with the addition of a local coverage and a positioning accuracy requirement of 1 m vertical (95%)
Category 3 (0.1m horizontal accuracy requirement)	Marine Engineering : Dredging and construction works Inland Waterways: bridge collision warning systems	0.1m horizontal and vertical accuracy 95% 99.8% availability over any 30 day, 0.25m horizontal alert limit, Time to alarm smaller than 10 s, Integrity risk smaller than 10-5 per 3 hours, Local coverage Position fixes at least once per second
Category 3+ (same as 3 – no vertical accuracy + continuity requirements)	Operations: Docking	Requirements differs from category 3 with vertical accuracy, which is not applicable and a continuity requirement of 99,97 % over 15 minutes
Category 3++ (same as 3 + stringent TTA requirement)	Port Operations: Cargo handling	Requirements are identical to category 3, except a stringent integrity requirement with a time to alarm smaller than 1 s

Source: (European GNSS Agency, 2019).

The table above shows various category maritime and IWW users' requirements for port applications.

1.5 Methodology

To assess low-cost user device performance, two sets of experiments were conducted at two different locations.

a. Test 1: Dynamic tests at Kvarken Ports Vaasa.
   Devices include Topcon GNSS Reference system, two dual frequency GNSS receivers (u-blox ZED-F9P-(1), and ZED-F9P-(2)), a single frequency GNSS receiver (u-blox EVK-M8T), and GNSS-enabled smartphone (Samsung Galaxy s8).
b. Test 2: Stationary tests at Fabrikki Building rooftop, University of Vaasa.
   Devices include a dual frequency GNSS receivers (u-blox ZED-F9P), a single frequency GNSS receiver (u-blox EVK-M8T), and GNSS-enabled smartphone (Samsung Galaxy s8).

For each test case, a 64-bit PC with AMD Ryzen 3 PRO 2300U w/Radeon Vega Mobile Gfx 2.00GHz processor, 8.00GB RAM is used to obtain GNSS observation and navigation data (in *.ubx format) from low-cost u-blox™ consumer-grade GNSS receivers continuously for one month. During data collection, various GNSS modes are selected/enabled (GPS, GLONASS, Galileo, and SBAS) and logged separately for evaluation. The data obtained is converted to RINEX format by the means of a third-party *.ubx to RINEX converter. Converted RINEX data is then inputted into the RTKLib software (Takasu, T., 2007-2013, pg. 1) for Standard Point Positioning (SPP), differential GNSS and EGNOS-corrected, RTK, and Precise Point Positioning (PPP) evaluations with RAIM-FDE enabled, and also repeated with RAIM-FDE disabled.

Broadcast ephemeris, precise orbits and clocks, and ionosphere corrections are used for all for all GNSS post processing modes being evaluated, and for both kinematic and stationary tests. Data from the EUREF Reference station is used for analysis. The VAA200FIN reference station is selected with a baseline of 18.3 km.

For PPP and RTK, Pseudo range smoothing is also experimented by using the Fix and Hold Integer ambiguity algorithm. Further analysis such as NEU (North-East-Up) positioning error, Horizontal (2D) and Vertical errors, Dilution of Precision (DOP), and analysis of Availability, and precision based on RAIM-FDE will be performed, Results will compared across devices and processing modes, and an optimal GNSS solution is suggested for asset monitoring and management in a port environment.

1.6 Expectation

The thesis will demonstrate and suggests optimal GNSS solutions suitable for future port applications such as automated asset monitoring and management. The analysis will also compare results across different GNSS frequency receivers and computational modes. Outcome of this work will serve as a foundation for future low-cost Kinematic Precise Point Positioning analysis of the university's student LEO cube satellite for its precision positioning solution in orbit.

2. GLOBAL SATELLITE NAVIGATION SYSTEMS

2.1 Fundamentals of Satellite Navigation Systems

GNSS is a group of several satellite navigation (SATNAV) systems and their augmentations. These SATNAV systems provide global or regional satellite coverage. GNSS provides position, velocity and time based on the Coordinated Universal Time (UTC) timescale. GNSSs consist of core constellations; a group of 24 or more satellites located in the medium earth orbit (MEO) arranged in 3 or 6 orbital planes with four or more satellites per plane, and a network of earth ground stations to monitor the health and status of the core constellations, and communicate for example, navigation data with other satellites. These systems use a direct sequence spread spectrum technique to broadcast UTC synchronized ranging codes and navigation data on two or more frequencies. The navigation data contains the location of the satellite at the time of signal transmission. The ranging code provides the user receiver with signal propagation time data to estimate satellite-to-user range and compute the PVT solution.

Time of Arrival (TOA) is a ranging technique used by GNSS to determine user position. With the aid of TOA measurements from multiple satellites, it is possible to achieve three-dimensional positioning (Kaplan et al., 2006, pg. 24; Kaplan et al., 2017 pg. 37). To achieve this positioning, ranging codes or signals that travel at the speed of light (3×10^8 m/s) from a transmitting satellite are used. On-board satellite clocks are used to control the timing of the code or signal. All satellites within a SATNAV constellation are synchronized to an internal systems time scale known as system time. The ranging signal is embedded with this timing information to enable a receiver to compute the difference between the time of signal transmission and arrival (satellite-to-user propagation time). To compute the satellite-to-user range, the satellite-to-user propagation time is multiplied by the speed of the ranging signal (the speed of light). Using ranging codes simultaneously from three satellites, a user can be in one of the two points where the spheres around these satellites intersect

as shown in the Figures 1a and b. Other methods such as the use of reference coordinate systems, and augmentation systems are used to precisely select the user location. To achieve the 3Dimensional PVT navigation solution, a minimum of four satellites is required.

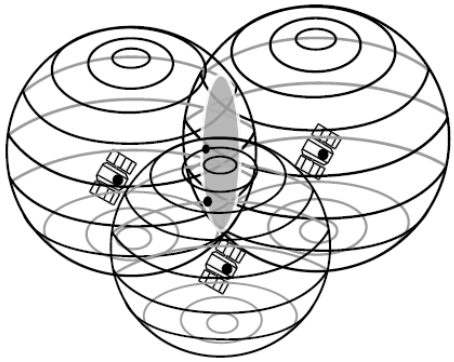

Figure 1. User located at one of two points on shaded circle.

(Sources: Kaplan et al., 2006, pg. 27; Kaplan et al., 2017, pg. 40).

In the figure above, a user is located at one of the two points on the shaded area.

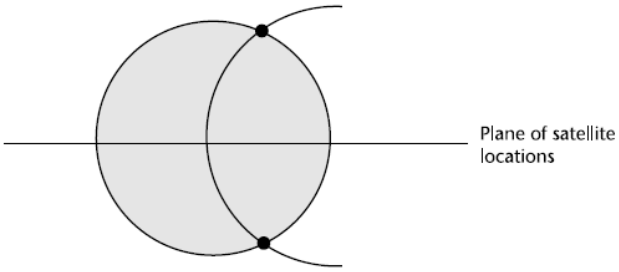

Figure 2. User located at one of two points on circle perimeter.

(Sources: Kaplan et al., 2006, pg. 40; Kaplan et al., 2017 pg. 27).

In the figure above, a user is located at one of the two points on circle perimeter.

2.1.1 Reference coordinate systems

Reference coordinate systems are Cartesian coordinate systems used to represent the position and velocity vectors of the satellite and receiver. They can be categorized into Inertial and rotating systems, Earth-centred systems and local (topocentric) systems.

a. Earth-Centred Inertial (ECI) Coordinate System

   This coordinate system is used to measure and determine the orbits of satellites. Earth's center of mass is used as the origin, while the axis points in fixed direction with respect to the stars. However, Earth's oblate shape, polar motion, nutation and precession causes change in the ECI orientation axis. To solve this problem, the axis is defined at a particular time instance or epoch.

b. Earth-Centred Earth-Fixed (ECEF) Coordinate System

   This is used to calculate the GNSS receiver position. With this system, latitude, longitude, and height can be computed with ease. The XY-plane is placed concurrently to the equatorial plane of the earth. Transformation between ECI and ECEF is made for high precision GNSS orbit computation. With ECEF, polar motion, nutation and precession are limited (Kaplan et al., 2006 pg. 49; Kaplan et al., 2017 pg. 32).

c. Local Tangent Plane (Local Level) Coordinate Systems

   Its principle of depends on the local vertical direction and the rotation of Earth's axis. Three coordinates make up the system: Northern axis position, local eastern axis position, and vertical axis position. The configuration of these axis coordinates can be east, north, up (ENU) or north, east, down (NED). They are used in aviation and marine cybernetics to represent state vectors (Wikipedia, 2020a).

d. Local Body Frame Coordinate Systems

   This is used to ascertain an object's attitude, orientation or in atmospheric drag modelling. The center of the object may serve as the origin (not

compulsory), while the body frame coordinate axes depend on the principal axes or symmetry axes of the object.

e. Geodetic (Ellipsoidal) Coordinates

This system considers the true geoid shape of the earth. Here, the reference ellipsoid serves as the reference surface, on which the geoid latitude, longitude, and elevation are computed. The NGA (National Geospatial-Intelligence Agency) EGM2008 - WGS 84 version Geopotential Model, now referred to as EGM2008 is the best-known global geoid model (Kaplan et al., 2017, pg. 50).

f. International Terrestrial Reference Frame (ITRF)

ITRF uses the ECEF Cartesian coordinates system. It is important to note that the reference system discussed in the previous sections are theoretical systems for determining position, and coordinates as defined by the International Earth Rotation and Reference Systems Service (IERS) (Kaplan et al., 2017, pg. 51). The reference frame is used for the actual implementation. The IERS manages and reviews various ITRF implementations such as ITRF94, ITRF96, ITRF97, ITRF2000, ITRF2005, ITRF2008, and ITRF2014 (Kaplan et al., 2017, pg. 52). The International GNSS Service (IGS) enables users to gain access to the reference frame for GNSS applications with the aid of more than 400 reference Stations. This data comprises of troposphere and ionosphere parameters, orientation of the earth, and models of satellite antennas to achieve accurate GNSS orbits and clocks computation (International GNSS Service, 2020).

2.1.2 Satellite Navigation (SATNAV) Segments

GNSS are made up of three segments. Space segment, Control segment and User segment as shown in Figure 3.

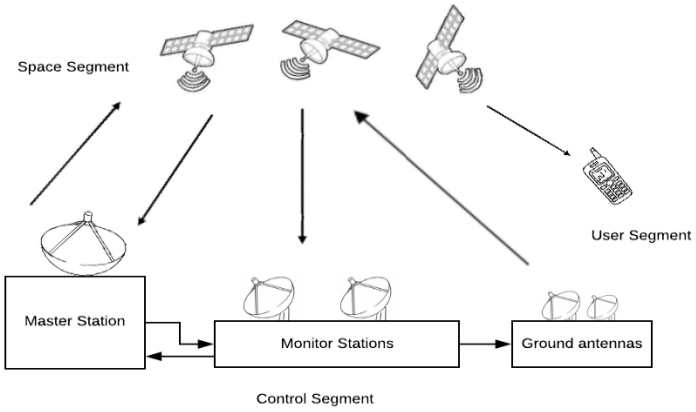

Figure 3. SATNAV Segments.

a. Space segment

The space segment comprises of a constellation of space satellites called space vehicles (SVs). It is used to broadcast the pseudo random number (PRN) codes on multiple frequencies. In GPS, these SVs contain a primary navigation payload used for PVT computation, a secondary nuclear detonation (NUDET) detection system for detecting and reporting radiation phenomena that occurs on Earth, and a vehicle control subsystem for maintaining the SVs orbital position (Kaplan et al., 2006, pg. 67; Kaplan et al., 2017 pg. 104).

b. Control segment

This segment is used for station keeping and system health (Electrical Power System monitoring, and orbital position maintenance), and daily updates of the satellite clock, ephemeris, almanac data, pseudorange and carrier phase measurements for satellite error correction, with the aid of master control station (MCS), monitor stations and ground antenna. (Kaplan et al., 2006 pg. 68; Kaplan et al., 2017 pg. 105).

c. User segment

The User segment is any GNSS enabled receiver or equipment. A typical GNSS receiver comprises of the antennas, Receiver front end, Processor, user control display unit, and Power supply. It receives the navigation data on multiple frequencies and from multiple constellations, acquires the signal by identifying the satellite PRN codes, and coarsely estimating the time delay and Doppler shifts. It also tracks the signal by finely estimating the time delay and Doppler shifts, synchronizes the navigation data, measures the pseudoranges and carrier phase, decodes the navigation message, computes the PVT solution, corrects for positioning errors by using data from a Differential GNSS (DGNSS) interface such as EGNOS, and displays the information on a user interface as shown in Figure 4 below:

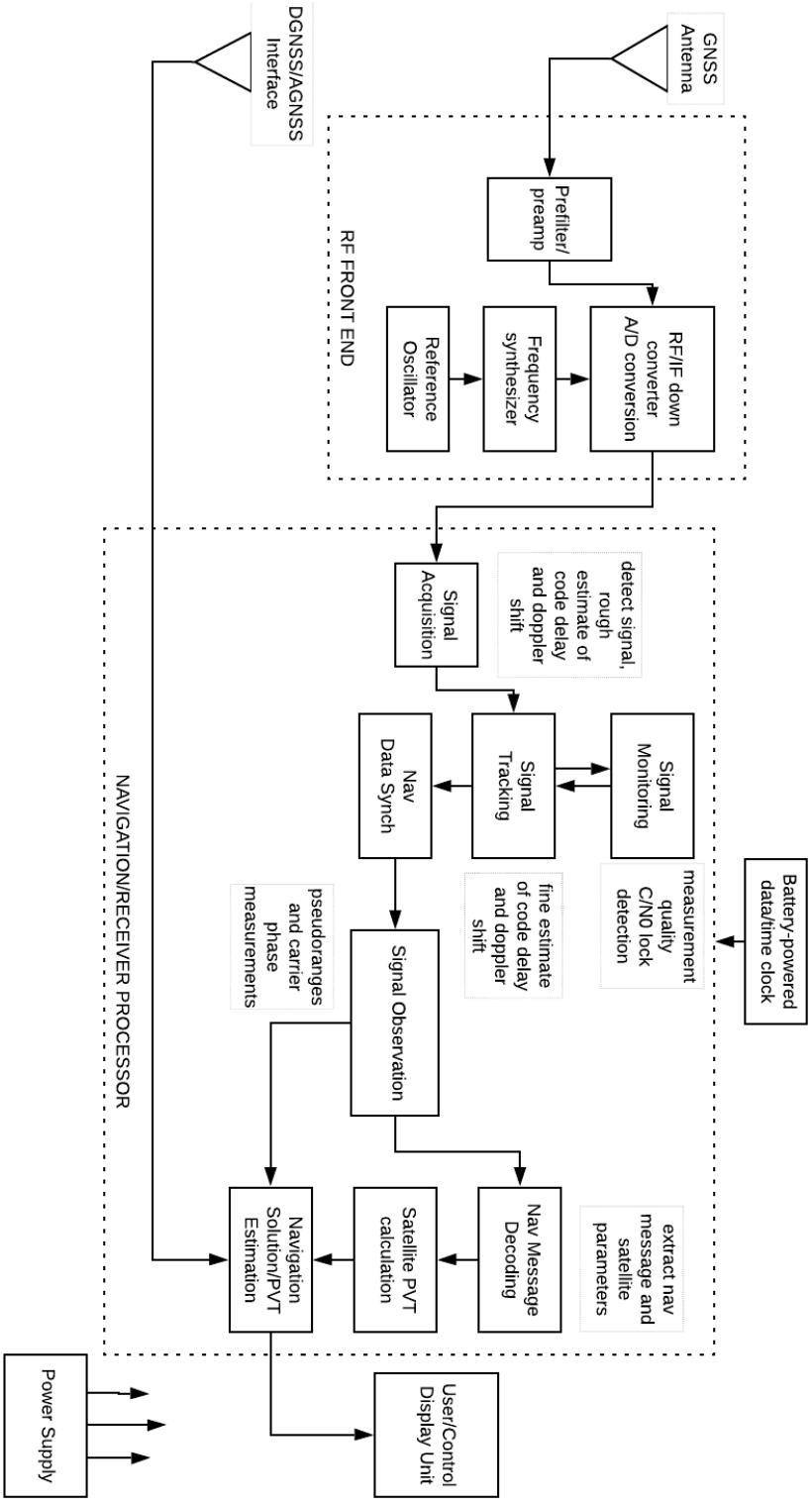

Figure 4. A Typical GNSS receiver.

(Adapted from: Kaplan et al., 2006 pg. 107; Kaplan et al., 2017 pg. 154; Gleason et al., 2009 pg. 12).

2.1.3 Software Defined GNSS receiver

Software defined GNSS receivers can be used for flexibility. The flowchart of a GNSS software defined receiver (see Figure 5) explains how the PVT solution is obtained.

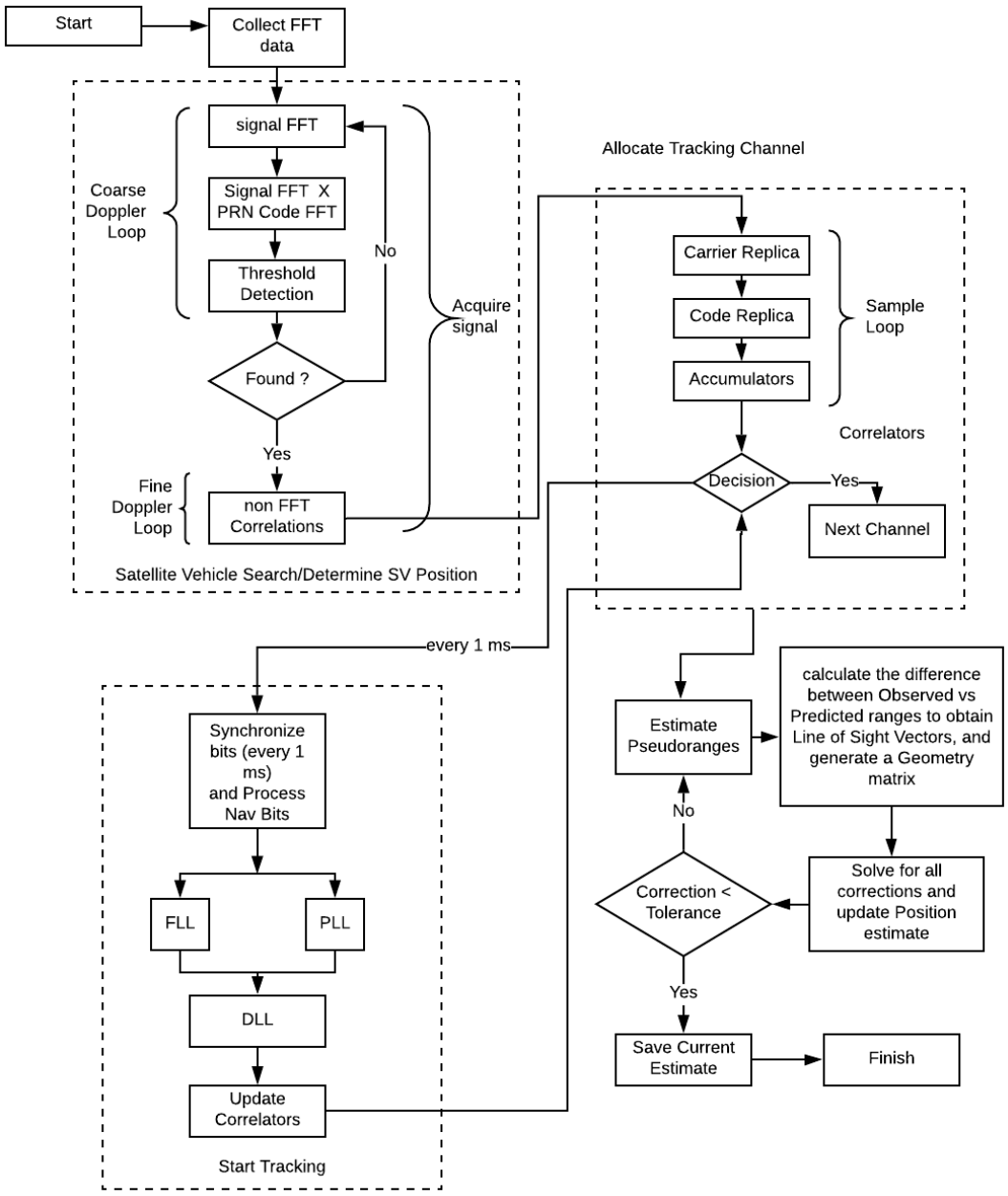

Figure 5. Software defined GPS receiver acquisition, tracking and navigation process. (Adapted from: Gleason et al., 2009a pg. 62; Gleason et al., 2009b).

a. Acquisition

Acquisition is a technique used to obtain a rough estimate (within +/- 0.5 chips) of a GPS/GLONASS/Beidou//Galileo satellite's Coarse/Acquisition (C/A) signal. It is important to consider frequency and time uncertainties when designing acquisition systems.

For acquisition, a fair amount of data is gathered and used for FFT acquisition. To achieve this, the satellite to search for is specified by scanning coarse Doppler bins. Then an FFT is applied on the sample input buffer. Afterwards, the sample FFT is multiplied with the pre-calculated PRN code FFT (the PRN is used to identify the satellite). Furthermore, an inverse FFT and a search for peaks exceeding the detection threshold is performed. Once a signal is obtained, a fine Doppler search is performed and the results (perform debug searches if specified) is stored. Finally, signals are allocated to a tracking channel.

b. Tracking

Tracking is the act of finding and maintaining fine synchronization. Phase-locked-loops (PLL) and Frequency-Locked-Loops (FLL) are used to achieve tracking and synchronization. PLLs are used for obtaining carrier phase information. FLLs are used to obtain carrier frequency information. It is important to consider the receiver noise error and tracking error when designing a GNSS code and carrier tracking loop system.

After acquisition, to achieve tracking the sample tracking loop is called every 1ms. Bit synchronization and process navigation bits are applied to the signal. It is then passed through a Frequency Locked loop (FLL) to obtain frequency information or Phase locked loop (PLL) to obtain Phase information. After which it is passed through a Delay Locked loop (DLL) to obtain the code information. Correlators are updated, and the next channel is searched/tracked.

c. Navigation Solution

Pseudo ranges and carrier phases are computed together with the navigation messages (decoded) to obtain a navigation solution of position, velocity and time. The Navigation process allows the PVT to be calculated and obtained.

To begin, the satellite position is determined by the Code delay and Doppler shift values. A rough estimate is used to guess the satellites position. Then signal observations are used to estimate the pseudoranges. To achieve this, a correction vs tolerance decision method is used. If the correction is greater than the tolerance, the pseudoranges are recomputed. Then the difference between the observed signal and the predicted ranges is noted to obtain Line of sight Unit vectors, and further Geometry Matrix. Functions are used to solve for corrections and the position estimate is updated until the correction is less than the tolerance value. At this point, the estimate is saved.

2.2 Global Satellite Navigation Systems (GNSS) Constellations

SATNAV systems can be categorized into two broad systems based on region of coverage. Global SATNAV systems and Regional SATNAV systems. Global SATNAV systems consist of the United States of America's Global Positioning System (GPS), Russian Global Navigation Satellite System (GLONASS), European Union (EU) Galileo Satellite System, and China's BeiDou Navigation Satellite System (BDS). Regional SATNAV Systems consist of, Indian Regional Navigation Satellite System (IRNSS) known by the operating name NavIC, and Japan's Quasi-Zenith Satellite System (QZSS). The major difference between these two categories is that Global SATNAV systems use geo-stationary orbit while the Regional SATNAV systems use inclined orbit to cover area of interest. Table 3 below shows the launch date, coverage area, coordinate reference frame, frequency/coding, and precision of various GNSS constellations.

Table 3. GNSS Constellations, Bands, Frequencies and Signals

Constellation	Coverage Category	Owner	No of Satellites in orbit	Orbit	Orbit Radius (Km)	Coordinate Reference Frame	Time /Period/Rev. or Sidereal time	Time start	Frequency/Coding	Precision
GPS	Global	USA	31	MEO	20,200	WGS84	GPST 11.97 h (11 h 58 min) /2	06 Jan 1980	1.563–1.587 GHz (L1) 1.215–1.2396 GHz (L2) 1.164–1.189 GHz (L5) CDMA	5m (no DGPS or WAAS)
GLONASS	Global	Russia	24	MEO	19,130	PZ-90	GLONASST 11.26 h (11 h 16 min) /2.125	02 Oct 1982	1.593–1.610 GHz (G1) 1.237–1.254 GHz (G2) 1.189–1.214 GHz (G3) FDMA/CDMA	4.5m – 7.4m
Galileo	Global	European Union	24	MEO	23,222	GTRF	GST 14.08 h (14 h 5 min) /1.7	22 Aug 1999	1.559–1.592 GHz (E1) 1.164–1.215 GHz (E5a/b) 1.260–1.300 GHz (E6) CDMA	1m (Public) 0.01m (Encrypted)
BeiDou	Global	China	33	GEO IGSO MEO	35,786 35,786 21,528	CGCS200 0	BDT 12.63 h (12 h 38 min) /1.888	30 Oct 2000	1.561098 GHz (B1) 1.589742 GHz (B1-2) 1.20714 GHz (B2) 1.26852 GHz (B3) CDMA	10m (Public) 0.1m (Encrypted)
IRNSS (NavIC)	Regional	India	7	GEO GSO	36,000	WGS 84	IRNWT 23.93 h (23 h 56 min) /1	01 July 2013	1176.45 MHz(L5) 2492.028 MHz (S) CDMA	1m (Public) 0.1m (Encrypted)
QZSS	Regional	Japan	4	GSO GEO	32,600 39,000	QZSSRT	QZSST 23.93 h (23 h 56 min) /1	01 Nov 2018	1575.42MHz (L1C/A,L1C,L1S) 1227.60MHz (L2C) 1176.45MHz (L5,L5S) 1278.75MHz (L6) CDMA	1m (Public) 0.1m (Encrypted)

The table above shows various GNSS constellations, their bands, frequencies and precision.

2.3 GNSS basic observables/ measurements

2.3.1 Radio Frequency Carrier

Radio frequency multiple carriers are used by GNSSs for signal propagation. This frequency is expressed as:

$$f_0 = \frac{1}{T_0}, \quad \text{expressed in units of cycles/second.} \qquad \text{(E.2.1)}$$

For GPS, the L band (1 – 2 GHz) is used. All other constellations use frequencies between 1 and 2 GHz. The carrier frequency is modulated with a modulation signal to convey all necessary satellite data and achieve precise user equipment localization. The modulation frequency is expressed as:

$$s(t) = a(t)\cos[2\pi f(t)t + \phi(t)] \qquad \text{(E.2.2)}$$

The parameters are as follows: Signal voltage $\boldsymbol{s(t)}$, amplitude $\boldsymbol{a(t)}$, frequency $\boldsymbol{f(t)}$, and phase offset $\phi(\boldsymbol{t})$. This signal can be phase, frequency or amplitude modulated.

2.3.2 Modulated Signal

To obtain a modulated signal, the unmodulated RF carrier is multiplied with the information signal to generate a waveform by Binary Phase Shift Keying (BPSK) modulation techniques.

Mathematically, the data waveform $\boldsymbol{d(t)}$ can be described as:

$$d(t) = \sum_{k=-\infty}^{\infty} \mathrm{d_k} P(\mathrm{t} - \mathrm{kTb}) \qquad \text{(E.2.3)}$$

Where, $\boldsymbol{d_k}$ is the kth data bit (in the set [−1, +1]) and pulse shape $\boldsymbol{p(t)}$.

The data waveform $\boldsymbol{d(t)}$ is a baseband signal because its frequency is concentrated around zero hertz. Modulating this data waveform with an RF carrier creates a band pass signal. The band pass signal's frequency content is concentrated around the carrier frequency.

2.3.3 GNSS Signal

A GNSS signal is product of the carrier frequency, the spreading code (PRN (pseudo random noise)) $\boldsymbol{C(t)}$ and the navigation data $\boldsymbol{D(t)}$.

It is given by the equation:

$$GNSS_s(t) = \sqrt{2P}C(t)D(t)cos[2\pi f\ (t)t + \phi\ (t)] \quad \text{(E.2.4)}$$

2.3.4 Pseudoranges

The pseudorange is the distance between the both antennas of a GNSS receiver and satellites when taking into account all biases such as satellite and receiver clock offsets, atmospheric delays etc.). It is measured as a function of signal transmission and reception time.

It is given by:

$$R_P(t) = c\ [t_r(T_2) - t^s(T_1)] \quad \text{(E.2.5)}$$

Where:

$\boldsymbol{c}$ = speed of light = 299,792,458 (m/s), $\boldsymbol{t_r(T_2)}$ is the signal reception time in the receiver clock time scale, and $\boldsymbol{t^s(T_1)}$ signal transmission time, in the satellite clocks time scale. (Kaplan et al., 2017 pg. 510).

The Pseudorange $\boldsymbol{R_P}$ measurement can be expressed as the geometric range $\boldsymbol{\rho}$ between the antennas of both the satellite and the receiver antenna phase centres $\left(\boldsymbol{\rho_r^s}\right)$ at transmission and reception time respectively, their respective clock biases $(\boldsymbol{dT^s})$ and

$(\boldsymbol{dt_r})$, tropospheric delay $\boldsymbol{T_r^s}$, ionospheric delay $\boldsymbol{I_{r,i}^s}$, measurement error $\boldsymbol{\varepsilon_P}$ caused by the receiver noise, and other sources of errors and biases as shown in (E.2.6):

$$R_P = \rho_r^s + c\ (dt_r(\ t_r) - dT^s(\ t^s)) + K_{P,r} - K_P{}^s + I_{r,i}^s + T_r^s + M_P + \varepsilon_P \quad \text{(E.2.6)}$$

$\boldsymbol{K_{P,r}}$, and $\boldsymbol{K_P^s}$ are the instrumental delays from the receiver and satellite. While $\boldsymbol{M_P}$, is the effect of multipath. $\boldsymbol{K_{P,r}}$, $\boldsymbol{M_P}$, and $\boldsymbol{K_P^s}$ are code and frequency dependent.

2.3.5 Carrier phase and phase-range measurements

Apart from the code, the distance between the satellite and the receiver can be measured with the carrier phase $(\boldsymbol{L}_i)$ of the signal. This model is termed carrier phase measurement model. It is defined as the beat frequency between the reference frequency generated by the receiver (generated by the local oscillator) and the received satellite signal's carrier frequency (Gurtner, W., 2007).

The carrier phase measurements ($\Phi^s_{r,i} = \lambda_i \phi^s_{r,i}$) can be modelled as:

$$\boldsymbol{\Phi}^s_{r,i} = \rho^s_r + c\left(dt_r(t_r) - dT^s(t^s)\right) - I^s_{r,i} \\ \ldots + T^s_r + \lambda_i B^s_{r,i} + d\Phi^s_{r,i} + \varepsilon_\phi \qquad \text{(E.2.7)}$$

Where, $\boldsymbol{\Phi}^s_{r,i}$ is the phase-range of the transmitted satellite navigation signal; and receiver local oscillator, λ_i is the wavelength of the carrier, $B^s_{r,i}$ is the phase bias of the carrier, and $d\Phi^s_{r,i}$ is the correction terms the carrier-phase. These terms are as follows: Offsets in the Antenna phase center, station displacements caused by earth tides, satellite clock relativity, and phase windup effect.

It is more precise (in the order magnitude of two) than the code measurements. However, the integer number of wavelength $(\lambda_i N)$ are ambiguous, and needs to be resolved, hence the term integer ambiguity resolution. Range discontinuities or signal jumps occur as a result of random ambiguities changes each time the receiver loses signal lock with the satellites. From (E.2.7), the phase bias $B^s_{r,i}$ can be derived as shown in (E.2.8):

$$B^s_{r,i} = \Phi_{r,0,i} - \Phi^s_{0,i} + N^s_{r,i} \qquad \text{(E.2.8)}$$

Where $N^s_{r,i}$ is the carrier-phase integer ambiguity, carrier-cycle ambiguity.

It can be observed that the ionospheric term is negative for both code and phase. This implies that the carrier phase measurement is advanced as a result of the ionosphere. This advance is equal to the delay on the code measurements. (Navipedia, 2020c; Navipedia, 2020d).

2.3.6 Geometric range between satellite antennas and receiver antennas

Geometric range is the real distance between the antenna phase center positions of the satellites and receivers in the inertial coordinate system.

It is given by:

$$\rho_r^s = \|U(t_r)r_r(t_r) - U(t^s)r^s(t^s)\| \quad \text{(E.2.9)}$$

Where, $U(t)$ is the coordinate transformation matrix at the time t from ECEF to ECI (earth center inertial), $r_r(t_r) = (x_r, y_r, z_r)^T$ is the receiver antenna phase center position at time t_r, and $r^s(t^s) = (x^s, y^s, z^s)^T$ is the satellite antenna phase center position at signal transmission time t^s using the ECEF (earth center earth fixed) coordinates system.

Accounting for the effect of earth rotation $\boldsymbol{\omega}_e$ as shown in Figure 6, (E.2.9) can be expressed as shown in (E.2.9b) with a precision level of 1mm.

$$\rho_r^s \approx \|r_r(t_r) - R_z\big(\boldsymbol{\omega}_\mathbf{e}(t_r - t^s)\big)r^s(t^s)\| \quad \text{(E.2.9b)}$$

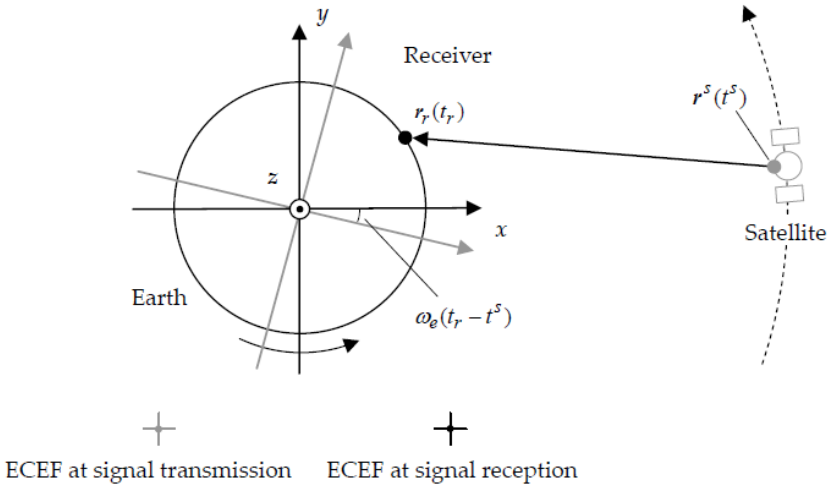

Figure 6. Diagram of Geometric Range between satellite antennas and receiver antennas.

(Source: Takasu, T., 2007-2013, pg. 140).

The figure above shows the geometric range between satellite and receiver antennas.

In this thesis, the effect of earth rotation will be corrected with IGS rapid combined earth rotation parameter (EOP) orbit solutions.

2.3.7 Direction of Satellite's Azimuth and elevation angles.

The signal propagation between the receiver and the antenna expressed as a unit LOS (line-of-sight) vector in the ECEF coordinate is given by:

$$e_r^s = \frac{r^s(t^s) - r_r(t_r)}{\|r^s(t^s) - r_r(t_r)\|} \quad \text{(E.2.10)}$$

From (E.2.8), the angles of azimuth Az_r^s and elevation El_r^s from the receiver to the satellite as:

$$e_{r,enu}^s = E_r e_r^s = (e_e, e_n, e_u)^T \quad \text{(E.2.11)}$$

$$Az_r^s = arctan(e_e, e_n) \quad \text{(E.2.12)}$$

$$El_r^s = arcsin(e_u) \quad \text{(E.2.13)}$$

E_r is the coordinate rotation matrix from ECEF to the receiver's local coordinates. Figure 7 shows the receiver elevation and azimuth angles, and local coordinates.

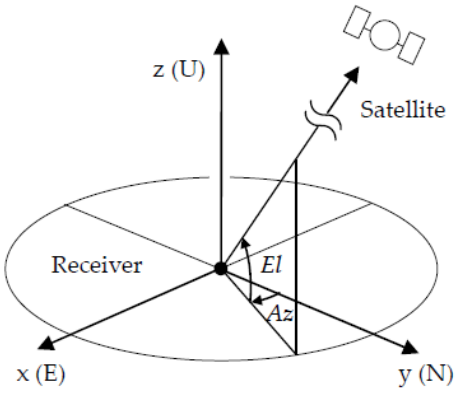

Figure 7. Receiver elevation and azimuth angles, and local coordinates.

(Source: Takasu, T., 2007-2013 pg. 141).

The figure above shows Receiver elevation and azimuth angles, and local coordinates.

For this thesis, an elevation mask angle of 10 degrees was selected.

2.4 GNSS error sources

GNSS suffers from a variety of errors. These errors negatively impact the GNSS receiver PVT solution. Table 4 shows various error sources, their description, error ranges and compensation.

Table 4. GNSS errors, description, error range and correction.

(Source: Novatel, 2020a)

S/N	Source	Description	Error Range	Error Compensation and solution.
1	Satellite Clocks	Clock error of 10 nanoseconds results in 3 metres position error.	±2 m	Augment with precise clock data from SBAS, PPP service providers. Use RTK or DGNSS receiver configuration.
2	Orbit Errors	Orbital changes or perturbations cause position errors.	±2.5 m	Download precise ephemeris data from SBAS, PPP service providers. Use RTK or DGNSS receiver configuration.
3	Ionospheric Delays	Ions in the atmosphere (at 80km - 600km above earth) delay satellite signals leading to significant satellite position error. It is difficult to predict as it depends on earth and space weather conditions.	±5 m	Use Multiple satellite transmission frequencies, and RTK or DGNSS systems.
4	Tropospheric Delays	Caused by earth weather conditions such as atmospheric temperature, humidity and pressure in the troposphere.	±0.5 m	Use RTK and DGNSS systems.
5	Receiver Noise	Caused by receiver hardware and software.	±0.3 m	Use high-end / quality receivers.
6	Multipath	Caused by reflecting surfaces near the receiver.	±1 m	Select an open location for the antenna. Use quality receivers.

The table above shows various GNSS error sources and methods to resolve them.

The errors due to the ionosphere and troposphere can be modelled mathematically as stated below:

2.4.1 Troposphere Model

The mathematical expression for the standard atmosphere is:

$$p = 1013.25 \times (1 - \ 2.2557 \times 10^{-5}\ h)^{5.2568} \quad \text{(E.2.14)}$$

$$T = 15.0 - \ 6.5 \ \times 10^{-3} h + 273.15 \quad \text{(E.2.15)}$$

$$e = 6.108 \ \times \exp\left\{\frac{17.15T - 4684.0}{T - 38.45}\right\} \times \frac{h_{rel}}{100} \quad \text{(E2.16)}$$

From (E.2.14, E.2.15, and E.2.16), the tropospheric delay T_r^S also known as the Saastamoinen model is derived as:

$$T_r^S = \frac{0.002277}{\cos z}\left\{p + \left(\frac{1255}{T} + 0.05\right) e - \tan^2 z\right\} \quad \text{(E.2.17)}$$

Where the total pressure (hPa) is denoted as p, the absolute air temperature (K) as T.

The partial pressure (hPa) of water vapour is termed as e, while h is the geodetic height above MSL (mean sea level. h_{rel} is the relative humidity, and $z = \frac{\pi}{2} - El_{\mathrm{r}}^{S}$ is the angle of zenith (expressed in radians).

In our experiments, the Saastamoinen model was used for tropospheric corrections. This RTKLib configuration approximates the geodetic height as the ellipsoidal height, and fixes the relative humidity at 70% (Takasu, T., 2007-2013, pg. 149).

2.4.2 Broadcast Ionosphere Model

GPS, and QZSS navigation data use the following broadcast parameters to correct for ionospheric errors in single frequency GNSS devices:

$$p_{ion} = (\alpha_0, \alpha_1, \alpha_2, \alpha_3, \beta_0, \beta_1, \beta_2, \beta_3)^T \quad \text{(E.2.18)}$$

From the above equation, the L_1 ionospheric delay I_r^S (m) also known as the Klobuchar model can be obtained as (IS-GPS-200F 2011):

$$I_r^S = \{ \begin{matrix} F \times (5\times10^{-9} & (|x|>1.57) \\ F \times \left(5\times10^{-9} + \sum_{n=1}^{4} \alpha_n \varphi_m^n \times \left(1 - \frac{x^2}{2} + \frac{x^4}{24}\right)\right) & (|x|\leq 1.57) \end{matrix} \} \quad \text{(E.2.19)}$$

Where:

$$\Psi = \frac{0.0137}{El+0.11} - 0.022 \quad \text{(E.2.20)}$$

$$\varphi_i = \varphi + \Psi \cos Az \quad \text{(E.2.21)}$$

$$\lambda_i = \lambda + \frac{\Psi \sin Az}{cos\ \varphi_i} \quad \text{(E.2.22)}$$

$$\varphi_m = \varphi_i + 0.064 \cos(\lambda_i - 1.617) \quad \text{(E.2.23)}$$

$$t = 4.32 \times 10^4 \lambda_i + t \quad \text{(E.2.24)}$$

$$F = 1.0 + 16.0 \times (0.53 - El)^3 \quad \text{(E.2.25)}$$

$$x = \frac{2\pi(t-50400)}{\sum_{n=0}^{3} \beta_n \varphi_m^n} \quad \text{(E.2.26)}$$

2.4.3 Ionosphere-free LC (linear combination)

The presence of dual frequency GNSS signal measurements allows for the elimination of errors caused by the ionosphere. To achieve this a LC (linear combination) of dual-frequency measurements is used in GNSS data processing.

The expression is given below:

$$P_{r,LC}^S = C_i P_{r,i}^S + C_j P_{r,j}^S \quad \text{(E.2.27)}$$

$$\Phi_{r,LC}^S = C_i \Phi_{r,i}^S + C_j \Phi_{r,j}^S \quad \text{(E.2.28)}$$

Where $P_{r,LC}^S$ is the ionosphere-free LC of L_i and L_j is the pseudorange, and $\Phi_{r,LC}^S$ is the phase-range.

The coefficients C_i, and C_j can be expressed as:

$$C_i = \frac{f_i^2}{f_i^2 - f_j^2} \quad \text{(E.2.29)}$$

$$C_j = \frac{-f_j^2}{f_i^2 - f_j^2} \quad \text{(E.2.30)}$$

The frequencies (Hz) of L_i and L_j measurements are f_i and f_j respectively.

The frequencies, L_1 and L_2 are used for GPS, GLONASS and QZSS, while L_1, and L_5 are used for Galileo in current version of RTKLib.

It is important to note that the Ionosphere-free LC (linear combination) was not used in during this master thesis because it increases the 2D error. Future experiments will investigate why this occurred. Therefore the broadcast ionosphere model was used as the ionosphere corrections for both single and dual frequency GNSS devices.

2.4.4 GNSS satellite ephemerides and clocks

Broadcast ephemerides are data which contain information on the current and predicted location (position, and velocity), timing, and health of a GNSS satellite. This information is used to estimate the relative location of the satellite in respect to its earth position. This data can be used for future satellite condition predictions, and for scheduling GNSS data collection. The broadcast ephemeris data (in RINEX format) is valid for only 30 days (NASA's Archive of Space Geodesy Data, CDDIS, 2021a).

Precise ephemerides and clock data are station and satellite orbit solutions used for GNSS post processing. The clock data is used for determining the precise coordinates of observation stations, gravity field parameters and earth orientation parameters (EOP).

Earth Orientation Parameters (EOP) contains information on the earth's rotation.

In this research work, the broadcast ephemerides will be obtained from the ublox GNSS devices, while the earth orientation parameters (EOP), precise ephemerides and clock data will be obtained from NASA's CDDIS archives in SP3-c (Hilla, S., 2010), and clock RINEX (Ray, J., & Gurtner, W., 2010), formats respectively.

The final, most consistent IGS orbit solutions with the highest quality generated 13 days after the end of the solution week will be used. While the IGS rapid combined earth rotation parameter solution will be used as the EOP data. The Extended Standard Product- 3 (SP3c) format is used for all orbit solutions (NASA's Archive of Space Geodesy Data, CDDIS, 2021b).

2.5 Differential GNSS

Differential GNSS is a technique commonly used to improve GNSS performance. It uses conventional surveying techniques to determine to a high degree of accuracy, the position of a fixed GNSS receiver known as a base station. Furthermore, ranges to GNSS satellites in-view are determined by the base station with the following techniques:

- The code-based positioning technique.
- Satellite coordinate determination using precisely known orbit ephemerides and satellite time.

A comparison is made between the surveyed position and the position calculated from the satellite ranges by the base station. Any difference in position is as a result of atmospheric delay, satellite ephemeris and clock errors. These errors are sent to other receivers (rovers) by the base station to include them in the rovers' positional calculations. To apply real-time corrections, a minimum of four GNSS satellites in view and a data link is always required between the base station and a rover. The rover's computed position absolute accuracy is dependent on that of the base station. Signals from satellites used by both base station and rovers experience similar atmospheric conditions if the base station and rovers are not too distant from each other. Hence, Differential GNSS can be used in cases where tens of kilometres separation exist between base stations and receivers. (Source: Novatel, 2020b).

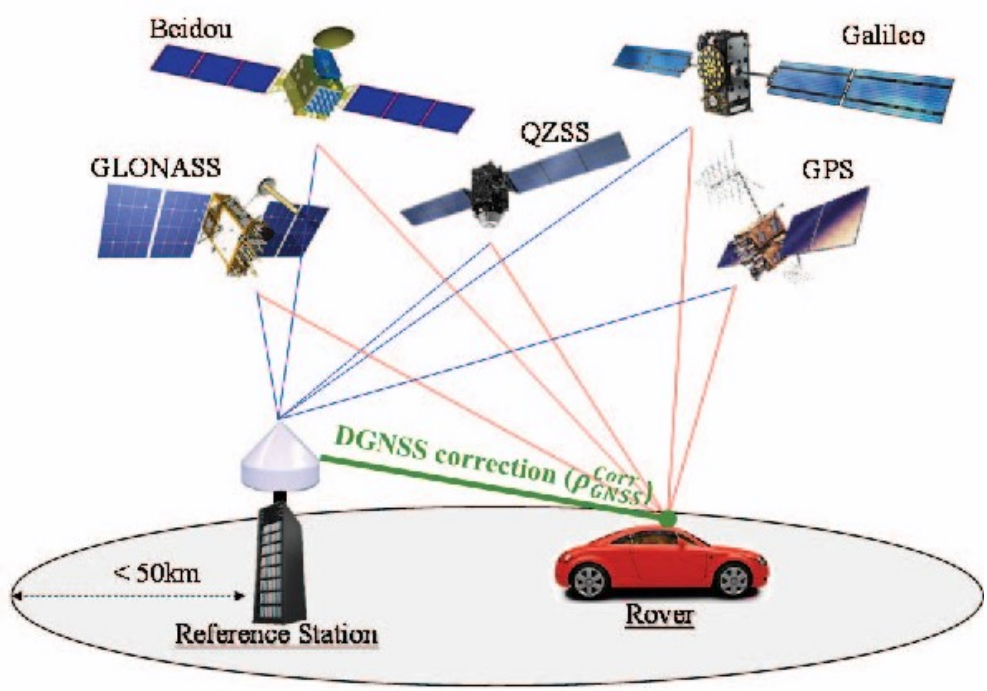

Figure 8. Schematic of a differential GNSS system.

(Source: Li-Ta Hsu et al., 2016).

The figure above shows the Schematic of a differential GNSS system. In the figure, major GNSS constellations such as GPS, Galileo and GLONAS are shown.

Types of DGNSS techniques include, Real Time Kinematics (RTK), and Wide Area Real Time Kinematics (WARTK). Both techniques are based on carrier-phase measurements.

(Navipedia, 2020c).

Examples of commercial DGNSS are:

a. Trimble provides various navigation solutions for different industry sectors such as; maritime, agriculture and automotive industries. For example, Trimble GNSS Planning Online ™ enables users to select various combinations of satellites constellations, view radio frequency properties, availability and coverage area. (GNSS Planning Online, 2017-2018)
b. Geotrim Oy is an organization that provides GNSS positioning, spatial data and geospatial resources in Finland. For instance its Trimnet VRS service ® provides

24/7 customizable, flexible GNSS measurement solutions with an accuracy classes of 1 mm, 1 cm, 10 cm, 30 cm and 50 cm. It is also an authorised reseller of Trimble products. (Geotrim Oy, 2020a and b).

c. Leica Geosystems provides surveying solutions such as smart antennas, GNSS software, and receivers. For example, the Leica GNSS Spider ™ is a continuously operating reference network. While the Leica CrossCheck Service™ is a web-based GNSS Quality control/deformation monitoring service. (Leica Geosystems, 2020a and b).
d. The Finnish Reference (FinnRef) Station is a free DGNSS services provided by the National Land and Survey of Finland (NLS). The NLS also provides other spatial data positioning services (FinnRef, 2020). Other DGNSS services providers in the Nordic region include (Mattias Eriksson, 2017):
e. The Swedish Maritime Administration (Swedish Maritime Administration, 2020).
f. The Norwegian Mapping Authority (Norwegian Mapping Authority, 2020).
g. National Land Survey of Iceland (NLSI) with a GNSS Permanent Tracking Station Reykjavik, Iceland managed by Sonel (National Land Survey of Iceland, 2020a and b).
h. The EUREF Permanent GNSS Network (EUREF Permanent GNSS Network, 2020).

2.6 Satellite-based augmentation systems

An SBAS system (shown in figure 9) is comprised of geosynchronous satellites, reference stations, and master stations/uplink stations.

GNSS signals from satellites are received by geographically distributed reference stations (in a SBAS service area), and forwarded to master stations. Wide-area corrections can be computed by the master stations as the location of these reference stations are precisely known. These corrections are then uploaded to the

SBAS satellite by the master stations and broadcasted to the GNSS receivers located within the SBAS coverage area.

The corrections are received by the user equipment and applied in range calculations.

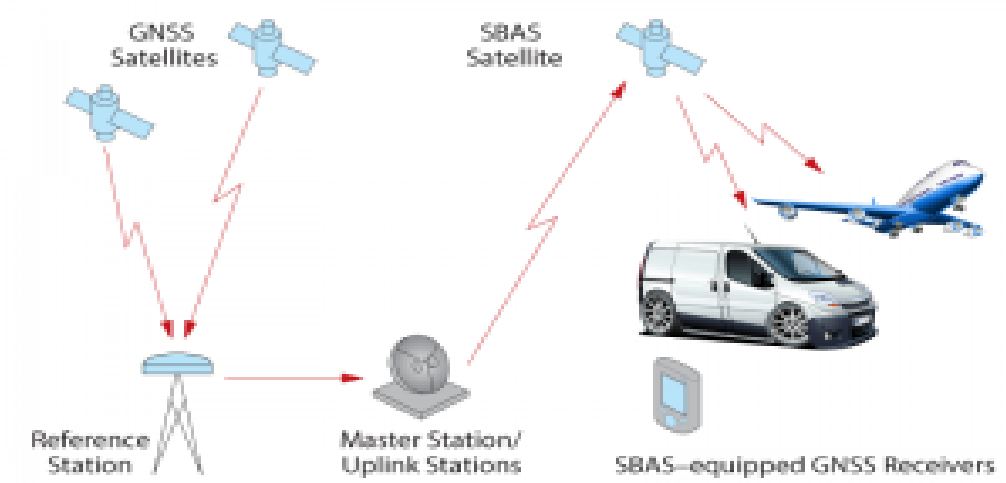

Figure 9. SBAS (Satellite-based Augmentation System) schematic diagram.

(Source: Novatel, 2020e).

The figure above shows an SBAS system comprising of a reference station, master stations, GNSS satellites, SBAS satellites and SBAS-equipped GNSS receivers.

Satellite-based Augmentation Systems (SBAS) are used for position accuracy enhancements in application for which DGNSS would be expensive or impractical; for instance where rovers are sparsely dispersed over a large geographical area. It is a geosynchronous satellite system that provides GNSS signal accuracy, integrity and availability improvement services. To improve the positioning accuracy, wide-area corrections for GNSS errors are transmitted by SBAS network. Integrity enhancements is achieved by detecting satellite signal errors, and notifying receivers not to track those satellites. The SBAS network transmits satellite ranging signals to improve signal availability as shown in figure 10.

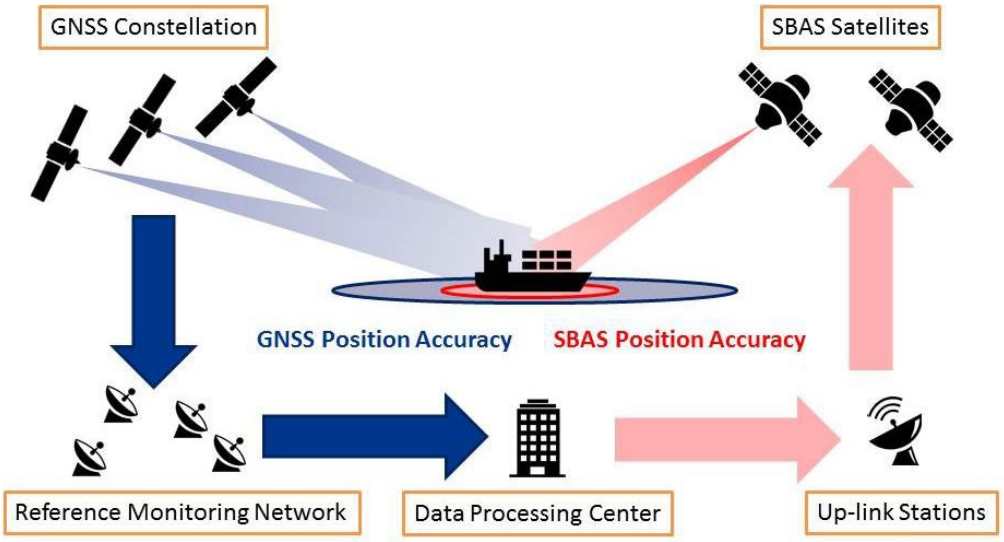

Figure 10. EGNOS architecture.

(Source: Sergio Magdaleno et al., 2019).

The figure above shows the architecture of The European Geostationary Navigation Overlay Service (EGNOS). This architecture is comprised of GNSS constellations, SBAS satellites, Reference monitoring network, data processing centres and up-link stations.

Various SBAS services is being planned or implemented such as:

a. Wide Area Augmentation System (WAAS)

   It was developed by the US Federal Aviation Administration (FAA). It provides GPS corrections and a certified level of integrity to the aviation industry, thereby assisting aircraft in carrying out precision approaches at airports. Civilian users in North America can use these corrections without paying a fee.

   The GPs data is received by a Wide Area Master Station (WMS) from Wide Area Reference Stations (WRS) located across the United States. Differential corrections are calculated by the WMS, which then uploads them to two WAAS geostationary satellites. The WAAS broadcasts these corrections to receivers throughout the United States. Corrections for ionospheric delay, satellite timing, and satellite orbits are computed and processed separately on demand by user application.

Correction data is broadcasted on the same GPS frequency, hence the same antenna and receiver equipment can be used. Line of sight (LOS) is required for correction data transmission from one of the WAAS satellites. (Federal Aviation Administration, 2020).

b. European Geostationary Navigation Overlay Service (EGNOS)

The European Geostationary Navigation Overlay Service (EGNOS) is an augmentation system developed by the European Space Agency in partnership with the European Commission (EC) and EUROCONTROL (European Organization for the Safety of Air Navigation).

With EGNOS, the accuracy of positions derived from GNSS signals is improved. Users are also alerted on GPS signal reliability. Several European countries and member states within the European Union are served by three EGNOS satellites. Differential correction data is broadcasted publicly and can be used for safety-of-life applications. These satellites are located over the eastern Atlantic Ocean, the Indian Ocean, and the African mid-continent (European GNSS Agency, 2020a)

c. MTSAT Satellite-based Augmentation Navigation System (MSAS)

MSAS is an SBAS providing augmentation services to Japan. Two Multi-functional Transport Satellites (MTSAT) and a network of ground stations are used for GPS signals augmentation. (NEC Corporation, 2020).

d. GPS-Aided GEO Augmented Navigation System (GAGAN)

Flight navigation over the Indian airspace is supported by the GAGAN. This SBAS system uses three geostationary satellites, 15 reference stations, three uplink stations and two control centres. It is compatible with other SBAS systems, such as WAAS, EGNOS and MSAS. (Government of India, 2020).

e. System for Differential Corrections and Monitoring (SDCM)

The SDCM was developed by the Russian Federation for both the GLONASS and GPS navigation integrity monitoring and accuracy improvements. Plans for L1 SBAS coverage over the Russian territory was slated for 2016, and L1/L5 coverage by 2018. Additional services in L1/L3 GLONASS for Precise Point

Positioning (PPP) was scheduled for 2018. (Russian System of Differential Correction and Monitoring (Russian SDCM), 2020).

Other SBAS systems include China's SNAS (Satellite Navigation Augmentation System) and South Korea's Wide Area Differential Global Positioning System (WADGPS). (European GNSS Agency, 2020b).

f. Ground-Based Augmentation System

A Ground Based Augmentation System (GBAS) uses VHF radio link to provide receivers with differential corrections and satellite integrity monitoring. It is also known as a Local Area Augmentation System (LAAS). It is comprised of several GNSS antennas positioned at known locations, a central control system and a VHF radio transmitter. Coverage area is small (by GNSS standards). It is used by applications (such as airports) requiring high levels of accuracy, availability and integrity. (Novatel, Satellite-based Augmentation Systems 2020).

3. POSITION, VELOCITY, TIME (PVT) ESTIMATION

3.1 Code based positioning (standard positioning algorithms)

3.1.1 Least Squares Estimation Method (LSE)

To obtain an optimal user position solution, pseudorange errors of visible satellites are assumed to be Gaussian (independent and identically distributed).

The weighted least squares (WLS) estimate is given by:

$$\Delta\mathbf{x} = (\mathbf{G}^T\mathbf{R}^{-1}\mathbf{G})^{-1}\mathbf{G}^T\mathbf{R}^{-1}\delta\rho \quad \text{(E.3.1)}$$

Where **R** is the covariance matrix of the pseudorange errors, Δx is offset in the position of the user and time bias relative to the linearization point, and, $\delta\rho$ is the net error in the pseudorange values.

Excluding $\mathbf{R}^{-1}$ and $\delta\rho$ gives the least-squares solution matrix or pseudoinverse:

$$\Delta\mathbf{x} = (\mathbf{G}^{\mathrm{T}}\mathbf{G})^{-\mathbf{1}}\mathbf{G}^{\mathrm{T}} \quad \text{(E.3.2)}$$

In cases of signal quality differences in pseudorange measurements, a weighted estimation procedure is applied on the user equivalent range errors (UEREs) by expressing these UEREs as an observation covariance matrix R:

$$\mathbf{R} = \mathbf{C}_{\delta\rho\delta\rho} = \begin{bmatrix} \sigma_1^2 & 0 & 0 \\ 0 & \ddots & 0 \\ 0 & 0 & \sigma_n^2 \end{bmatrix} \quad \text{(E.3.3)}$$

Various signal properties such as thermal noise in receiver, multipath (treated as a noise-like quantity), and signal-to-noise ratio of measurements make up the data in the covariance matrix, **R**. It is common practice to arbitrarily choose the data in covariance matrix.

The Least Square Estimation algorithm is used for obtaining both SPP (single point positioning), and SPP (with SBAS corrections) solutions. RTKLib uses an iterated weighted Least Square Estimator.

Propagation of covariance:

The propagation of covariance is used to determine the covariance matrix of any arbitrary linearly combined measurement whose property (expected values

characteristics) is expressed as a data covariance matrix as shown in (E.3.4, and E.3.5):

For an arbitrary linear equation: $\boldsymbol{y} = \boldsymbol{Ax}$ where $\boldsymbol{V_{xx}}$ is the covariance matrix of x

The propagation of covariance is given by:

$$\boldsymbol{V}_{yy} =< yy^T >=< \boldsymbol{Axx^T}\, \boldsymbol{A^T} >= \mathbf{A} < \mathbf{xx^T} > \mathbf{A^T} \quad \text{(E.3.4)}$$

$$\boldsymbol{V}_{yy} = \boldsymbol{AV}_{xx}\boldsymbol{A^T} \quad \text{(E.3.5)}$$

Applying the rules of (E.3.4, and E.3.5) to the weighted least squares problem gives:

$$\hat{\mathbf{x}} = \begin{bmatrix}\delta \mathrm{x} \\ \delta b\end{bmatrix} = (\mathbf{G}^T\mathbf{R}^{-1}\mathbf{G})^{-1}\mathbf{G}^T\mathbf{R}^{-1}\delta\rho \quad \text{(E.3.6)}$$

$$< \hat{\mathbf{x}}\hat{\mathbf{x}}^T >= (\mathbf{G}^{\mathrm{T}}\mathbf{R}^{-1}\mathbf{G})^{-1}\mathbf{G}^{\mathrm{T}}\mathbf{R}^{-1}\ < \delta\rho\delta\rho^T >\ \mathbf{R}^{-1}\ \mathbf{G}(\mathbf{G}^{\mathrm{T}}\mathbf{R}^{-1}\mathbf{G})^{-1} \quad \text{(E.3.7)}$$

$$\mathbf{V}_{\hat{\mathbf{x}}\,\hat{\mathbf{x}}}\ = \mathbf{C}_{\left[\begin{smallmatrix}\delta \mathrm{x} \\ \delta b\end{smallmatrix}\right]\left[\begin{smallmatrix}\delta \mathrm{x} \\ \delta b\end{smallmatrix}\right]} = (\mathbf{G}^{\mathrm{T}}\mathbf{R}^{-1}\mathbf{G})^{-1} \quad \text{(E.3.8)}$$

Where $\mathbf{V}_{\hat{\mathbf{x}}\,\hat{\mathbf{x}}}$ is the parameter estimate covariance, and $\mathbf{R}$ is the measurement's covariance matrix.

Post-fit residuals:

The differences between observed parameters and estimated parameters are called post-fit residuals ($\mathbf{v}$). They occur as a result of the absorption of noise measurements into the estimated parameters. They are not the same as the errors in the data. The post-fit residuals' covariance matrix can be derived from the propagation of covariance (see E.3.4, E.3.5) as shown below:

$$\delta\rho = \mathbf{G}\begin{bmatrix}\delta \mathbf{x} \\ b\end{bmatrix} + \ \tilde{\varepsilon}_T \quad \text{(E.3.9)}$$

$$\begin{bmatrix}\delta \mathbf{x} \\ b\end{bmatrix} = (\mathbf{G}^{\mathrm{T}}\mathbf{R}^{-1}\mathbf{G})^{-1}\mathbf{G}^{\mathrm{T}}\mathbf{R}^{-1}\delta\rho \quad \text{(E.3.10)}$$

$$\mathbf{v} =\ \delta\rho -\ \mathbf{G}\begin{bmatrix}\delta \mathrm{x} \\ b\end{bmatrix} = [\mathbf{I} - \underbrace{\mathbf{G}(\mathbf{G}^{\mathrm{T}}\mathbf{R}^{-1}\mathbf{G})^{-1}\mathbf{G}^{\mathrm{T}}\mathbf{R}^{-1}}_{\text{Amount error reduced}}]\tilde{\varepsilon}_T \quad \text{(E.3.11)}$$

$$\mathbf{C}_{\mathrm{vv}} =< \mathbf{vv}^T >= \mathbf{R} -\ \mathbf{G}(\mathbf{G}^{\mathrm{T}}\mathbf{R}^{-1}\mathbf{G})^{-1}\mathbf{G}^{\mathrm{T}} \quad \text{(E.3.12)}$$

Where, $\mathbf{vv}^T$ is the minimum normalized squared residuals.

3.2 Carrier phase-based positioning algorithms

3.2.1 Real Time Kinematics (RTK)

RTK is a carrier-based ranging technique (see figure 11). Ranging accuracy are more precise than that of code-based positioning by large magnitudes (Novatel, 2020d). In RTK the range is computed by estimating the number of carrier cycles between the satellite and the rover station. This value is multiplied with the wavelength of the carrier. The range contains errors from satellite clocks and ephemerides, ionosphere and troposphere. These errors are eliminated by an "ambiguity resolution" process which determines the number of whole cycles, and obtains precise integer carrier-based measurements. In high precision GNSS receivers, ambiguities can be resolved almost instantaneously. The rover's position is determined by using algorithms that incorporate ambiguity resolution and differential correction. These corrections are dependent on the base station's location, and quality of its ephemerides.

The position accuracy is dependent on the accuracy of the differential corrections, the quality of base station and rover transceivers, and the distance between base station and the rover (known as a baseline). It is important to select the right location so as to minimize interference and multipath.

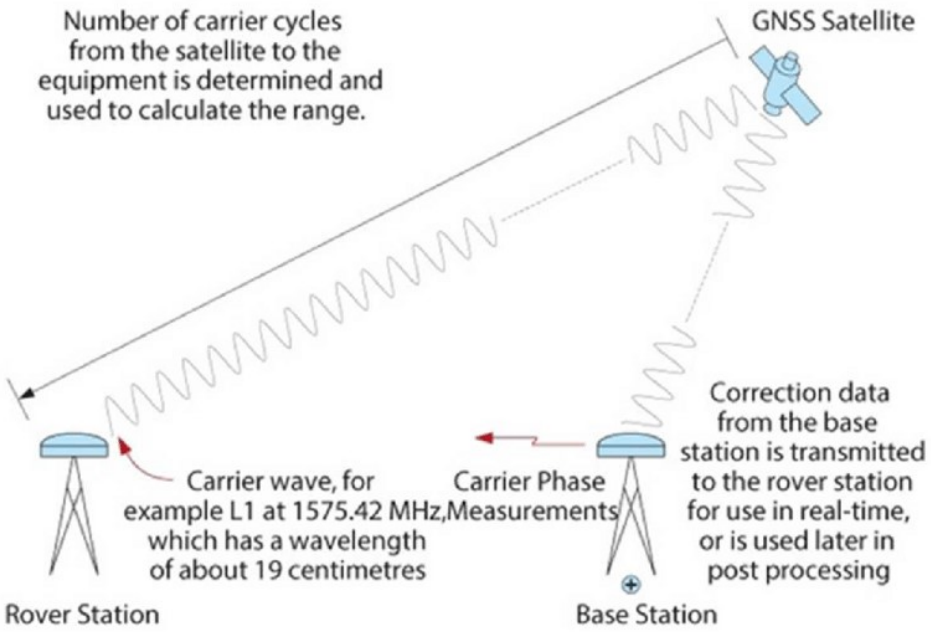

Figure 11. Real time Kinematics (RTK) Schematic.

(Source: Novatel, 2020d).

The figure above shows a schematic diagram of a Real time Kinematic (RTK) system comprising of GNSS satellites, rover and base stations.

Network RTK is implemented with a number of widely spaced permanent stations. In Network RTK, a central processing station receives positioning data from the permanent stations regularly. When needed, user terminals send their approximate location to the central station, while and the central station transmits corrected position information to the user terminal. By doing so, the number of required RTK base stations is reduced. Data can also be transmitted over various wireless media such as cellular radio.

a. Kalman Filters:

   The Kalman filter is used GNSS PVT (position, velocity, and timing) applications. It incorporates past measurements and facilitate the fusion of GNSS measurements with measurements from other sensors. This mathematical algorithm produces estimates of the state vector x at discrete

epochs of time (indexed by subscript k) using a vector of noisy measurements **z** with (possibly time-varying) covariance **R** that is assumed to be available at each epoch. In general, the state vector x is the set of variables of interest. Since the Kalman filter algorithm necessarily operates in discrete time, the dynamics matrix F can be assumed piece-wise constant and well approximated over discrete time intervals by the corresponding $\mathbf{\Phi}$ matrix:

$$\mathbf{\Phi} = \mathbf{I} + \mathbf{F}\Delta t + \mathbf{F}^2 \Delta t^2/2 + \ldots. \qquad \text{(E.3.13)}$$

Where **I** represents the *n* × *n* identity matrix; *n* is the dimension of the state vector; and Δt represents the propagation interval.

Depending on the severity of the host's dynamics, an approximation to $\mathbf{\Phi}$ of first or second order in $\boldsymbol{\Delta t}$ is generally adequate. As an alternative to including more terms in the expansion of $\mathbf{\Phi}$, the size of $\boldsymbol{\Delta t}$ can be reduced, resulting in multiple propagation steps of the filter for each measurement update step as shown in figure 12 below:

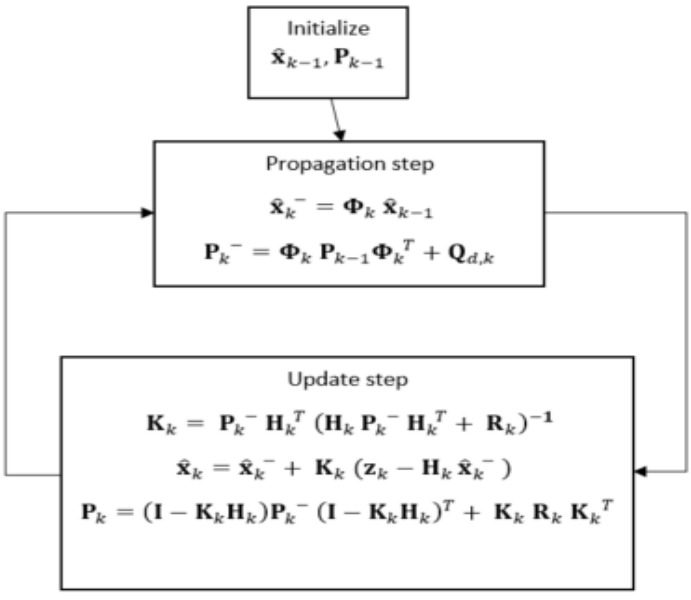

Figure 12. Kalman filter processing architecture.

(Source: Kaplan et al., 2015, pg. 813).

The figure above shows the processing architecture of a Kalman filter with Initialization, propagation and update steps.

b. Extended Kalman Filter (EKF):

In RTKLib, EKFs are used to obtain DGNSS, RTK, and static final solutions.

The EKF a weighted, recursive least squares estimator. The outputs from an EKF will often be better than those from the least squares method. EKF assumes some knowledge of the receiver dynamics. When these assumptions are incorrect, problems can arise quickly. The basic concept behind the EKF filter is that some of the parameters being estimated are random processes and as data are added to the filter, the parameter estimates depend on new data and the changes in the process noise between measurements. (Kaplan et al., 2015 pg. 813).

With EKF, A measurement vector $\mathbf{z}_k$ at epoch $\mathbf{t}_k$ can be used to estimate the state vector $\mathbf{x}$, covariance matrix $\mathbf{P}$ of an unknown model parameter as shown in (E.3.14):

$$\hat{\mathbf{x}}_k = \hat{\mathbf{x}}_k^- + \mathbf{K}_k\,(\mathbf{z}_k - \mathbf{H}_k\,\hat{\mathbf{x}}_k^-) \qquad \text{(E.3.14)}$$

$$\mathbf{P}_k = (\mathbf{I} - \mathbf{K}_k\mathbf{H}_k)\mathbf{P}_k^-\,(\mathbf{I} - \mathbf{K}_k\mathbf{H}_k)^T + \mathbf{K}_k\,\mathbf{R}_k\,\mathbf{K}_k^T \qquad \text{(E.3.14)}$$

$$\mathbf{K}_k = \mathbf{P}_k^-\,\mathbf{H}_k^T\,(\mathbf{H}_k\,\mathbf{P}_k^-\,\mathbf{H}_k^T + \mathbf{R}_k)^{-\mathbf{1}} \qquad \text{(E.3.15)}$$

$\hat{\mathbf{x}}_k$ is the estimated state vector and $\mathbf{P}_k$ is the covariance matrix at epoch time $\mathbf{t}_k$.

Assuming system non-linearity, the EKFs state vector update time and covariance matrix are:

$$\hat{\mathbf{x}}_{k+1}^- = \mathbf{F}_k^{\mathbf{k+1}}\,\hat{\mathbf{x}}_k \qquad \text{(E.3.16)}$$

$$\mathbf{P}_{k+1}^- = \mathbf{F}_k^{\mathbf{k+1}}\mathbf{P}_k\left(\mathbf{F}_k^{\mathbf{k+1}}\right)^T + \mathbf{Q}_k^{\mathbf{k+1}} \qquad \text{(E.3.17)}$$

With state transition matrix $\mathbf{F}_k^{\mathbf{k+1}}$, and System noise covariance matrix $\mathbf{Q}_k^{\mathbf{k+1}}$ between epoch time $\mathbf{t}_k$ and $\mathbf{t}_{k+1}$.

c. DD (Double-Difference):

With the DD (Double-Difference) RTK algorithm, and other biases can be eliminated. From (E.2.7 and E.2.8), a simplified carrier phase observation equation for a given satellite and epoch can be derived as:

$$\phi = \rho - I + Tr + c(b_{Rx} - b_{Sat}) + \ [\![N\lambda + \varepsilon]\!]_{\phi} \qquad \text{(E.3.18)}$$

Where $\boldsymbol{I}$, is ionosphere delay, $\boldsymbol{Tr}$ is the troposphere delay; $\boldsymbol{b_{Rx}}$, is the offset of the receiver clock from the reference (GPS) time; $\boldsymbol{b_{Sat}}$, is the offset of the satellite clock from the reference (GPS) time; $\boldsymbol{c}$, is the speed of light in vacuum; $\boldsymbol{\lambda}$, is the carrier nominal wavelength; $\boldsymbol{N}$, is the carrier-phase ambiguity (integer number); $\boldsymbol{\varepsilon_{\phi}}$, are the measurement noise components, multipath and other effects;

Computing the geometrical range $\boldsymbol{\rho}$, between the satellite and the receiver as a function of coordinates of the satellite $(\mathrm{x_{Sat}}, \mathrm{y_{Sat}}, \mathrm{z_{Sat}})$ and receiver $(\mathrm{x_{Rx}}, \mathrm{y_{Rx}}, \mathrm{z_{Rx}})$ gives:

$$\rho = \sqrt{[\![(x_{Sat} - \mathrm{x_{Rx}})]\!]^2 + [\![(y_{Sat} - \mathrm{y_{Rx}})]\!]^2 + [\![(z_{Sat} - \mathrm{z_{Rx}})]\!]^2} \qquad \text{(E.3.19)}$$

Assuming that there are two receivers *a,* and *b* making simultaneous measurements at the same nominal time to satellites *1* and *2*, the double difference observable becomes:

$$\phi_a^{12} - \phi_b^{12} = \rho_a^{12} - \rho_b^{12} - I_a^{12} + I_b^{12} + Tr_a^{12} - Tr_b^{12} + \cdots$$

$$\ldots + \lambda\left(N_a^{12} - N_b^{12}\right) + \varepsilon_a^{12} - \varepsilon_b^{12} \qquad \text{(E.3.20)}$$

From (E.3.15), clock offsets and hardware biases of both the satellite and receiver cancel out. Note that $N_a^{12} - N_b^{12}$ is the single difference ambiguities difference, and can be parameterized as a new ambiguity parameter N_{ab}^{12}. N_{ab}^{12} is therefore an integer as all other non-integer terms caused by clock offsets and other biases in the GPS carrier phase observation has been eliminated. This is the advantage of the double-difference algorithm.

It is also possible to estimate the double difference ambiguity using a float approach instead of an integer one. However, accuracy will decrease from cm-level to dm-level. Therefore, it is standard RTK practice to fix ambiguities to integer figures.

Integer Ambiguity Resolution:

This is the process of resolving the float carrier-phase ambiguities into integer values after the estimated position of the receiver antenna (rover), velocity and float single difference carrier-phase biases has been obtained. It is done to improve the accuracy and convergence time. The best accuracy occurs when RTK carrier phase ambiguities are fixed to integers. Integer ambiguities are resolved in the following ways:

a. LAMBDA method: The LAMBDA method is an efficient search strategy (Teunissen et al., 1995). In RTKLib, and extension of this method called MLAMBDA (Chang et al., 2005). It uses a linear transformation and a tree-search algorithm to reduce the integer vector space and obtain integer ambiguities $\underset{\wedge}{\mathrm{N}}$ and their corresponding covariance matrix $\mathbf{Q_N}$ by eliminating the initial phase terms of the receiver as shown in (E.3.21) below:

$$\check{\mathrm{N}} = \mathrm{argmin}_{\mathrm{N}\in\mathrm{Z}}\left(\left(\check{\mathrm{N}} - \underset{\wedge}{\mathrm{N}}\right)^{\mathrm{T}} \mathrm{Q_N}^{-1}\left(\check{\mathrm{N}} - \underset{\wedge}{\mathrm{N}}\right)\right) \qquad \text{(E.3.21)}$$

Where $\check{\mathrm{N}}$ is the most fitting integer vector.

The solution $\boldsymbol{R}$ is validated by comparing the weighted sum of the squared residuals of the second best solution $\check{\mathrm{N}}_2$ to the best $\check{\mathrm{N}}$ to a threshold R_{thres} as stated in (E.3.21) below:

$$R = \frac{\left(\left(\check{\mathrm{N}}_2 - \underset{\wedge}{\mathrm{N}}\right)^{\mathrm{T}} \times \mathrm{Q_N}^{-1}\left(\check{\mathrm{N}}_2 - \underset{\wedge}{\mathrm{N}}\right)\right)}{\left(\left(\check{\mathrm{N}} - \underset{\wedge}{\mathrm{N}}\right)^{\mathrm{T}} \mathrm{Q_N}^{-1}\left(\check{\mathrm{N}} - \underset{\wedge}{\mathrm{N}}\right)\right)} > R_{thres} \qquad \text{(E.3.22)}$$

$$\begin{pmatrix}\check{\mathrm{r}}_{\mathrm{r}} \\ \tilde{\mathrm{v}}_r\end{pmatrix} = \begin{pmatrix}\hat{\mathrm{r}}_{\mathrm{r}} \\ \dot{\mathrm{V}}_r\end{pmatrix} - \mathrm{Q_{RN}}\mathrm{Q_N}^{-1}\left(\underset{\wedge}{\mathrm{N}} - \check{\mathrm{N}}\right) \qquad \text{(E.3.23)}$$

Finally, (E.3.23) is used to obtain the FIXED position of the rover

antenna $\check{\mathrm{r}}_{\mathbf{r}}$ and velocity of the receiver antenna $\tilde{\mathrm{v}}_{r}$ or the FLOAT solutions of $\hat{\mathrm{r}}_{\mathrm{r}}$ and $\dot{\mathrm{v}}_{\boldsymbol{r}}$ if the validation fails.

RTKLib employs four types of integer ambiguity resolution technique, namely: Continuous, Instantaneous, Fix and Hold, and Ambiguity resolution in PPP (PPP-AR). In Continuous mode, the static integers are resolved by estimating the phase biases continuously, over every epoch with the aid of a default Kalman Filter with filter updates from the float solution only. In the Instantaneous mode, phase bias estimates are recalculated every epoch. In Fix-and-Hold, the filter update is achieved by using the pseudo-measurements generated by the fixed solution. (Tim Everett, 2021a). (E.3.21, E.3.22, and E.3.23) are also used for Fix-and-Hold method, except that the carrier-phase bias DD parameters are tightly constrained to the fixed/resolved integer values.

In this research, the Minimum Ratio to Fix Ambiguity will be set to a default value of 3.0, a minimum fix count of 0 and the “Fix-and-Hold” method will be used. The Fix and Hold method will be selected as it enables the tracking of moving GNSS receivers (Takasu, T., 2007-2013, pgs. 165-169).

b. Other methods include Double Difference Ambiguity fixing and Undifferenced Ambiguity Fixing.
(Novatel, 2020a; Navipedia, 2020d; Navipedia, 2020e).

3.2.2 Wide Area Real Time Kinematics (WARTK)

The Wide-Area Real-Time Kinematics (WARTK) technique was developed by the gAGE/UPC group. It extends the scale of local area real-time carrier phase ambiguity resolution services. This creates wide area services with greater than 100 km baselines.

For dual and tri-frequency systems, WARTK uses an optimal combination of accurate ionospheric and geodetic models in a permanent reference stations network.

The range is limited to a few ten of kilometres as a result of differential ionospheric correction. The use of ionosphere correction data prevents resolving integer ambiguities in real-time thereby limiting accuracy to sub-decimetre levels. One way to improve accuracy is by using multiple reference stations with shorter baselines (<20 km). However, a very large amount of this stations would be needed to serve the European region.

To increase the service area of dual and tri-frequency RTK/NRTK systems, optimal processing of carrier-phase GNSS observables and accurate real-time ionospheric-correction computations are needed. (Navipedia, 2020f; Navipedia, 2020g; European GNSS Agency, 2020c).

3.2.3 Precise Point Positioning (PPP)

PPP is a positioning technique that provides high-level accuracy from a single receiver without a base station (Wikipedia, 2020b). To achieve this, GNSS system errors are modelled and removed with the aid of satellite clock and orbit corrections, obtained globally networked reference stations. Satellite or internet services are used to deliver these corrections to the end users resulting centimetre-level accuracy (3cm). The GNSS observables for a PPP system are carrier phase and differential delays between different GNSS frequency signals. Significant convergence time is required to resolve biases and achieve decimetre level accuracy. To increase positioning accuracy, PPP systems provide corrections similar to those of an SBAS system. However, users have to pay for these corrections. Unlike the SBAS system which is regional, PPP systems are global. Figure 13 shows the schematic diagram of a typical PPP system.

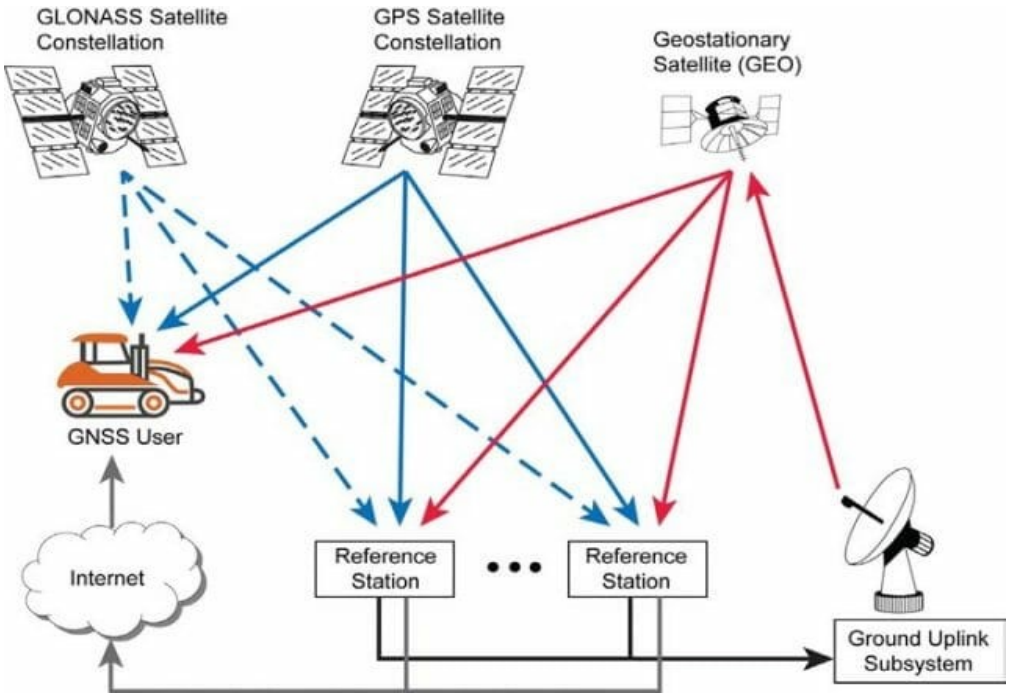

Figure 13. Schematic diagram of a Precise Point Positioning (PPP) System

(Source: Novatel, 2020c).

The figure above shows the schematic diagram of a PPP system. Data from the reference station via the Internet are also provided to the GNSS user.

Precise positioning are used in robotics, autonomous navigation, agriculture, construction, and mining. Its primary weakness, when compared to other conventional consumer GNSS solutions are higher power processing requirement, longer full-accuracy convergence times of up to tens of minutes, and external ephemeris correction connections. As a result of this, applications such as fleet tracking and asset management may not be willing to pay for a PPP service only to gain a few extra centimetre of precision. However, PPP services may be useful in robotic applications where on-board processing power and regular data transfer are assumed.

The following methods can be used to reduce errors in PPP:

a. Dual-Frequency Operation: By using a combination of dual-frequency GNSS measurements, the first-order ionospheric delay can totally be eliminated as it is proportional to the carrier wave frequency.

b. External Error Correction Data: Satellite orbit and clock corrections such as the TerraStar service (TerraStar, 2021) from Novatel (Hexagon, 2021) can be used. The TerraStar service uses Inmarsat satellites to generate and broadcast corrections to end-users. Other PPP service providers exist such VERIPOS (VERIPOS, 2021), and OmniSTAR (OmniSTAR, 2021).

c. Tropospheric delay modelling: The UNB3m model, an improved version of UNB3 is a neutral atmosphere delay model developed by the University of New Brunswick in Canada. It is used to correct tropospheric delay errors (Leandro et al., 2006).

d. PPP Filter Algorithms: An EKF is used for the PPP estimation. With an EKF, states of the position, receiver clock error, troposphere delay and carrier-phase ambiguities are estimated. The algorithm minimizes noise in the system and achieves centimetre level positioning accuracy. Successive GNSS measurements are used to improve the estimates of the EKF states until they converge to stable and accurate values. In PPP, the convergence time for less than 10cm horizontal error is typically between 20 and 40 minutes and depends on the number of satellites available, satellite geometry, quality of the correction products, method of correction application, receiver multipath environment and atmospheric conditions.

   ZD (Zero-Difference) measurement models:

   The ZD (zero-difference) measurement equations similar to the single point positioning model is used for PPP instead of DD (Double-difference) measurement model utilized in RTK. The ZD (zero-difference) measurement model is stated below:

$$\boldsymbol{\Phi}^{s}_{r,LC} = \rho^{s}_{r} + c\,(dt_r(t_r) - dT^{s}(t^{s})) + T^{s}_{r} + B^{s}_{r,LC} + d\Phi^{s}_{r,LC} + \varepsilon_{\phi} \quad \text{(E.3.24)}$$

$$\boldsymbol{P}^{s}_{r,LC} = \rho^{s}_{r} + c\,(dt_r(t_r) - dT^{s}(t^{s})) + T^{s}_{r} + \varepsilon_{P} \quad \text{(E.3.25)}$$

   Where $\boldsymbol{\Phi}^{s}_{r,LC}$ is phase-range of the ionosphere-free LC, $P^{s}_{r,LC}$ is the pseudorange measurements. Comparing with (E.3.27), ionosphere delay has

been eliminated by using the ionosphere-free LC. (Novatel, 2020c; Wikipedia, 2020b).

3.3 Receiver Autonomous Integrity Monitoring (RAIM) Fault Detection and Exclusion (FDE)

RAIM is a user receiver algorithm used to ascertain the integrity of the GNSS solution. To achieve this, the algorithm compares each smoothed pseudorange measurement with each other to check for consistency in satellite measurements. The receiver contains the RAIM algorithm. A minimum of six visible satellites is required to detect and exclude a satellite causing large position errors from the navigation solution without interruptions.

To achieve this, the RAIM algorithm takes noise assumptions and geometry measurements, probabilities of the maximum false starts allowed, and missed detections. These metrics are then used to produce the Horizontal Protection Level (HPL) (Kaplan et al., 2017).

Before RAIM-FDE is applied, the solution has to be validated. From (E.3.12), the solution is validated if the normalized squared residuals $\mathbf{vv}^T$ is less than the chi-square distribution of the number of estimated parameters and measurements as shown in (E3.26). If the SSE (sum of squared errors) of a satellite exceed a threshold, the satellite is excluded as shown below:

$$\frac{\mathbf{vv}^{\boldsymbol{T}}}{m-n-1} < \chi^2_{\alpha}(m-n-1) \qquad \text{(E.3.26)}$$

$$\mathrm{GDOP} < \mathrm{GDOP}_{\mathrm{thres}} \qquad \text{(E.3.27)}$$

Where the number of estimated parameters is $\mathbf{n}$, the number of measurements is $\mathbf{m}$, with chi-square distribution of $\mathbf{n}$ degree of freedom $\boldsymbol{\chi^2_{\alpha}(n)}$, at $\boldsymbol{\alpha = 0.1\%}$.

In RTKLib, with RAIM-FDE enabled, the final solution is the minimum normalized squared residuals $\mathbf{vv}^T$ (see E.3.12) if the chi-square test in (E3.26) fails.

3.4 GNSS accuracy metrics

3.4.1 Dilution of Precision (DOP)

Dilution of precision is a term used to characterize the accuracy of the position time solution. There are separate DOP metrics such as, HDOP – horizontal dilution of precision, VDOP – vertical dilution of precision, PDOP – position (3D) dilution of precision, TDOP – time dilution of precision, and GDOP – geometric dilution of precision.

The Geometric Dilution of precision is ratio of the change in the output location (the x, y, z position) to the change in the measured data (pseudoranges) at time t. It is fairly the ratio of position error to range error.

From (E.3.2, and E.3.3), for $\boldsymbol{X}_T = (x_u, y_u, z_u, ct_b)$ the covariance matrix $\boldsymbol{Q}$ of the partial derivative of the pseudoranges of x, y and z position, and with respect to its receiver clock bias (t) of the satellites can be derived:

$$\mathbf{Q} = \begin{bmatrix} \sigma_{x_u}^2 & \sigma_{x_u y_u}^2 & \sigma_{x_u z_u}^2 & \sigma_{x_u ct_b}^2 \\ \sigma_{x_u y_u}^2 & \sigma_{y_u}^2 & \sigma_{y_u z_u}^2 & \sigma_{y_u ct_b}^2 \\ \sigma_{x_u z_u}^2 & \sigma_{y_u z_u}^2 & \sigma_{z_u}^2 & \sigma_{z_u ct_b}^2 \\ \sigma_{x_u ct_u}^2 & \sigma_{y_u ct_b}^2 & \sigma_{z_u ct_b}^2 & \sigma_{ct_b}^2 \end{bmatrix} \quad \text{(E.3.28)}$$

$$PDOP = \frac{\left(\sqrt{\sigma_{x_u}^2 + \sigma_{y_u}^2 + \sigma_{z_u}^2}\right)}{\sigma_{UERE}} \quad \text{(E.3.29)}$$

$$TDOP = \frac{\left(\sqrt{\sigma_{ct_b}^2}\right)}{\sigma_{UERE}} \quad \text{(E.3.30)}$$

$$GDOP = \frac{\left(\sqrt{\sigma_{x_u}^2 + \sigma_{y_u}^2 + \sigma_{z_u}^2 + \sigma_{ct_b}^2}\right)}{\sigma_{UERE}} \quad \text{(E.3.31)}$$

$$GDOP = \frac{\left(\sqrt{PDOP^2 + TDOP^2}\right)}{\sigma_{UERE}} \quad \text{(E.3.32)}$$

$$HDOP = \frac{\left(\sqrt{\sigma_{x_u}^2 + \sigma_{y_u}^2}\right)}{\sigma_{UERE}} \quad \text{(E.3.33)}$$

$$VDOP = \frac{\left(\sqrt{\sigma_{z_u}^2}\right)}{\sigma_{UERE}} \quad \text{(E.3.34)}$$

Note that the positions of the satellites, and clock bias will be estimated by using satellite ephemerides and clocks from a reference station. The table below shows the accuracy ratings for various DOP levels.

Table 5. Dilution of Precision (DOP) accuracy ratings.

DOP Value	Rating	Description
1	Ideal	Highest precision and confidence level in positional measurements for sensitive applications e.g. Aviation
1-2	Excellent	Excellent precision and confidence level in positional measurements.
2-5	Good	Minimum acceptable confidence level for good positional prediction.
5-10	Moderate	Positional measurements can be used for calculations. Recommends open sky view, and improvement in fix quality.
10-20	Fair	Low confidence level of positional measurements should be used only for rough estimation.
>20	Poor	Poor confidence level of positional measurements with errors up to 300 meters for a 6-meter accuracy device. Discard measurements.

The table above show various DOP values, their corresponding rating and description.

DOP statistics from GNSS devices used for this experiments will be observed and recorded (See Chapter 4).

3.4.2 GNSS Availability

GNSS Availability is the percentage of time in which the services of a navigation system is usable. GNSS accuracy is expressed as:

$$\sigma_P = DOP \times \sigma_{UERE} \qquad \text{(E.3.35)}$$

Where σ_P is the positioning accuracy standard deviation, and σ_{UERE} is the satellite pseudorange measurement' standard deviation. Various DOPs such as HDOP, PDOP, GDOP, and VDOP can be used to determine this accuracy. The geometry of the satellites at any given location and time of the day determines the accuracy of GNSS availability (Kaplan et al., (2017)).

GNSS Availability is influenced by GNSS almanac data, location, date of prediction (GNSS almanacs are accurate for up to a week), elevation mask angle, terrain mask, satellite outages, and maximum DOP (Kaplan et al., 2017).

The desired Accuracy is affected by the threshold of the maximum acceptable DOP value. Hence, the commonly used service availability threshold in GIS performance standards is a PDOP (position dilution of precision) ≤ 6 (U.S. Department of Defense, Global Positioning System Standard Positioning Service Performance Standard, 2008).

For this research, an elevation mask angle of 10 degrees, and a maximum DOP of 5.0 will be used. This implies that the reject threshold of GDOP (Geometric Dilution of precision) is 5.0 for all GNSS devices. Consequently, the GNSS is declared unavailable if the DOP exceeds 5.0 by the processing software (in our case, RTKLib). The author experimented with lower GDOP threshold and observed that lower threshold below 5.0 resulted in no signal availability for the Samsung Galaxy s8 mobile device. Signal availability was noticed in the u-blox GNSS receivers at a lower threshold of 1.5.

3.5 GNSS post processing software

RTKLIB is an open source program package for standard and precise positioning with GNSS (global navigation satellite system). RTKLIB consists of a portable program library and several APs (application programs) utilizing the library for real-time and post-processing. Various processing modes such as Single, DGPS/DGNSS, Kinematic, Static, Moving-Baseline, Fixed, PPP-Kinematic, PPP-Static and PPP-Fixed are supported. Standard formats and protocols such as RINEX, RTCM, BINEX, NTRIP 1.0, NMEA 0183, SP3-c, ANTEX 1.4, IONEX 1.0, NGS PCV and EMS 2.0 are also supported. With RTKLIB, proprietary messages from GNSS vendors like NovAtel, u-blox, Furuno, JAVAD, etc. can be read, decoded and processed.

The GNSS post processing mode available in RTKLib are explained below:

a. Code based Single Point Processing Mode in RTKLIB

   RTKLIB employs an iterated weighted LSE (least square estimation) for the ”Single” (single point positioning) mode with or without SBAS corrections. To perform a single point positioning with SBAS corrections, an input SBAS file is necessary. Ionosphere Correction options can be set by applying a broadcast ionospheric model, SBAS ionospheric model, Ionosphere-free linear combination with dual frequencies, Estimate ionospheric parameter STEC (slant total electron content), broadcast ionosphere model provided by QZSS, or by using IONEX TEC grid data.

   A user should set Troposphere Correction (zenith total delay at rover and base-station positions) parameters by applying the Saastamoinen model, SBAS tropospheric model (MOPS), Estimate ZTD (zenith total delay) parameters as EKF states, Estimate ZTD and horizontal gradient parameters as EKF states.

b. Code-based DGPS/DGNSS Processing Mode in RTKLIB

   The EKF (extended Kalman filter), GNSS signal measurement and ephemeris, ionosphere and troposphere correction models are used to obtain the final solutions for DGPS/DGNSS Processing Mode.

c. Carrier-phase Processing Modes in RTKLIB

   For Carrier-phase processing, the following processing modes are supported:

   a. Static: Carrier-based Static positioning
   b. Kinematic: Carrier-based Kinematic positioning
   c. Moving-Base: Moving baseline
   d. Fixed: Rover receiver position is fixed
   e. PPP Kinematic: Precise Point Positioning with kinematic mode
   f. PPP Static: Precise Point Positioning with static mode
   g. PPP Fixed: Rover receiver position is fixed with PPP mode

Final solutions for the above processing modes are obtained with the EKF (extended Kalman filter), and integer ambiguity resolution algorithms. (Takasu, T., 2007-2013, pg. 1).

4. LOW - COST IMPLEMENTATION OF SPP, SPP+SBAS, PPP AND RTK

GNSS Data were acquired from stationary and dynamic tests at two different locations over different time periods using various GNSS receivers as shown in Figure 14 and 15 respectively.

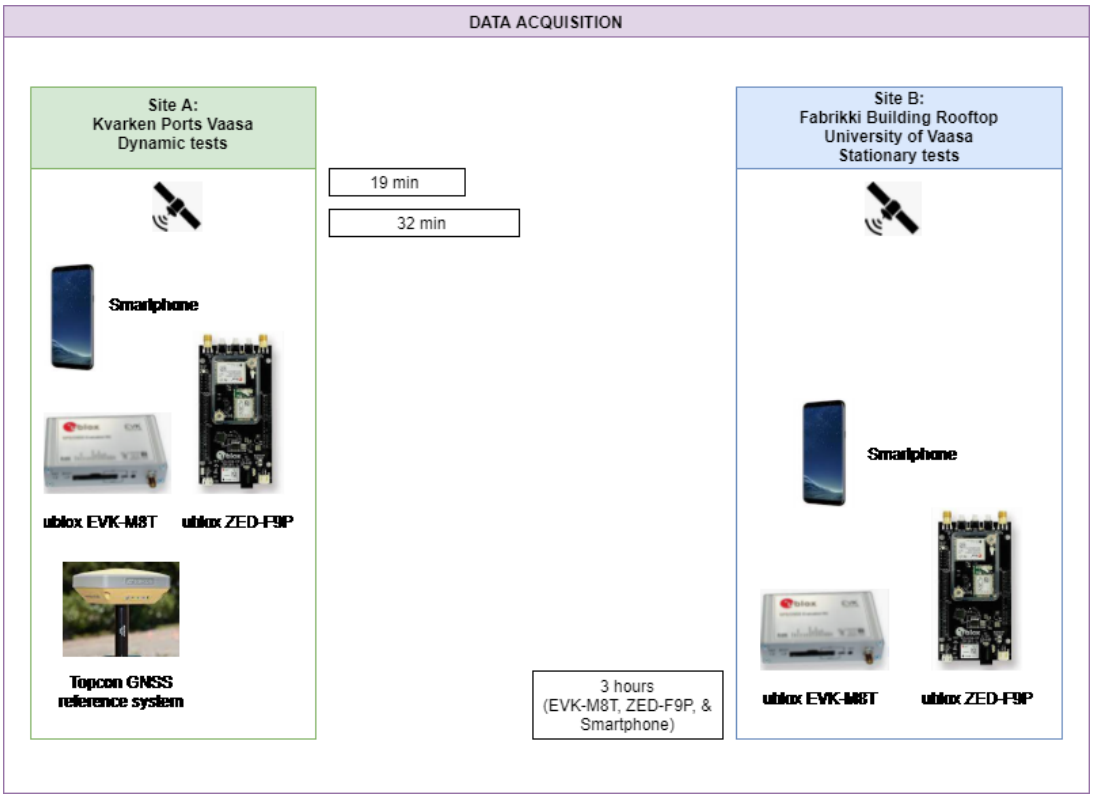

Figure 14. Synthetic outline of data acquisition procedures.

In the figure above, various GNSS devices such as dual frequency u-blox ZED-F9P, single frequency u-blox EVK-M8T, and smartphone are used to collect data for a duration of 19 and 32 minutes during the dynamic tests at site A, and for 3 hours during the stationary tests at site B.

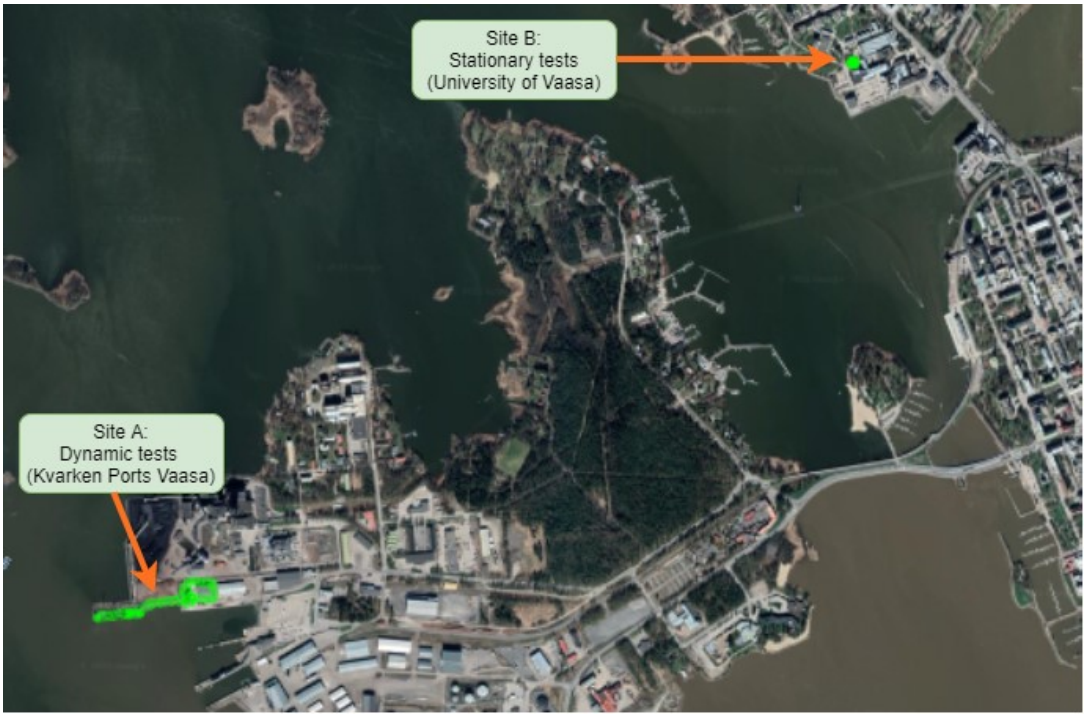

Figure 15. Google map with KML plots of experiments.

(Source: Google Earth Engine, 2021. All rights reserved).

In the figure above, Site A is a port test location with high multi-path environment characteristics, and shadowing. Site B is located at the University of Vaasa. The roof top of Fabrikki building was used to collect static data.

4.1 Stationary test setup at University of Vaasa

Static data were obtained from the roof top of Fabrikki building at the University of Vaasa. Data collected from all receivers for an observation period of 3 hours as shown in Table 6.

Table 6. GNSS Observation Information for stationary tests.

LOCATION	**FABRIKKI BUILDING ROOFTOP, UNIVERSITY OF VAASA**
Date of observation	02.10.2020
Session length	3 hours (180 minutes)
Time (seconds of the day)	34200 – 45000
Week number	276
Day number	2 (Tuesday)
GPS Time of Week since 1st epoch	2125
Rover Observation Data	GNSS Receivers
Base Station Observation	VAA200FIN_R_20202760000 _01D_30S_MO.00o
Satellite and station clock solution	igs21255.clk
Ionospheric Correction	igsg2760.20i
EOP (Earth Orientation Parameters) Data	igr21255.erp
SBAS Data	276-PRN123-h00-h23.ems

The table above shows information on observation date, session length, base station and correction parameters used for stationary tests.

Test Equipment:

a. U-blox ZED-F9P-01B-00 (C099-F9P-1-03) Dual Frequency Receiver with Multi-band antenna.
b. U-blox EVK-M8T-0-01 (NEO-M8T-0-10) GNSS Evaluation Kit; Single Frequency receiver.
c. Samsung Galaxy S8 Android 9 Smartphone, Model Number: SM-G950F, Build-number: PPR1.180610.011.G950FXXU9DTF1.
d. Geo++ RINEX 2.1.6 (GNSS data logger for smartphones).

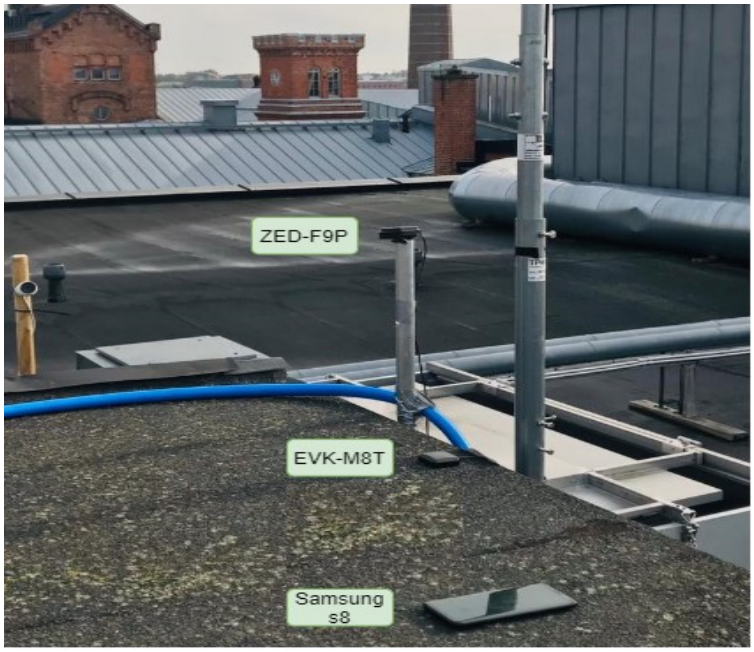

Figure 16. Stationary test Layout (Side View).

The photo above shows the layout (side view) of the stationary test with various receivers such as ZED-F9P (dual frequency receiver), EVK-M8T (single frequency receiver), and Samsung s8 (smartphone).

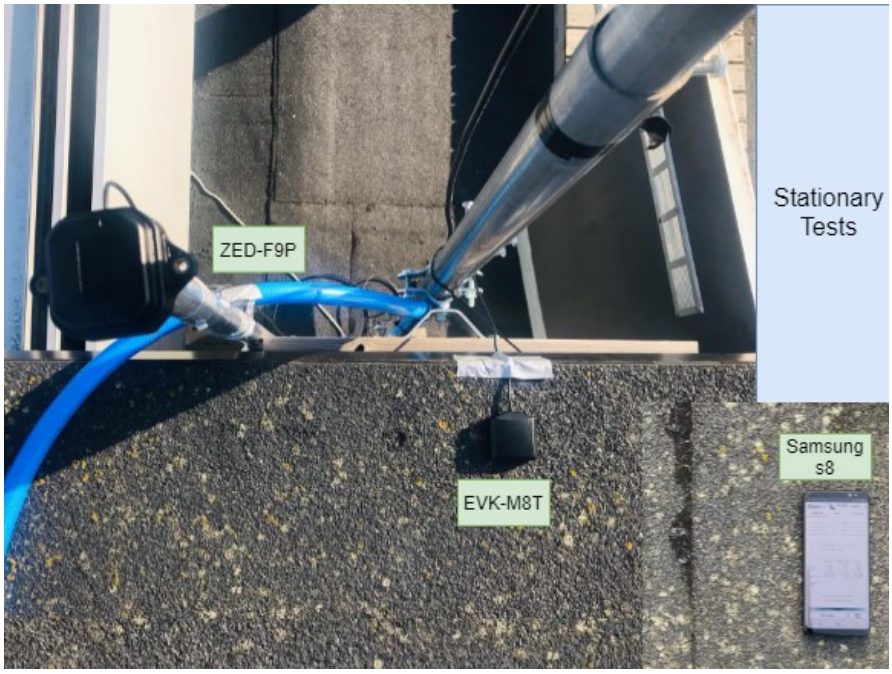

Figure 17. Stationary test Layout (Top View).

The photo above shows the layout (top view) of the stationary test with various receivers such as ZED-F9P (dual frequency receiver), EVK-M8T (single frequency receiver), and Samsung s8 (smartphone).

Ground Truth Estimation:

The mean of fixed (resolved integers) epoch RTK static solutions were used as the estimated true position for the ZED-F9P (dual frequency receiver). Extrapolations where made for other GNSS devices based on their relative positions to the ZED-F9P as shown in the Figure 18 and 19 below:

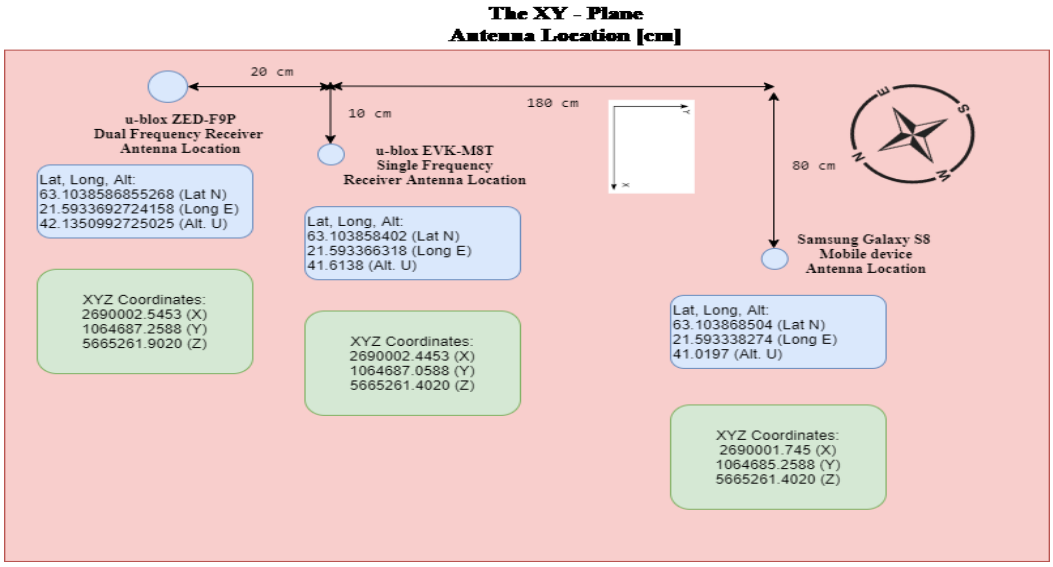

Figure 18. Stationary test Layout XY Plane.

The figure above shows the layout (XY plane) of the stationary test with various receivers such as ZED-F9P (dual frequency receiver), EVK-M8T (single frequency receiver), and Samsung s8 (smartphone) with their corresponding coordinates (Latitude, Longitude and Altitude), and horizontal distances (in centimetres) between each receiver.

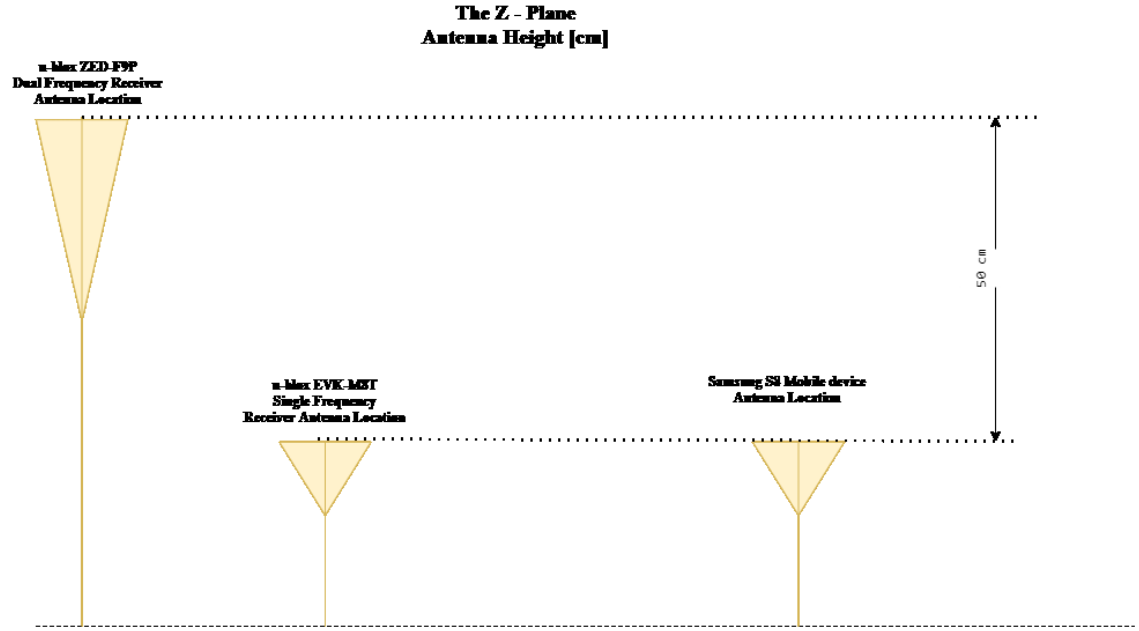

Figure 19. Stationary test Layout Z Plane.

The figure above shows the layout (Z plane) of the stationary test with various receivers such as ZED-F9P (dual frequency receiver), EVK-M8T (single frequency receiver), and Samsung s8 (smartphone) with height differences (in centimetres).

4.2 Dynamic test setup at Kvarken ports Vaasa

Kinematic (Dynamic) tests were conducted at the harbour with a pedestrian average speed of approximately 6 km/h. The environment has high multi-path and shadowing characteristics.

Data collected from all receivers including Topcon GNSS reference receivers were segmented into observation periods of 19, and 32 minutes to assess accuracy as a function of observation time as shown in Table 7 below:

Table 7. GNSS Observation Information for dynamic tests.

LOCATION	**KVARKEN PORTS VAASA**
Date of observation	24.09.2020
Session length	19, and 32 minutes
Week number	268
Day number	4 (Thursday)
GPS Time of Week since 1st epoch	2124
GNSS Reference System	Topcon GNSS Reference Receiver
Rover Observation Data	GNSS Receivers
Base Station Observation	VAA200FIN_R_20202680000_01D_30S_MO.00o
Satellite orbit solution	igs21244.sp3
Satellite and station clock solution	igs21244.clk
Ionospheric Correction	igsg2680.20i
EOP (Earth Orientation Parameters) Data	igr21244.erp
SBAS Data	268-PRN123-h12-h23.ems

The table above shows information on observation date, session length, base station and correction parameters used for dynamic tests.

Test Equipment (see figures 20, 21, and 22 below):

a. A Topcon GNSS Reference Receiver (in motion with other GNSS receivers) from Novia University of Applied Sciences.
b. Two (2) u-blox ZED-F9P-01B-00 (C099-F9P-1-03) Dual Frequency Receivers with Multi-band antennas for repeatability.
c. U-blox EVK-M8T-0-01 (NEO-M8T-0-10) GNSS Evaluation Kit; Single Frequency receiver.
d. Samsung Galaxy S8 Android 9 Smartphone, Model Number: SM-G950F, Build number: PPR1.180610.011.G950FXXU9DTF1.
e. Geo++ RINEX 2.1.6 (GNSS data logger for smartphones).

Estimating the ground truth:

Comparisons will be made with the results of the high end Topcon GNSS Reference Receiver (labelled TPC) and other low cost receivers and smartphones.

Given the high cm-level accuracy of the Topcon GNSS Reference Receivers (Trimble for post processing), its position will serve as the reference to evaluate all other receivers' derived positions.

Figure 20. Dynamic tests at Kvarken Ports Vaasa.

The photo above shows the layouts (top view, and side view) of the dynamic test with various receivers such as Topcon GNSS reference system, ZED-F9P-(1) (dual frequency receiver 1), ZED-F9P-(2) (dual frequency receiver 2), EVK-M8T (single frequency receiver), and Samsung Galaxy s8 (smartphone). In the lower left end of the picture, the aerial map of the test site is shown.

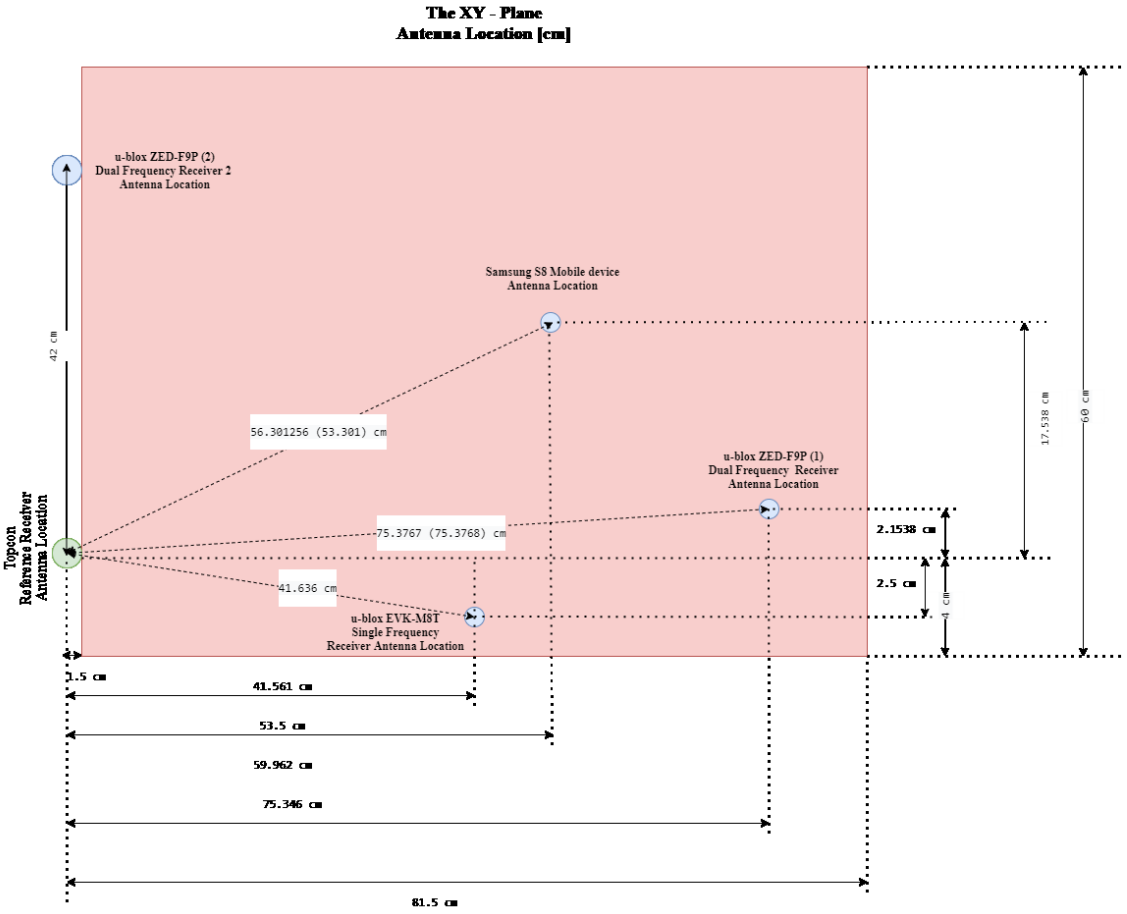

Figure 21. Dynamic test Layout XY Plane.

The figure above shows the layout (XY plane) of the dynamic test with various receivers such as Topcon GNSS reference system, ZED-F9P-(1) (dual frequency receiver 1), ZED-F9P-(2) (dual frequency receiver 2), EVK-M8T (single frequency receiver), and Samsung Galaxy s8 (smartphone) and horizontal distances (in centimetres) between each receiver.

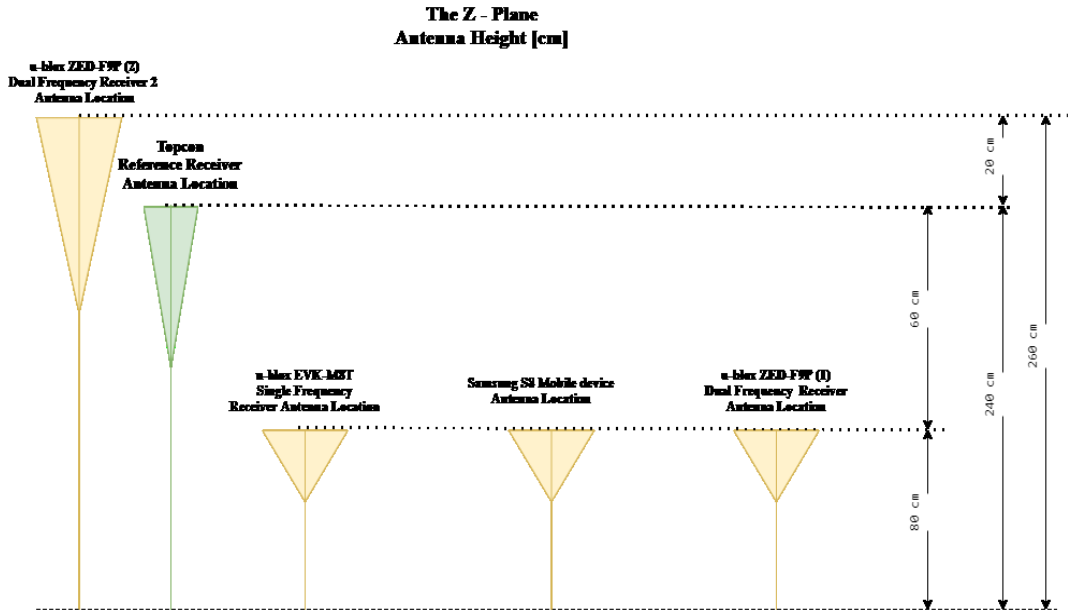

Figure 22. Dynamic test Layout Z Plane.

The figure above shows the layout (Z plane) of the dynamic test with various receivers such as Topcon GNSS reference system, ZED-F9P-(1) (dual frequency receiver 1), ZED-F9P-(2) (dual frequency receiver 2), EVK-M8T (single frequency receiver), and Samsung Galaxy s8 (smartphone) and height differences (in centimetres) between each receiver.

Device Performance during dynamic tests:

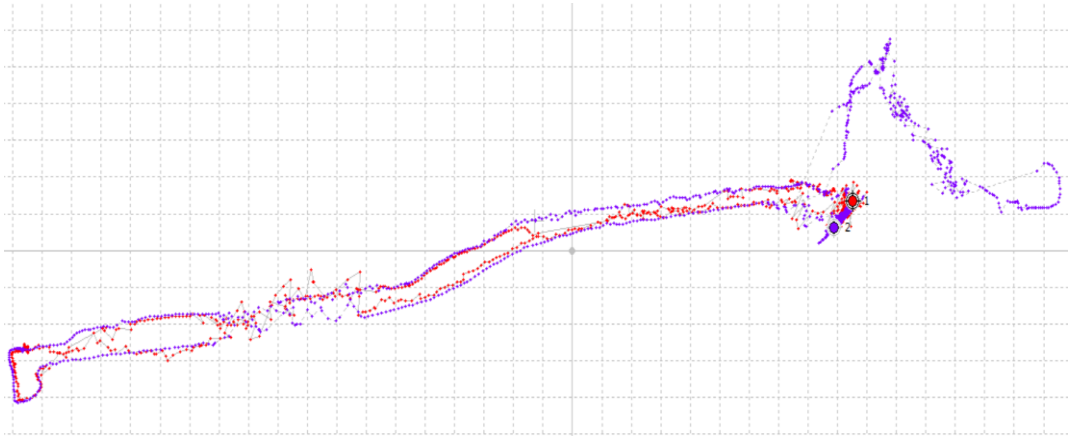

Figure 23. Device performance of dual frequency receivers' ublox ZED-F9P-(1) and ZED-F9P-(2) during 19 minutes dynamic tests.

(Source: RTKLib™ RTKPOST™).

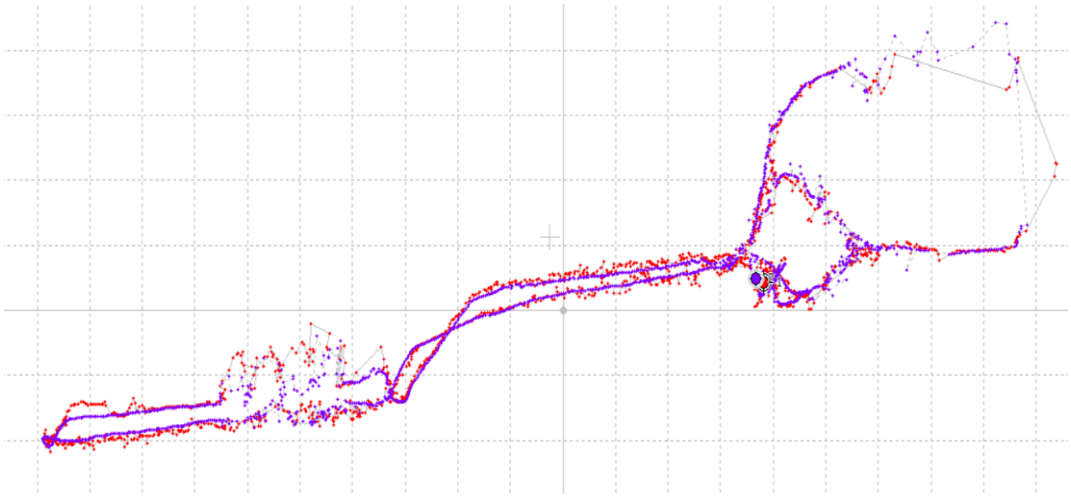

Figure 24. Device performance of dual frequency receivers' ublox ZED-F9P-(1) and ZED-F9P-(2) during 32 minutes dynamic tests.

(Source: RTKLib™ RTKPOST™).

Figure 23 shows the performance of ublox ZED-F9P-(1) (red colour) versus ZED-F9P-(2) (purple colour). It is evident that the first ublox device (ZED-F9P-(1)) experienced outage problems during the 19 min observation session. Similar behaviour were observed in all GNSS processing solutions of ZED-F9P-(1) as compared to ZED-F9P-

(2). As a result, statistical comparison cannot be made between ZED-F9P-(1) and ZED-F9P-(2) for a session length of 19 min. Loss of signal was registered during the 32 min observation in areas of signal obstruction, and overhead construction works as shown in figure 24. Both devices were available at all time of the experiment. In all cases, ZED-F9P-(1) suffers from greater multipath due to antenna placement.

4.3 GNSS data post processing setup and methods

Various tools and methods were employed for GNSS data post processing. Figure 25 shows a synthetic outline of these procedures.

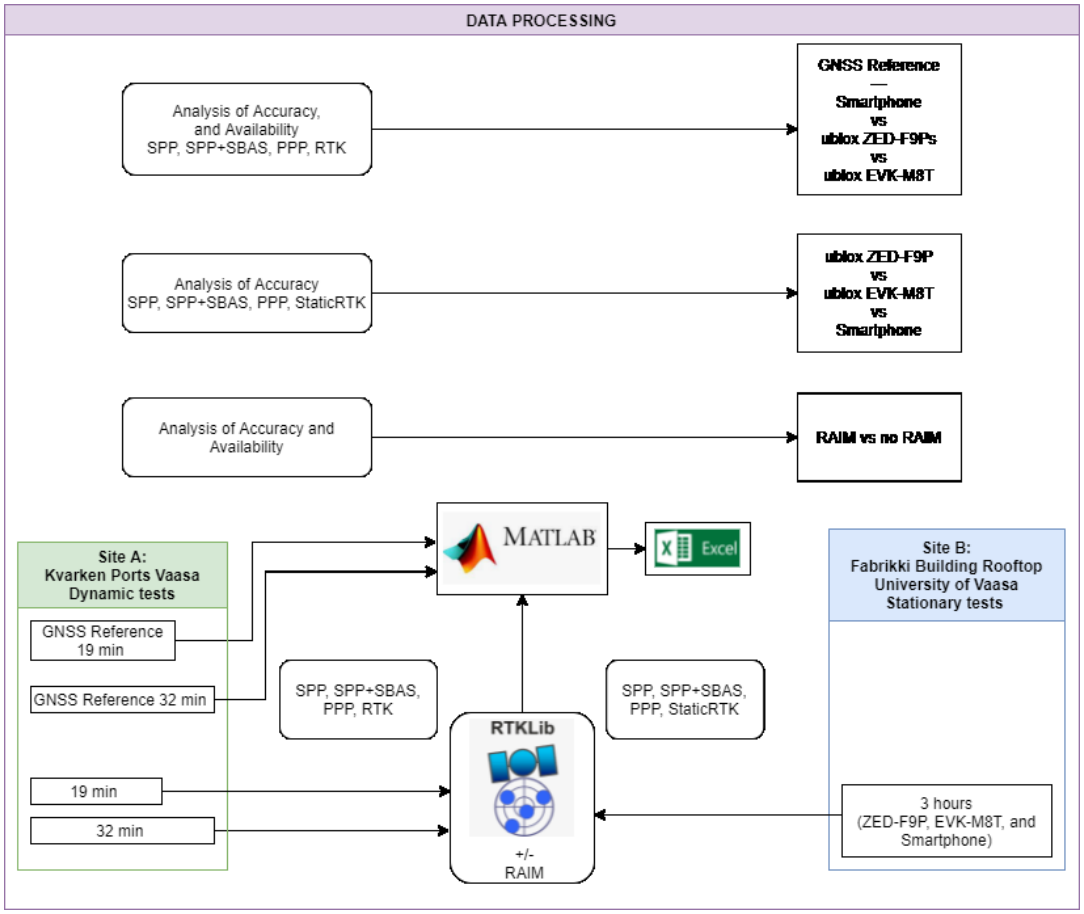

Figure 25. Synthetic outline of data processing procedures.

The figure above shows the data processing procedures, tools and methods used for GNSS data processing.

Step 1: RTKLib GNSS Post processing.

Single Positioning (SP), Single Positioning with SBAS (SPP+SBAS), Precise Point Positioning (PPP), and Real-time Kinematics (RTK) performance evaluation were performed using RTKLib, a well-known open source software.

Two sets of post-processing were carried out: with RAIM-FDE setting enabled, and without RAIM-FDE setting enabled.

For SPP, PPP and RTK, the Saastamoinen model was selected for troposphere corrections, while the Broadcast ephemeris was used to reduce ionospheric errors.

For SPP+SBAS, the SBAS model was used for troposphere and ionosphere corrections.

The Minimum elevation angle used for holding ambiguity has been set to 0.

A reject GDOP threshold of 5.0 was selected as the standard across all devices as the selection of a lower GDOP threshold excludes all GNSS observation from the mobile device. The smoother combined solution (with forward and backward Kalman filter solutions) was used to guarantee a fix for every data point in case of data anomalies, to provide extra validation of results and increase the confidence of the fix or float solution. With combined mode, higher fix percentages and fix confidence is achievable (Tim Everett, 2021b).

To improve the PPP and RTK solution, a filter iteration of 1000 was selected for some cases (see Table 8 for more details).

Step 2: Statistical Analysis with MATLAB™.

MATLAB a well-known proprietary software was used for data cleaning, and calculation of Availability, Horizontal and Vertical errors (2-sigma: 95% confidence level). It was also used for performing graphical statistical comparisons amongst various devices and GNSS processing modes.

Step 3: Visualization with Microsoft© Excel™.

Finally, Microsoft© Excel™ was used for data visualization and presentation. These visualizations include: analysis of availability, and positioning accuracy.

Table 8. RTKLIB parameters used for data processing.

RTKLIB Parameters	Dynamic tests Location: Kvarken Ports Vaasa	Stationary tests Location: Fabrikki Building Rooftop, University of Vaasa
Software Version	RTKLib v. 2.4.3 (RTKCONV, RTKPOST)	RTKLib v. 2.4.2(RTKPOST); v.2.4.3 (RTKCONV)
Elevation Angle	10 °	10 °
Observations	L1 and L2	L1and L2
Session Length	32 min, 19 min	3 hours
Time format	Coordinated Universal Time (UTC)	GPS Time (GPST)
Constellations	GPS, GLONASS, Galileo, QZSS, Beidou	GPS, GLONASS, Galileo, QZSS, Beidou
Troposphere	Saastamoinen	Saastamoinen
Ephemeris	Broadcast, SBAS	Broadcast, SBAS
IGS Corrections	Satellite orbit solution, Satellite and station clock solution, Earth Rotation Parameters, and Ionospheric corrections.	Satellite and station clock solution, Earth Rotation Parameters, and Ionospheric corrections.
Reference Station	VAA200FIN (Vaasa, FIN) 18.0 - 18.3km Baseline	VAA200FIN (Vaasa, FIN) 18.0 - 18.3km Baseline
Processing modes	Single with broadcast ephemeris corrections	Single with broadcast ephemeris corrections
	Single with broadcast and SBAS ephemeris corrections	Single with broadcast and SBAS ephemeris corrections
	PPP	PPP
	RTK	Static-RTK
RAIM	Reject Threshold of GDOP value: 5.0	Reject Threshold of GDOP value: 5.0
Ambiguity	Fix and hold* (LAMBDA)	Fix and hold* (LAMBDA)
Min ratio to fix ambiguity	3	3
Minimum fix count	for integer ambiguity resolution is set to 0	for integer ambiguity resolution is set to 0
Minimum elevation ambiguity hold	Minimum elevation angle used for holding ambiguity has been set to 0.	Minimum elevation angle used for holding ambiguity has been set to 0.
Filter type	Smoother combined solution with forward and backward Kalman filter solutions**	Smoother combined solution with forward and backward Kalman filter solutions**
Number of filter iterations	1***(for mobile device) and 1000***(u-blox GNSS receivers)	1*** for mobile device and u-blox GNSS receivers)

Footnotes: * RTK, PPP. ** RTK, PPP. *** RTK, PPP.

The table above shows the RTKLib parameters used for GNSS data post processing. In the table, filter type, number of filter iterations, ambiguity method, and reject threshold of GDOP value are shown.

4.4 GNSS frequencies used for stationary tests

GNSS receivers use various frequencies in various constellation to generate a PNT solution. Tables 9 - 12 show the constellations and corresponding frequencies used for Positioning, Navigation and Timing (PNT) during stationary tests.

Table 9. GNSS frequencies used in obtaining the PNT solution for stationary tests (GPS).

LOCATION: FABRIKKI BUILDING ROOFTOP, UNIVERSITY OF VAASA					
DURATION OF OBSERVATION			**3 hours Observation**		
Constellation	Channel	Satellite Vehicle Number (SV)	u-blox ZED-F9P	u-blox EVK-M8T	Samsung Galaxy s8
GPS	L1C/A	G1	-	-	X
		G2	X	X	-
		G3	X	X	X
		G4	X	X	X
		G6	X	X	X
		G8	-	-	X
		G9	X	X	X
		G10	-	-	X
		G11	-	-	X
		G12	-	-	X
		G17	X	X	X
		G19	X	X	X
		G21	-	-	X
		G22	X	X	X
		G26	-	X	X
		G28	-	-	X
		G31	X	X	X
		G32	-	-	X
	L2CL	G1	-	-	-
		G3	X	-	-
		G4	X	-	-
		G6	X	-	-
		G9	X	-	-
		G17	X	-	-
		G31	X	-	-

The table above shows the GPS channels, and corresponding satellite vehicle number used in obtaining the PNT solution for stationary tests.

Table 10. GNSS frequencies used in obtaining the PNT solution for stationary tests (Galileo).

LOCATION: FABRIKKI BUILDING ROOFTOP, UNIVERSITY OF VAASA					
DURATION OF OBSERVATION			**3 hours Observation**		
Constellation	Channel	Satellite Vehicle Number (SV)	u-blox ZED-F9P	u-blox EVK-M8T	Samsung Galaxy s8
GALILEO	E1C	E1	-	-	-
		E4	X	X	-
		E9	X		-
		E11	-	X	-
		E19	X	X	-
		E21	X	X	-
		E27	X	X	-
		E36	X	X	-
	E5BQ	E1	-	-	-
		E4	X	-	-
		E9	X	-	-
		E11	X	-	-
		E19	X	-	-
		E21	X	-	-
		E27	X	-	-
		E36	X	-	-

The table above shows the Galileo channels, and corresponding satellite vehicle number used in obtaining the PNT solution for stationary tests.

Table 11. GNSS frequencies used in obtaining the PNT solution for stationary tests (GLONASS).

LOCATION: FABRIKKI BUILDING ROOFTOP, UNIVERSITY OF VAASA					
DURATION OF OBSERVATION			**3 hours Observation**		
Constellation	Channel	Satellite Vehicle Number (SV)	u-blox ZED-F9P	u-blox EVK-M8T	Samsung Galaxy s8
GLONASS	L1OF	R1	-	-	X
		R2	X	X	X
		R3	X	X	X
		R7	-	-	X
		R8	-	-	X
		R9	-	-	X
		R10	-	X	X
		R11	X	X	X
		R12	X	X	X
		R17	-	X	X
		R18	X	X	X
		R19	X	X	-
		R23	-	-	X
		R24	-	-	X
	L2OF	R1	-	-	-
		R2	X	-	-
		R3	X	-	-
		R8	-	-	-
		R11	X	-	-
		R12	X	-	-
		R18	X	-	-
		R19	X	-	-

The table above shows the GLONASS channels, and corresponding satellite vehicle number used in obtaining the PNT solution for stationary tests.

Table 12. GNSS frequencies used in obtaining the PNT solution for stationary tests (Beidou and QZSS).

LOCATION: FABRIKKI BUILDING ROOFTOP, UNIVERSITY OF VAASA					
DURATION OF OBSERVATION			**3 hours Observation**		
Constellation	Channel	Satellite Vehicle Number (SV)	u-blox ZED-F9P	u-blox EVK-M8T	Samsung Galaxy s8
BEIDOU	B1D1	B6	X	-	X
		B9	X	-	X
		B11	X	-	X
		B16	X	-	X
		B19	-	-	X
		B21	X	-	X
		B22	-	-	X
		B28	X	-	-
		B34	-	-	X
		B36	-	-	X
	B2D1	B6	X	-	-
		B9	X	-	-
		B11	X	-	-
		B14	-	-	-
		B16	X	-	-
QZSS	L2C	Q2	X	X	X

The table above shows the Beidou and QZSS channels, and their corresponding satellite vehicle number used in obtaining the PNT solution for stationary tests.

4.5 GNSS frequencies used for dynamic tests

GNSS receivers use various frequencies in various constellations to generate a PNT solution. Tables 13 – 16 show the constellations and corresponding frequencies used for Positioning, Navigation and Timing (PNT) during dynamic tests.

Table 13. GNSS frequencies used in obtaining the PNT solution for dynamic tests (GPS).

LOCATION: KVARKEN PORTS VAASA										
DURATION OF OBSERVATION			19 min Observation				32 min Observation			
Constellation	**Channel**	**Satellite Vehicle Number (SV)**	**u-blox ZED-F9P (1)**	**u-blox ZED-F9P (2)**	**u-blox EVK-M8T**	**Samsung Galaxy s8**	**u-blox ZED-F9P (1)**	**u-blox ZED-F9P (2)**	**u-blox EVK-M8T**	**Samsung Galaxy s8**
GPS	L1C/A	G1	X	X	X	X	X	X	X	X
		G3	X	X	X	X	X	X	X	X
		G4	X	X	X	X	X	X	X	X
		G6	-	-	X	-	X	X	X	X
		G11	X	X	X	X	-	-	-	X
		G12	X	-	X	X	X	X	X	X
		G17	X	X	X	X	X	X	X	X
		G19	X	X	-	X	X	X	X	X
		G22	X	X	X	X	X	X	X	X
		G25	-	-	-	-	X	X	X	-
		G31	X	X	X	X	X	X	X	X
		G32	X	X	X	-	X	-	X	-
	L2CL	G1	X	X	-	-	X	X	-	-
		G3	X	X	-	-	X	X	-	-
		G4	X	X	-	-	X	X	-	-
		G6	-	-	-	-	X	X	-	-
		G12	X	-	-	-	X	X	-	-
		G17	X	X	-	-	X	X	-	-
		G25	-	-	-	-	-	X	-	-
		G31	-	X	-	-	X	X	-	-
		G32	-	X	-	-	X	X	-	-

The table above shows the GPS channels, and corresponding satellite vehicle number used in obtaining the PNT solution for dynamic tests.

Table 14. GNSS frequencies used in obtaining the PNT solution for dynamic tests (Galileo).

LOCATION: KVARKEN PORTS VAASA										
DURATION OF OBSERVATION			19 min Observation				32 min Observation			
Constellation	**Channel**	**Satellite Vehicle Number (SV)**	**u-blox ZED-F9P (1)**	**u-blox ZED-F9P (2)**	**u-blox EVK-M8T**	**Samsung Galaxy s8**	**u-blox ZED-F9P (1)**	**u-blox ZED-F9P (2)**	**u-blox EVK-M8T**	**Samsung Galaxy s8**
GALILEO	E1C	E1	X	X	X	-	X	X	X	-
		E3	X	X	X	-	X	X	X	-
		E5	X	X	X	-	X	X	X	-
		E9	-	-	X	X	X	X	-	X
		E13	X	X	X	-	X	X	X	-
		E15	X	X	X	-	X	X	X	-
		E31	X	X	-	-	X	X	X	-
	E5b	E1	X	X	-	-	X	X	-	-
		E3	X	X	-	-	X	X	-	-
		E5	X	X	-	-	X	X	-	-
		E9	X	X	-	-	-	X	-	-
		E13	X	X	-	-	X	X	-	-
		E15	X	X	-	-	X	X	-	-
		E31	X	-	-	-	X	X	-	-
	E5BQ	E1	X	X	-	-	X	X	-	-
		E3	X	X	-	-	X	X	-	-
		E5	X	X	-	-	X	X	-	-
		E9	X	X	-	-	-	X	-	-
		E13	X	X	-	-	X	X	-	-
		E15	X	X	-	-	X	X	-	-
		E31	X	-	-	-	X	X	-	-

The table above shows the Galileo channels, and corresponding satellite vehicle number used in obtaining the PNT solution for dynamic tests.

Table 15. GNSS frequencies used in obtaining the PNT solution for dynamic tests (GLONASS).

LOCATION: KVARKEN PORTS VAASA										
DURATION OF OBSERVATION			19 min Observation				32 min Observation			
Constellation	**Channel**	**Satellite Vehicle Number (SV)**	**u-blox ZED-F9P (1)**	**u-blox ZED-F9P (2)**	**u-blox EVK-M8T**	**Samsung Galaxy s8**	**u-blox ZED-F9P (1)**	**u-blox ZED-F9P (2)**	**u-blox EVK-M8T**	**Samsung Galaxy s8**
GLONASS	L1OF	R1	X	X	-	X	X	X	-	X
		R2	X	X	X	X	X	X	X	X
		R3	-	-	-	-	X	X	-	X
		R8	X	X	-	X	-	-	-	-
		R10	-	X	-	-	-	-	-	-
		R11	-	-	-	-	X	X	-	X
		R17	X	X	X	X	X	X	-	X
		R18	X	X	X	X	X	X	X	X
		R19	-	-	-	-	-	X	-	-
		R24	X	X	X	X	-	-	-	X
	L2OF	R1	X	X	-	-	X	X	-	-
		R2	X	X	-	-	X	X	-	-
		R3	-	-	-	-	X	X	-	-
		R8	X	X	-	-	-	-	-	-
		R11	-	-	-	-	X	X	-	-
		R17	X	X	-	-	X	X	-	-
		R18	X	X	-	-	X	X	-	-
		R19	-	-	-	-	-	X	-	-
		R24	X	X	-	-	-	-	-	-

The table above shows the GLONASS channels, and corresponding satellite vehicle number used in obtaining the PNT solution for dynamic tests.

Table 16. GNSS frequencies used in obtaining the PNT solution for dynamic tests (Beidou and QZSS).

LOCATION: KVARKEN PORTS VAASA										
DURATION OF OBSERVATION			19 min Observation				32 min Observation			
Constellation	**Channel**	**Satellite Vehicle Number (SV)**	**u-blox ZED-F9P (1)**	**u-blox ZED-F9P (2)**	**u-blox EVK-M8T**	**Samsung Galaxy s8**	**u-blox ZED-F9P (1)**	**u-blox ZED-F9P (2)**	**u-blox EVK-M8T**	**Samsung Galaxy s8**
BEIDOU	B1D1	B11	X	X	-	-	-	-	-	-
		B14	X	X	-	-	X	X	-	-
		B16	-	X	-	X	-	X	-	X
		B21	-	X	-	X	X	X	-	X
		B26	-	-	-	-	X	X	-	-
		B27	-	X	-	-	-	X	-	-
		B28	X	X	-	X	X	X	-	X
		B33	-	X	-	X	X	X	-	X
		B34	-	-	-	X	-	-	-	-
		B36	-	-	-	X	-	-	-	-
	B2D1	B6	-	X	-	X	X	-	-	X
		B9	X	X	-	-	-	-	-	-
		B11	X	X	-	-	-	-	-	-
		B14	X	X	-	-	X	X	-	-
		B16	-	X	-	-	X	-	-	-
QZSS	L2C	Q2	-	-	-	-	X	-	-	X

The table above shows the Beidou and QZSS channels, and their corresponding satellite vehicle number used in obtaining the PNT solution for dynamic tests.

4.6 Observed DOP statistics from GNSS devices

4.6.1 Observed DOP statistics from devices during stationary tests

Tables 17 and 18 show DOP values registered by the OEM software (u-center) for dual frequency and single frequency devices during stationary tests.

Table 17. DOP values of Dual frequency device (3 hr) during stationary tests.

Device : ZED-F9P		3 hr Observations			
Description	Minimum	Maximum	Average	Deviation	Unit
Velocity Accuracy 3D	0.04	0.16	0.07	0.02	m/s
DOP Horizontal	0.4	0.7	0.5	0	-
DOP Vertical	0.7	1.3	0.8	0.1	-
DOP Geometric	1	1.7	1.1	0.1	-

The table above shows minimum, maximum and average DOP values of Dual frequency device (3 hr) during stationary tests.

Table 18. DOP values of Single frequency device (3 hr) during stationary tests.

Device : EVK-M8T		3 hr Observations			
Description	Minimum	Maximum	Average	Deviation	Unit
Velocity Accuracy 3D	0.01	0.03	0.02	0.01	m/s
DOP Horizontal	0.5	0.8	0.5	0	-
DOP Vertical	0.7	1.2	0.8	0.1	-
DOP Geometric	0.9	1.6	1.1	0.1	-

The table above shows minimum, maximum and average DOP values of Single frequency device (3 hr) during stationary tests.

4.6.2 Observed DOP statistics from devices during dynamic tests

Tables 19 - 24 show DOP values registered by the OEM software (u-center) for dual frequency and single frequency devices during dynamic tests.

Table 19. DOP values of Dual frequency-(1) device (19 min) during dynamic tests.

Device : ZED-F9P-(1)		19 min Observations			
Description	Minimum	Maximum	Average	Deviation	Unit
Velocity Accuracy 3D	0.05	0.23	0.09	0.03	m/s
DOP Horizontal	0.5	0.6	0.5	0	-
DOP Vertical	0.8	1	0.9	0	-
DOP Geometric	1	1.4	1.1	0	-

The table above shows minimum, maximum and average DOP values of Dual frequency-(1) device (19 min) during dynamic tests.

Table 20. DOP values of Dual frequency-(2) device (19 min) during dynamic tests.

Device : ZED-F9P-(2)		19 min Observations			
Description	Minimum	Maximum	Average	Deviation	Unit
Velocity Accuracy 3D	0.04	0.17	0.07	0.02	m/s
DOP Horizontal	0.5	0.6	0.5	0	-
DOP Vertical	0.8	1.1	0.8	0	-
DOP Geometric	1	1.5	1.1	0.1	-

The table above shows minimum, maximum and average DOP values of Dual frequency-(2) device (19 min) during dynamic tests.

Table 21. DOP values of Single frequency device (19 min) during dynamic tests.

Device : EVK-M8T		19 min Observations			
Description	Minimum	Maximum	Average	Deviation	Unit
Velocity Accuracy 3D	0.01	0.2	0.02	0.01	m/s
DOP Horizontal	0.6	2.3	0.7	0.2	-
DOP Vertical	0.8	2.9	0.9	0.2	-
DOP Geometric	1.1	4.5	1.3	0.3	-

The table above shows minimum, maximum and average DOP values of Single frequency device (19 min) during dynamic tests.

Table 22. DOP values of Dual frequency-(1) device (32 min) during dynamic tests.

Device : ZED-F9P-(1)		32 min Observations			
Description	Minimum	Maximum	Average	Deviation	Unit
Velocity Accuracy 3D	0.05	0.25	0.08	0.02	m/s
DOP Horizontal	0.5	0.9	0.5	0.1	-
DOP Vertical	0.7	1.4	0.8	0.1	-
DOP Geometric	1	1.9	1.1	0.1	-

The table above shows minimum, maximum and average DOP values of Dual frequency-(1) device (32 min) during dynamic tests.

Table 23. DOP values of Dual frequency-(2) device (32 min) during dynamic tests.

Device : ZED-F9P-(2)		32 min Observations			
Description	Minimum	Maximum	Average	Deviation	Unit
Velocity Accuracy 3D	0.04	0.13	0.06	0.02	m/s
DOP Horizontal	0.5	0.8	0.5	0	-
DOP Vertical	0.7	1.3	0.8	0.1	-
DOP Geometric	1	1.8	1.1	0.1	-

The table above shows minimum, maximum and average DOP values of Dual frequency-(2) device (32 min) during dynamic tests.

Table 24. DOP values of Single frequency device (32 min) during dynamic tests.

Device : EVK-M8T		32 min Observations			
Description	Minimum	Maximum	Average	Deviation	Unit
Velocity Accuracy 3D	0.01	0.38	0.02	0.02	m/s
DOP Horizontal	0.5	3.4	0.7	0.3	-
DOP Vertical	0.8	5.7	1.1	0.4	-
DOP Geometric	1.1	8.7	1.5	0.7	-

The table above shows minimum, maximum and average DOP values of Single frequency device (32 min) during dynamic tests.

5. DISCUSSION

5.1 Statistical analysis and data visualization of stationary tests

5.1.1 Statistical analysis of stationary tests without RAIM-FDE enabled

a. Dual frequency u-blox ZED-F9P 3 hr stationary test (without RAIM-FDE).

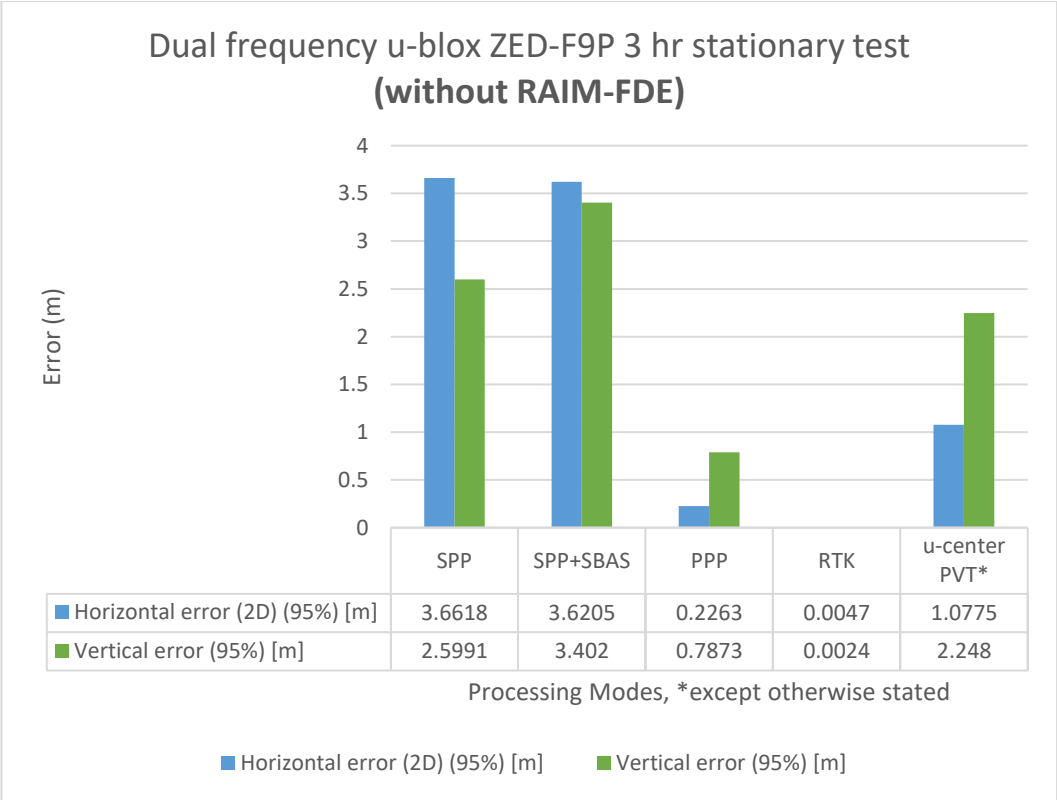

Figure 26. Data visualisation of dual frequency u-blox ZED-F9P 3 hr stationary test (without RAIM-FDE).

From Figure 26, it can be observed that 2D and vertical error reduces from code based positioning techniques to carrier-phase positioning techniques. The best GNSS solution is the RTK solution with a horizontal accuracy of 0.47 cm, and vertical accuracy of 0.24 cm. More information can be found on Table 25.

Table 25. Statistical analysis of dual frequency u-blox ZED-F9P 3 hr stationary test (without RAIM-FDE).

GNSS Post-Processing Modes Session length = 3 hrs **u-blox ZED-F9P** **(without RAIM-FDE)**	SPP	SPP+SBAS	PPP	RTK	u-center PVT*
Horizontal error (2D) [m] (95%)	3.6618	3.6205	0.2263	0.0047	1.0775
Vertical error [m] (95%)	2.5991	3.4020	0.7873	0.0024	2.2480
Horizontal Min [m]	0.0112	0.0155	0.0038	0.0004	0.0078
Horizontal Max [m]	14.3975	7.6567	0.2515	0.0105	1.4971
Horizontal Mean [m]	1.5340	1.5213	0.1182	0.0018	0.5290
Horizontal SD [m]	1.1200	1.0174	0.0613	0.0015	0.2823

b. Single frequency u-blox EVK-M8T 3 hr stationary test (without RAIM-FDE).

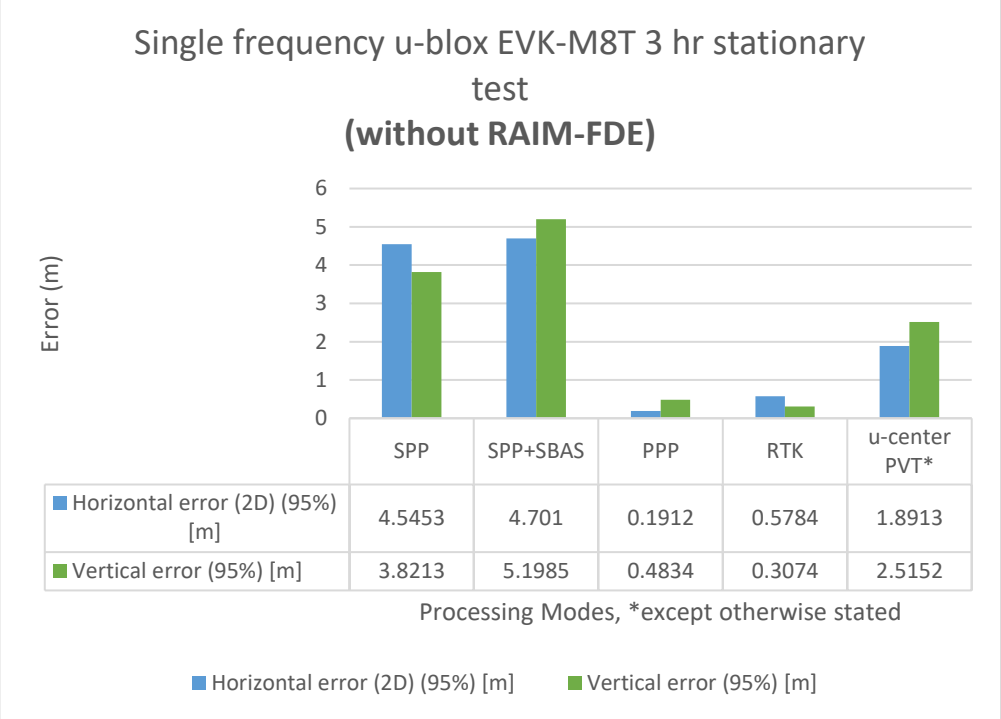

Figure 27. Data visualisation of single frequency u-blox EVK-M8T 3 hr stationary test (without RAIM-FDE).

From Figure 27, it can be observed that 2D and vertical error reduces from code based positioning techniques to carrier-phase positioning techniques. The best GNSS solution is the RTK solution with a horizontal accuracy of 57.84 cm, and vertical accuracy of 30.74 cm. More information can be found on Table 26.

Table 26. Statistical analysis of single frequency u-blox EVK-M8T 3 hr stationary test (without RAIM-FDE).

GNSS Post-Processing Modes Session length = 3 hrs **u-blox EVK-M8T (without RAIM-FDE)**	SPP	SPP+SBAS	PPP	RTK	u-center PVT*
Horizontal error (2D) [m] (95%)	4.5453	4.7010	0.1912	0.5784	1.8913
Vertical error [m] (95%)	3.8213	5.1985	0.4834	0.3074	2.5152
Horizontal Min [m]	0.0299	0.0322	0.0047	0.0070	0.0220
Horizontal Max [m]	12.2925	8.3388	0.2236	0.7915	2.9667
Horizontal Mean [m]	2.0555	2.1462	0.0901	0.1774	0.9302
Horizontal SD [m]	1.3097	1.3079	0.0511	0.1540	0.5148

c. Samsung Galaxy s8 smartphone 3 hr stationary test (without RAIM-FDE).

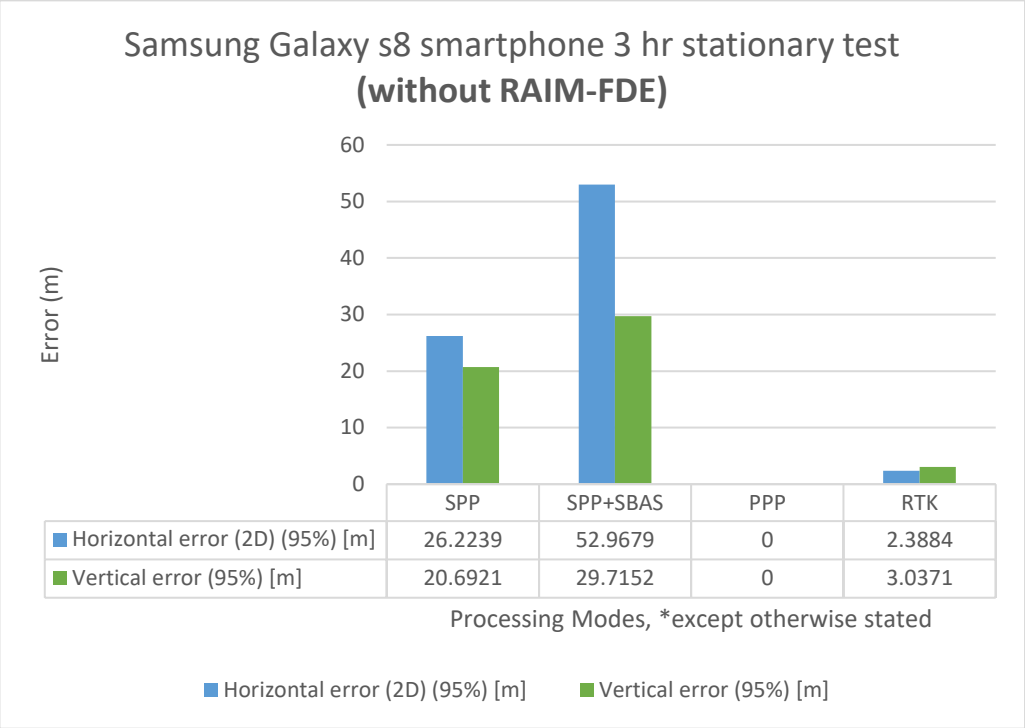

Figure 28. Data visualisation of Samsung Galaxy s8 smartphone 3 hr stationary test (without RAIM-FDE).

From Figure 28, it can be observed that 2D and vertical error reduces from code based positioning techniques to carrier-phase positioning techniques. The best GNSS solution is the RTK solution with a horizontal accuracy of 2.39 m, and vertical accuracy of 3.04 m. More information can be found on Table 27.

Table 27. Statistical analysis of Samsung Galaxy s8 smartphone 3 hr stationary test (without RAIM-FDE).

GNSS Post-Processing Modes Session length = 3 hrs **u-blox Samsung s8 (without RAIM-FDE)**	SPP	SPP+SBAS	PPP	RTK
Horizontal error (2D) [m] (95%)	26.2239	52.9679	N/A	2.3884
Vertical error [m] (95%)	20.6921	29.7152	N/A	3.0371
Horizontal Min [m]	0.0926	0.3392	N/A	0.4633
Horizontal Max [m]	69.2910	117.7133	N/A	2.4249
Horizontal Mean [m]	10.7473	16.6093	N/A	1.0899
Horizontal SD [m]	7.8315	16.0563	N/A	0.6967

5.1.2 Statistical analysis of stationary tests with RAIM-FDE enabled

a. Dual frequency ublox ZED-F9P 3 hr stationary test (with RAIM-FDE).

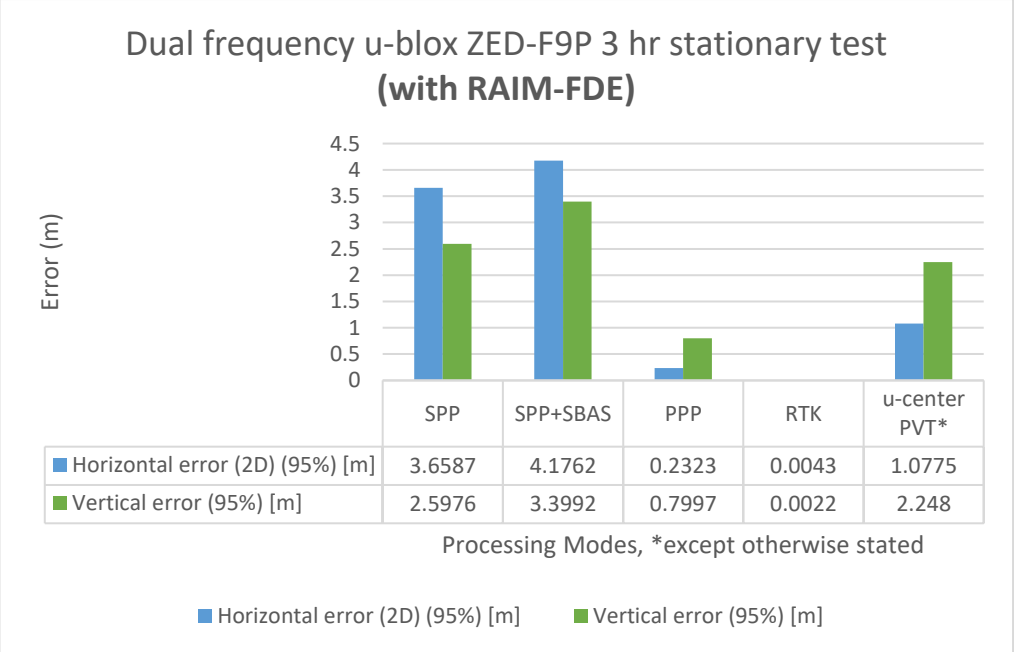

Figure 29. Data visualisation of dual frequency u-blox ZED-F9P 3 hr stationary test (with RAIM-FDE).

From Figure 29, it can be observed that 2D and vertical error reduces from code based positioning techniques to carrier-phase positioning techniques. The best GNSS solution is the RTK solution with a horizontal accuracy of 0.43 cm, and vertical accuracy of 0.2 cm. More information can be found on Table 28.

Table 28. Statistical analysis of dual frequency u-blox ZED-F9P 3 hr stationary test (with RAIM-FDE).

GNSS Post-Processing Modes Session length = 3 hrs **u-blox ZED-F9P (with RAIM-FDE)**	SPP	SPP+SBAS	PPP	RTK	u-center PVT*
Horizontal error (2D) [m] (95%)	3.6587	4.1762	0.2323	0.0043	1.0775
Vertical error [m] (95%)	2.5976	3.3992	0.7997	0.0022	2.2480
Horizontal Min [m]	0.0047	0.0059	0.0064	0.0004	0.0078
Horizontal Max [m]	14.4049	9.8678	0.2380	0.0113	1.4971
Horizontal Mean [m]	1.5387	1.6617	0.1205	0.0018	0.5290
Horizontal SD [m]	1.1224	1.2676	0.0615	0.0014	0.2823

b. Single frequency ublox EVK-M8T 3 hr stationary test (with RAIM-FDE).

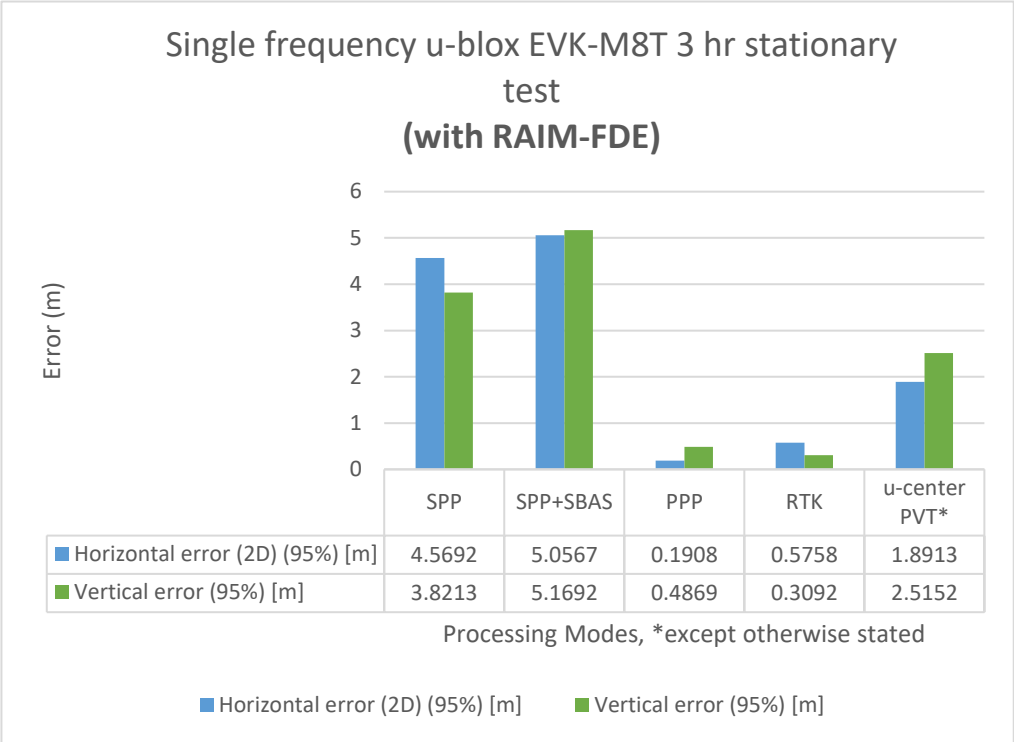

Figure 30. Data visualisation of single frequency u-blox EVK-M8T 3 hr stationary test (with RAIM-FDE).

From Figure 30, it can be observed that 2D and vertical error reduces from code based positioning techniques to carrier-phase positioning techniques. The best GNSS solution is the RTK solution with a horizontal accuracy of 57.58 cm, and vertical accuracy of 30.92 cm. More information can be found on Table 29.

Table 29. Statistical analysis of single frequency u-blox EVK-M8T 3 hr stationary test (with RAIM-FDE).

GNSS Post-Processing Modes Session length = 3 hrs **u-blox EVK-M8T (with RAIM)**	SPP	SPP+SBAS	PPP	RTK	u-center PVT*
Horizontal error (2D) [m] (95%)	4.5692	5.0567	0.1908	0.5758	1.8913
Vertical error [m] (95%)	3.8269	5.1692	0.4869	0.3092	2.5152
Horizontal Min [m]	0.0249	0.0034	0.0112	0.0097	0.0220
Horizontal Max [m]	12.3002	19.7384	0.2201	0.7952	2.9667
Horizontal Mean [m]	2.0617	2.3362	0.0916	0.1784	0.9302
Horizontal SD [m]	1.3212	1.5479	0.0500	0.1544	0.5148

c. Samsung Galaxy s8 smartphone 3 hr stationary test (with RAIM-FDE).

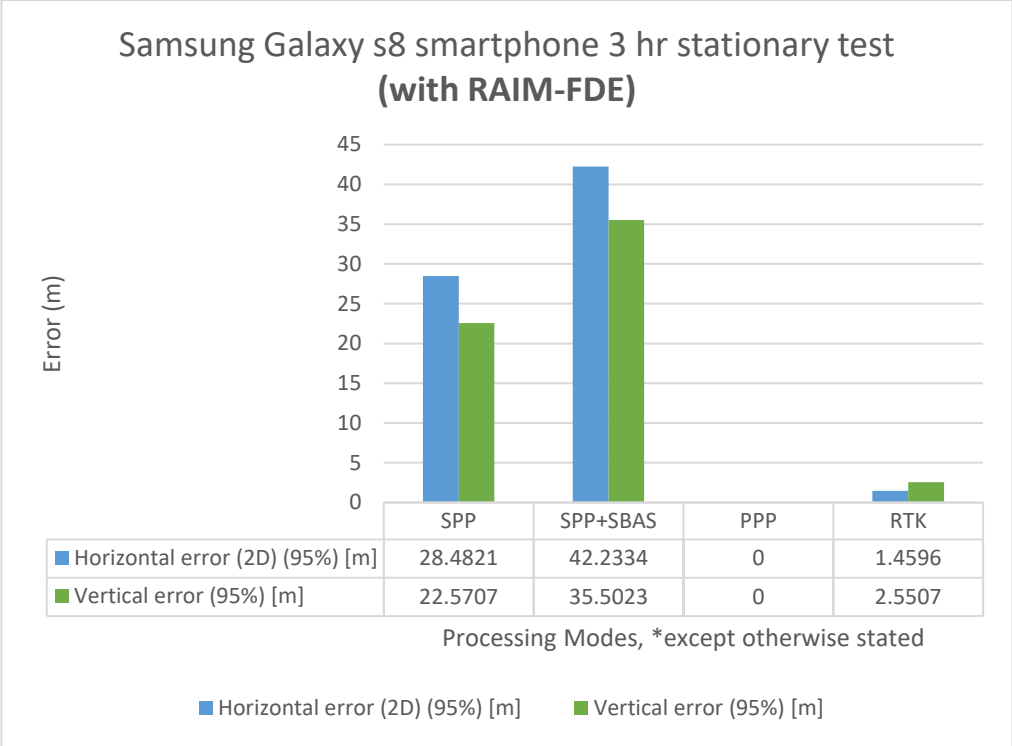

Figure 31. Data visualisation of Samsung Galaxy s8 smartphone 3 hr stationary test (with RAIM-FDE).

From Figure 31, it can be observed that 2D and vertical error reduces from code based positioning techniques to carrier-phase positioning techniques. The best GNSS solution is the RTK solution with a horizontal accuracy of 1.46 m, and vertical accuracy of 2.55 m. More information can be found on Table 30.

Table 30. Statistical analysis of Samsung Galaxy s8 smartphone 3 hr stationary test (with RAIM-FDE).

GNSS Post-Processing Modes Session length = 3 hrs **u-blox Samsung s8 (with RAIM)**	SPP	SPP+SBAS	PPP	RTK
Horizontal error (2D) [m] (95%)	28.4821	42.2334	N/A	1.4596
Vertical error [m] (95%)	22.5707	35.5023	N/A	2.5507
Horizontal Min [m]	0.0943	0.2215	N/A	0.1804
Horizontal Max [m]	106.3466	118.3552	N/A	12.1589
Horizontal Mean [m]	11.4582	15.3874	N/A	1.1658
Horizontal SD [m]	8.9357	13.0185	N/A	2.4776

5.2 Statistical analysis and data visualization for dynamic tests

5.2.1 Statistical analysis of dynamic tests without RAIM-FDE enabled

5.2.1.1 19 minutes dynamic tests (without RAIM-FDE)

a. Dual frequency u-blox ZED-F9P-(1) 19 min dynamic test (without RAIM-FDE).

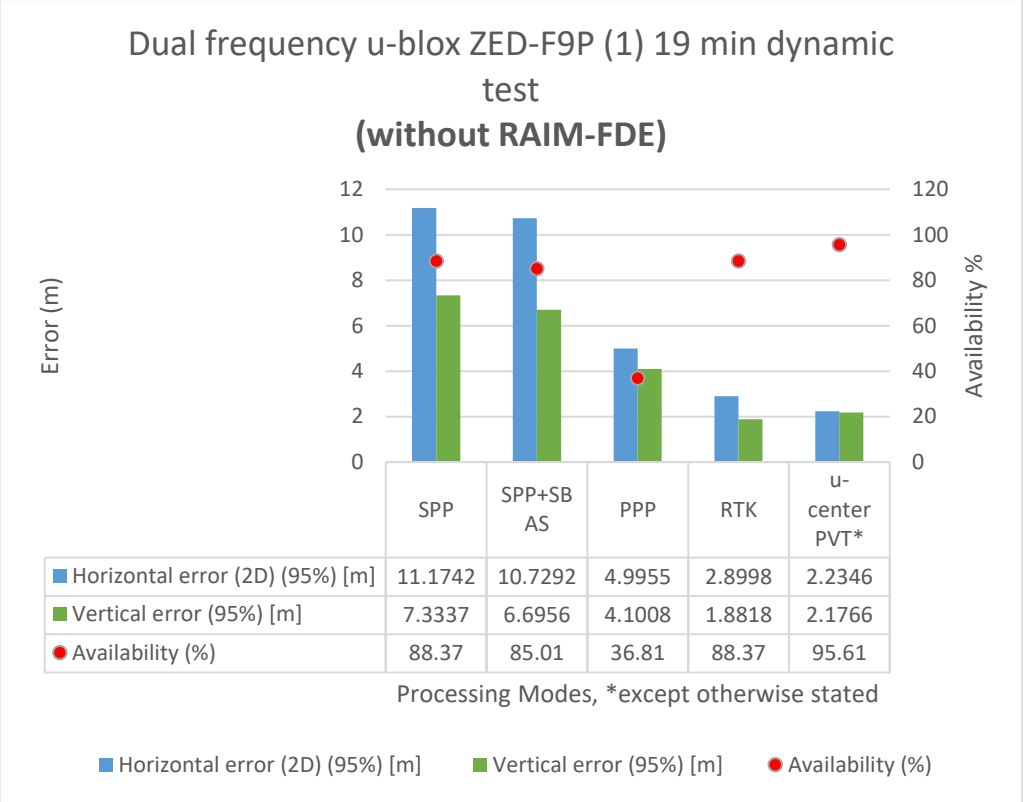

Figure 32. Data visualisation of dual frequency u-blox ZED-F9P-(1) 19 min dynamic test (without RAIM-FDE).

From Figure 32, it can be observed that 2D and vertical error reduces from code based positioning techniques to carrier-phase positioning techniques. The best GNSS solution is the RTK solution with a horizontal accuracy of 2.9 m, and vertical accuracy of 1.9 m.

SPP, and RTK have equal highest availabilities. PPP has the lowest availability. SPP with EGNOS corrected ephemeris (SPP+SBAS) applied has a higher accuracy than SPP as a result of applied ephemeris corrections. More information can be found on Table 31 below:

Table 31. Statistical analysis of dual frequency u-blox ZED-F9P-(1) 19 min dynamic test (without RAIM-FDE).

GNSS Post-Processing Modes Session length = 11 min **u-blox ZED-F9P (1)** (without RAIM-FDE)	SPP	SPP +SBAS	PPP	RTK	u-center PVT*
Availability (%)	88.37	85.01	36.81	88.37	95.61
(Total no of minutes) Seconds of the day	(10.75mins) 40558s - 41203s	(10.783mins) 40556s - 41203s	(9.917mins) 40570s - 41165s	(10.75mins) 40558s - 41203s	(11mins) 40542s - 41202s
Horizontal error (2D) [m] (95%)	11.1742	10.7292	4.9955	2.8998	2.2346
Vertical error [m] (95%)	7.3337	6.6956	4.1008	1.8818	2.1766
Horizontal Min [m]	0.4641	0.1603	0.3088	0.1478	0.3565
Horizontal Max [m]	22.9996	24.0339	8.1674	4.4038	2.7959
Horizontal Mean [m]	4.3029	3.6760	1.9703	1.6962	1.4601
Horizontal SD [m]	3.6299	3.1650	1.2806	0.7107	0.5428

b. Dual frequency u-blox ZED-F9P-(2) 19 min dynamic test (without RAIM-FDE).

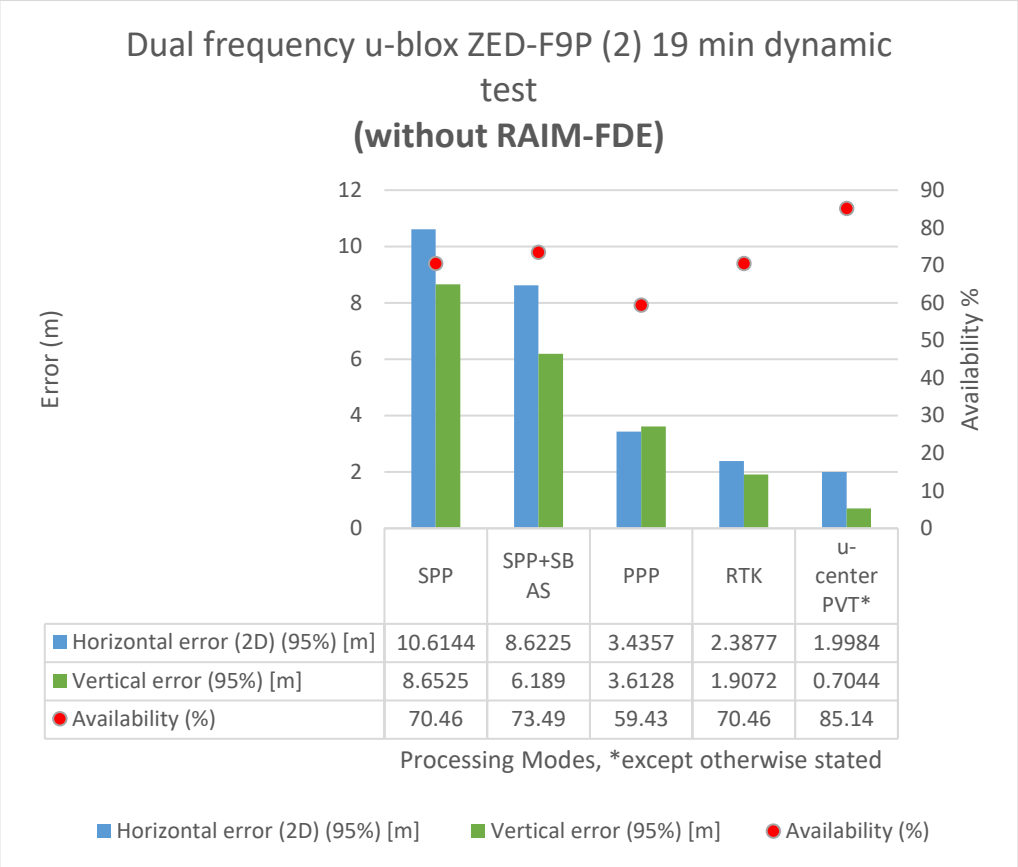

Figure 33. Data visualisation of dual frequency u-blox ZED-F9P-(2) 19 min dynamic test (without RAIM-FDE).

From Figure 33, it can be observed that 2D and vertical error reduces from code based positioning techniques to carrier-phase positioning techniques. The best GNSS solution is the RTK solution with a horizontal accuracy of 2.4 m, and vertical accuracy of 1.9 m. SPP and RTK have equal availabilities. PPP has the lowest availability. SPP with EGNOS corrected ephemeris (SPP+SBAS) applied has a higher accuracy than SPP as a result of applied ephemeris corrections. More information can be found on Table 32 below:

Table 32. Statistical analysis of dual frequency u-blox ZED-F9P-(2) 19 min dynamic test (without RAIM-FDE).

GNSS Post-Processing Modes Session length = 19 min **u-blox ZED-F9P (2)** (without RAIM-FDE)	SPP	SPP +SBAS	PPP	RTK	u-center PVT*
Availability (%)	70.46	73.49	59.43	70.46	85.14
Total no of minutes: 18.733 min Seconds of the day: 40542s - 41666s	-	-	-	-	-
Horizontal error (2D) [m] (95%)	10.6144	8.6525	3.4357	2.3877	1.9984
Vertical error [m] (95%)	6.3624	6.1890	3.6128	1.9072	0.7044
Horizontal Min [m]	0.0226	0.0406	0.0488	0.0319	0.0953
Horizontal Max [m]	23.0000	38.9856	10.6033	7.7384	3.0121
Horizontal Mean [m]	2.7034	2.2330	1.4955	0.9163	0.8777
Horizontal SD [m]	3.2617	3.1973	1.0684	0.8093	0.5167

c. Single frequency u-blox EVK-M8T 19 min dynamic test (without RAIM-FDE).

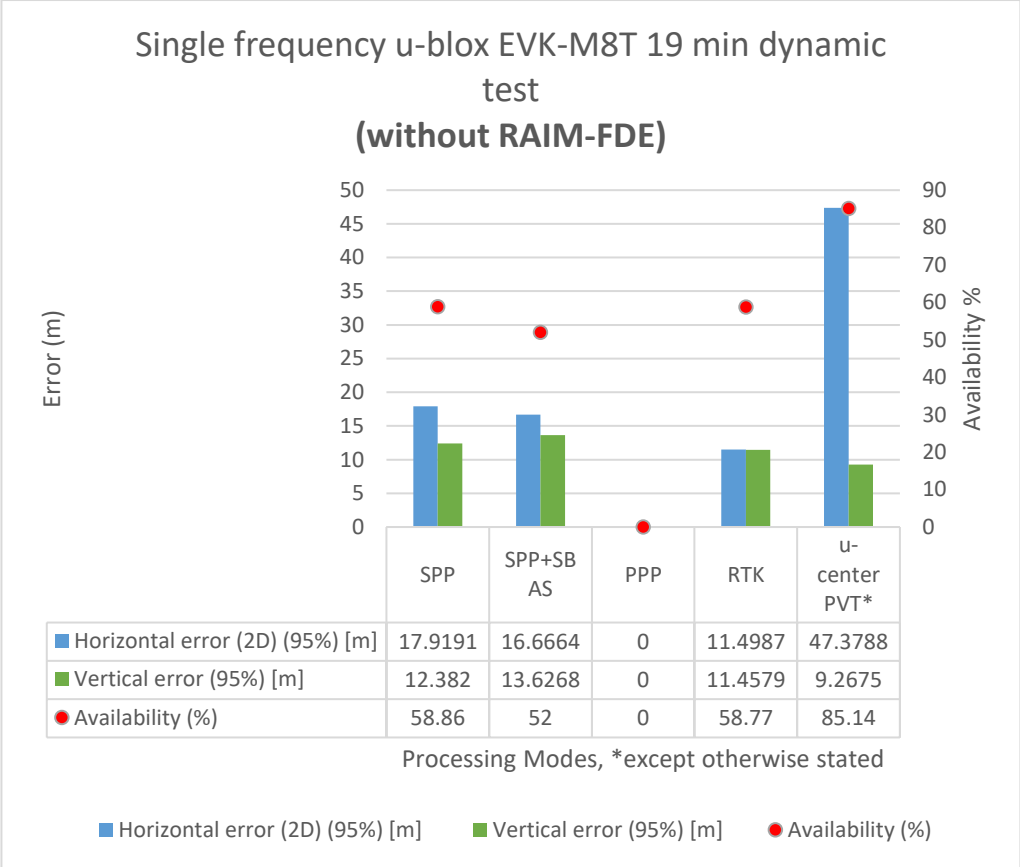

Figure 34. Data visualisation of single frequency u-blox EVK-M8T 19 min dynamic test (without RAIM-FDE).

From Figure 34, it can be observed that 2D and vertical error reduces from code based positioning techniques to carrier-phase positioning techniques. The best GNSS solution is the RTK solution with a horizontal accuracy of 11.5 m, and vertical accuracy of 11.5 m.

PPP is unavailable. SPP with EGNOS corrected ephemeris (SPP+SBAS) applied has a higher accuracy than SPP as a result of applied ephemeris corrections. More information can be found on Table 33 below:

Table 33. Statistical analysis of single frequency u-blox EVK-M8T 19 min dynamic test (without RAIM-FDE).

GNSS Post-Processing Modes Session length = 19 min **u-blox EVK-M8T** (without RAIM-FDE)	SPP	SPP +SBAS	PPP	RTK	u-center PVT*
Availability (%)	58.86	52.00	N/A	58.77	85.14
(Total no of minutes) Seconds of the day	(18.717 min) 40543s - 41666s	(18.717 min) 40543s - 41666s	N/A	(18.717 min) 40543s - 41666s	(18.733 min) 40542s - 41666s
Horizontal error (2D) [m] (95%)	17.9191	16.6664	N/A	11.4987	47.3788
Vertical error [m] (95%)	12.3820	13.6268	N/A	11.4579	9.2675
Horizontal Min [m]	0.2615	0.1619	N/A	0.0161	0.8799
Horizontal Max [m]	28.6561	35.8383	N/A	20.6858	71.5538
Horizontal Mean [m]	7.6662	7.5601	N/A	4.2492	21.4407
Horizontal SD [m]	5.1471	0.0074	N/A	3.2921	15.5471

d. Samsung Galaxy s8 smartphone 19 min dynamic test (without RAIM-FDE)

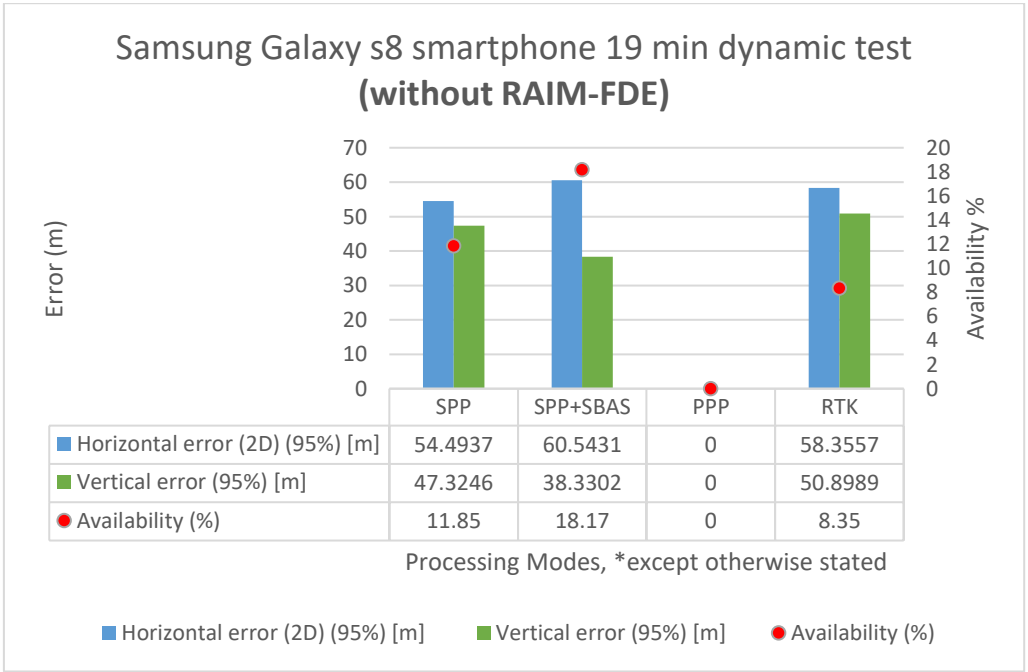

Figure 35. Data visualisation of Samsung Galaxy s8 smartphone 19 min dynamic test (without RAIM-FDE).

From Figure 35, it can be observed that 2D and vertical error reduces from code based positioning techniques to carrier-phase positioning techniques. The best GNSS solution is the RTK solution with a horizontal accuracy of 54.5 m, and vertical accuracy of 47.3 m. PPP is unavailable. More information can be found on Table 34 below:

Table 34. Statistical analysis of Samsung Galaxy s8 smartphone 19 min dynamic test (without RAIM-FDE).

GNSS Post-Processing Modes Session length = 19 min **Samsung Galaxy s8** (without RAIM-FDE)	SPP	SPP +SBAS	PPP	RTK
Availability (%)	11.85	18.17	N/A	8.35
(Total no of minutes) **Seconds of the day**	(18.567 min) 40542s - 41665s	(18.717 min) 40543s - 41666s	N/A	(18.567 min) 40542s - 41665s
Horizontal error (2D) [m] (95%)	54.4937	60.5431	N/A	58.3557
Vertical error [m] (95%)	47.3246	38.3302	N/A	50.8989
Horizontal Min [m]	2.6721	2.2239	N/A	0.7116
Horizontal Max [m]	158.5248	92.2811	N/A	126.5632
Horizontal Mean [m]	24.0751	26.3720	N/A	21.3158
Horizontal SD [m]	19.1180	17.5709	N/A	23.4858

5.2.1.2 32 minutes dynamic tests (without RAIM-FDE)

a. Dual frequency u-blox ZED-F9P-(1) 32 min dynamic test (without RAIM-FDE).

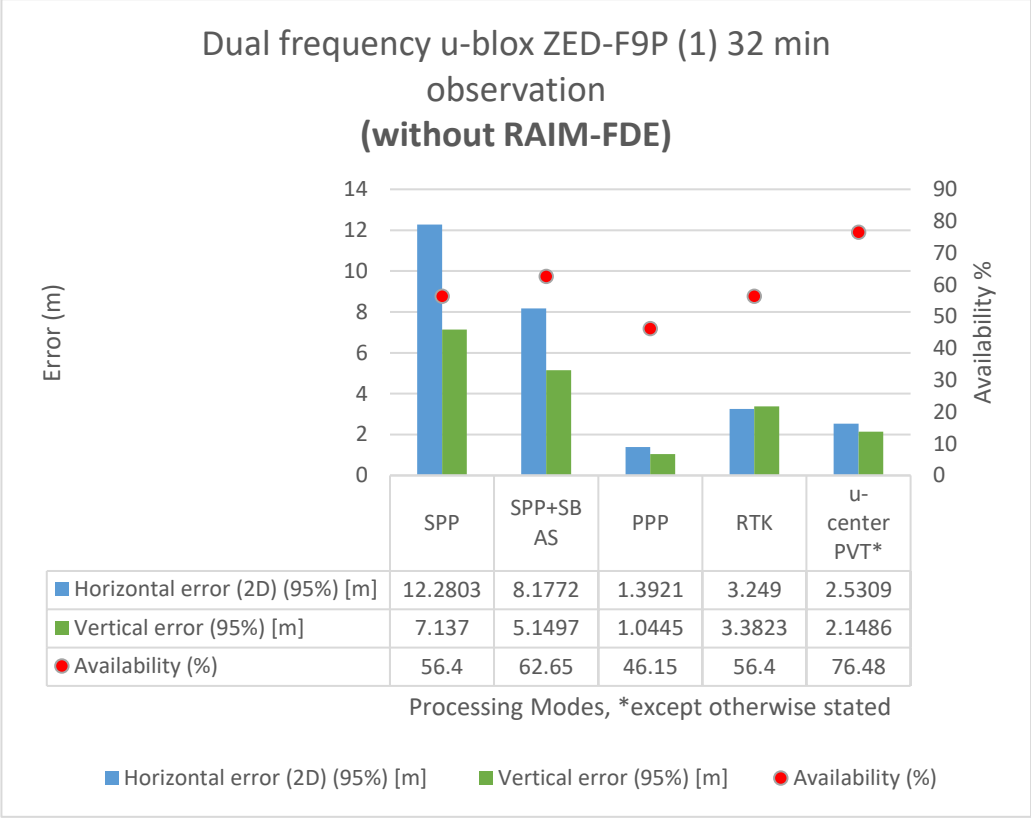

Figure 36. Data visualisation of dual frequency u-blox ZED-F9P-(1) 32 min dynamic test (without RAIM-FDE).

From Figure 36, it can be observed that 2D and vertical error reduces from code based positioning techniques to carrier-phase positioning techniques. The best GNSS solution is the RTK solution with a horizontal accuracy of 3.2 m, and vertical accuracy of 3.4 m. More information can be found on Table 35 below:

Table 35. Statistical analysis of dual frequency u-blox ZED-F9P-(1) 32 min dynamic test (without RAIM-FDE).

GNSS Post-Processing Modes Session length = 31 min **u-blox ZED-F9P-(1)** (without RAIM-FDE)	SPP	SPP +SBAS	PPP	RTK	u-center PVT*
Availability (%)	56.4	62.65	46.15	56.4	76.48
(Total no of minutes) Seconds of the day	(30.967 min) 41969s - 43827s	(30.967 min) 41969s - 43827s	(0.21667 min) 42293s - 42306s	(30.967 min) 41969s - 43827s	(30.967 min) 41969s - 43827s
Horizontal error (2D) [m] (95%)	12.2803	8.1772	1.3921	3.2490	2.5309
Vertical error [m] (95%)	7.1370	5.1497	1.0445	3.3823	2.1486
Horizontal Min [m]	0.0364	0.0822	0.2163	0.0837	0.1808
Horizontal Max [m]	22.0487	19.0137	1.3921	43.3517	3.6655
Horizontal Mean [m]	4.5063	3.2248	0.9080	1.9909	1.4644
Horizontal SD [m]	3.4768	2.3696	0.4905	1.8863	0.5531

b. Dual frequency u-blox ZED-F9P (2) 32 min dynamic test (without RAIM-FDE).

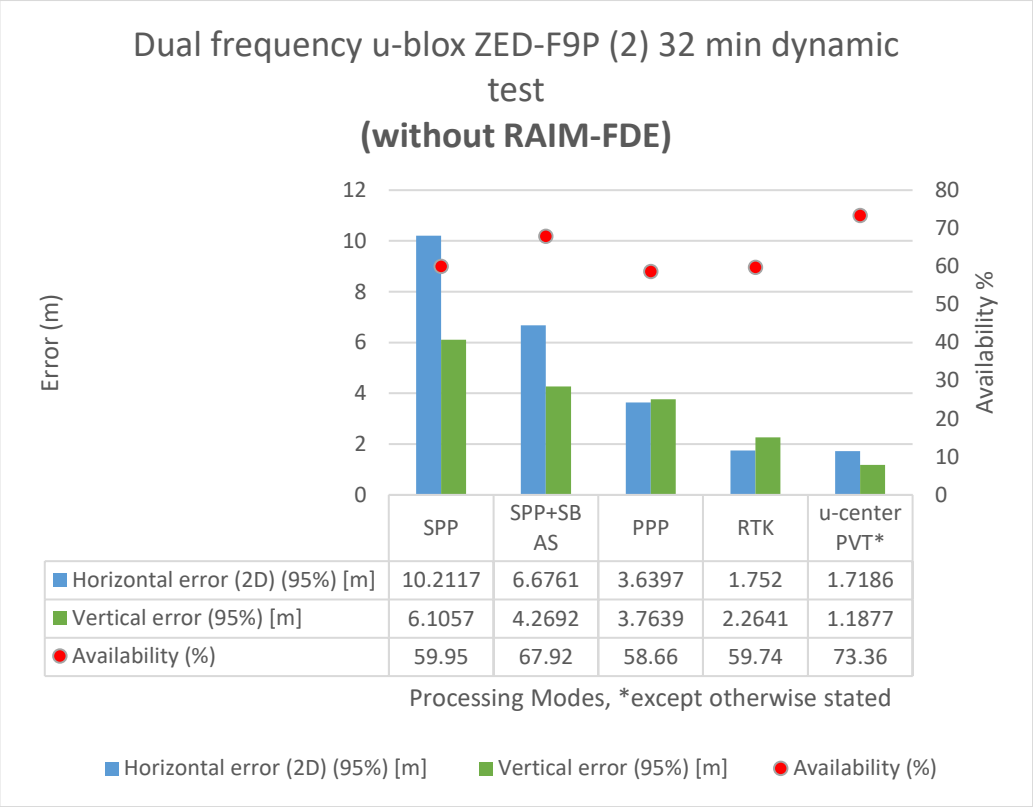

Figure 37. Data visualisation of dual frequency u-blox ZED-F9P-(2) 32 min dynamic test (without RAIM-FDE).

From Figure 37, it can be observed that 2D and vertical error reduces from code based positioning techniques to carrier-phase positioning techniques. The best GNSS solution is the RTK solution with a horizontal accuracy of 1.75 m. More information can be found on Table 36 below:

Table 36. Statistical analysis of dual frequency u-blox ZED-F9P-(2) 32 min dynamic test (without RAIM-FDE).

GNSS Post-Processing Modes Session length = 32 min **u-blox ZED-F9P-(2)** (without RAIM-FDE)	SPP	SPP +SBAS	PPP	RTK	u-center PVT*
Availability (%)	59.95	67.92	58.66	59.74	73.36
(Total no of minutes) Seconds of the day	(32.417 min) 41882s - 43827s	(30.967 min) 41969s - 43827s	(29.917m in) 42032s - 43827s	(32.417 min) 41882s - 43827s	(32.467 min) 41879s - 43827s
Horizontal error (2D) [m] (95%)	10.2117	6.6761	3.6397	1.7520	1.7186
Vertical error [m] (95%)	6.1057	4.2692	3.7639	2.2641	1.1877
Horizontal Min [m]	0.0603	0.0149	0.0810	0.0415	0.1004
Horizontal Max [m]	20.2629	18.2723	12.4929	20.2089	2.3677
Horizontal Mean [m]	2.4984	1.6828	1.7479	0.9114	0.9022
Horizontal SD [m]	3.2359	2.1966	1.1665	0.9492	0.4583

c. Single frequency u-blox EVK-M8T 32 min dynamic test (without RAIM-FDE).

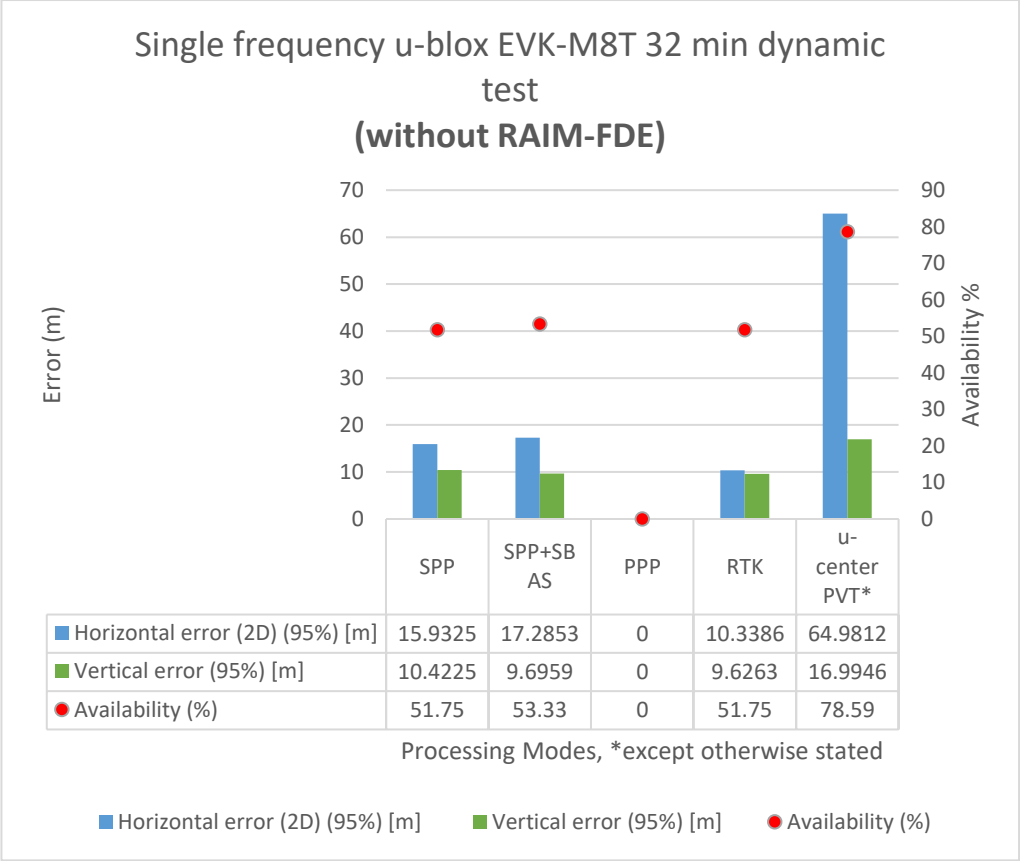

Figure 38. Data visualisation of single frequency u-blox EVK-M8T 32 min dynamic test (without RAIM-FDE).

From Figure 38, it can be observed that 2D and vertical error reduces from code based positioning techniques to carrier-phase positioning techniques. The best GNSS solution is the RTK solution with a horizontal accuracy of 10 m. More information can be found on Table 37 below:

Table 37. Statistical analysis of single frequency u-blox EVK-M8T 32 min dynamic test (without RAIM-FDE).

GNSS Post-Processing Modes Session length = 32 min **u-blox EVK-M8T** (without RAIM-FDE)	SPP	SPP +SBAS	PPP	RTK	u-center PVT*
Availability (%)	51.75	53.33	N/A	51.75	78.59
(Total no of minutes) Seconds of the day	(32.467 min) 41879s - 43827s	(30.283 min) 41879s - 43696s	N/A	(32.467 min) 41879s - 43827s	(32.467 min) 41879s - 43827s
Horizontal error (2D) [m] (95%)	15.9325	17.2853	N/A	10.3386	64.9812
Vertical error [m] (95%)	10.4225	9.6959	N/A	9.6263	16.9946
Horizontal Min [m]	0.2407	0.1813	N/A	0.0819	0.1521
Horizontal Max [m]	29.9689	36.5528	N/A	22.6997	82.9715
Horizontal Mean [m]	6.3606	7.1528	N/A	3.7874	15.9806
Horizontal SD [m]	4.4767	5.2466	N/A	3.2239	18.2042

d. Samsung Galaxy s8 smartphone 32 min dynamic test (without RAIM-FDE)

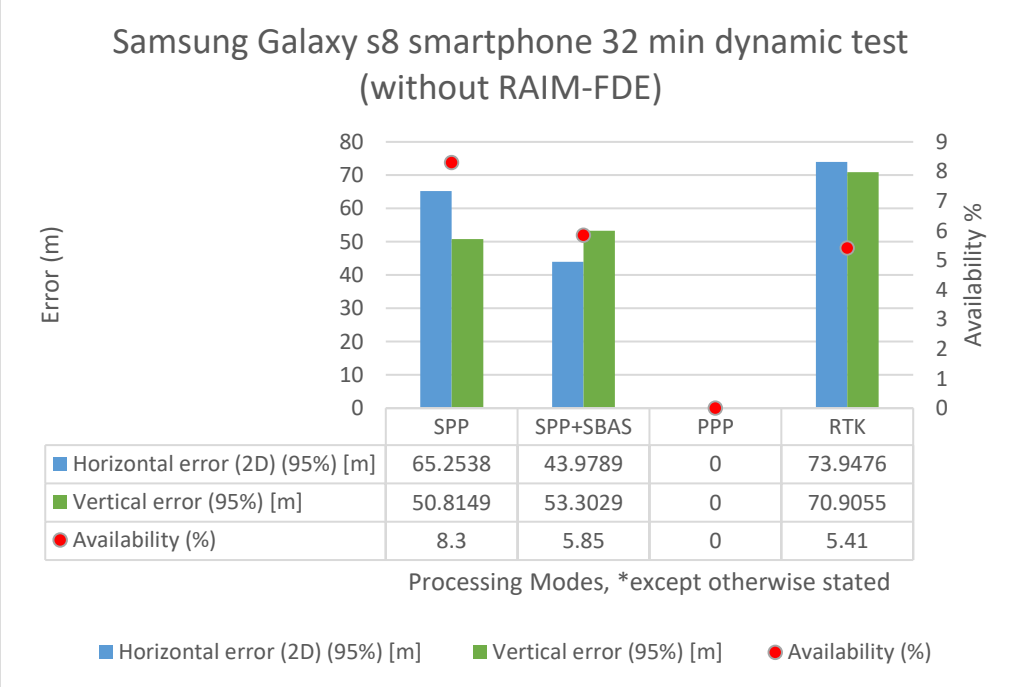

Figure 39. Data visualisation of Samsung Galaxy s8 smartphone 32 min dynamic test (without RAIM-FDE).

From Figure 39, it can be observed that 2D and vertical error reduces from code based positioning techniques to carrier-phase positioning techniques. The best GNSS solution is the SPP+SBAS solution with a horizontal accuracy of 44 m. More information can be found on Table 38 below:

Table 38. Statistical analysis of Samsung Galaxy s8 smartphone 32 min dynamic test (without RAIM-FDE).

GNSS Post-Processing Modes Session length =28 min **Samsung Galaxy s8** (without RAIM-FDE)	SPP	SPP +SBAS	PPP	RTK
Availability (%)	8.3	5.85	N/A	5.41
(Total no of minutes) **Seconds of the day**	(24.3 min) 42015s - 43473s	(23.633 min) 42094s - 43512s	N/A	(24.05 min) 42015s - 43458s
Horizontal error (2D) [m] (95%)	65.2538	43.9789	N/A	73.9476
Vertical error [m] (95%)	50.8149	53.3029	N/A	70.9055
Horizontal Min [m]	1.5519	0.7357	N/A	3.6593
Horizontal Max [m]	92.3091	64.6034	N/A	216.4757
Horizontal Mean [m]	28.9345	23.2717	N/A	24.9580
Horizontal SD [m]	19.6875	12.3138	N/A	29.4890

5.2.2 Statistical analysis of dynamic tests with RAIM-FDE enabled

5.2.2.1 19 minutes dynamic tests (with RAIM-FDE)

a. Dual frequency u-blox ZED-F9P-(1) 19 min dynamic test (with RAIM-FDE).

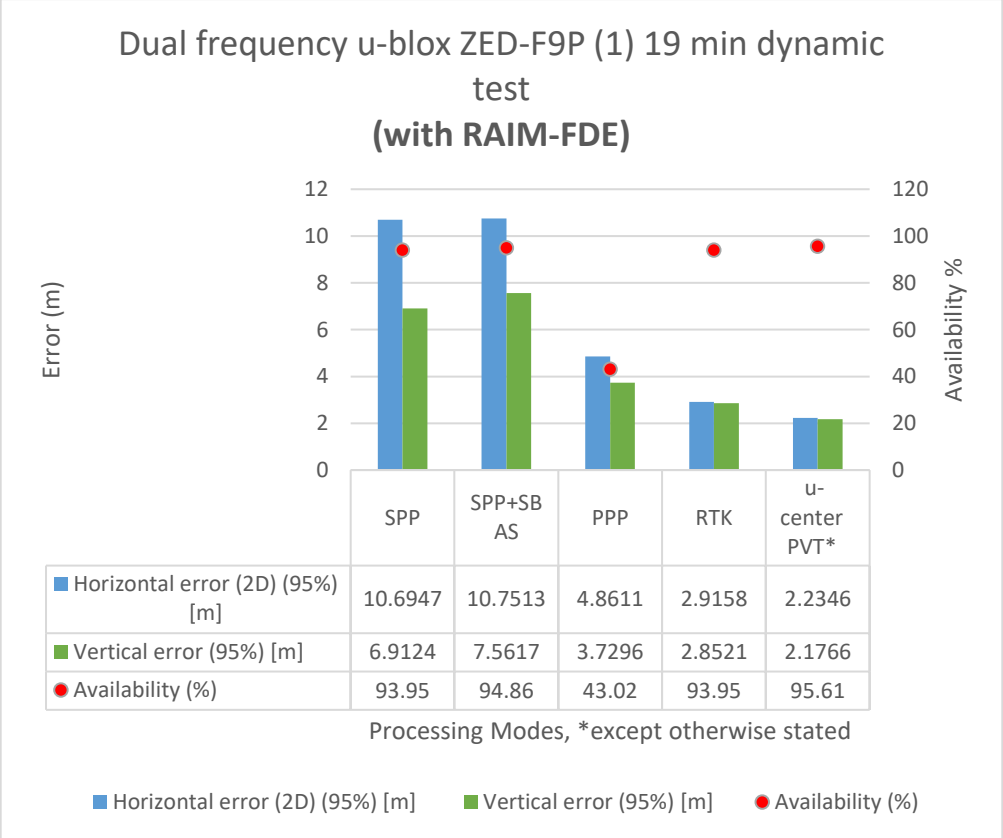

Figure 40. Data visualisation of dual frequency u-blox ZED-F9P-(1) 19 min dynamic test (with RAIM-FDE).

From Figure 40, it can be observed that 2D and vertical error reduces from code based positioning techniques to carrier-phase positioning techniques. The best GNSS solution is the RTK solution with a horizontal accuracy of 2.9 m. More information can be found on Table 39 below:

Table 39. Statistical analysis of dual frequency u-blox ZED-F9P-(1) 19 min dynamic test (with RAIM-FDE).

GNSS Post-Processing Modes Session length = 11 min **u-blox ZED-F9P-(1)** (with RAIM-FDE)	SPP	SPP +SBAS	PPP	RTK	u-center PVT*
Availability (%)	93.95	94.86	43.02	93.95	95.61
(Total no of minutes) Seconds of the day	(11.017 min) 40542s - 41203s	(11.017 min) 40542s - 41203s	(10.38 min) 40542s - 41165s	(11.017 min) 40542s - 41203s	(11 min) 40542s - 41202s
Horizontal error (2D) [m] (95%)	10.6947	10.7513	4.8611	2.9158	2.2346
Vertical error [m] (95%)	6.9124	7.5617	3.7296	2.8521	2.1766
Horizontal Min [m]	0.3649	0.816	0.0726	0.1326	0.3565
Horizontal Max [m]	22.9200	24.0604	2.3412	4.3154	2.7959
Horizontal Mean [m]	4.3393	3.7000	1.2487	1.6792	1.4601
Horizontal SD [m]	3.5227	3.1857	0.0059	0.7062	0.5428

b. Dual frequency u-blox ZED-F9P-(2) 19 min dynamic test (with RAIM-FDE).

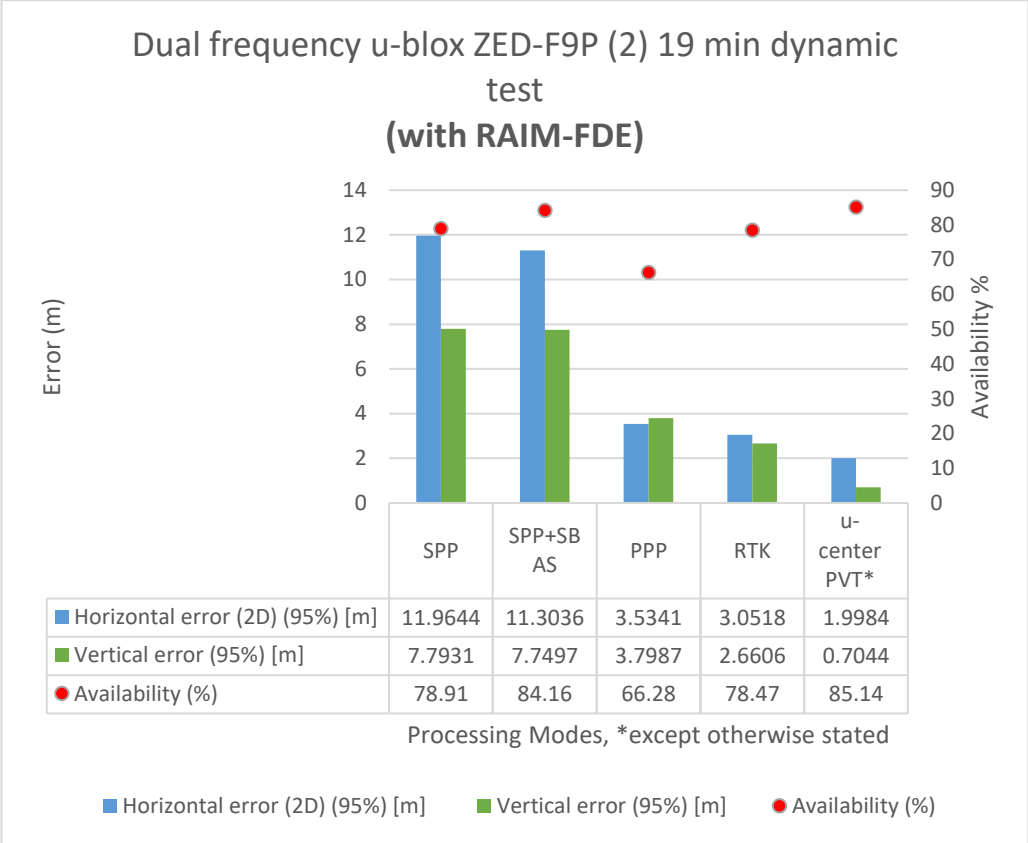

Figure 41. Data visualisation of dual frequency u-blox ZED-F9P-(2) 19 min dynamic test (with RAIM-FDE).

From Figure 41, it can be observed that 2D and vertical error reduces from code based positioning techniques to carrier-phase positioning techniques. The best GNSS solution is the RTK solution with a horizontal accuracy of 1.9 m. More information can be found on Table 40 below:

Table 40. Statistical analysis of dual frequency u-blox ZED-F9P-(2) 19 min dynamic test (with RAIM-FDE).

GNSS Post-Processing Modes Session length = 19 min **u-blox ZED-F9P-(2)** (with RAIM-FDE)	SPP	SPP +SBAS	PPP	RTK	u-center PVT*
Availability (%)	78.91	84.16	66.28	78.47	85.14
Total no of minutes: 18.733 min **Seconds of the day: 40542s - 41666s**	-	-	-	-	-
Horizontal error (2D) [m] (95%)	11.9644	11.3036	3.5341	3.0518	1.9984
Vertical error [m] (95%)	7.7931	7.7497	3.7987	2.6606	0.7044
Horizontal Min [m]	0.0433	0.0775	0.0126	0.0510	0.0953
Horizontal Max [m]	35.2124	40.4764	10.4631	9.6137	3.0121
Horizontal Mean [m]	3.4234	3.1020	1.5641	1.0879	0.8777
Horizontal SD [m]	4.1696	4.8369	1.1175	0.9611	0.5167

c. Single frequency u-blox EVK-M8T 19 min dynamic test (with RAIM-FDE).

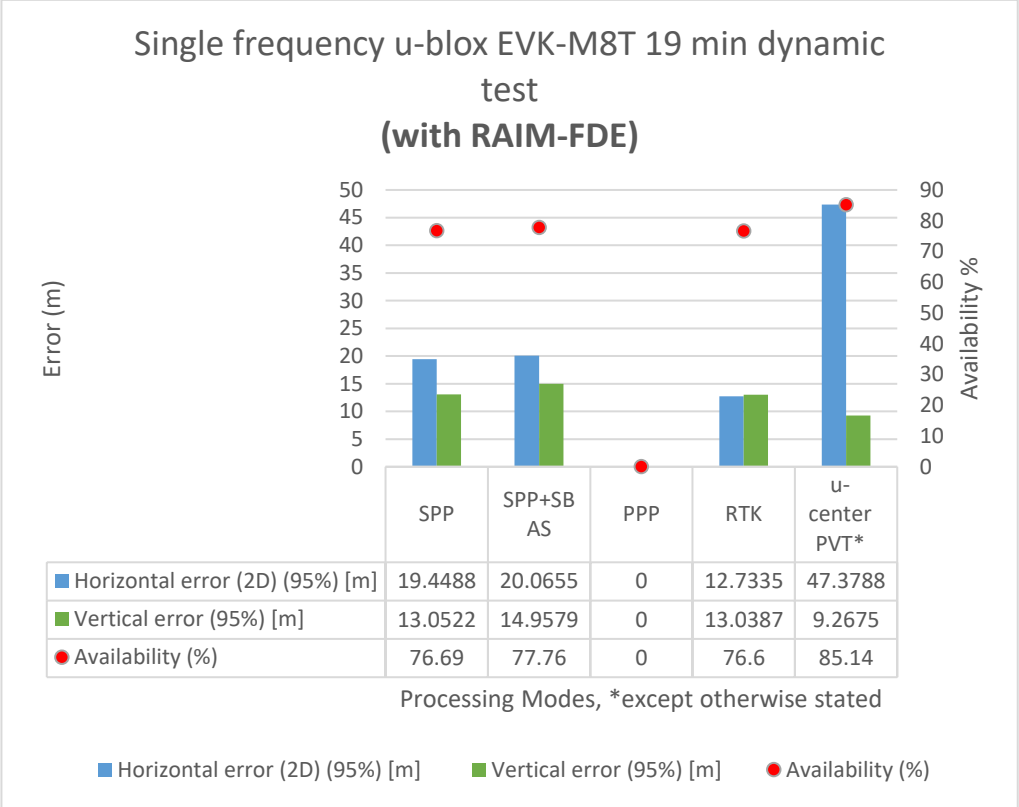

Figure 42. Data visualisation of single frequency u-blox EVK-M8T 19 min dynamic test (with RAIM-FDE).

From Figure 42, it can be observed that 2D and vertical error reduces from code based positioning techniques to carrier-phase positioning techniques. The best GNSS solution is the RTK solution with a horizontal accuracy of 12.7 m. More information can be found on Table 41 below:

Table 41. Statistical analysis of single frequency u-blox EVK-M8T 19 min dynamic test (with RAIM-FDE).

GNSS Post-Processing Modes Session length = 19 min **u-blox EVK-M8T** (with RAIM-FDE)	SPP	SPP +SBAS	PPP	RTK	u-center PVT*
Availability (%)	76.69	77.76	N/A	76.60	85.14
Total no of minutes: 18.733 min Seconds of the day: 40542s - 41666s	-	-	-	-	-
Horizontal error (2D) [m] (95%)	19.4488	20.0655	N/A	12.7335	47.3788
Vertical error [m] (95%)	13.0522	14.9579	N/A	13.0387	9.2675
Horizontal Min [m]	0.2770	0.2824	N/A	0.1026	0.8799
Horizontal Max [m]	30.3670	63.9454	N/A	29.5780	71.5538
Horizontal Mean [m]	8.2615	8.6353	N/A	4.6321	21.4407
Horizontal SD [m]	5.5095	6.5517	N/A	3.7258	15.5471

d. Samsung Galaxy s8 smartphone 19 min dynamic test (with RAIM-FDE).

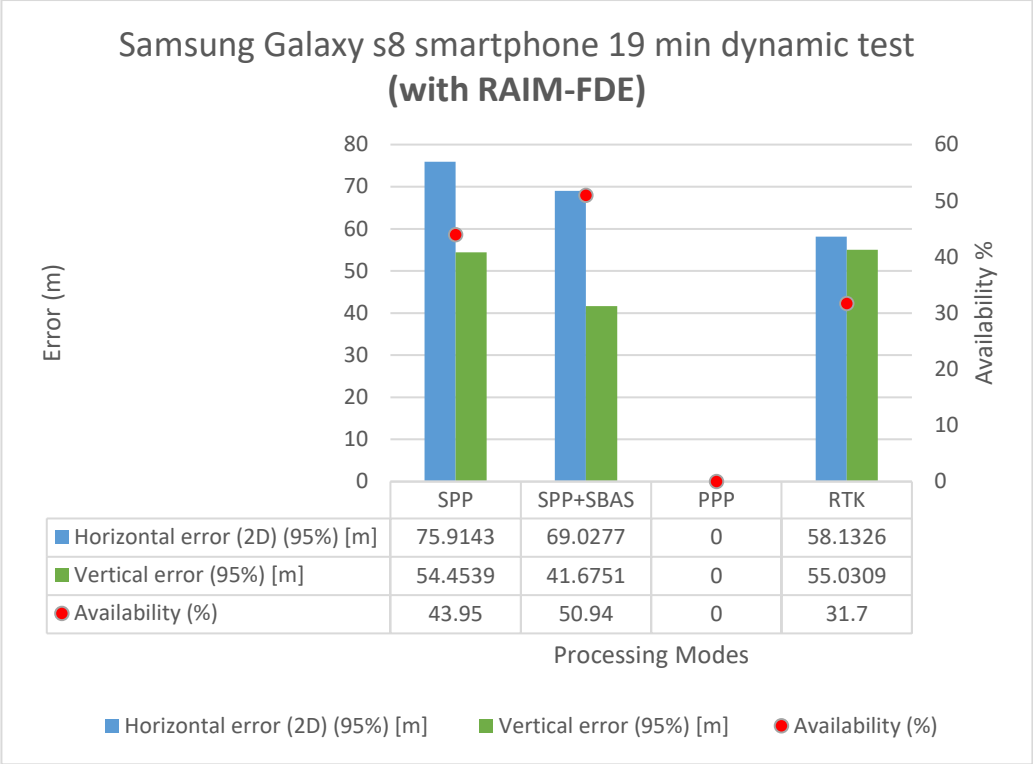

Figure 43. Data visualisation of Samsung Galaxy s8 smartphone 19 min dynamic test (with RAIM-FDE).

From Figure 43, it can be observed that 2D and vertical error reduces from code based positioning techniques to carrier-phase positioning techniques. The best GNSS solution is the RTK solution with a horizontal accuracy of 58 m. More information can be found on Table 42 below:

Table 42. Statistical analysis of Samsung Galaxy s8 smartphone 19 min dynamic test (with RAIM-FDE).

GNSS Post-Processing Modes Session length = 19 min **Samsung Galaxy s8** (with RAIM-FDE)	SPP	SPP +SBAS	PPP	RTK
Availability (%)	43.95	50.94	N/A	31.70
Total no of minutes: 18.733 min **Seconds of the day: 40542s - 41666s**	(18.733 min) 40542s - 41666s	(18.683 min) 40542s - 41663s	N/A	(18.717 min) 40542s - 41665s
Horizontal error (2D) [m] (95%)	75.9143	69.0277	N/A	58.1326
Vertical error [m] (95%)	54.4539	41.6751	N/A	55.0309
Horizontal Min [m]	1.5029	1.9221	N/A	0.8391
Horizontal Max [m]	162.3666	157.8586	N/A	133.5729
Horizontal Mean [m]	29.8387	29.8777	N/A	19.7137
Horizontal SD [m]	23.6040	20.9410	N/A	19.6326

5.2.2.2 32 minutes dynamic tests (with RAIM-FDE)

a. Dual frequency u-blox ZED-F9P-(1) 32 min dynamic test (with RAIM-FDE).

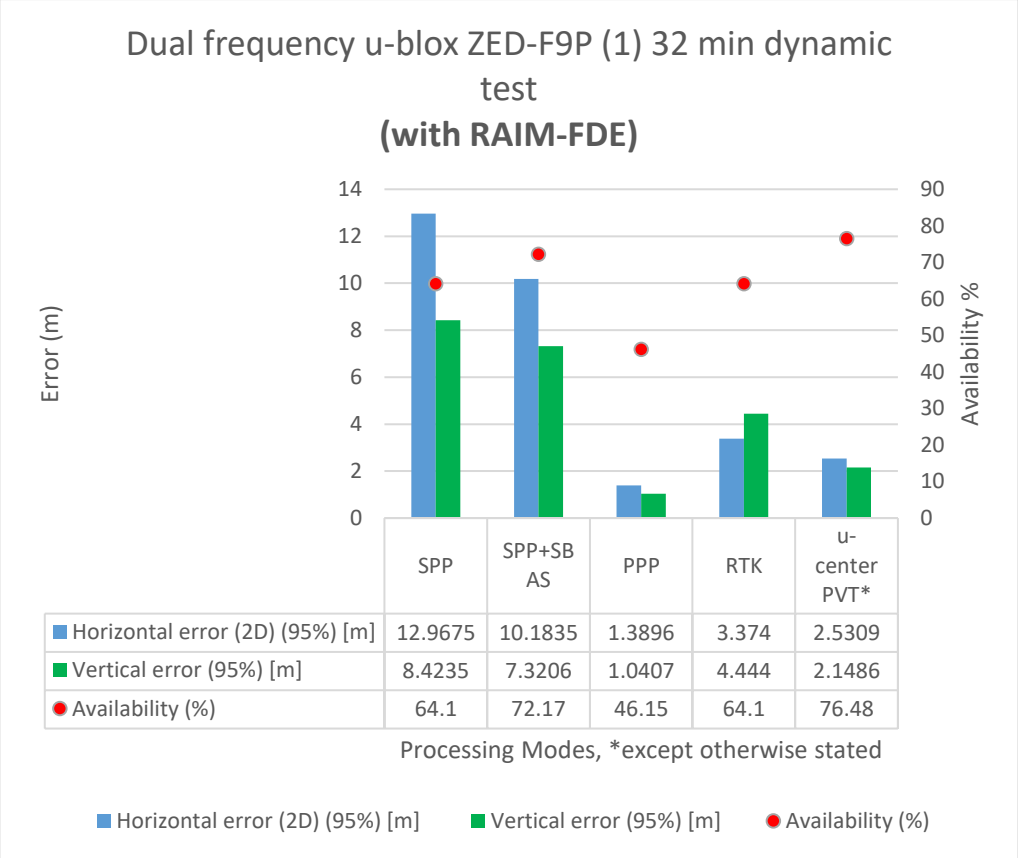

Figure 44. Data visualisation of dual frequency u-blox ZED-F9P-(1) 32 min dynamic test (with RAIM-FDE).

From Figure 44, it can be observed that 2D and vertical error reduces from code based positioning techniques to carrier-phase positioning techniques. SPP with EGNOS corrected ephemeris improves the SPP solution. More information can be found on Table 43 below:

Table 43. Statistical analysis of dual frequency u-blox ZED-F9P-(1) 32 min dynamic test (with RAIM-FDE).

GNSS Post-Processing Modes Session length = 31 min **u-blox ZED-F9P-(1)** (with RAIM-FDE)	SPP	SPP +SBAS	PPP	RTK	u-center PVT*
Availability (%)	64.10	72.17	46.15	64.10	76.48
(Total no of minutes) **Seconds of the day**	(30.967 min) 41969s - 43827s	(30.967 min) 41969s - 43827s	(0.21667 min) 42293s - 42306s	(30.967 min) 41969s - 43827s	(30.967 min) 41969s - 43827s
Horizontal error (2D) [m] (95%)	12.9675	10.1835	1.3896	3.3740	2.5309
Vertical error [m] (95%)	8.4235	7.3206	1.0407	4.4440	2.1486
Horizontal Min [m]	0.0327	0.0394	0.2183	0.1509	0.1808
Horizontal Max [m]	25.6795	55.4417	1.3896	11.7832	3.6655
Horizontal Mean [m]	4.8292	3.6899	0.9054	1.9829	1.4644
Horizontal SD [m]	3.7625	4.1236	0.4888	0.9810	0.5531

b. Dual frequency u-blox ZED-F9P-(2) 32 min dynamic test (with RAIM-FDE).

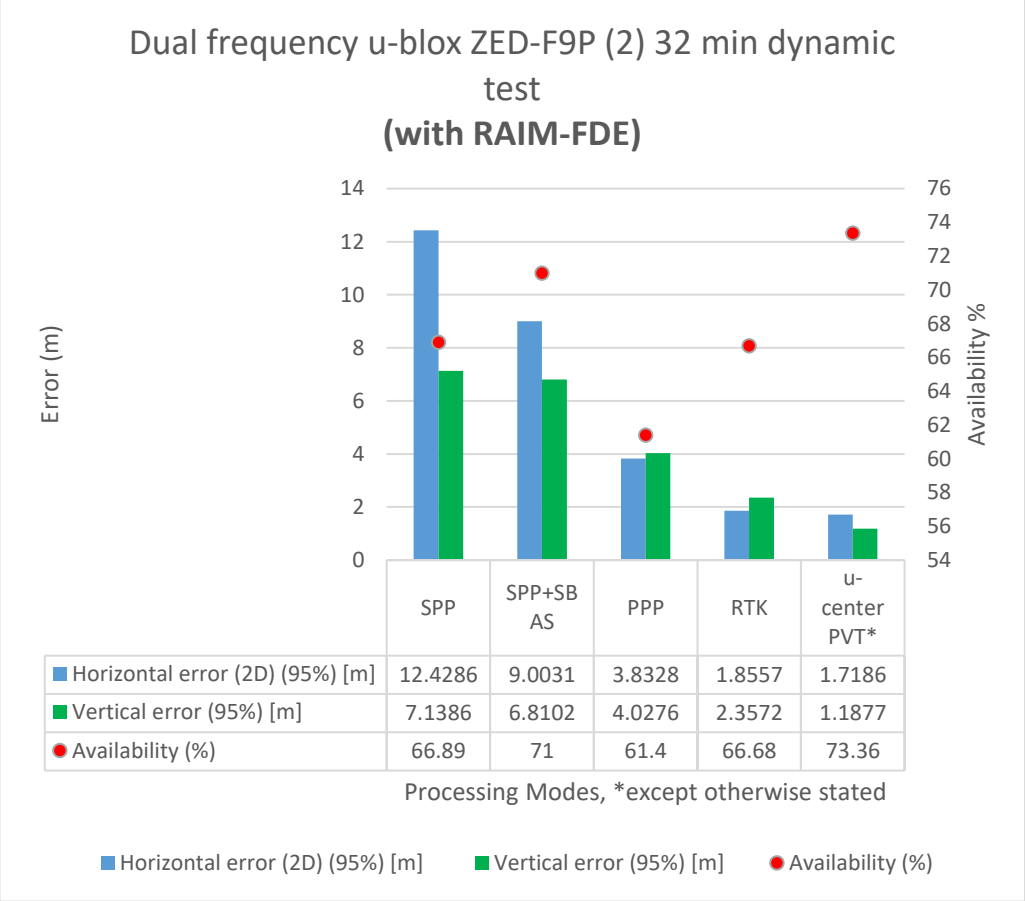

Figure 45. Data visualisation of dual frequency u-blox ZED-F9P-(2) 32 min dynamic test (with RAIM-FDE).

From Figure 45, it can be observed that 2D and vertical error reduces from code based positioning techniques to carrier-phase positioning techniques. SPP with EGNOS corrected ephemeris improves the SPP solution. More information can be found on Table 44 below:

Table 44. Statistical analysis of dual frequency u-blox ZED-F9P-(2) 32 min dynamic test (with RAIM-FDE).

GNSS Post-Processing Modes Session length = 32 min **u-blox ZED-F9P-(2)** (with RAIM-FDE)	SPP	SPP +SBAS	PPP	RTK	u-center PVT*
Availability (%)	66.89	71	61.40	66.68	73.36
Total no of minutes: 32.467 min Seconds of the day: 41879s – 43827s	-	-	-	-	-
Horizontal error (2D) [m] (95%)	12.4286	9.0031	3.8328	1.8557	1.7186
Vertical error [m] (95%)	7.1386	6.8102	4.0276	2.3572	1.1877
Horizontal Min [m]	0.0154	0.0179	0.0440	0.0753	0.1004
Horizontal Max [m]	22.5372	34.7969	12.8158	9.7283	2.3677
Horizontal Mean [m]	3.0165	2.4730	1.8039	0.9111	0.9022
Horizontal SD [m]	3.7582	4.4401	1.2282	0.6239	0.4583

c. Single frequency u-blox EVK-M8T 32 min dynamic test (with RAIM-FDE).

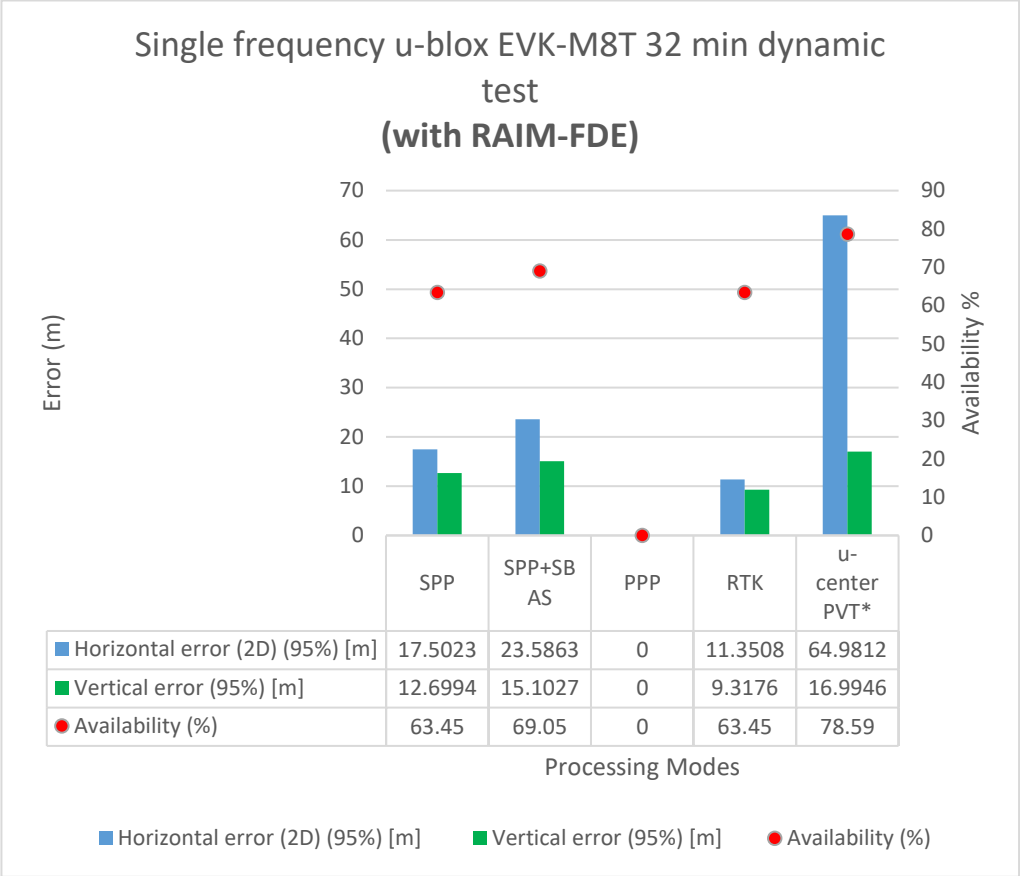

Figure 46. Data visualisation of single frequency u-blox EVK-M8T 32 min dynamic test (with RAIM-FDE).

From Figure 46, it can be observed that 2D and vertical error reduces from code based positioning techniques to carrier-phase positioning techniques with the RTK as the best solution. More information can be found on Table 45 below:

Table 45. Statistical analysis of single frequency u-blox EVK-M8T 32 min dynamic test (with RAIM-FDE).

GNSS Post-Processing Modes Session length = 32 min **u-blox EVK-M8T** (with RAIM-FDE)	SPP	SPP +SBAS	PPP	RTK	u-center PVT*
Availability (%)	63.45	69.05	N/A	63.45	78.59
(Total no of minutes) **Seconds of the day**	(32.467 min) 41879s – 43827s	(32.467 min) 41879s – 43827s	N/A	(32.467 min) 41879s – 43827s	(30.283 min) 41879s – 43696s
Horizontal error (2D) [m] (95%)	17.5023	23.5863	N/A	11.3508	64.9812
Vertical error [m] (95%)	12.6994	15.1027	N/A	9.3176	16.9946
Horizontal Min [m]	0.1671	0.1252	N/A	0.0640	0.1521
Horizontal Max [m]	30.9783	46.1038	N/A	26.6344	82.9715
Horizontal Mean [m]	7.1657	8.3245	N/A	4.1420	15.9806
Horizontal SD [m]	5.1438	6.8751	N/A	3.7120	18.2042

d. Samsung Galaxy s8 smartphone 32 min dynamic test (with RAIM-FDE).

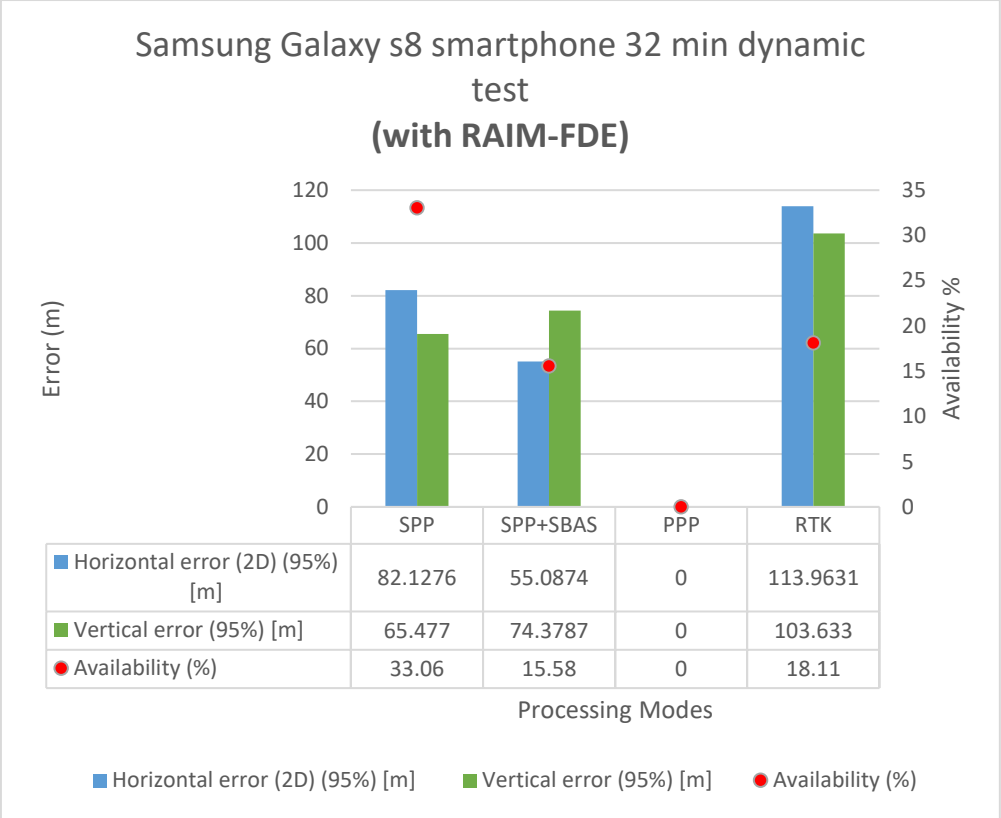

Figure 47. Data visualisation of Samsung Galaxy s8 smartphone 32 min dynamic test (with RAIM-FDE).

From Figure 47, the best solution is SPP+SBAS. Higher processing techniques do not improve the quality of the GNSS solution. More information can be found on Table 46 below:

Table 46. Statistical analysis of Samsung Galaxy s8 smartphone 32 min dynamic test (with RAIM-FDE).

GNSS Post-Processing Modes Session length = 32 min **Samsung Galaxy s8** (with RAIM-FDE)	SPP	SPP +SBAS	PPP	RTK
Availability (%)	33.06	15.58	N/A	18.11
(Total no of minutes) **Seconds of the day**	(28.683 min) 41969s – 43690s	(26.633 min) 42094s – 43692s	N/A	(28.433 min) 41969s – 43675s
Horizontal error (2D) [m] (95%)	82.1276	55.0874	N/A	113.9631
Vertical error [m] (95%)	65.4770	74.3787	N/A	103.6330
Horizontal Min [m]	0.1480	0.2838	N/A	0.5552
Horizontal Max [m]	154.8628	144.1454	N/A	175.4149
Horizontal Mean [m]	32.6425	25.9279	N/A	27.5699
Horizontal SD [m]	25.4448	17.5574	N/A	32.5640

5.3 Analysis of positioning accuracy for stationary tests

5.3.1 Analysis of positioning accuracy (device-to-device comparisons) for stationary tests

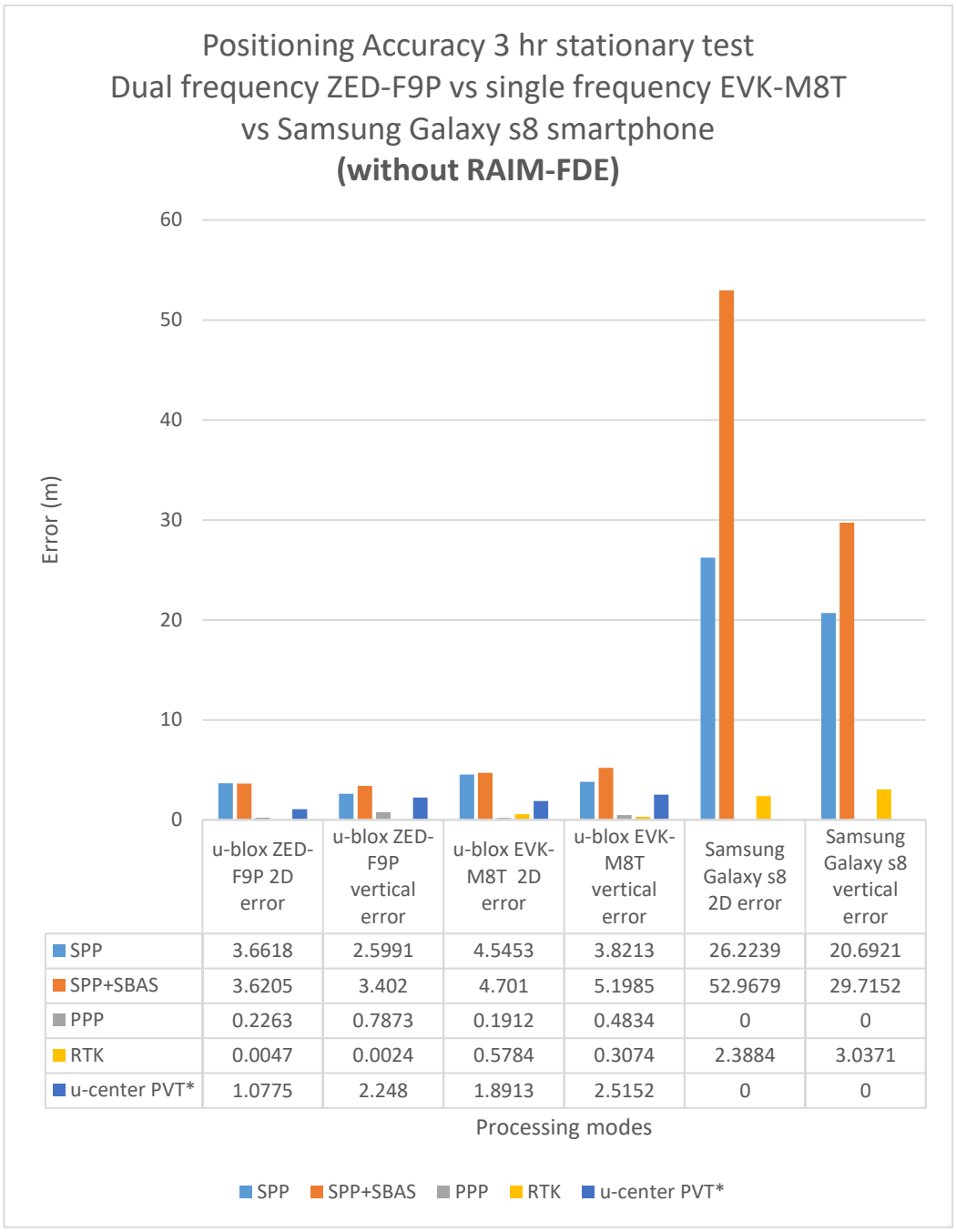

	u-blox ZED-F9P 2D error	u-blox ZED-F9P vertical error	u-blox EVK-M8T 2D error	u-blox EVK-M8T vertical error	Samsung Galaxy s8 2D error	Samsung Galaxy s8 vertical error
SPP	3.6618	2.5991	4.5453	3.8213	26.2239	20.6921
SPP+SBAS	3.6205	3.402	4.701	5.1985	52.9679	29.7152
PPP	0.2263	0.7873	0.1912	0.4834	0	0
RTK	0.0047	0.0024	0.5784	0.3074	2.3884	3.0371
u-center PVT*	1.0775	2.248	1.8913	2.5152	0	0

Figure 48. Positioning accuracy 3 hr stationary test for dual frequency vs single frequency vs smartphone (without RAIM-FDE).

From figure 48, dual frequency receivers (ZED-F9P) have better accuracy when compared to other devices. The smartphone is the poorest performer.

Typically, the accuracy improves across the different processing modes: SPP, SPP+SBAS, PPP, and RTK; with SPP being the poorest and RTK being the best. SPP+SBAS is the worst because the Geographic location suffers from poor EGNOS (SBAS) signal availability (Bhuiyan et al., 2017).

In absence of RAIM-FDE, a relatively good RTK centimetre level horizontal accuracy of 0.47 cm was achieved by the dual frequency receivers (ublox ZED-F9P), during a stationary test session length of 3 hours.

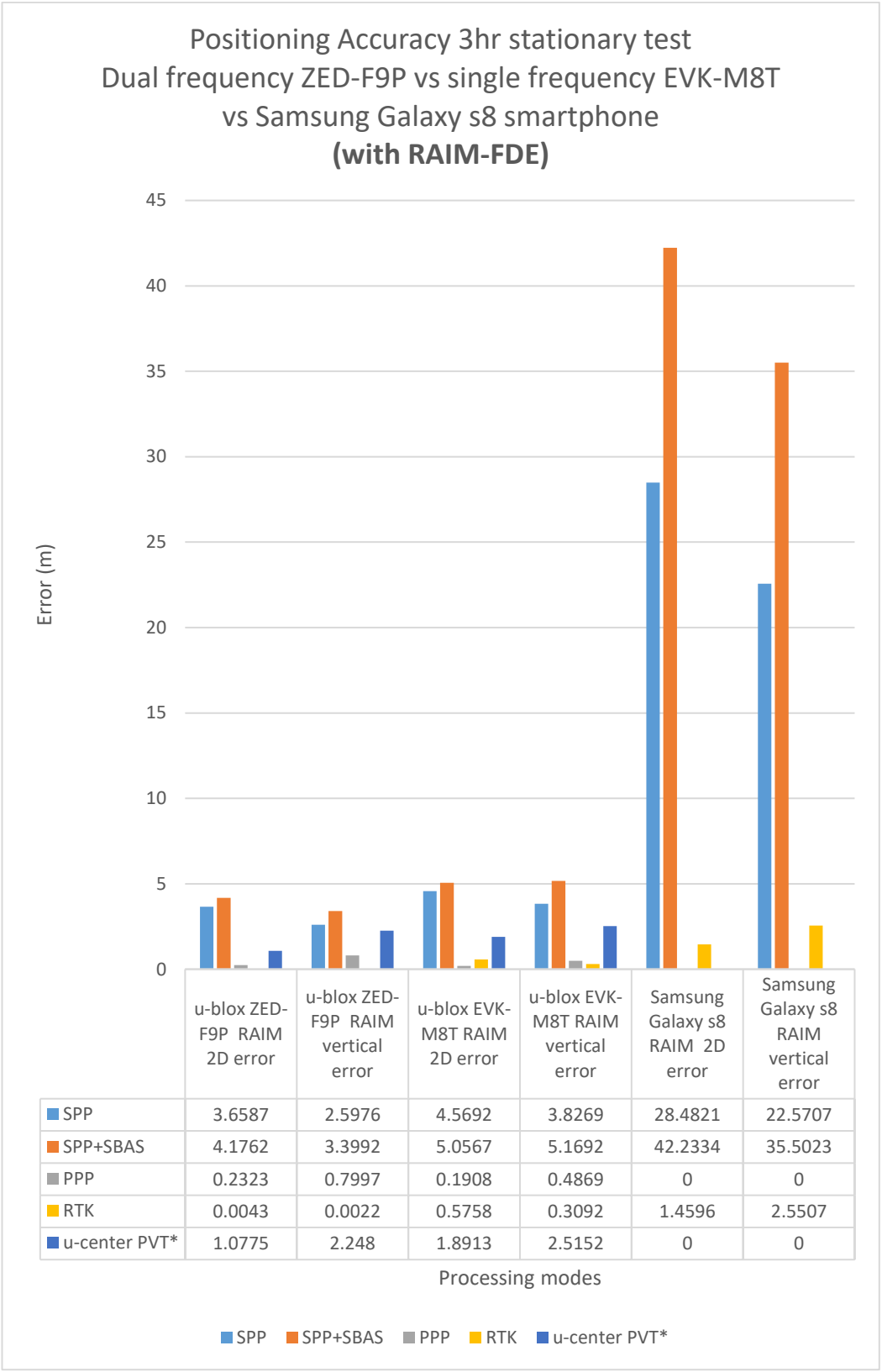

	u-blox ZED-F9P RAIM 2D error	u-blox ZED-F9P RAIM vertical error	u-blox EVK-M8T RAIM 2D error	u-blox EVK-M8T RAIM vertical error	Samsung Galaxy s8 RAIM 2D error	Samsung Galaxy s8 RAIM vertical error
SPP	3.6587	2.5976	4.5692	3.8269	28.4821	22.5707
SPP+SBAS	4.1762	3.3992	5.0567	5.1692	42.2334	35.5023
PPP	0.2323	0.7997	0.1908	0.4869	0	0
RTK	0.0043	0.0022	0.5758	0.3092	1.4596	2.5507
u-center PVT*	1.0775	2.248	1.8913	2.5152	0	0

Figure 49. Positioning accuracy 3 hr stationary test for dual frequency vs single frequency vs smartphone (with RAIM-FDE).

From figure 49, dual frequency receivers (ZED-F9P) have better accuracy when compared to other devices. The smartphone is the poorest performer.

Typically, the accuracy improves across the different processing modes: SPP, SPP+SBAS, PPP, and RTK; with SPP being the poorest and RTK being the best. SPP+SBAS is the worst because the Geographic location suffers from poor EGNOS (SBAS) signal availability (Bhuiyan et al., 2017).

In presence of RAIM-FDE, a relatively good RTK centimetre level horizontal accuracy of 0.43 cm was achieved by the dual frequency receivers (ublox ZED-F9P), during a stationary test session length of 3 hours.

5.3.2 Analysis of positioning accuracy (with RAIM-FDE vs without RAIM-FDE) for stationary tests

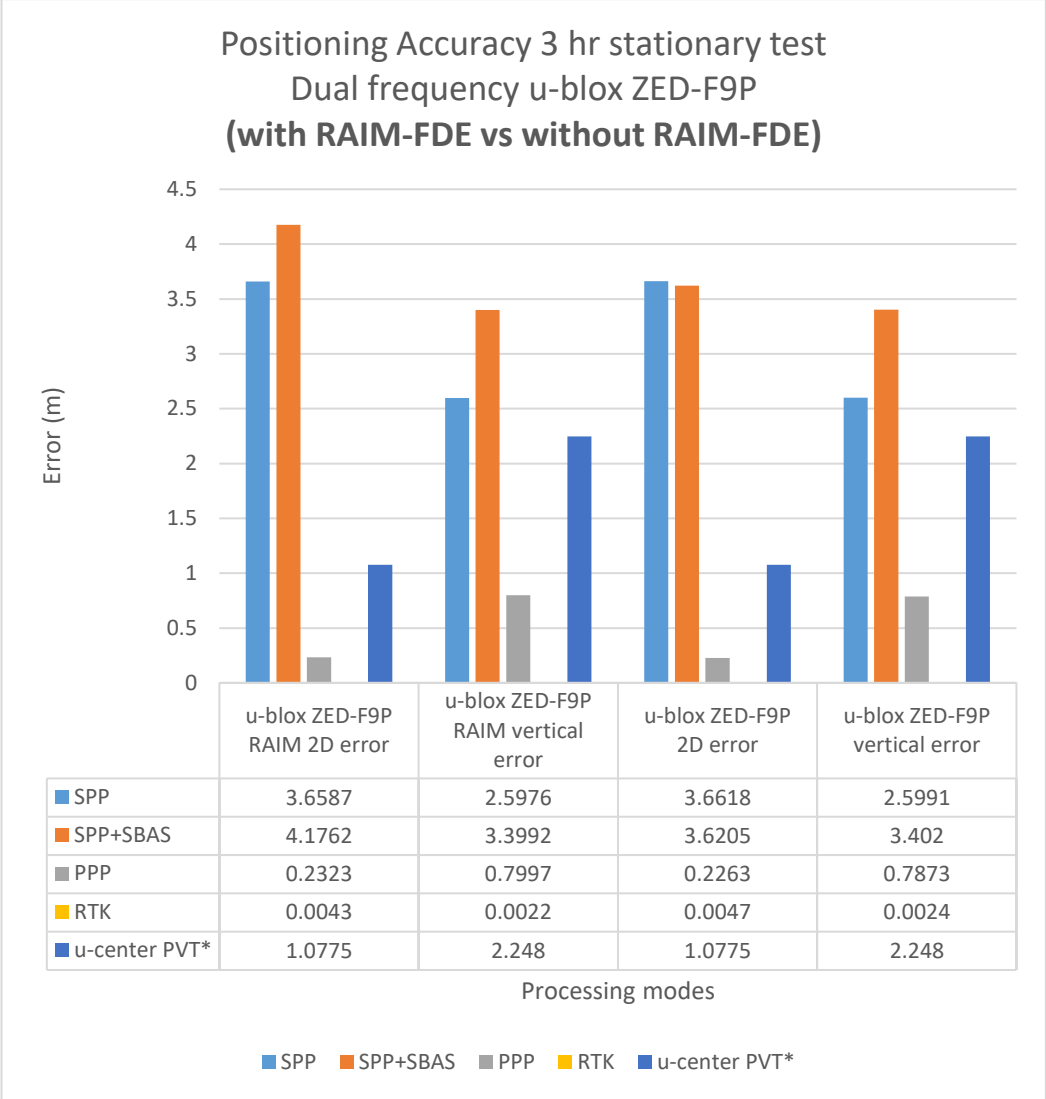

Figure 50. Positioning Accuracy 3 hr stationary test for dual frequency receiver (with RAIM-FDE vs without RAIM-FDE).

Enabling RAIM-FDE reduced the horizontal error of the dual frequency receivers (ublox ZED-F9P) from 0.47 cm to 0.43 cm (see figure 50).

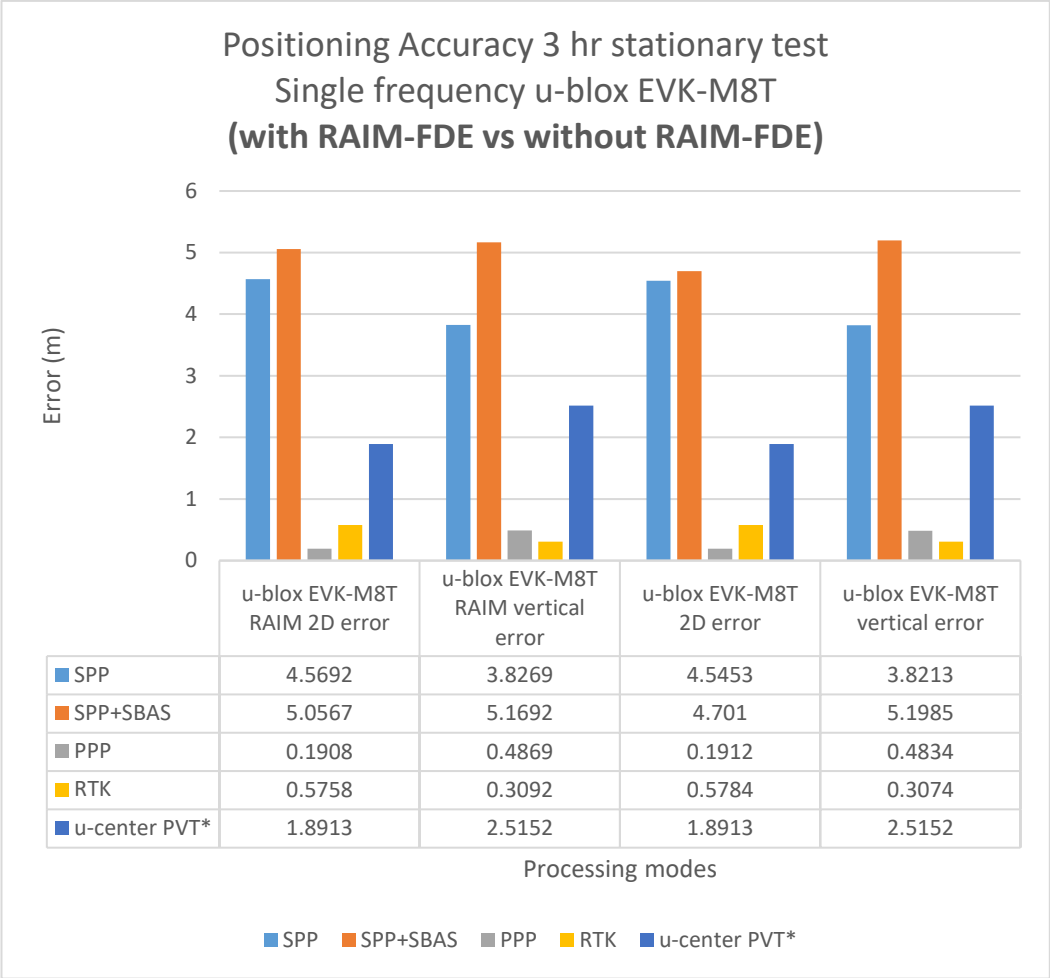

Figure 51. Positioning Accuracy 3 hr stationary test for single frequency receiver (with RAIM-FDE vs without RAIM-FDE).

There is no significant improvement in positioning accuracy with RAIM-FDE enabled for the single frequency device. In the RTK case, a slight improvement of 0.03cm is observed (see figure 51).

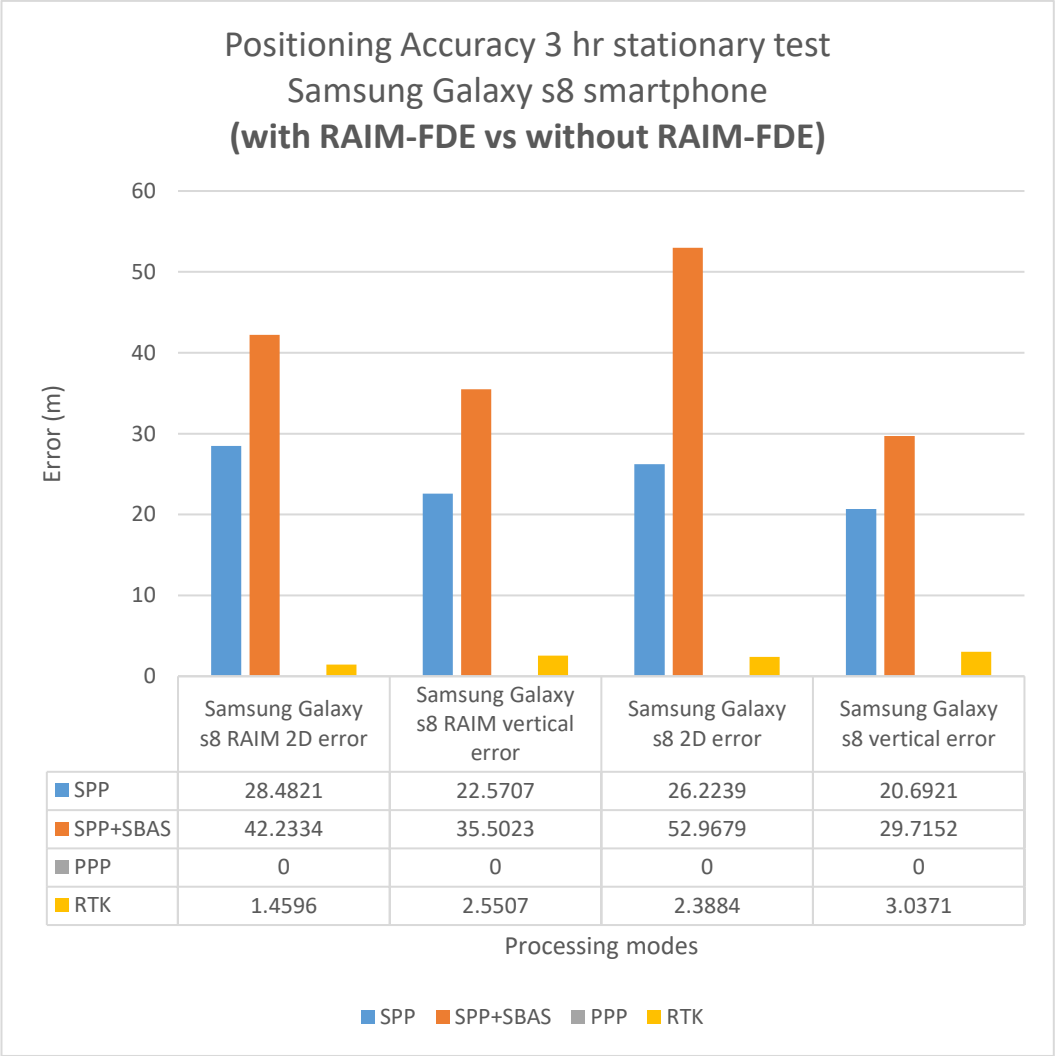

Figure 52. Positioning Accuracy 3 hr stationary test for smartphone (with RAIM-FDE vs without RAIM-FDE).

Enabling RAIM-FDE improves the horizontal and vertical accuracy in RTK and SPP with EGNOS (SPP+SBAS). There is no improvement for the SPP case.

5.4 Analysis of availability for dynamic tests.

5.4.1 Analysis of Availability (Device to device comparisons) for dynamic tests

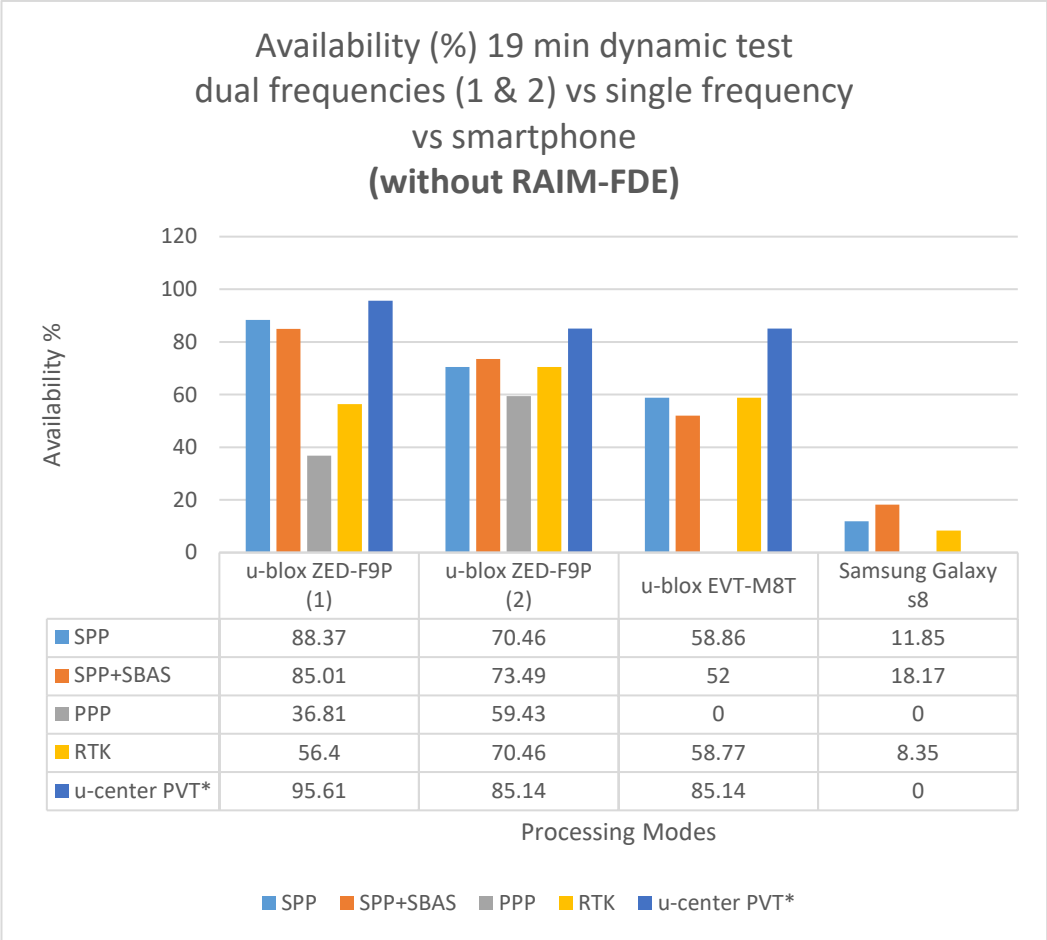

Figure 53. Analysis of availability - 19 min dynamic test - for dual frequencies (1 & 2) vs single frequency vs smartphone (without RAIM-FDE).

From figure 53, the largest availability occurs in the dual frequency receiver (ZED-F9P), while the least availability is recorded in the smartphone. There is also a decrease in availability across the various GNSS processing modes with SPP as the highest and PPP as the least.

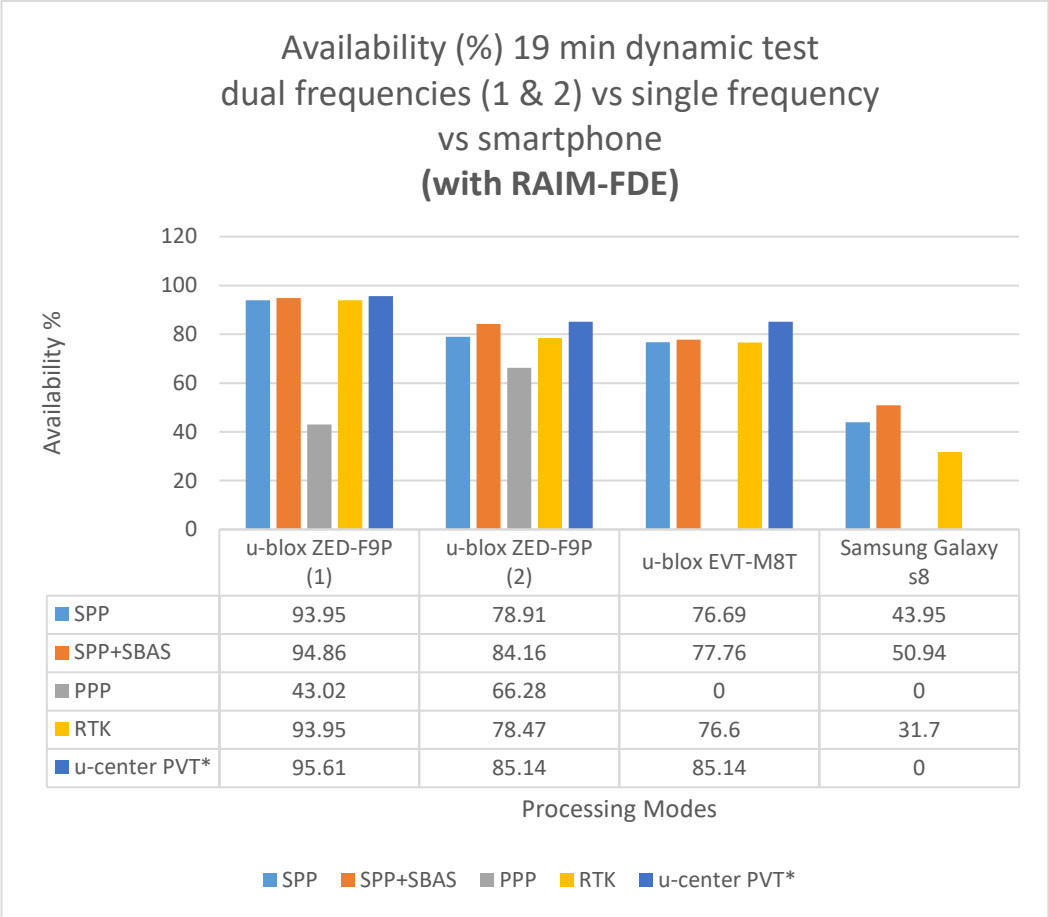

Figure 54. Analysis of availability - 19 min dynamic test - for dual frequencies (1 & 2) vs single frequency vs smartphone (with RAIM-FDE).

From figure 54, the largest availability occurs in the dual frequency receiver (ZED-F9P), while the least availability is recorded in the smartphone. There is also a decrease in availability across the various GNSS processing modes with SPP+SBAS as the highest, followed by SPP, RTK, and PPP. The availability of the u-center PVT* solution is displayed to show that 100% availability was not observed. Lesser availability is noticed after RTKLib GNSS processing due to software limitations.

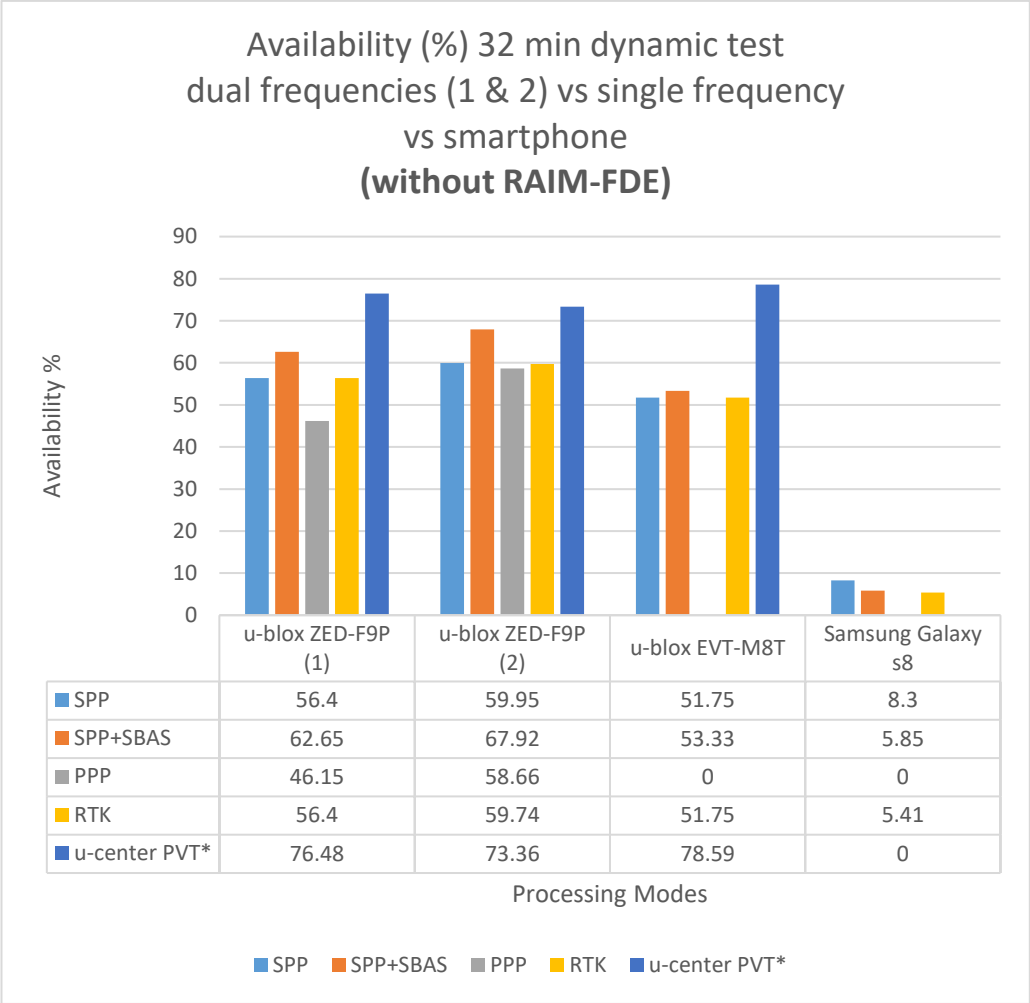

Figure 55. Analysis of availability - 32 min dynamic test - for dual frequencies (1 & 2) vs single frequency vs smartphone (without RAIM-FDE).

From figure 55, the largest availability occurs in the dual frequency receiver (ZED-F9P), while the least availability is recorded in the smartphone. There is also a decrease in availability across the various GNSS processing modes with SPP+SBAS as the highest, followed by SPP, RTK, and PPP. The availability of the u-center PVT* solution is displayed to show that 100% availability was not observed. Lesser availability is noticed after RTKLib GNSS processing due to software limitations.

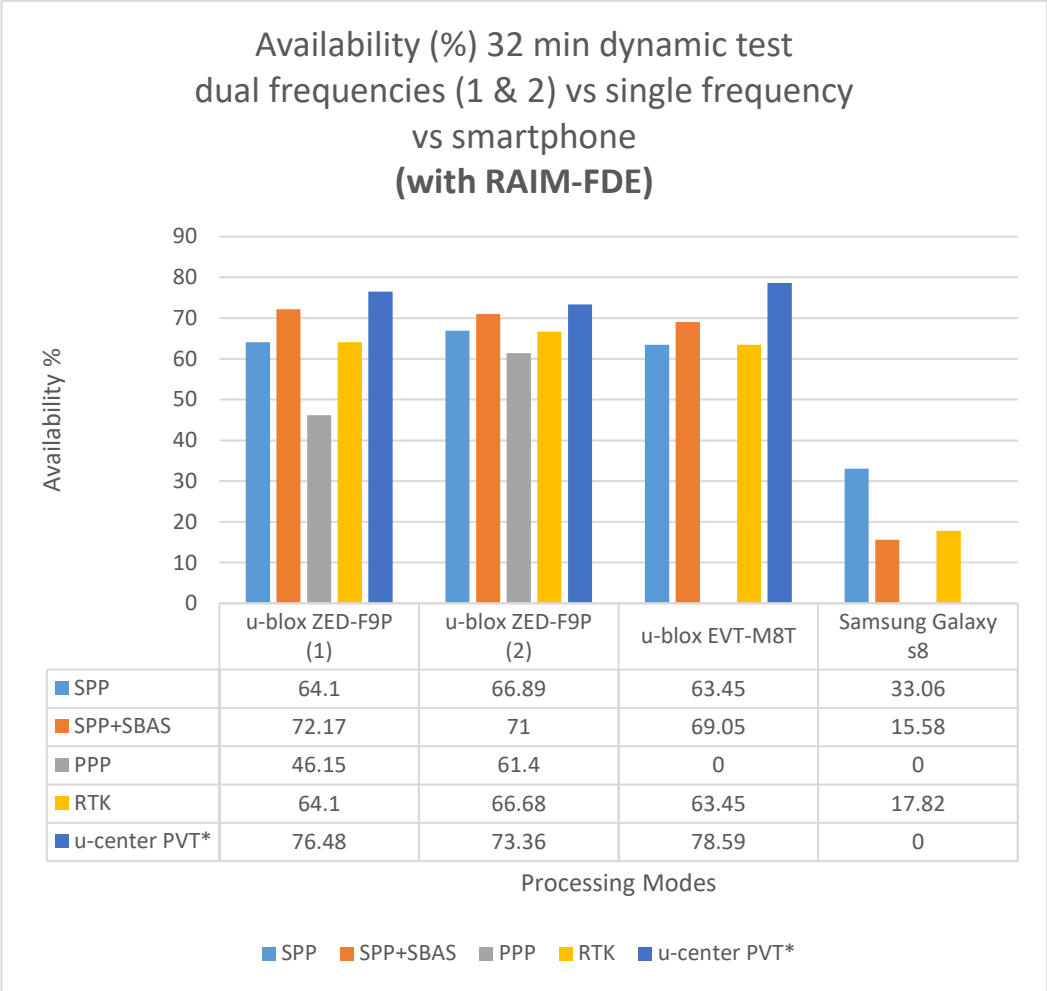

Figure 56. Analysis of availability - 32 min dynamic test - for dual frequencies (1 & 2) vs single frequency vs smartphone (with RAIM-FDE).

From figure 56, the largest availability occurs in the dual frequency receiver (ZED-F9P), while the least availability is recorded in the smartphone. There is also a decrease in availability across the various GNSS processing modes with SPP+SBAS as the highest, followed by SPP, RTK, and PPP. The availability of the u-center PVT* solution is displayed to show that 100% availability was not observed. Lesser availability is noticed after RTKLib GNSS processing due to software limitations.

5.4.2 Analysis of Availability (with RAIM-FDE vs without RAIM-FDE) for dynamic tests

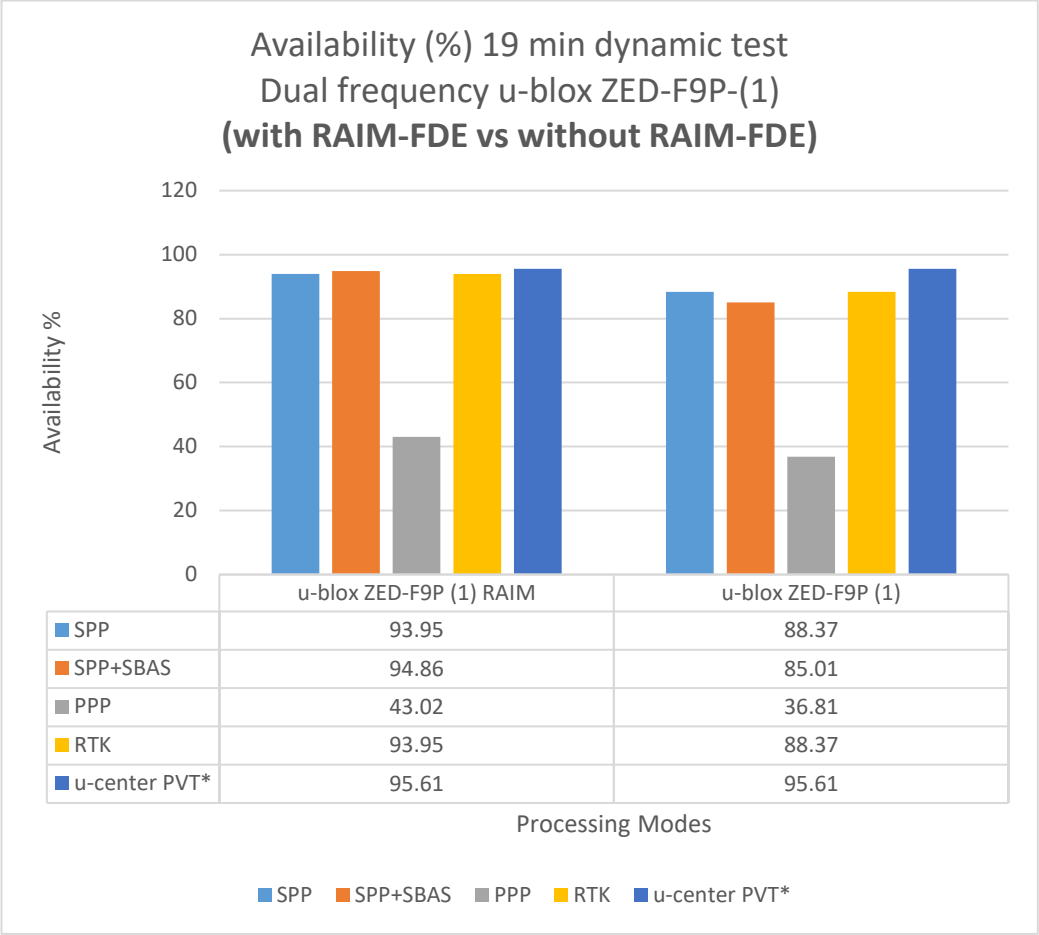

Figure 57. Analysis of availability - 19 min dynamic test - for dual frequency u-blox ZED-F9P-(1) (with RAIM-FDE vs without RAIM-FDE).

From figure 57, more availability is observed with RAIM-FDE solutions.

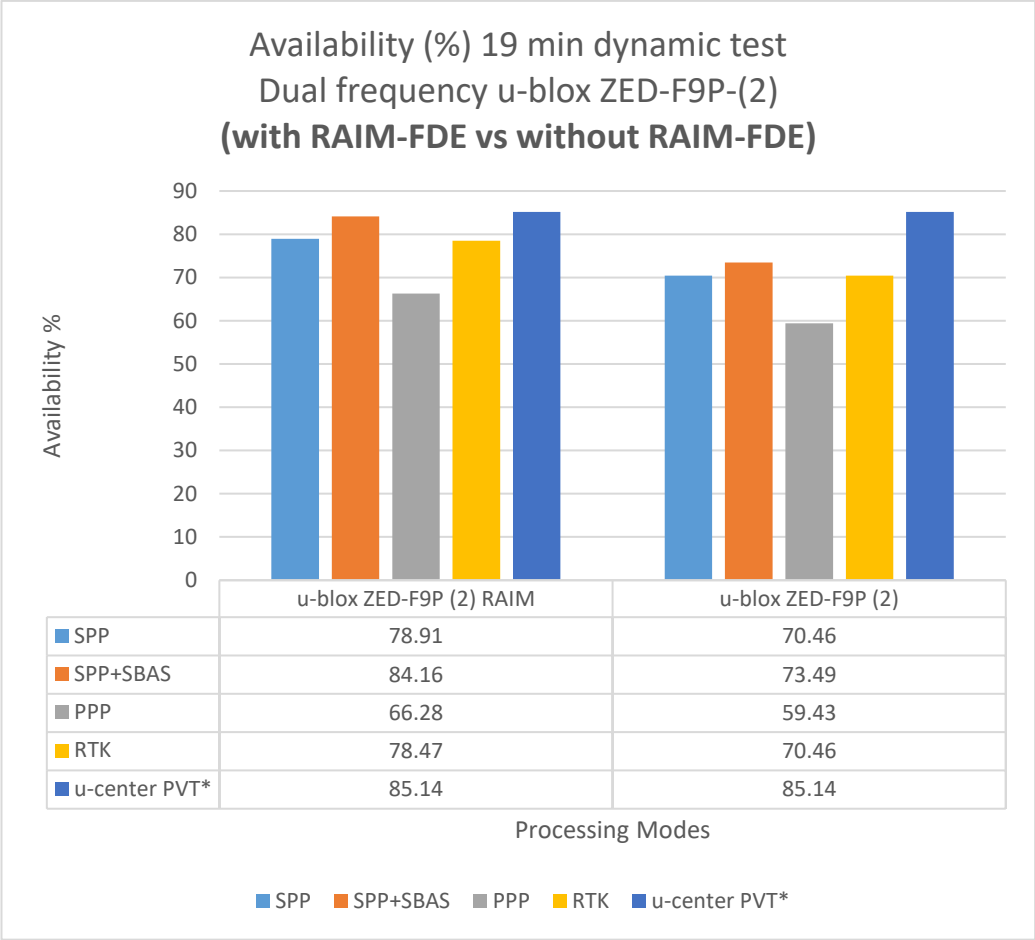

Figure 58. Analysis of availability - 19 min dynamic test - for dual frequency u-blox ZED-F9P-(2) (with RAIM-FDE vs without RAIM-FDE).

From figure 58, more availability is observed with RAIM-FDE solutions.

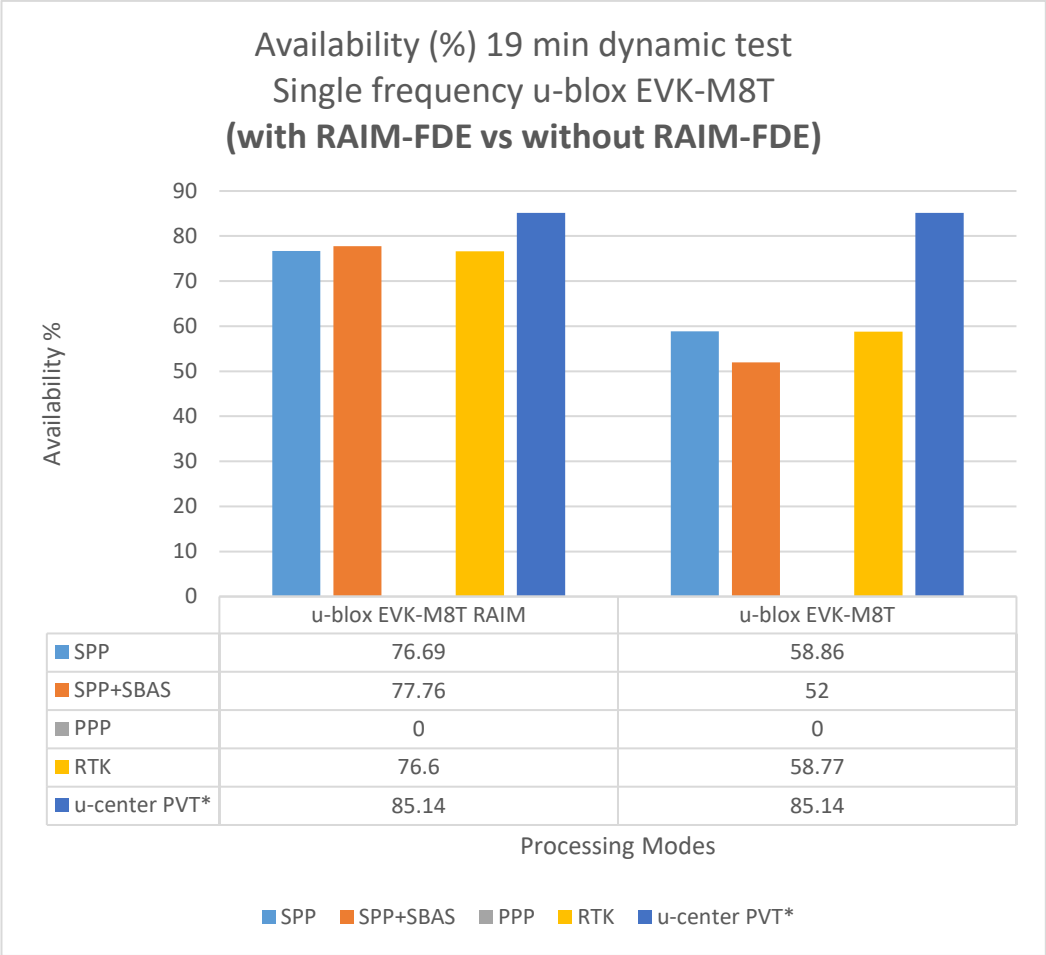

Figure 59. Analysis of availability - 19 min dynamic test - for single frequency u-blox EVK-M8T (with RAIM-FDE vs without RAIM-FDE).

From figure 59, more availability is observed with RAIM-FDE solutions.

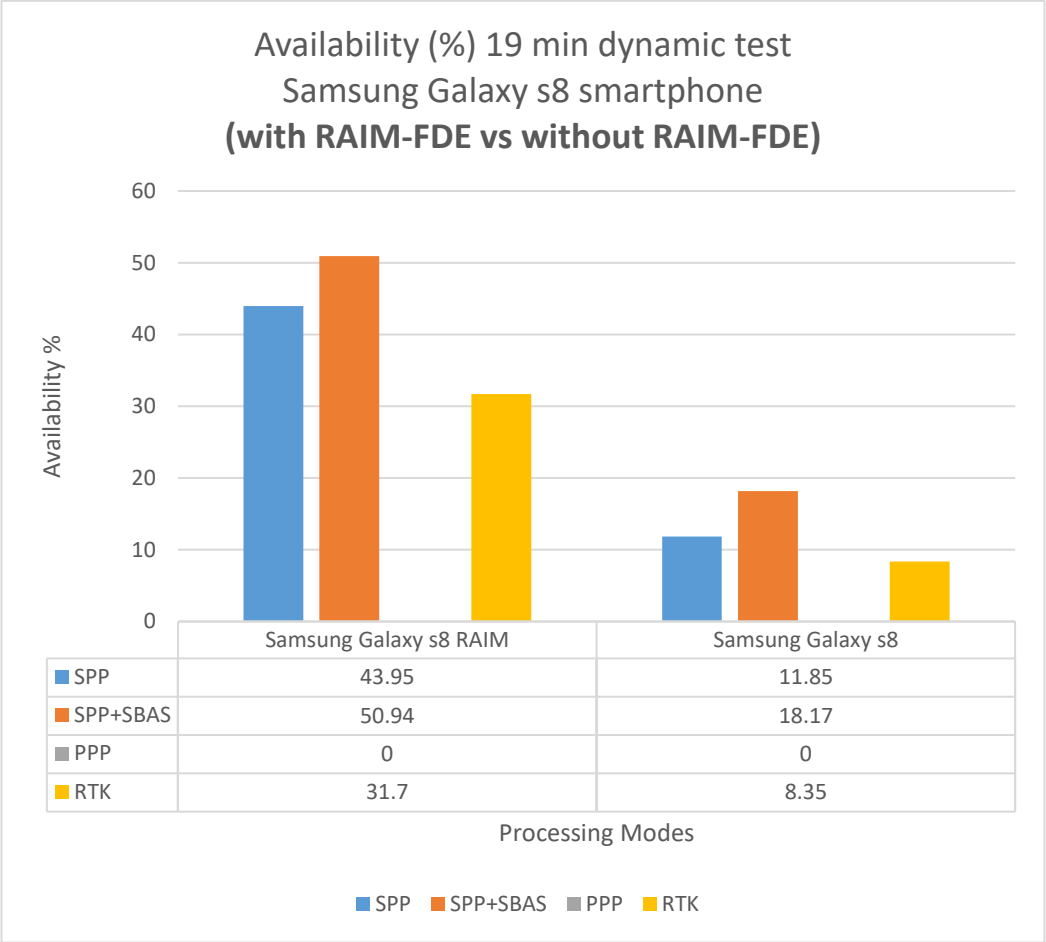

Figure 60. Analysis of availability - 19 min dynamic test - for Samsung Galaxy s8 smartphone (with RAIM-FDE vs without RAIM-FDE).

From figure 60, more availability is observed with RAIM-FDE solutions.

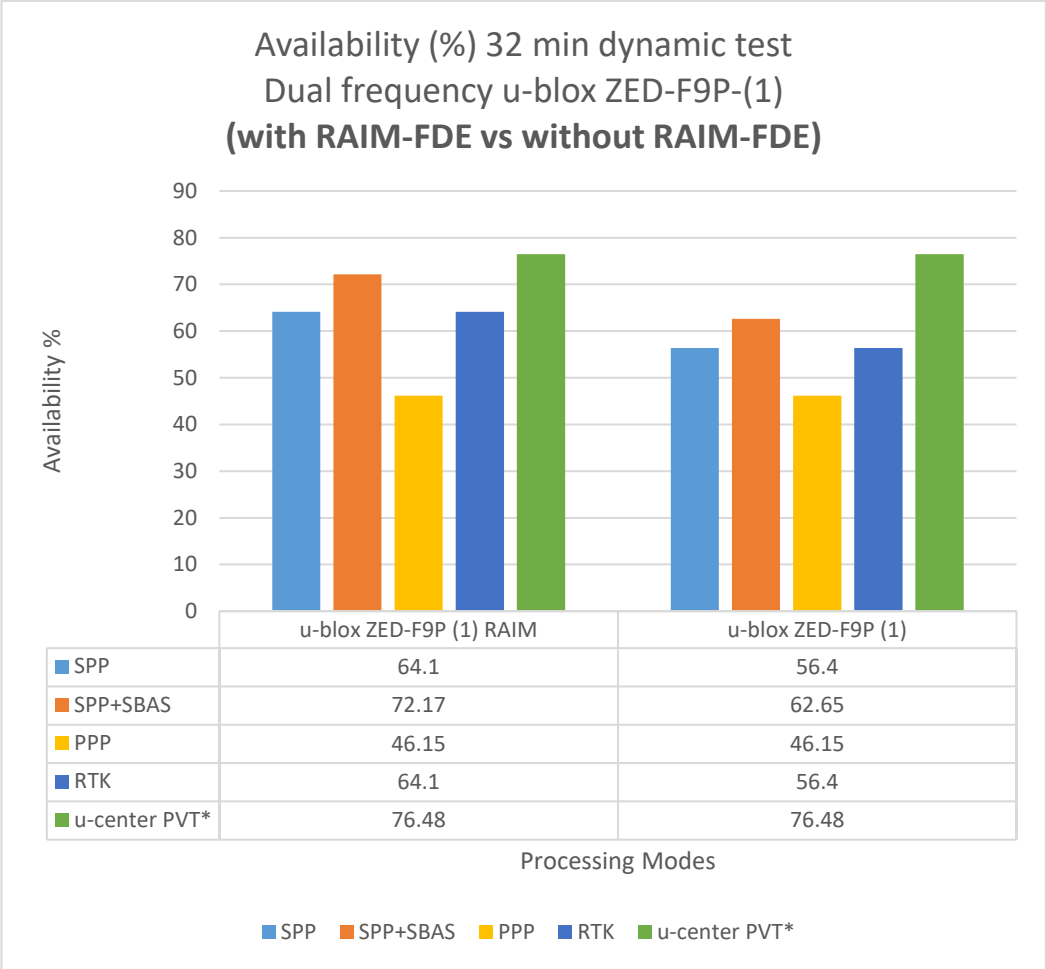

Figure 61. Analysis of availability - 32 min dynamic test - for dual frequency u-blox ZED-F9P-(1) (with RAIM-FDE vs without RAIM-FDE).

From figure 61, more availability is observed with RAIM-FDE solutions.

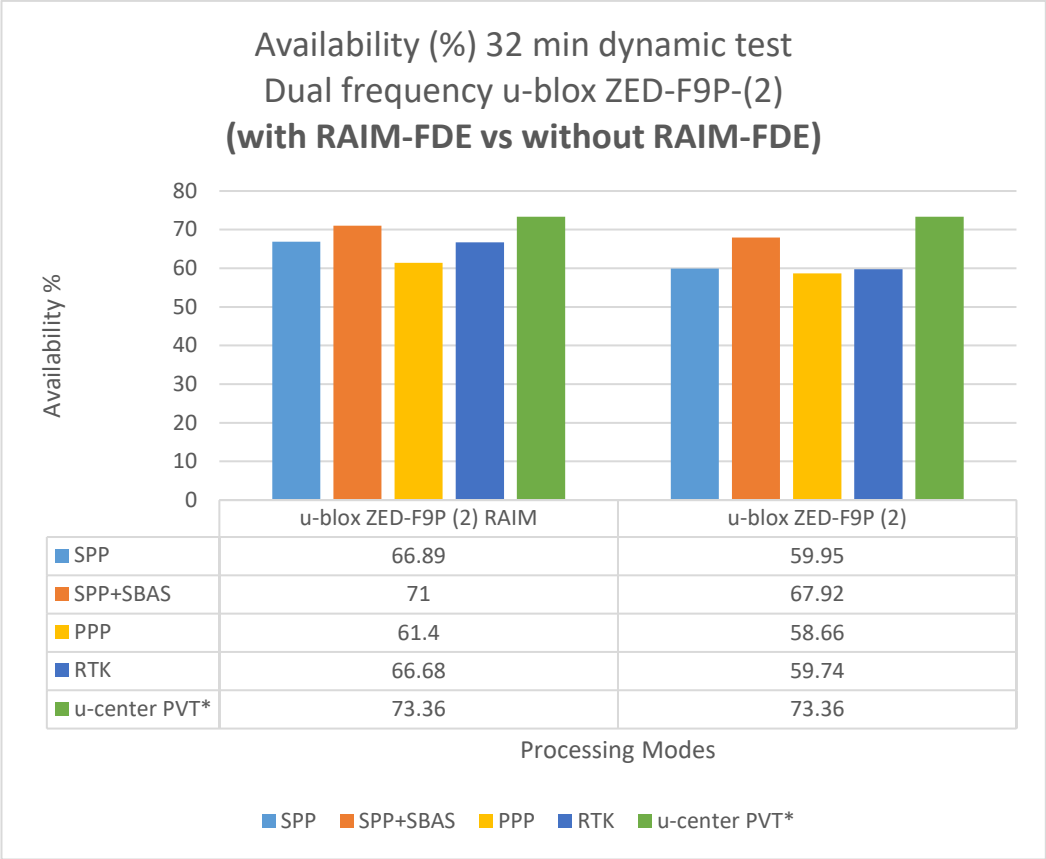

Figure 62. Analysis of availability - 32 min dynamic test - for dual frequency u-blox ZED-F9P-(2) (with RAIM-FDE vs without RAIM-FDE).

From figure 62, more availability is observed with RAIM-FDE solutions.

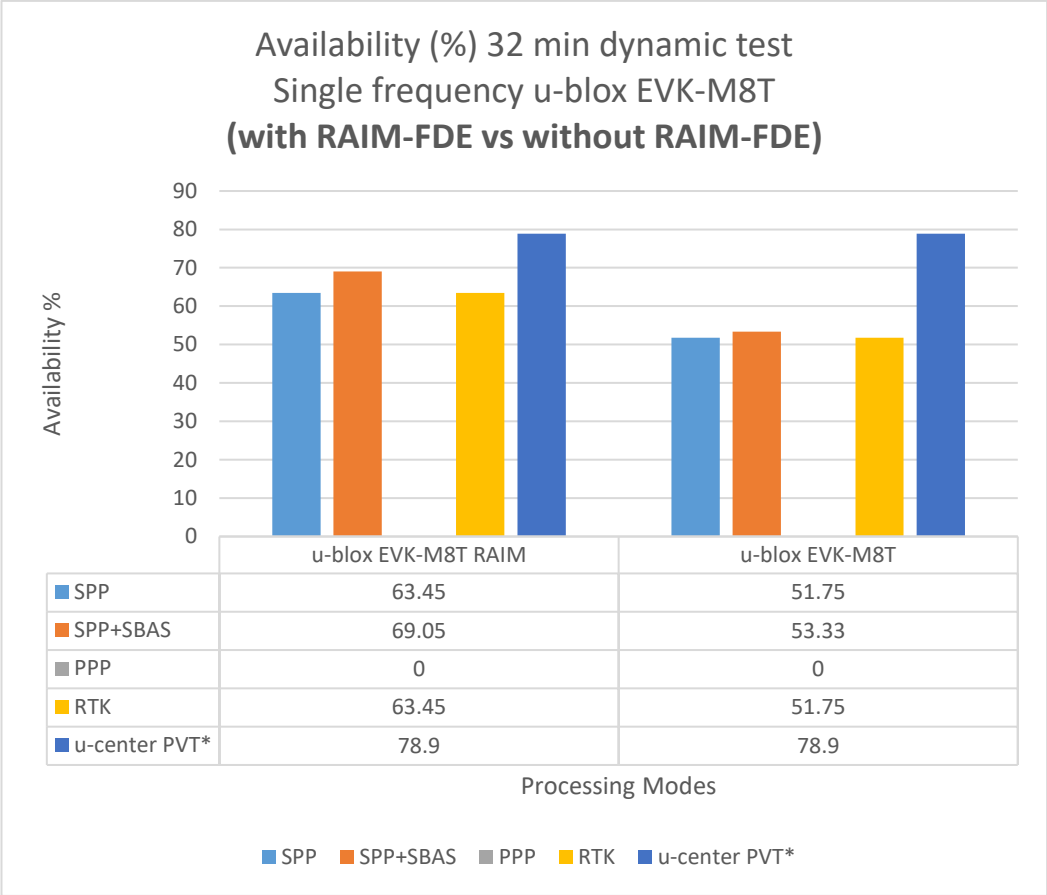

Figure 63. Analysis of availability - 32 min dynamic test - for single frequency u-blox EVK-M8T (with RAIM-FDE vs without RAIM-FDE).

From figure 63, more availability is observed with RAIM-FDE solutions.

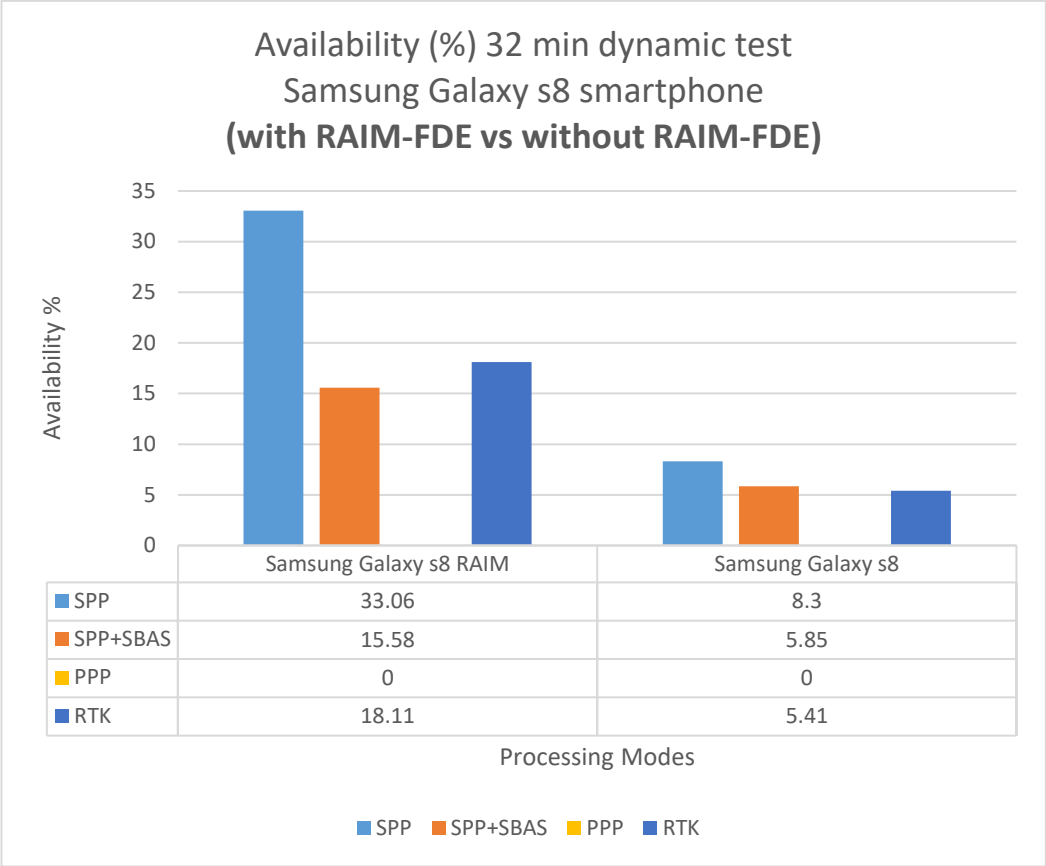

Figure 64. Analysis of availability - 32 min dynamic test - for Samsung Galaxy s8 smartphone (with RAIM-FDE vs without RAIM-FDE).

From Figures 57 – 64, RAIM-FDE enabled solutions typically have higher availability when compared to non-RAIM solutions across all devices.

5.5 Analysis of positioning accuracy for dynamic tests

5.5.1 Analysis of positioning accuracy (device-to-device comparisons) for dynamic tests

In this section, dual frequency (1) will not be displayed because it experienced signal outage after 11 minutes. Only analysis for dual frequency (2), single frequency and the smartphone will be displayed.

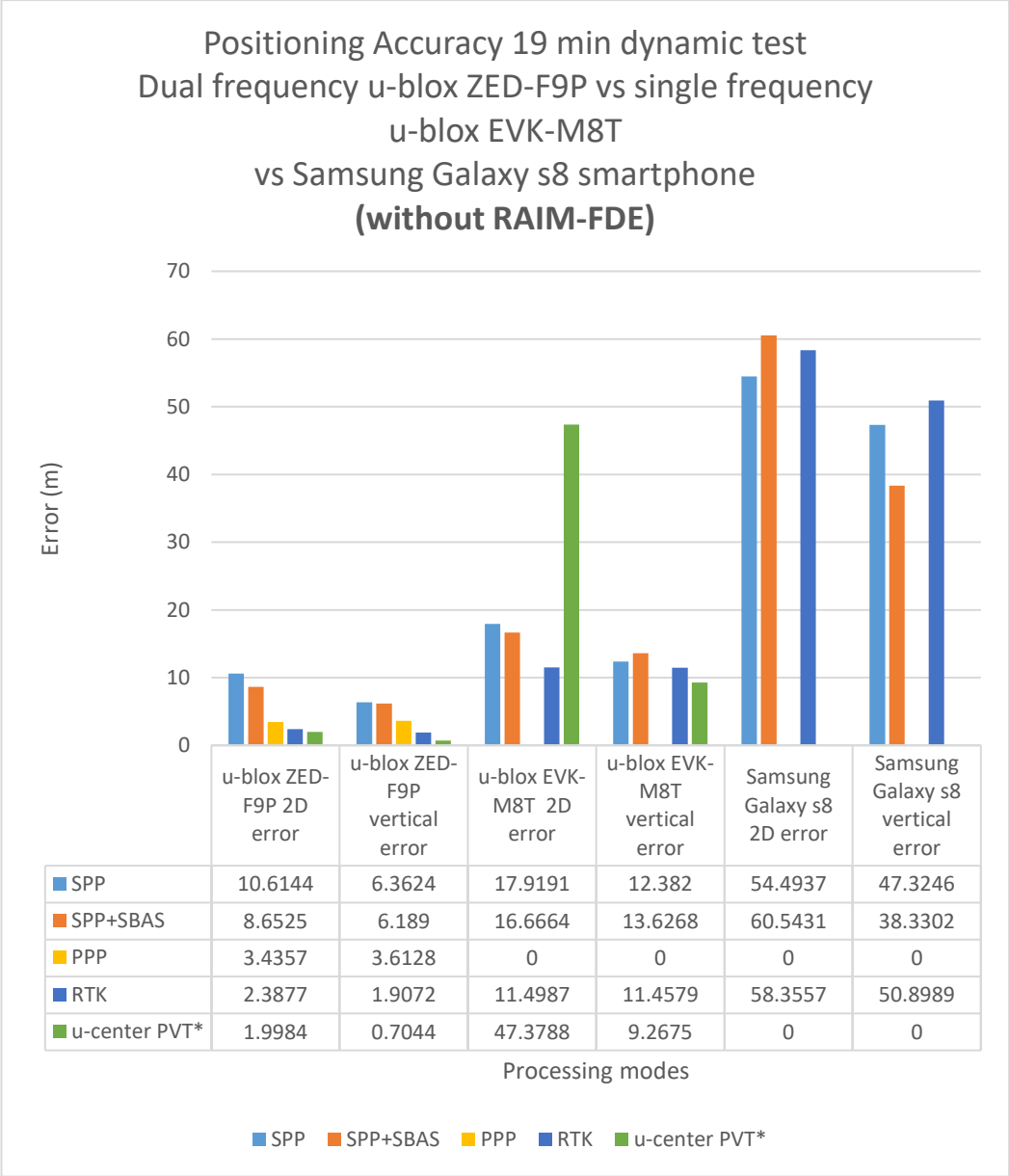

	u-blox ZED-F9P 2D error	u-blox ZED-F9P vertical error	u-blox EVK-M8T 2D error	u-blox EVK-M8T vertical error	Samsung Galaxy s8 2D error	Samsung Galaxy s8 vertical error
SPP	10.6144	6.3624	17.9191	12.382	54.4937	47.3246
SPP+SBAS	8.6525	6.189	16.6664	13.6268	60.5431	38.3302
PPP	3.4357	3.6128	0	0	0	0
RTK	2.3877	1.9072	11.4987	11.4579	58.3557	50.8989
u-center PVT*	1.9984	0.7044	47.3788	9.2675	0	0

Figure 65. Positioning accuracy - 19 min dynamic test - for dual frequency vs single frequency vs smartphone (without RAIM-FDE).

From figure 65, dual frequency receivers (ZED-F9P) have better accuracy when compared to other devices. The smartphone is the poorest performer.

Typically, the positioning accuracy improves across the different processing modes: SPP, SPP+SBAS, PPP, and RTK; with SPP being the poorest and RTK being the best.

In absence of RAIM-FDE, a relatively good RTK horizontal accuracy of 2.3 m was achieved by the dual frequency receivers (ublox ZED-F9P), during a dynamic test session length of 19 minutes.

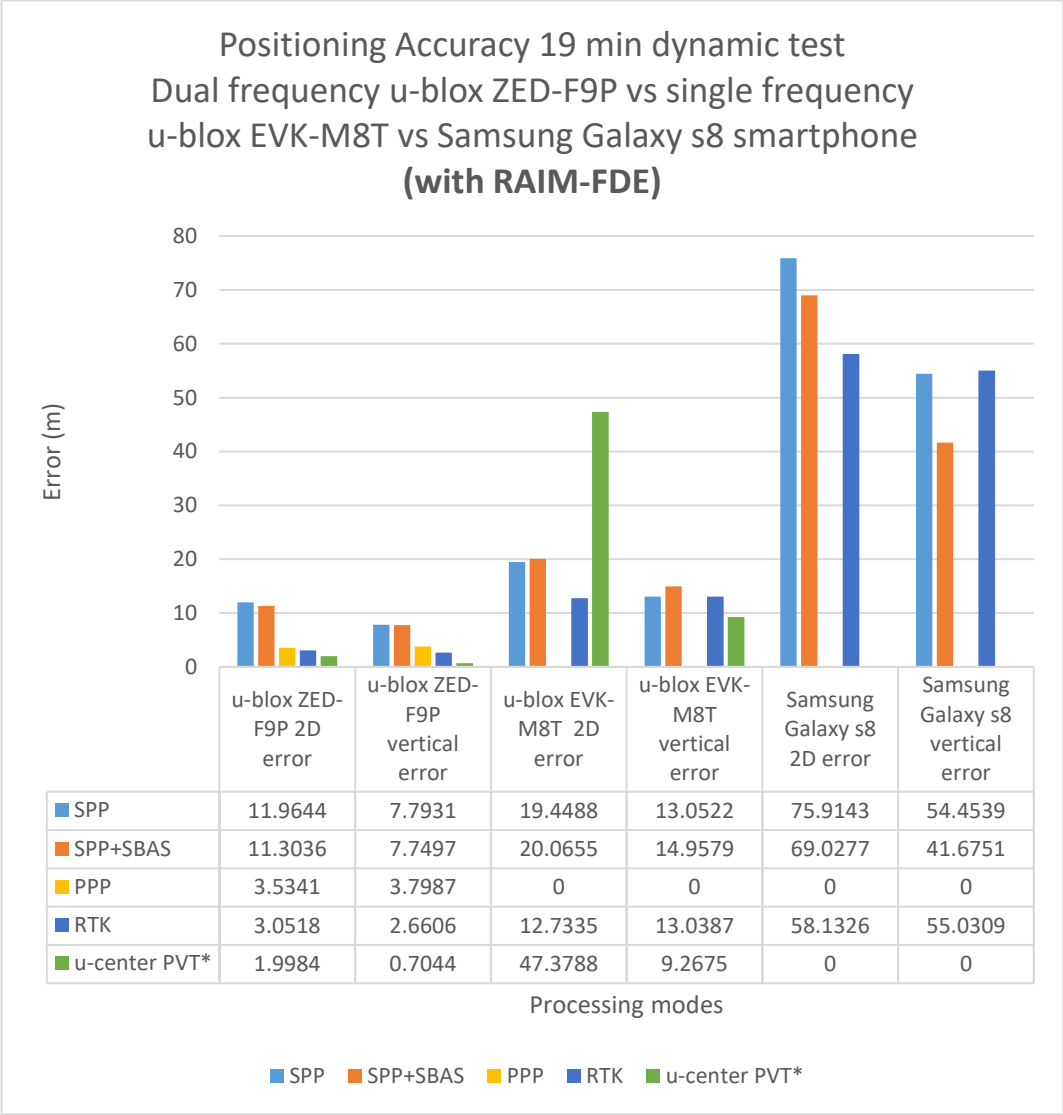

	u-blox ZED-F9P 2D error	u-blox ZED-F9P vertical error	u-blox EVK-M8T 2D error	u-blox EVK-M8T vertical error	Samsung Galaxy s8 2D error	Samsung Galaxy s8 vertical error
SPP	11.9644	7.7931	19.4488	13.0522	75.9143	54.4539
SPP+SBAS	11.3036	7.7497	20.0655	14.9579	69.0277	41.6751
PPP	3.5341	3.7987	0	0	0	0
RTK	3.0518	2.6606	12.7335	13.0387	58.1326	55.0309
u-center PVT*	1.9984	0.7044	47.3788	9.2675	0	0

Figure 66. Positioning accuracy - 19 min dynamic test - for dual frequency vs single frequency vs smartphone (with RAIM-FDE).

From figure 66 above, dual frequency receivers (ZED-F9P) have better accuracy when compared to other devices. The smartphone is the poorest performer.

Typically, the positioning accuracy improves across the different processing modes: SPP, SPP+SBAS, PPP, and RTK; with SPP being the poorest and RTK being the best.

In presence of RAIM-FDE, a relatively good RTK horizontal accuracy of 3.0 m was achieved by the dual frequency receivers (ublox ZED-F9P), during a dynamic test session length of 19 minutes.

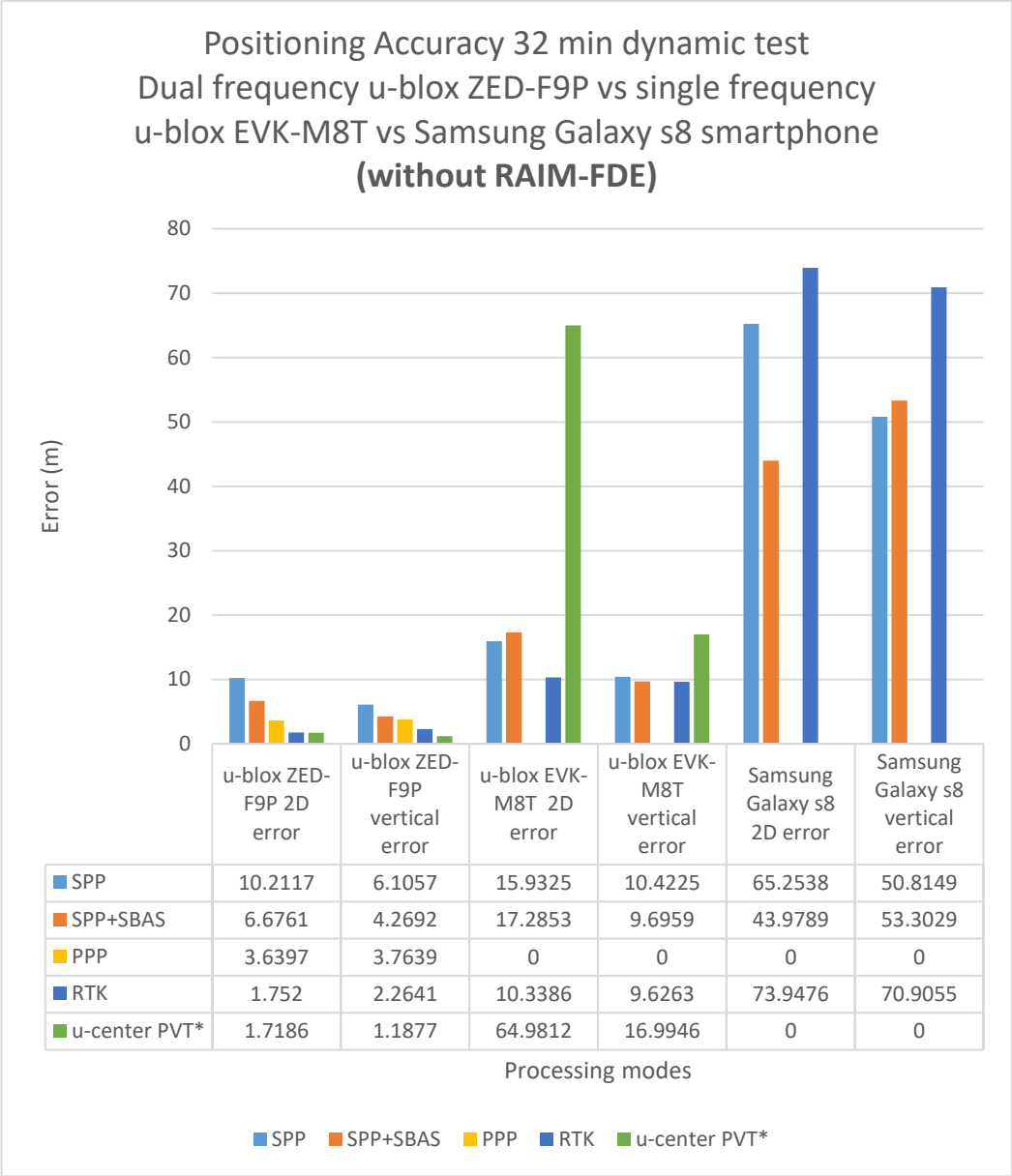

Figure 67. Positioning accuracy - 32 min dynamic test - for dual vs single frequency vs smartphone (without RAIM-FDE).

From figure 67 above, dual frequency receivers (ZED-F9P) have better accuracy when compared to other devices. The smartphone is the poorest performer.

Typically, the positioning accuracy improves across the different processing modes: SPP, SPP+SBAS, PPP, and RTK; with SPP being the poorest and RTK being the best.

In absence of RAIM-FDE, a relatively good RTK horizontal accuracy of 1.7 m was achieved by the dual frequency receivers (ublox ZED-F9P), during a dynamic test session length of 32 minutes.

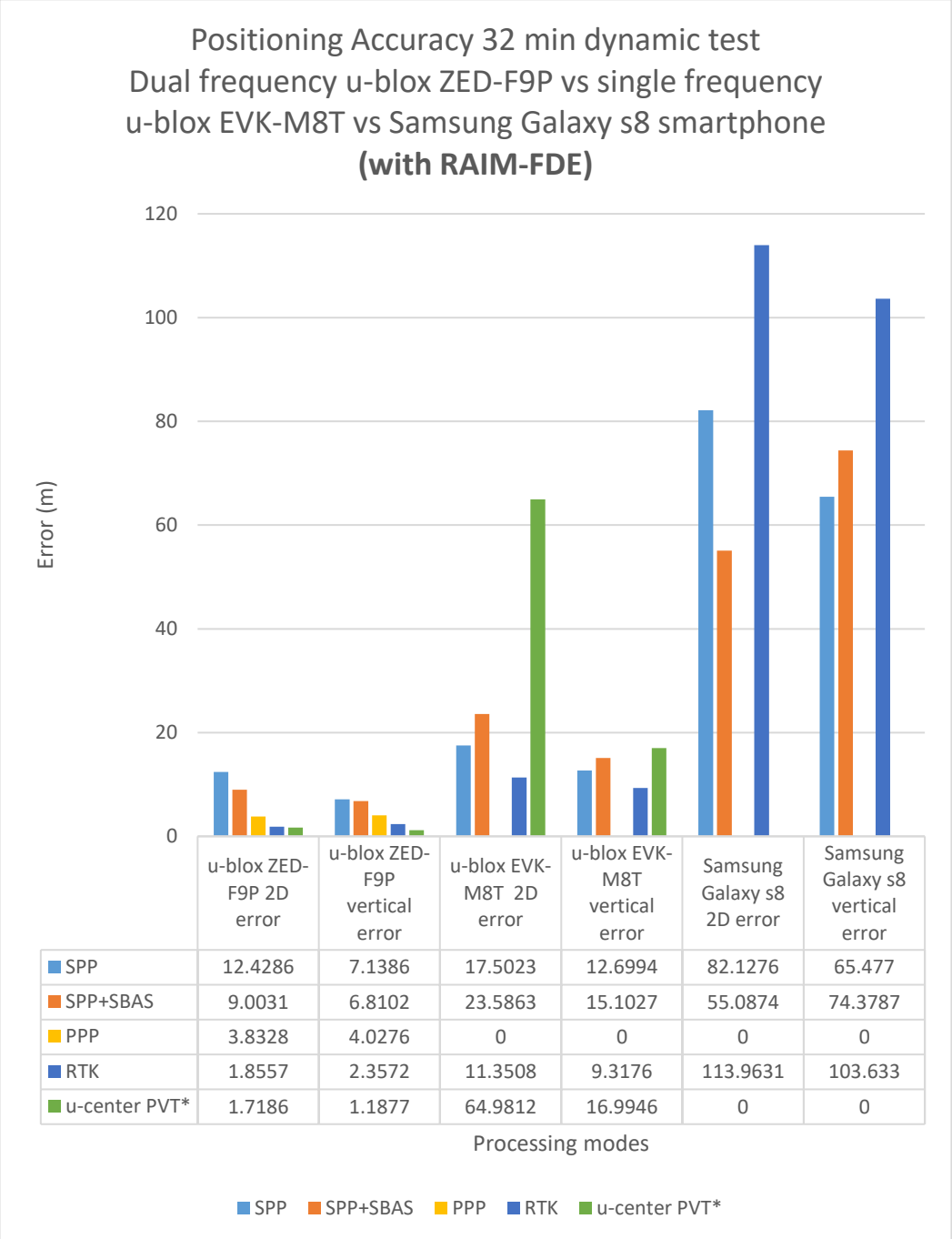

Figure 68. Positioning accuracy - 32 min dynamic test - for dual vs single frequency vs smartphone (with RAIM-FDE).

From figure 68, dual frequency receivers (ZED-F9P) have better accuracy when compared to other devices. The smartphone is the poorest performer.

Typically, the positioning accuracy improves across the different processing modes: SPP, SPP+SBAS, PPP, and RTK; with SPP being the poorest and RTK being the best.

In presence of RAIM-FDE, a relatively good RTK horizontal accuracy of 1.8 m was achieved by the dual frequency receivers (ublox ZED-F9P), during a dynamic test session length of 32 minutes.

5.5.2 Analysis of positioning accuracy (with RAIM-FDE vs without RAIM-FDE) for dynamic tests

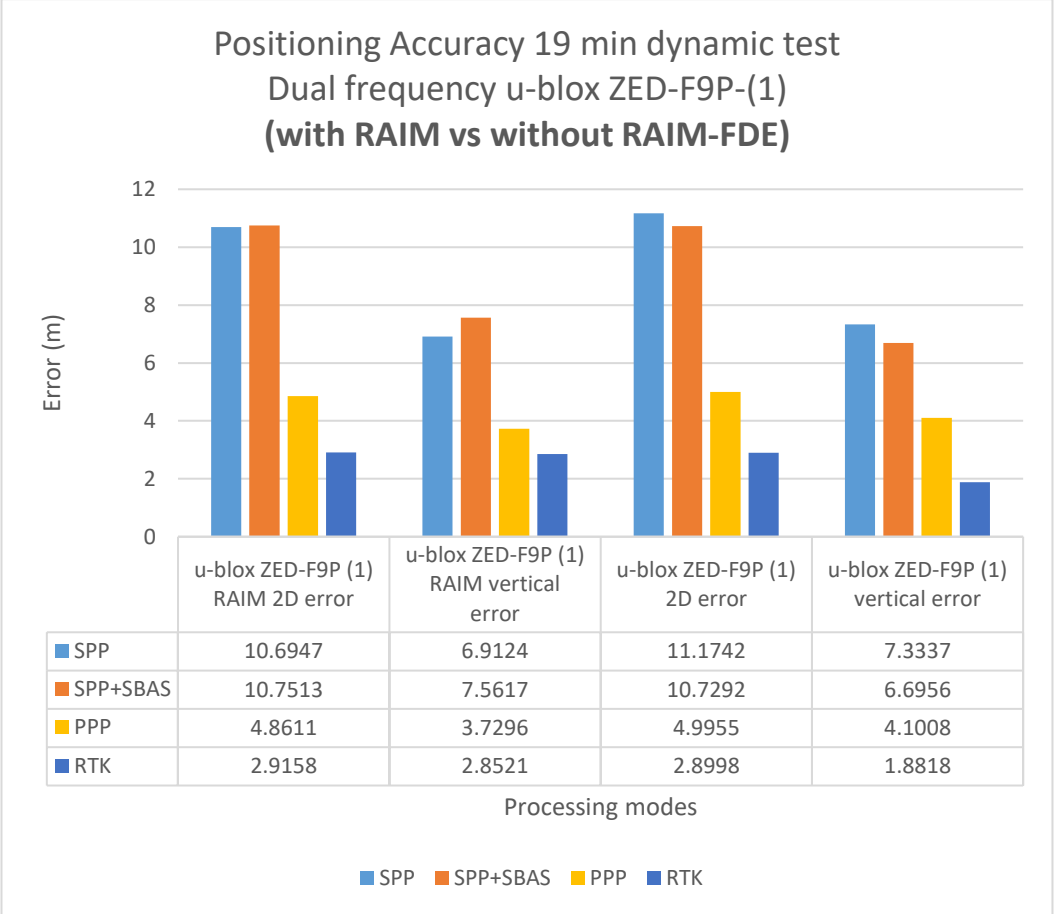

Figure 69. Positioning accuracy - 19 min dynamic test - for dual frequency u-blox ZED-F9P-(1) (with RAIM-FDE vs without RAIM-FDE).

From figure 69, enabling RAIM-FDE improves the positioning accuracy for SPP and PPP. There is no improvement for SPP+SBAS and RTK.

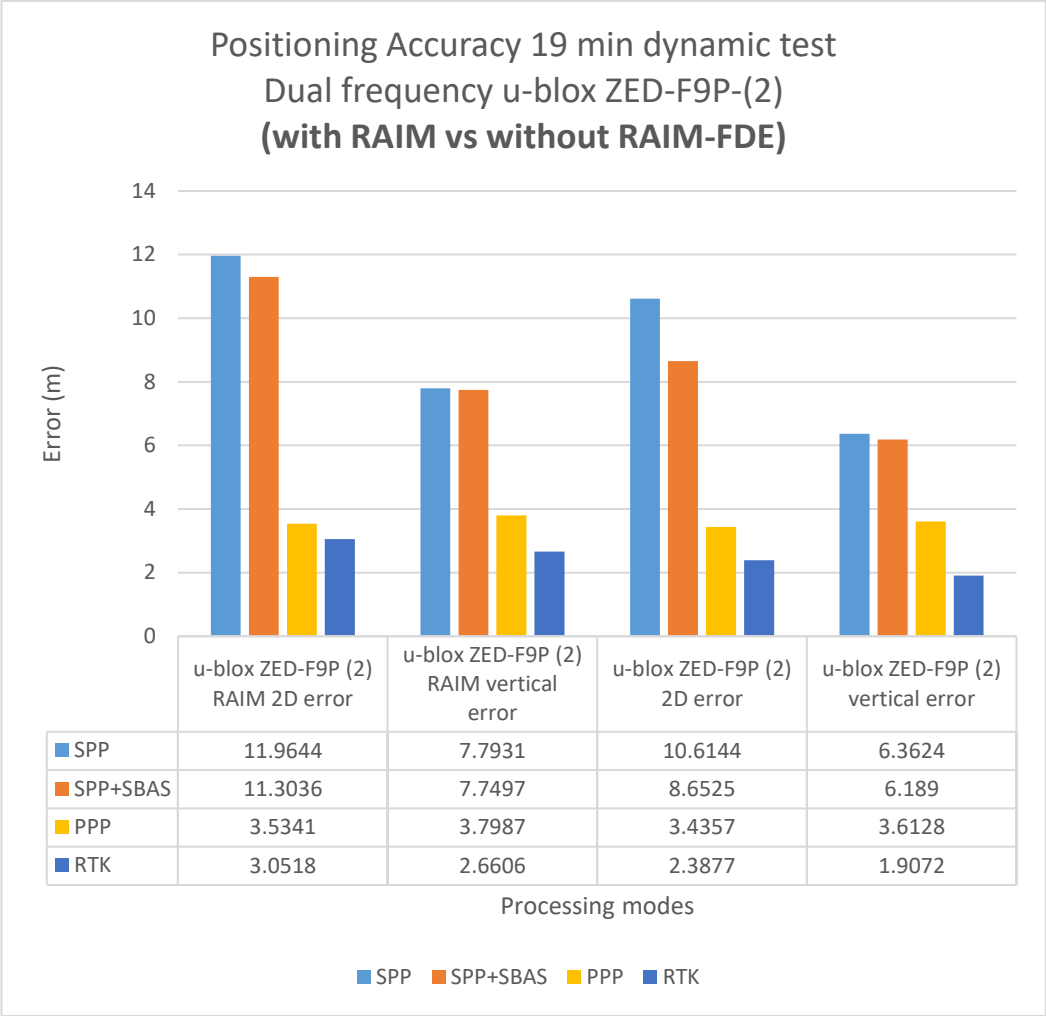

Figure 70. Positioning accuracy - 19 min dynamic test - for dual frequency u-blox ZED-F9P-(2) (with RAIM-FDE vs without RAIM-FDE).

From figure 70, enabling RAIM-FDE does not improve the positioning accuracy for all processing modes.

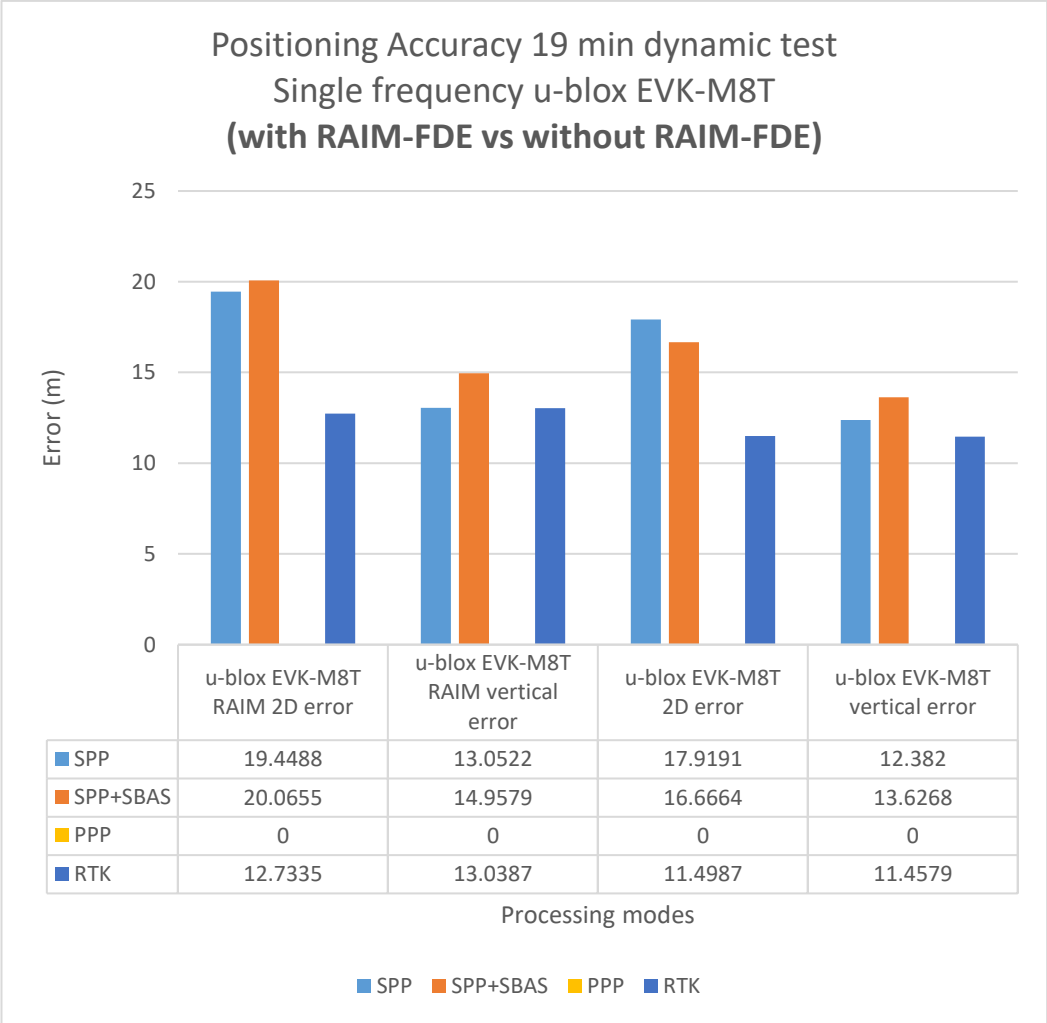

Figure 71. Positioning accuracy - 19 min dynamic test - for single frequency u-blox EVK-M8T (with RAIM-FDE vs without RAIM-FDE).

From figure 71, enabling RAIM-FDE does not improve the positioning accuracy for all processing modes in the single frequency receiver.

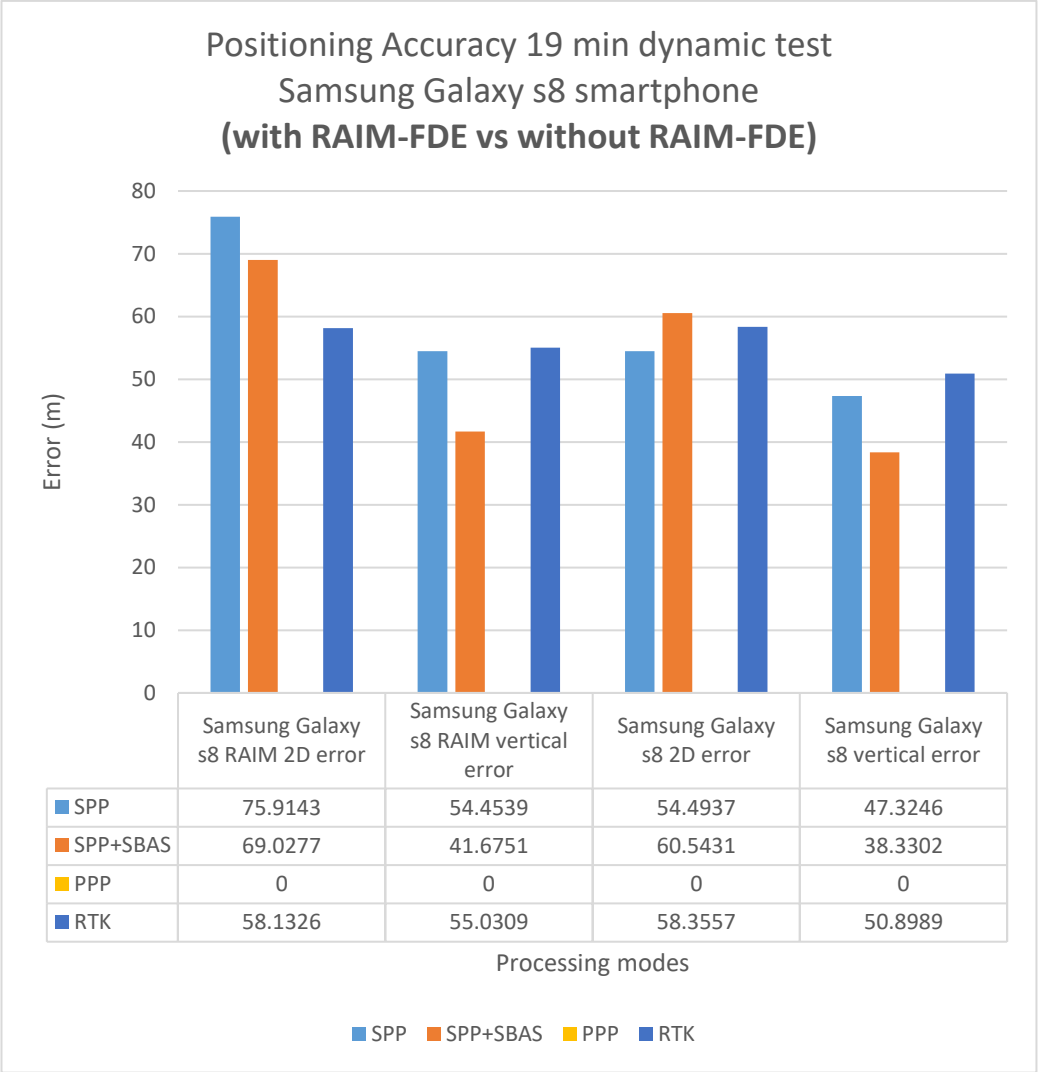

Figure 72. Positioning accuracy - 19 min dynamic test - for Samsung Galaxy s8 smartphone (with RAIM-FDE vs without RAIM-FDE).

From figure 72, enabling RAIM-FDE does not improve the positioning accuracy for all processing modes in the smartphone.

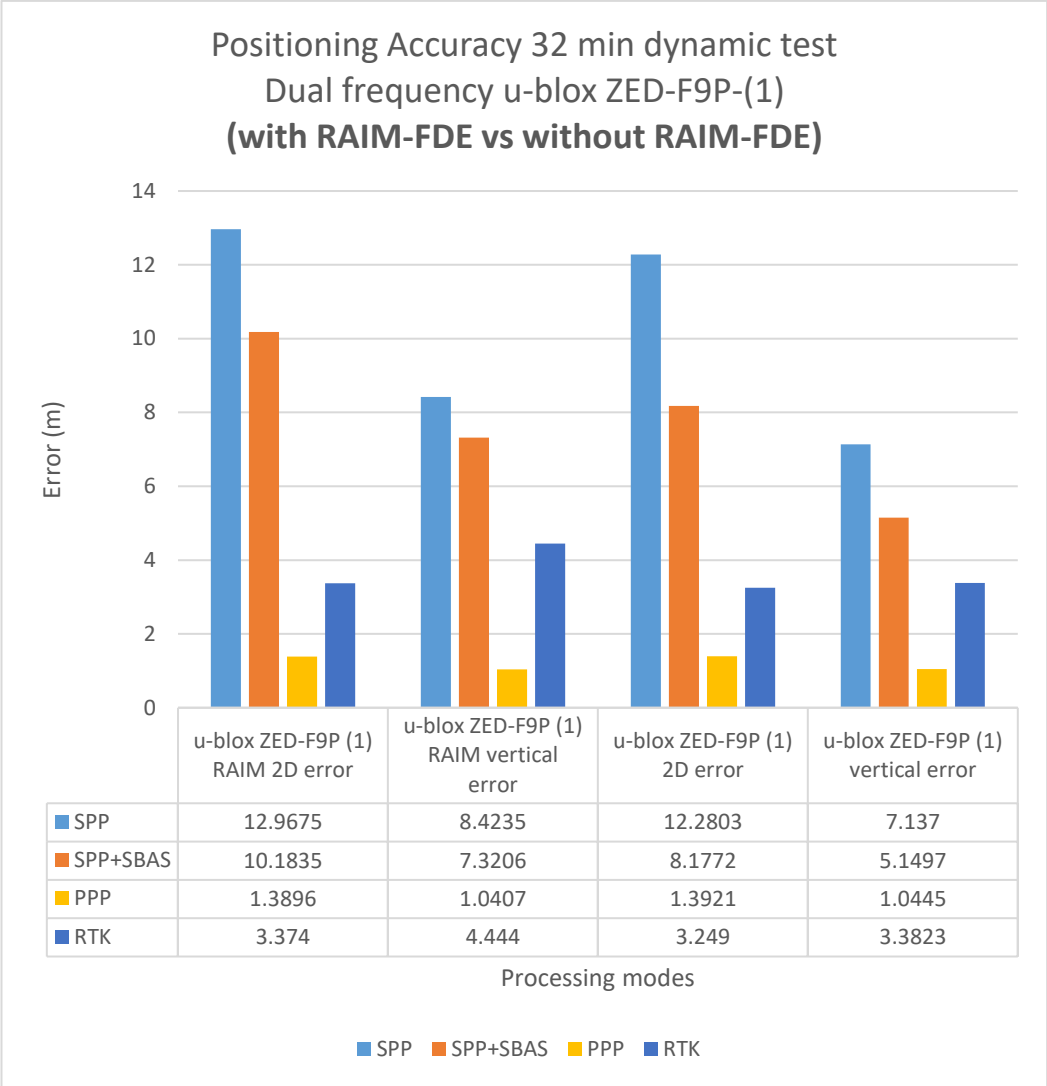

Figure 73. Positioning accuracy - 32 min dynamic test - for dual frequency u-blox ZED-F9P-(1) (with RAIM-FDE vs without RAIM-FDE).

From figure 73, enabling RAIM-FDE does not improve the positioning accuracy for all processing modes except PPP.

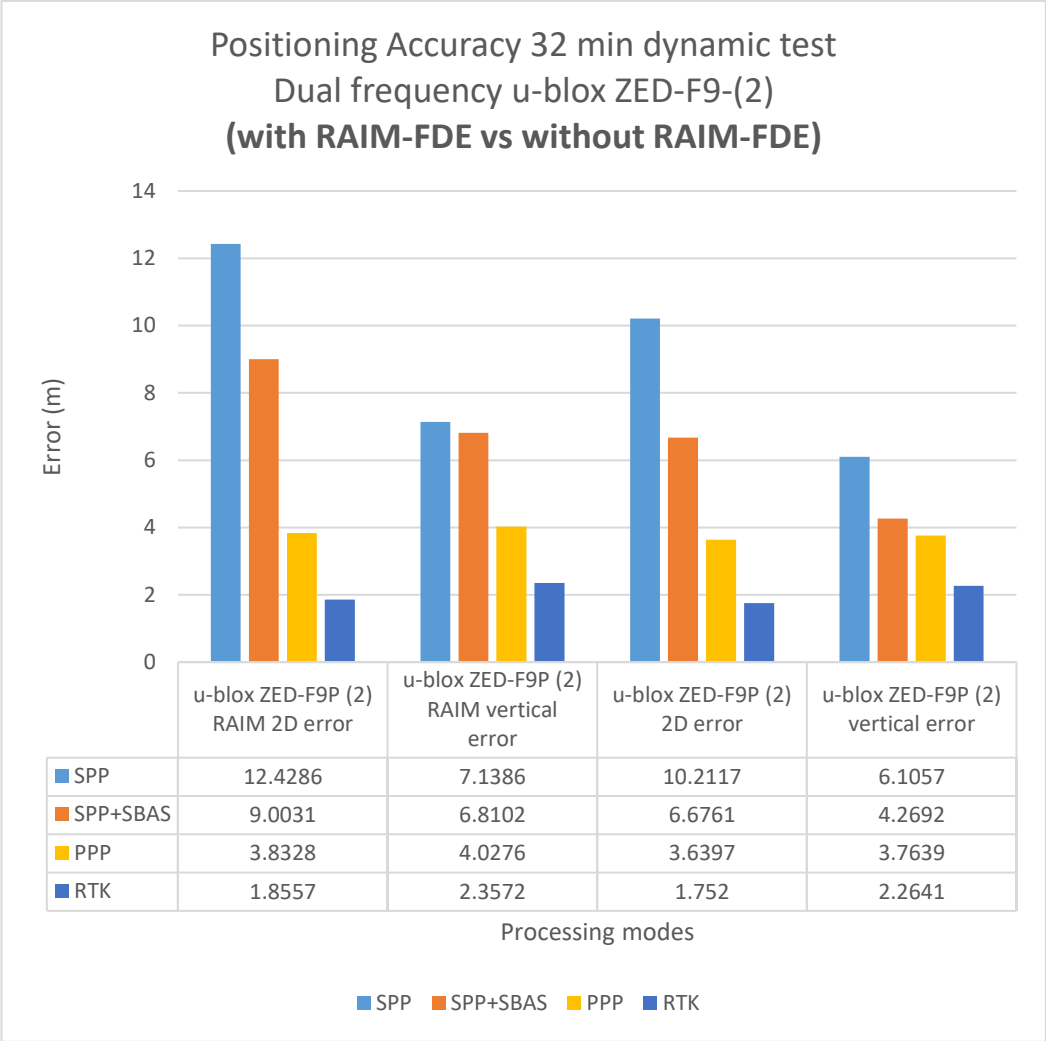

Figure 74. Positioning accuracy - 32 min dynamic test - for dual frequency u-blox ZED-F9P-(2) (with RAIM-FDE vs without RAIM-FDE).

From figure 74, enabling RAIM-FDE does not improve the positioning accuracy for all processing modes.

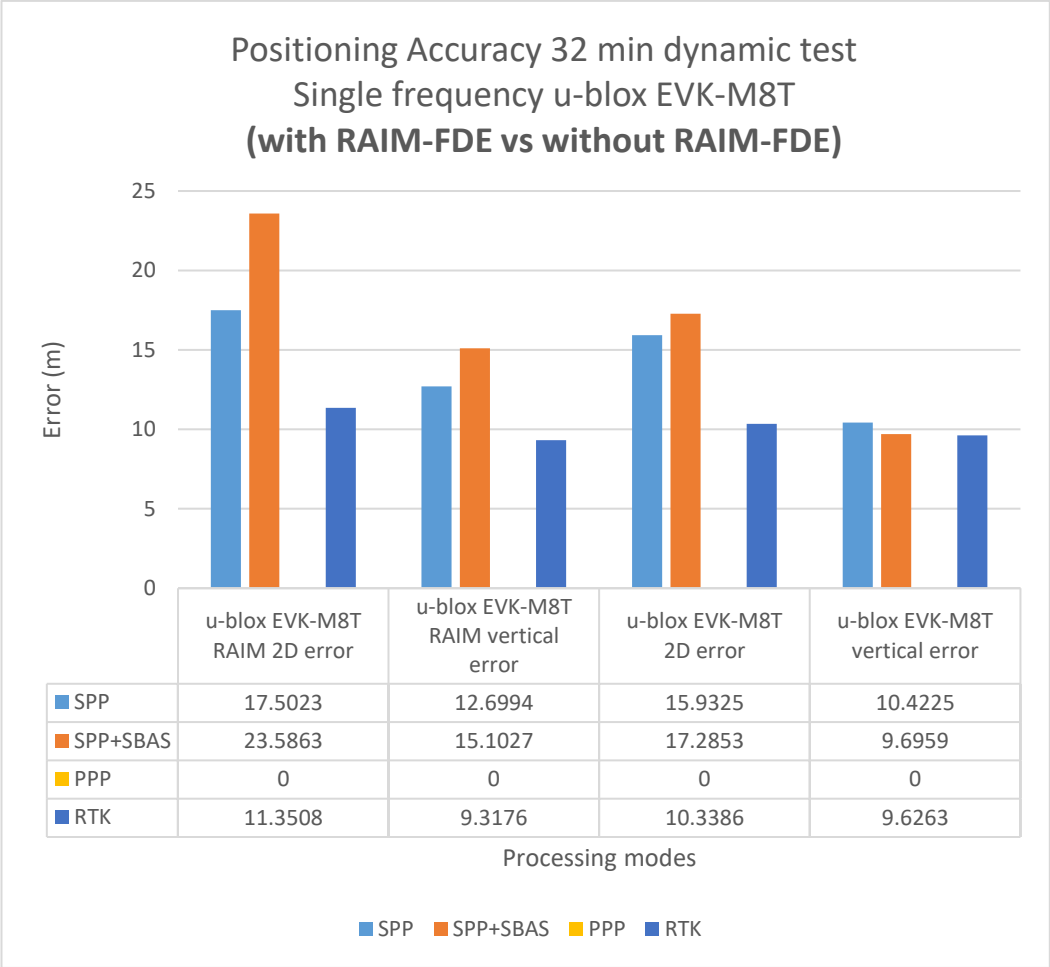

Figure 75. Positioning accuracy - 32 min dynamic test - for single frequency u-blox EVK-M8T (with RAIM-FDE vs without RAIM-FDE).

From figure 75, enabling RAIM-FDE does not improve the positioning accuracy for all processing modes in the single frequency receiver.

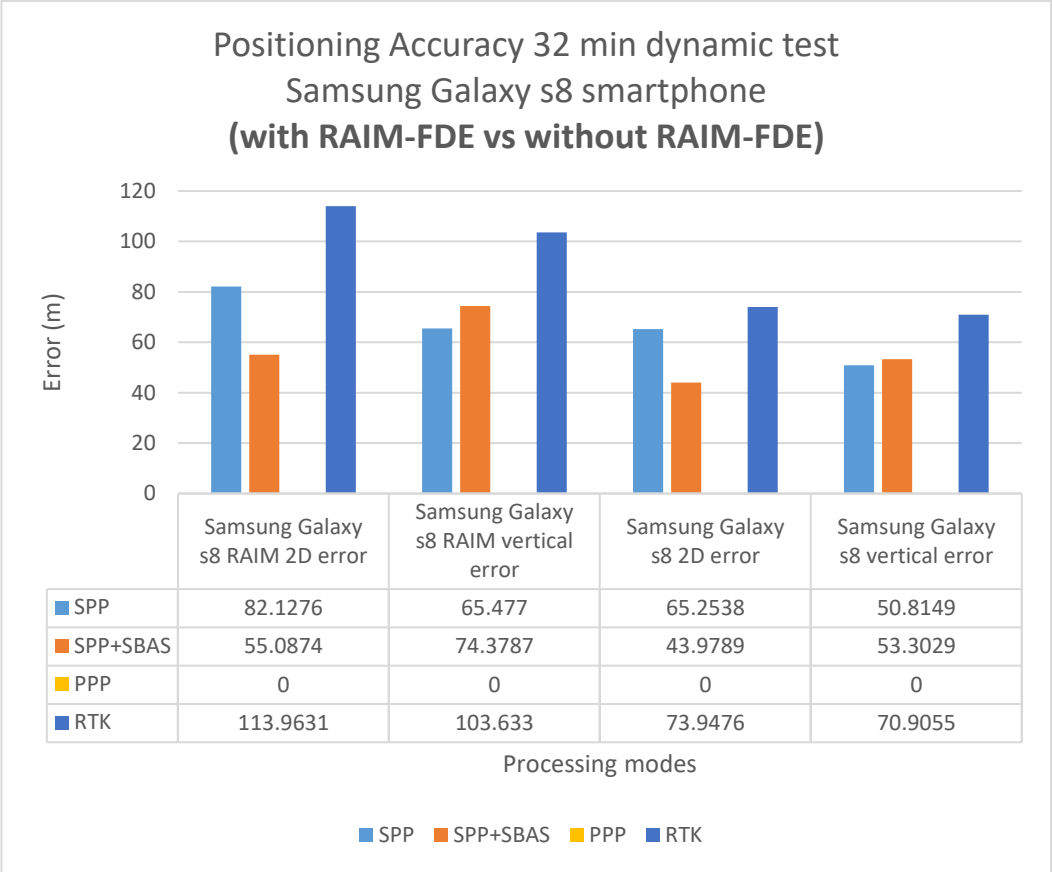

Figure 76. Positioning accuracy - 32 min dynamic test - for Samsung Galaxy s8 smartphone (with RAIM-FDE vs without RAIM-FDE).

From figure 76, enabling RAIM-FDE does not improve the positioning accuracy for all processing modes in the smartphone.

From figures 69 - 76, positioning accuracy typically improves from code-based GNSS processing techniques to carrier-phase based GNSS processing techniques with RTK as the best. The use of RAIM-FDE did not significantly improve the positioning accuracy during dynamic tests.

5.6 Ground track, ENU (east, north, up), horizontal and vertical error plots of various GNSS post-processing modes for stationary tests

For simplicity, only 3-hour stationary test (with RAIM-FDE) plots will be presented.

5.6.1 GNSS post-processing mode plots for Dual frequency ZED-F9P (with RAIM-FDE) during stationary test

5.6.1.1 SPP plots for Dual frequency ZED-F9P (with RAIM-FDE) during 3 hr stationary tests

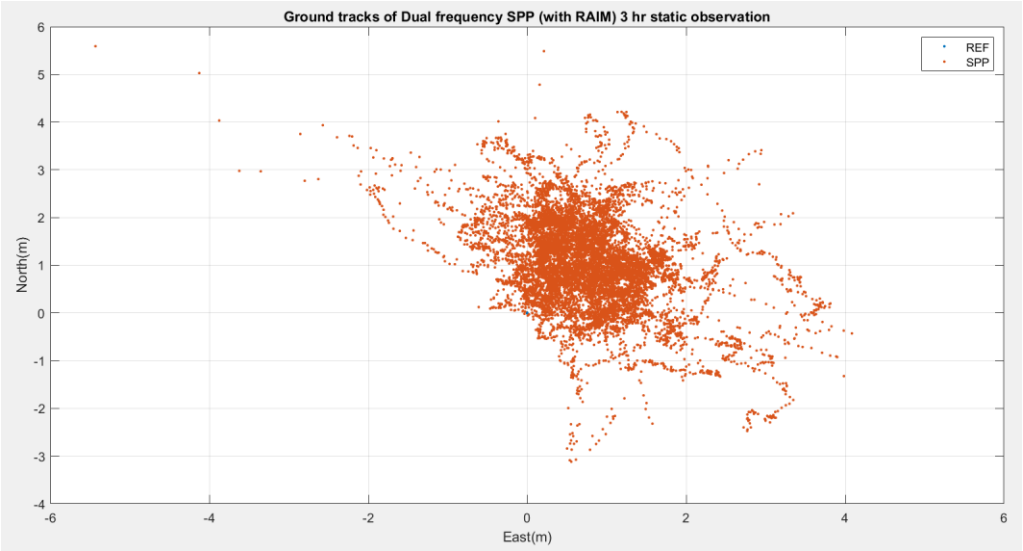

Figure 77. Ground tracks of Dual frequency SPP (with RAIM-FDE) during 3 hr stationary test.

The figure above shows the SPP solution (in red) and estimated true position (in blue).

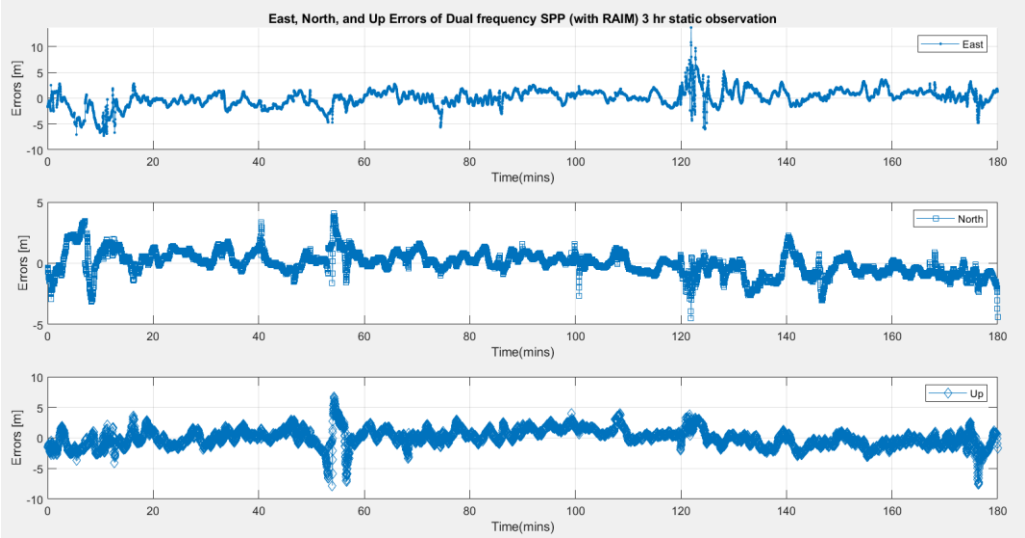

Figure 78. East, North, and Up Errors of Dual frequency SPP (with RAIM-FDE) during 3 hr stationary test.

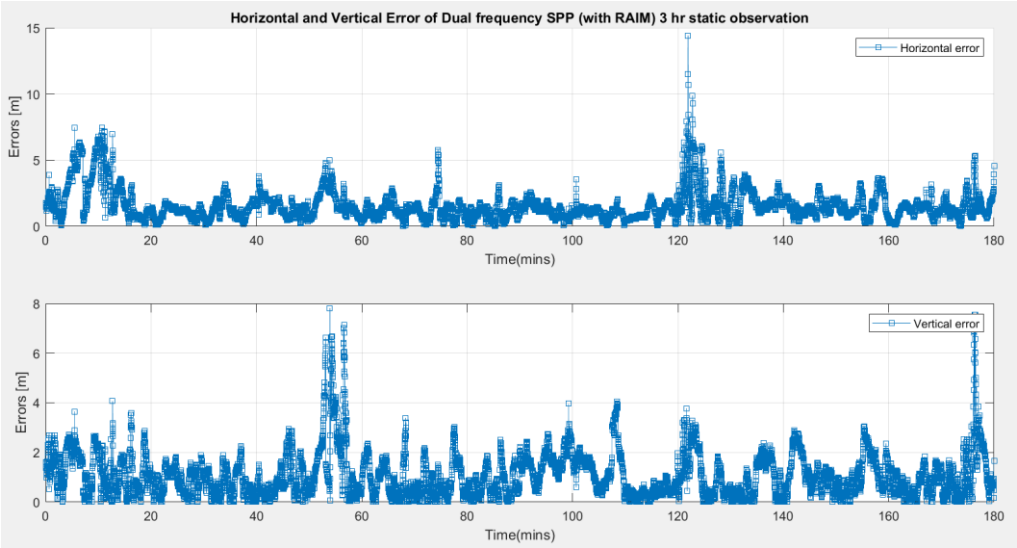

Figure 79. Horizontal and Vertical Error of Dual frequency SPP (with RAIM-FDE) during 3 hr stationary test.

From Figure 79, regions of higher 2D errors were observed at around 120 minutes (seconds of the day) as a result of multipath.

5.6.1.2 SPP+SBAS plots for Dual frequency ZED-F9P (with RAIM-FDE) during 3 hr stationary test

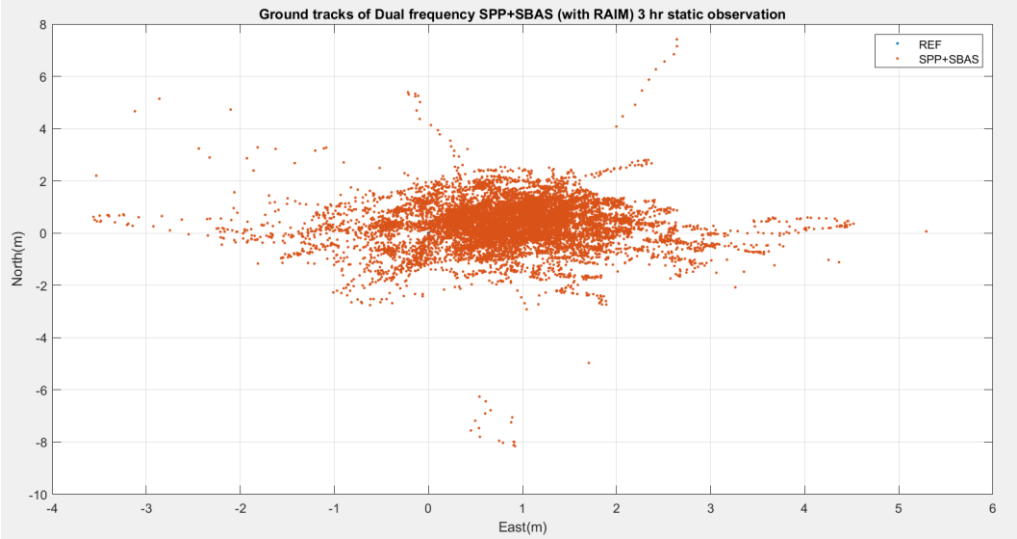

Figure 80. Ground tracks of Dual frequency SPP+SBAS (with RAIM-FDE) during 3 hr stationary test.

The figure above shows the SPP (with EGNOS) solution (in red) and estimated true position (in blue).

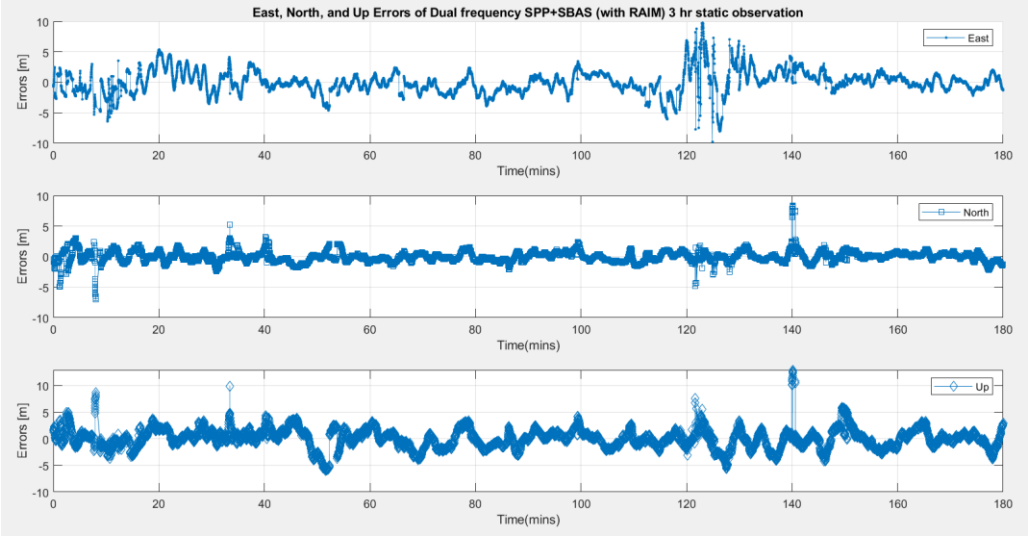

Figure 81. East, North, and Up Errors of Dual frequency SPP+SBAS (with RAIM-FDE) during 3 hr stationary test.

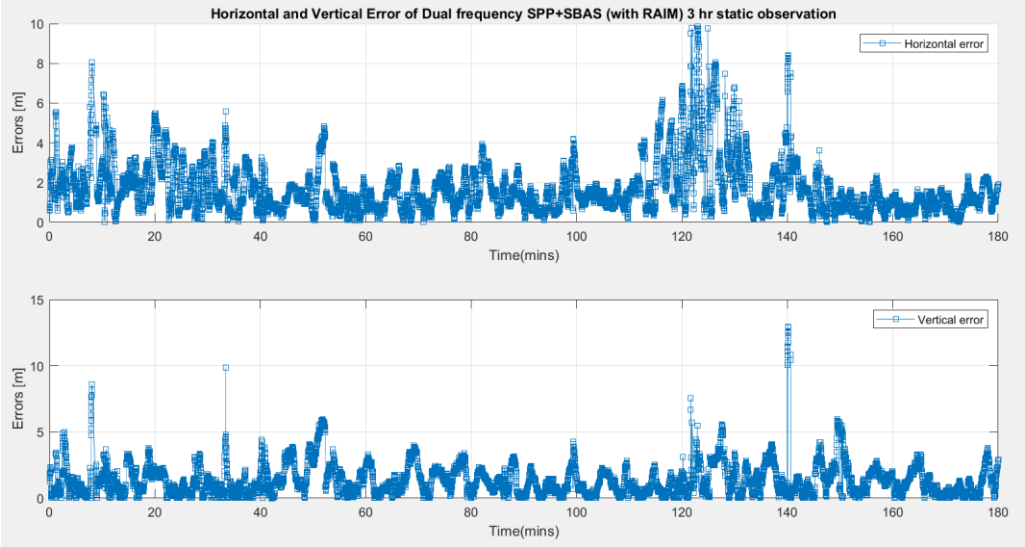

Figure 82. Horizontal and Vertical Error of Dual frequency SPP+SBAS (with RAIM-FDE) during 3 hr stationary test.

From Figure 82, regions of higher 2D errors were observed at around 120 minutes (seconds of the day) as a result of multipath.

5.6.1.3 PPP plots for Dual frequency ZED-F9P (with RAIM-FDE) during 3 hr stationary test

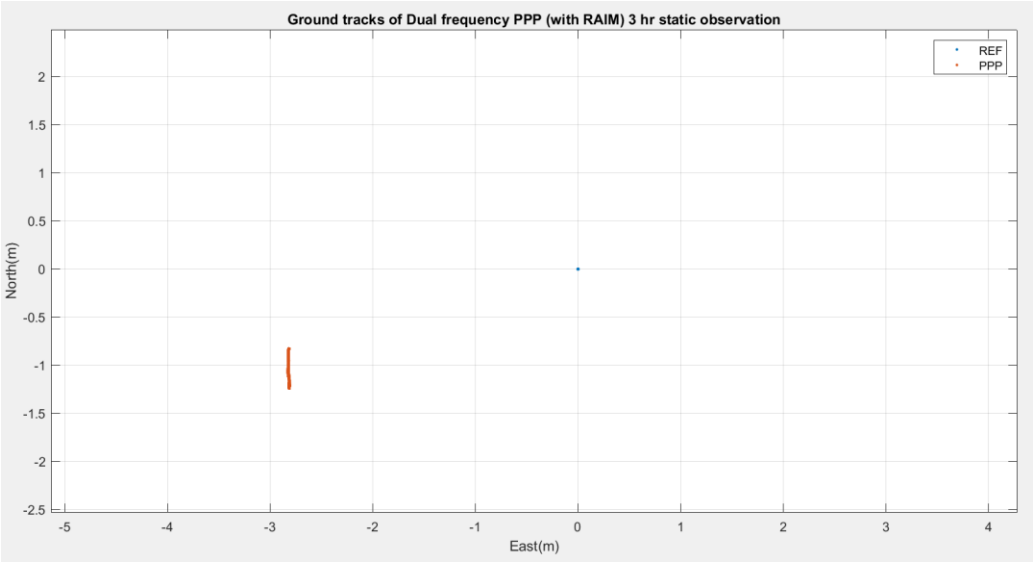

Figure 83. Ground tracks of Dual frequency PPP (with RAIM-FDE) during 3 hr stationary test.

The figure above shows the PPP solution (in red) and estimated true position (in blue).

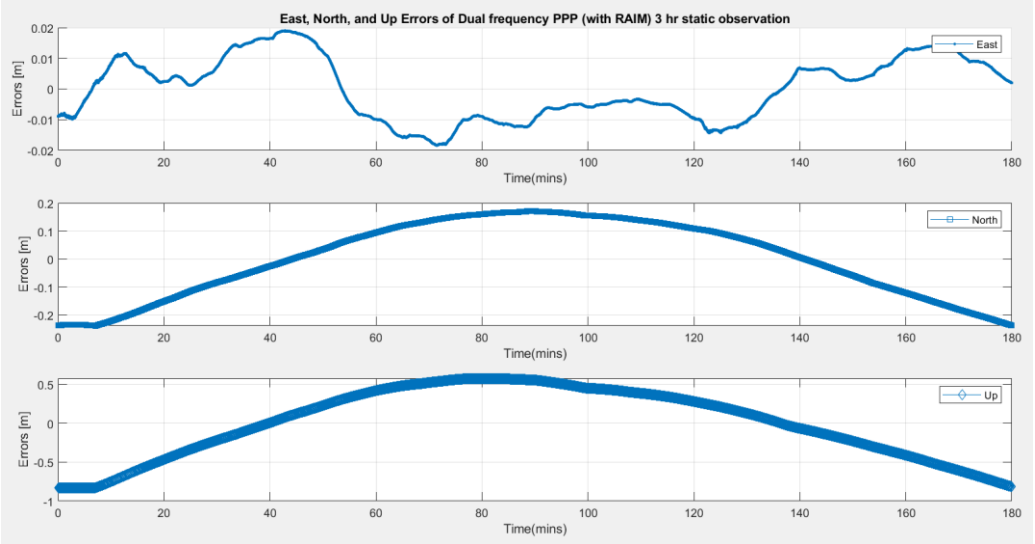

Figure 84. East, North, and Up Errors of Dual frequency PPP (with RAIM-FDE) during 3 hr stationary test.

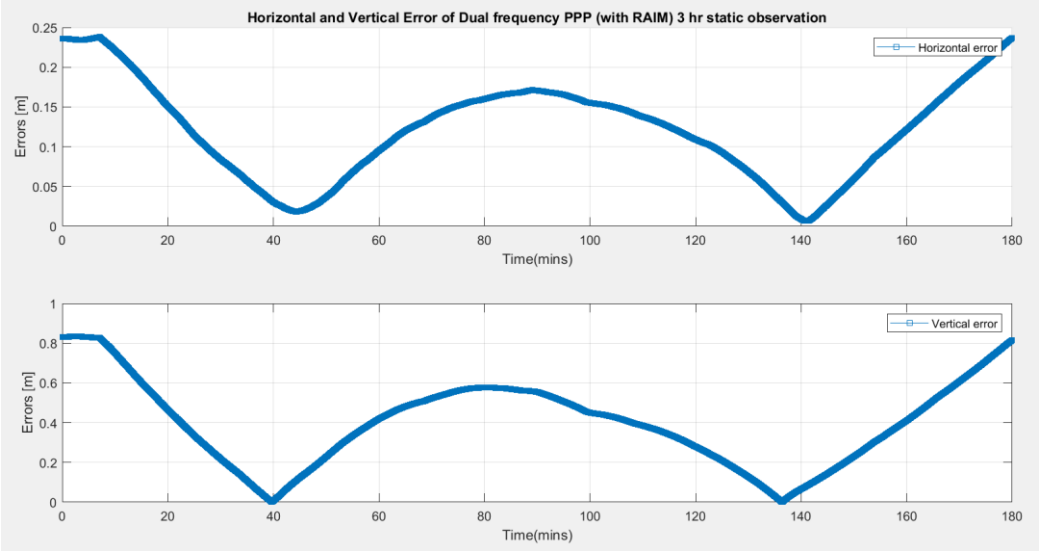

Figure 85. Horizontal and Vertical Error of Dual frequency PPP (with RAIM-FDE) during 3 hr stationary test.

5.6.1.4 RTK plots for Dual frequency ZED-F9P (with RAIM-FDE) during 3 hr stationary test

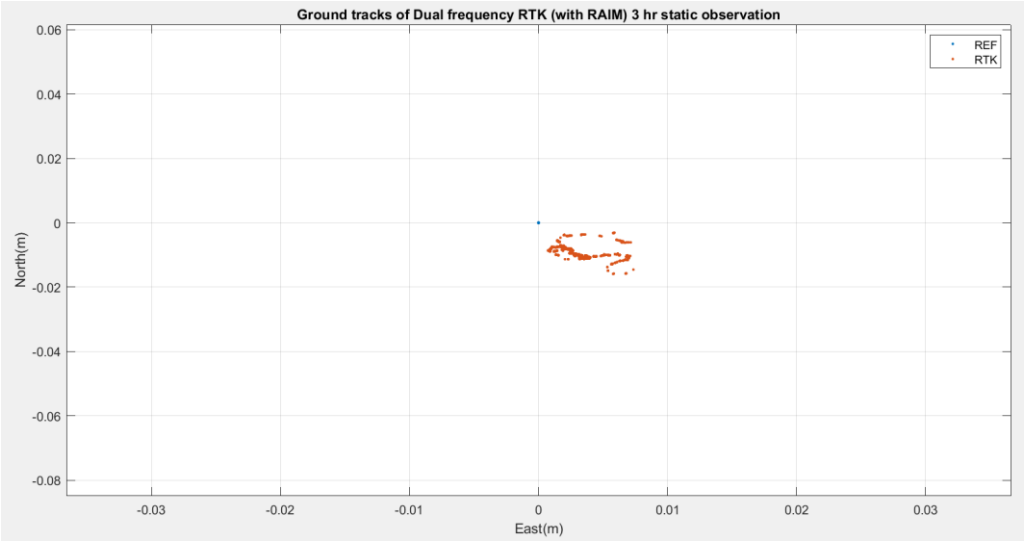

Figure 86. Ground tracks of Dual frequency RTK (with RAIM-FDE) during 3 hr stationary test.

The figure above shows the RTK solution (in red) and estimated true position (in blue).

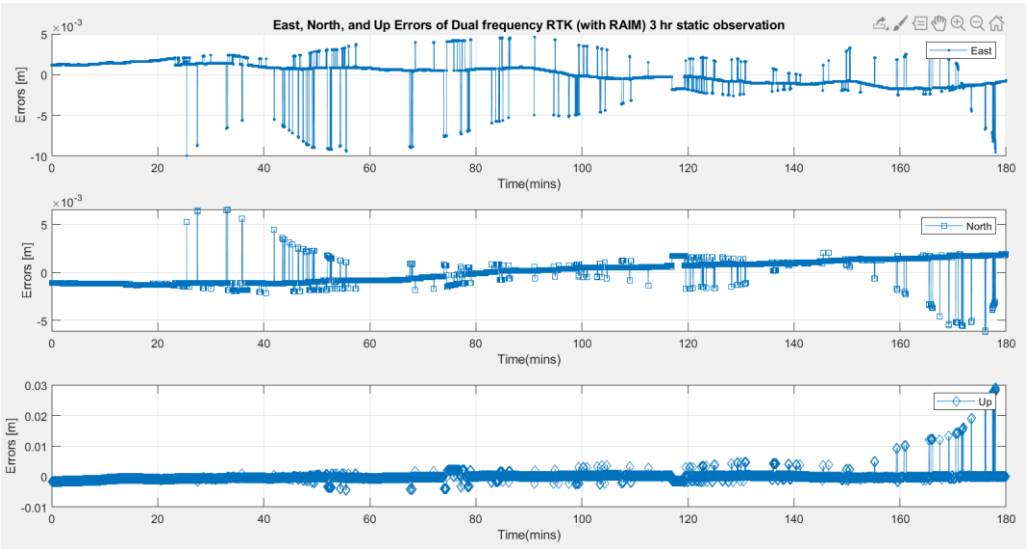

Figure 87. East, North, and Up Errors of Dual frequency RTK (with RAIM-FDE) during 3 hr stationary test.

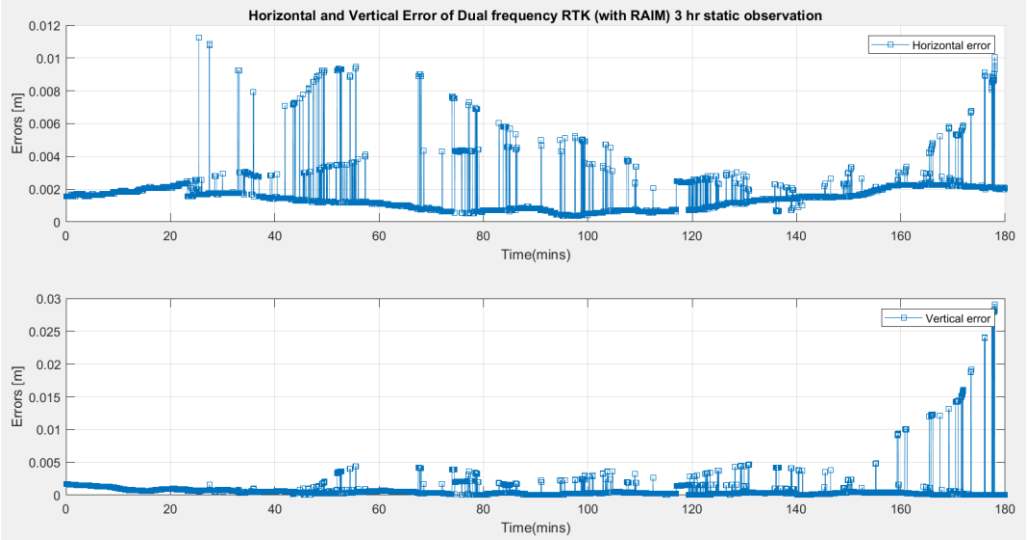

Figure 88. Horizontal and Vertical Error of Dual frequency RTK (with RAIM-FDE) during 3 hr stationary test.

From Figure 88, fixed integer RTK values are observed after the solution converges at around 25 minutes (seconds of the day). In situations where fixed solutions are not realized, a float solution is obtained.

5.6.2 GNSS post-processing mode plots for Single frequency EVK-M8T (with RAIM) during stationary test

5.6.2.1 SPP plots for Single frequency EVK-M8T (with RAIM-FDE) during 3 hr stationary test

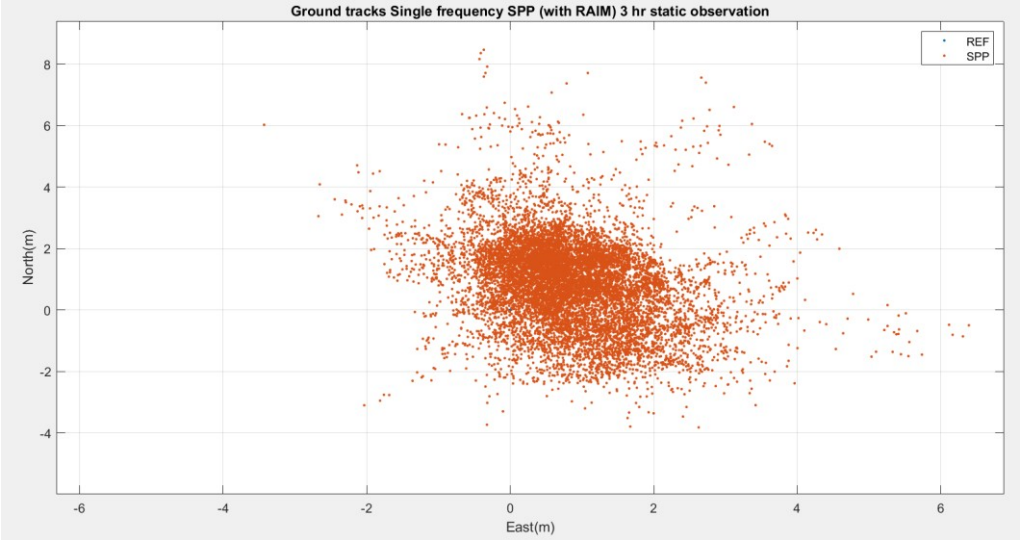

Figure 89. Ground tracks of Single frequency SPP (with RAIM-FDE) during 3 hr stationary test.

The figure above shows the SPP solution (in red) and estimated true position (in blue).

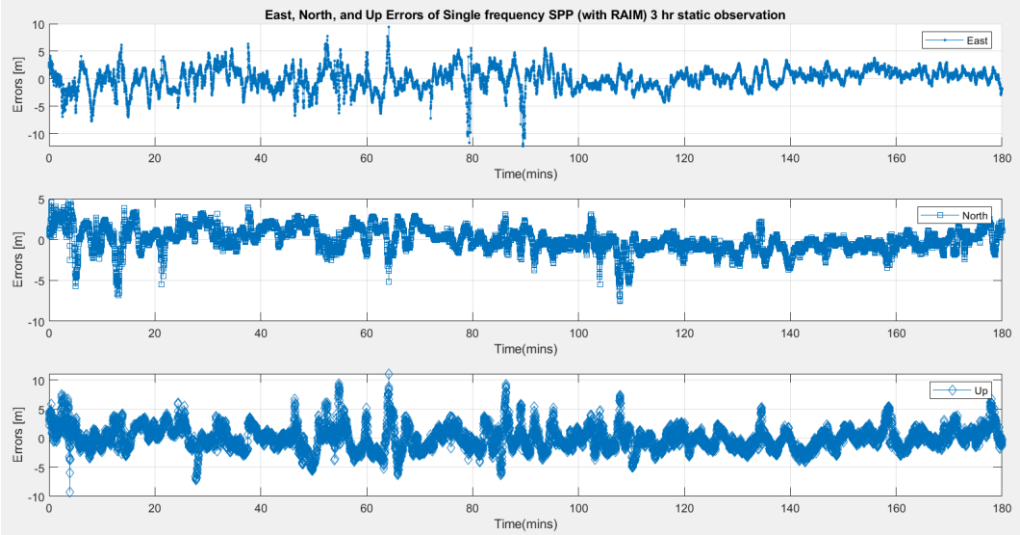

Figure 90. East, North, and Up Errors of Single frequency SPP (with RAIM-FDE) during 3 hr stationary test.

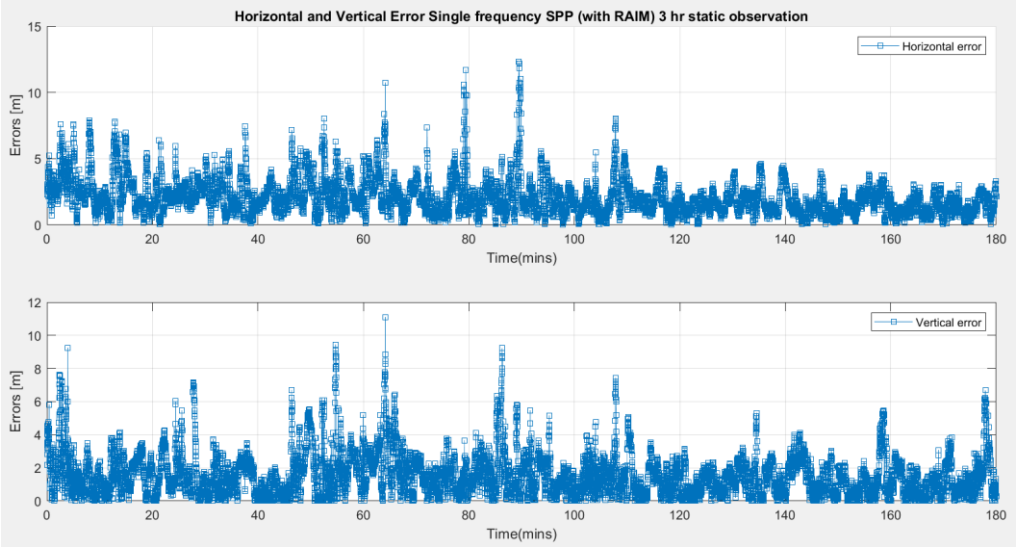

Figure 91. Horizontal and Vertical Error of Single frequency SPP (with RAIM-FDE) during 3 hr stationary test.

5.6.2.2 SPP+SBAS plots for Single frequency EVK-M8T (with RAIM-FDE) during 3 hr stationary test

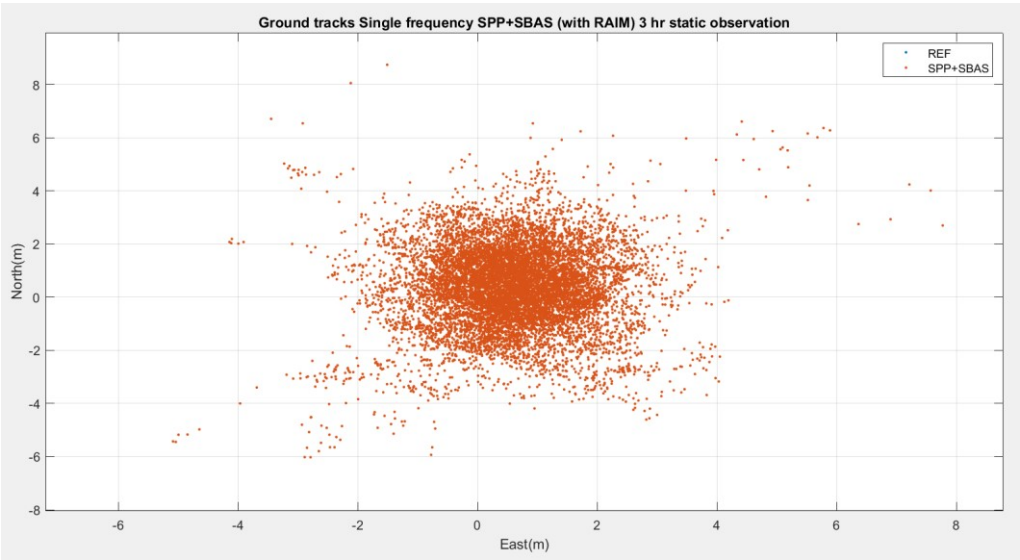

Figure 92. Ground tracks of Single frequency SPP+SBAS (with RAIM-FDE) during 3 hr stationary test.

The figure above shows the SPP (with EGNOS) solution (in red) and estimated true position (in blue).

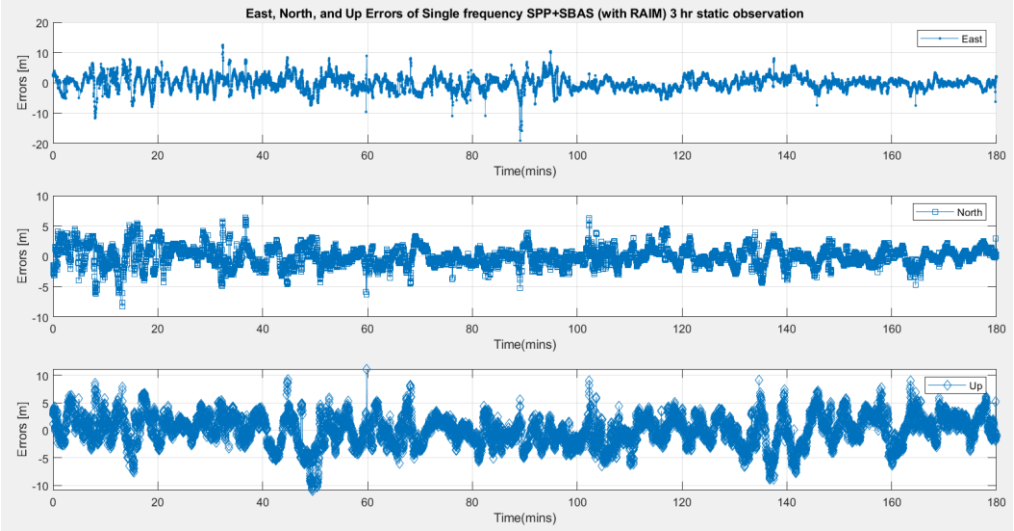

Figure 93. East, North, and Up Errors of Single frequency SPP+SBAS (with RAIM-FDE) during 3 hr stationary test.

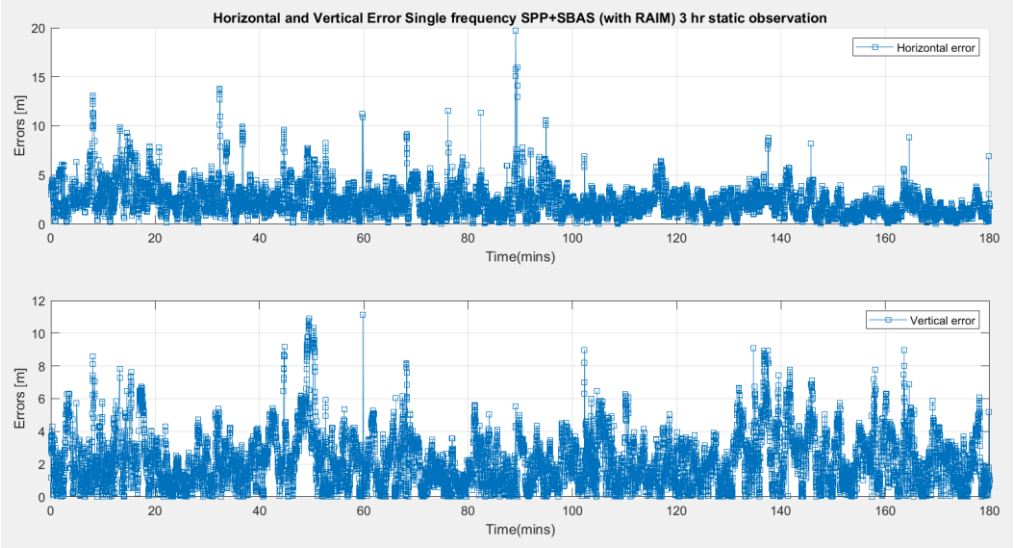

Figure 94. Horizontal and Vertical Error of Single frequency SPP+SBAS (with RAIM-FDE) during 3 hr stationary test.

From Figure 94, regions of higher 2D errors were observed across the entire observation as a result of multi-path effects.

5.6.2.3 PPP plots for Single frequency EVK-M8T (with RAIM-FDE) during 3 hr stationary test

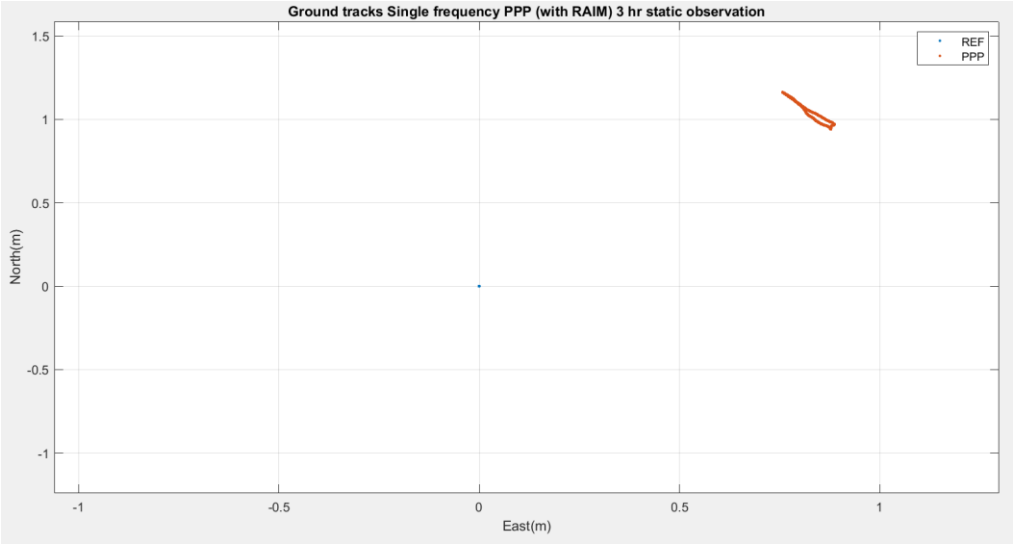

Figure 95. Ground tracks of Single frequency PPP (with RAIM-FDE) during 3 hr stationary test.

The figure above shows the PPP solution (in red) and estimated true position (in blue).

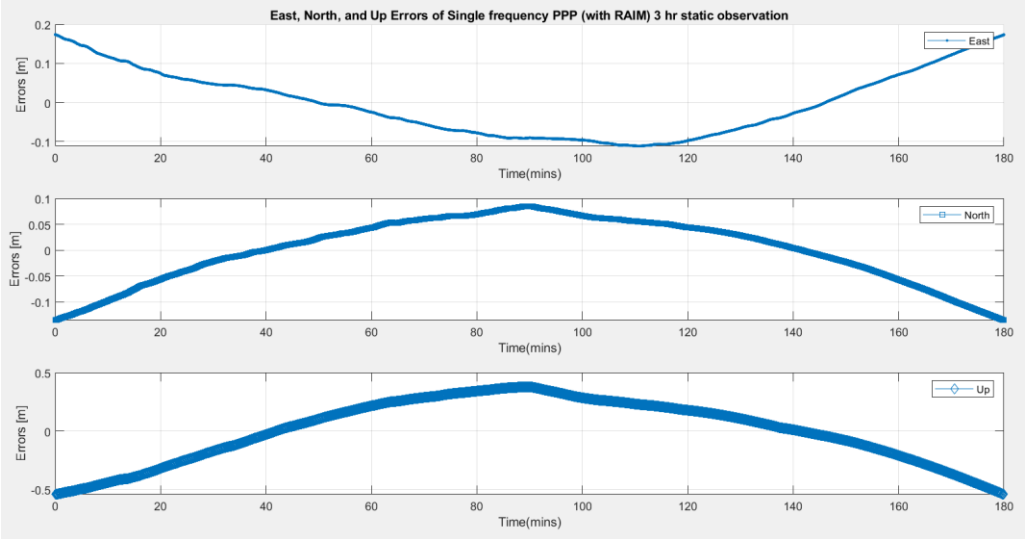

Figure 96. East, North, and Up Errors of Single frequency PPP (with RAIM-FDE) during 3 hr stationary test.

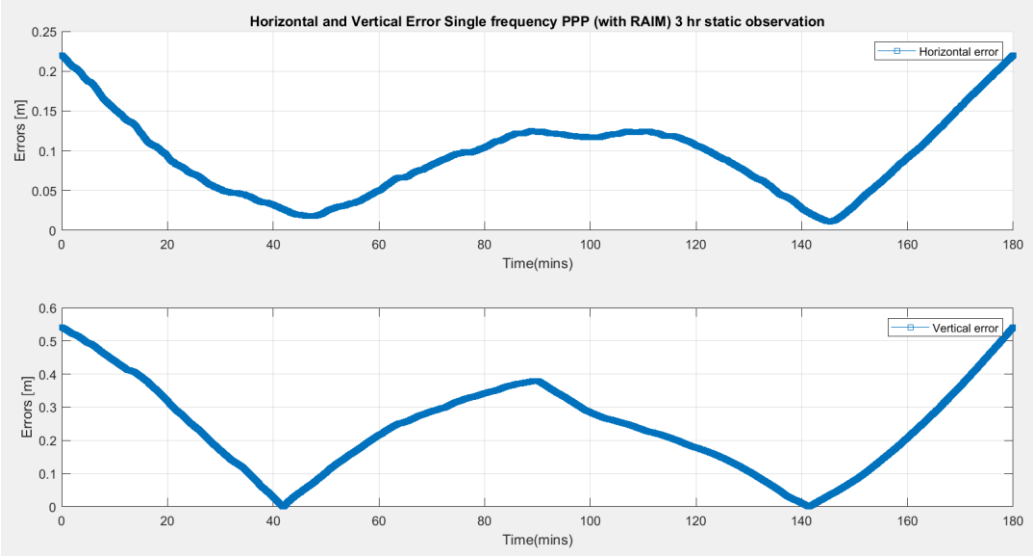

Figure 97. Horizontal and Vertical Error of Single frequency PPP (with RAIM-FDE) during 3 hr stationary test.

From Figure 97, only float RTK solutions are obtained.

5.6.2.4 RTK plots for Single frequency EVK-M8T (with RAIM-FDE) during 3 hr stationary test

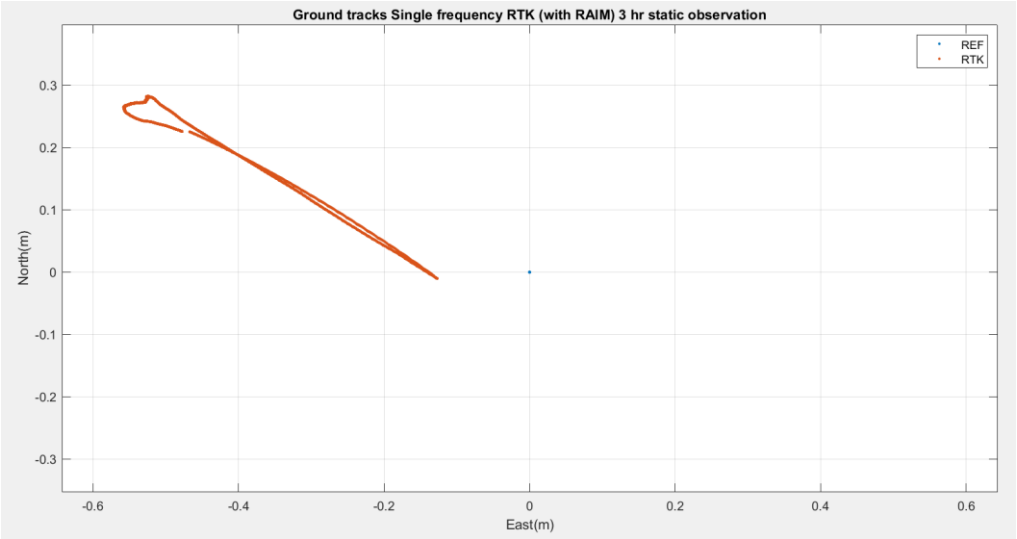

Figure 98. Ground tracks of Single frequency RTK (with RAIM-FDE) during 3 hr stationary test.

The figure above shows the RTK solution (in red) and estimated true position (in blue).

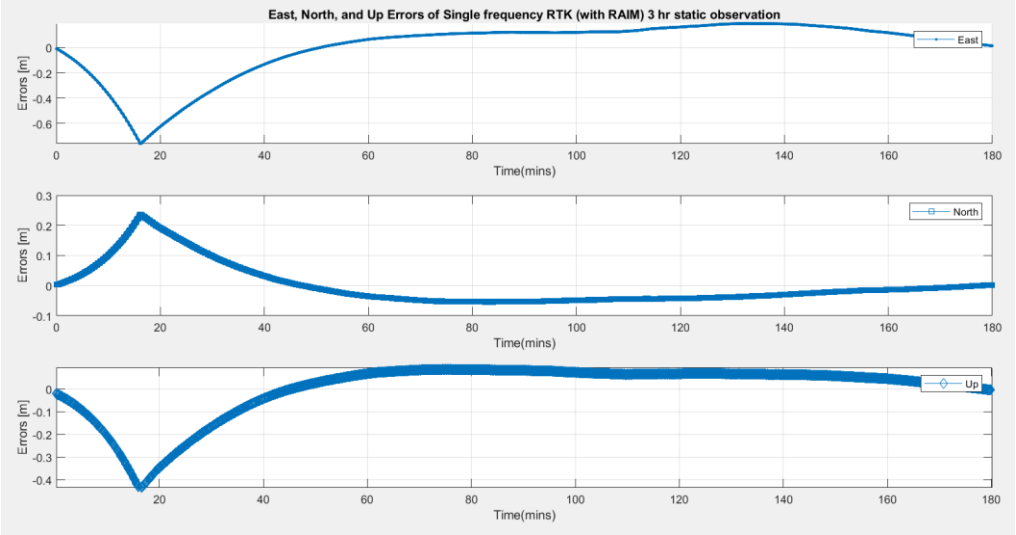

Figure 99. East, North, and Up Errors of Single frequency RTK (with RAIM-FDE) during 3 hr stationary test.

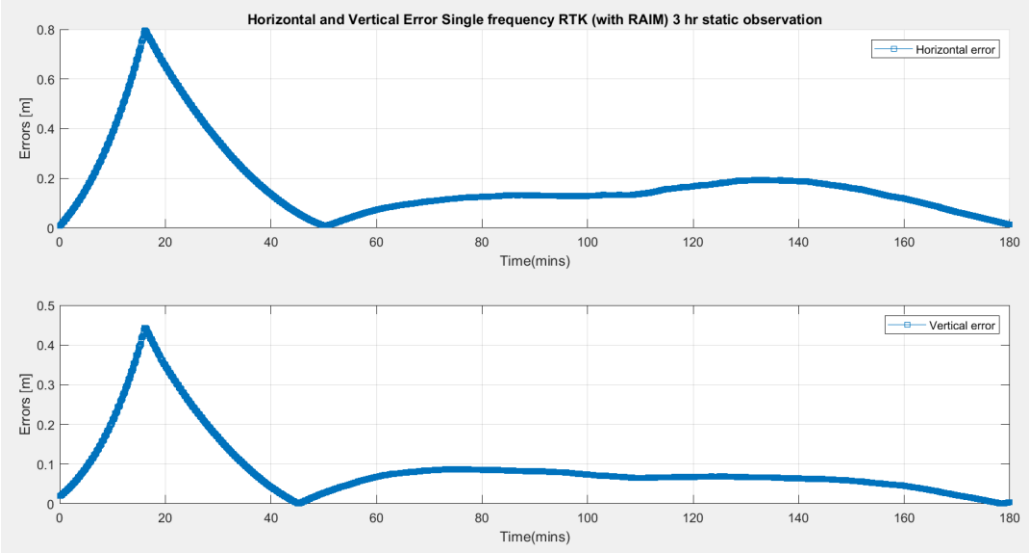

Figure 100. Horizontal and Vertical Error of Single frequency PPP (with RAIM-FDE) during 3 hr stationary test.

From Figure 100, only float RTK solutions are obtained.

5.6.3 GNSS post-processing mode plots for smartphone Samsung Galaxy s8 (with RAIM-FDE) during stationary test

5.6.3.1 SPP plots for Smartphone Samsung Galaxy s8 (with RAIM-FDE) during 3 hr stationary test

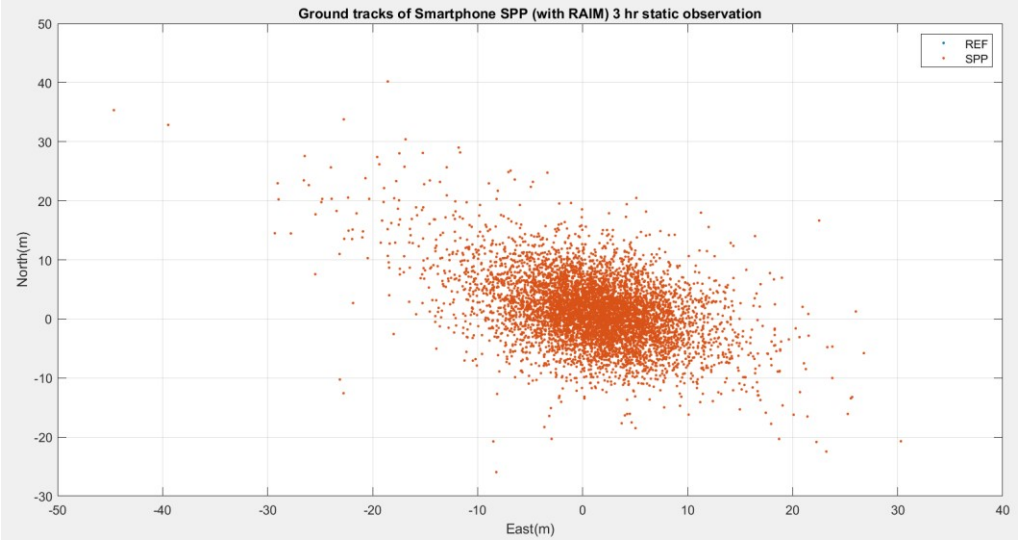

Figure 101. Ground tracks of Smartphone SPP (with RAIM-FDE) during 3 hr stationary test.

The figure above shows the SPP solution (in red) and estimated true position (in blue).

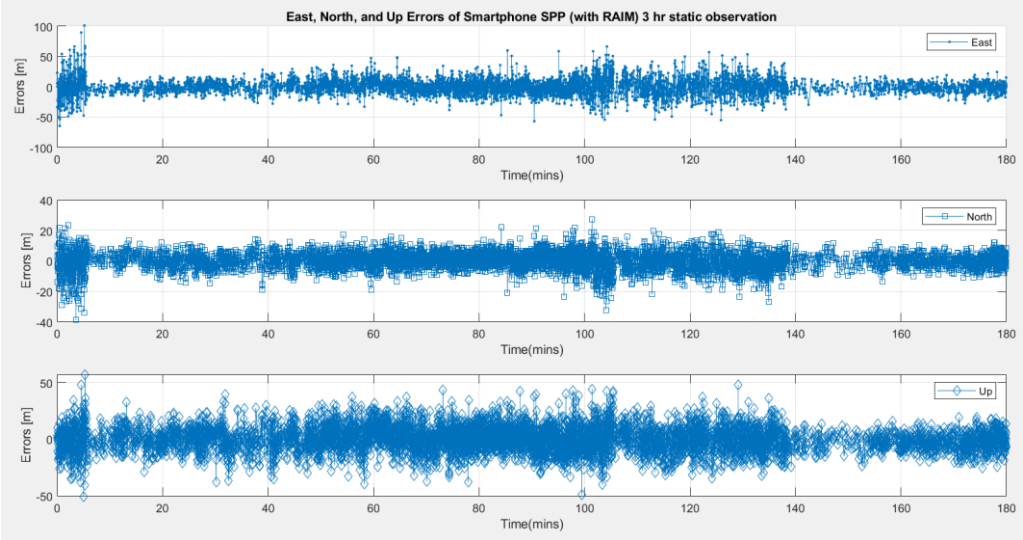

Figure 102. East, North, and Up Errors of Smartphone SPP (with RAIM-FDE) during 3 hr stationary test.

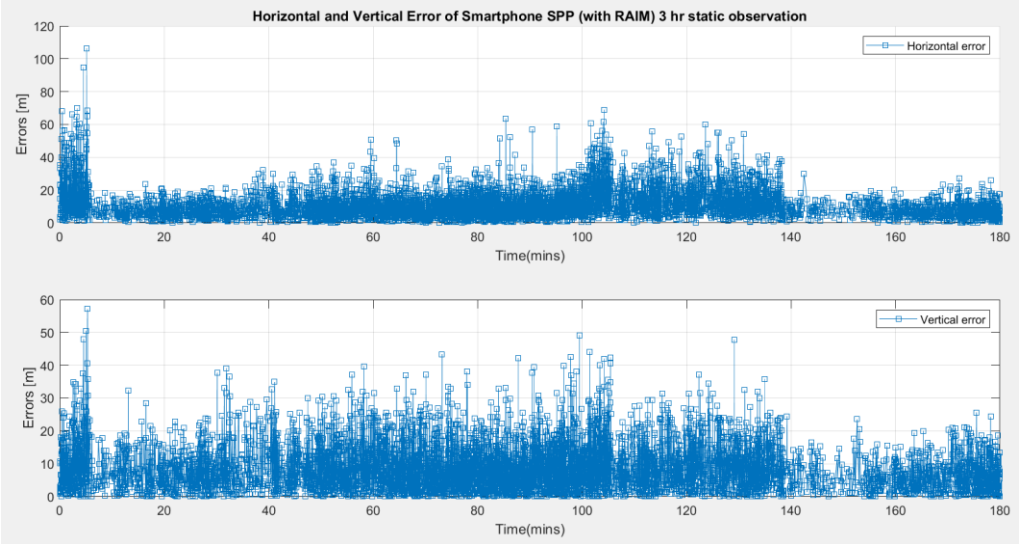

Figure 103. Horizontal and Vertical Error of Smartphone SPP (with RAIM-FDE) during 3 hr stationary test.

From figures 101, 102, and 103, high signal deviations and errors occur as a result of device constraints and capabilities.

5.6.3.2 SPP+SBAS plots smartphone Samsung Galaxy s8 (with RAIM-FDE) during 3 hr stationary test

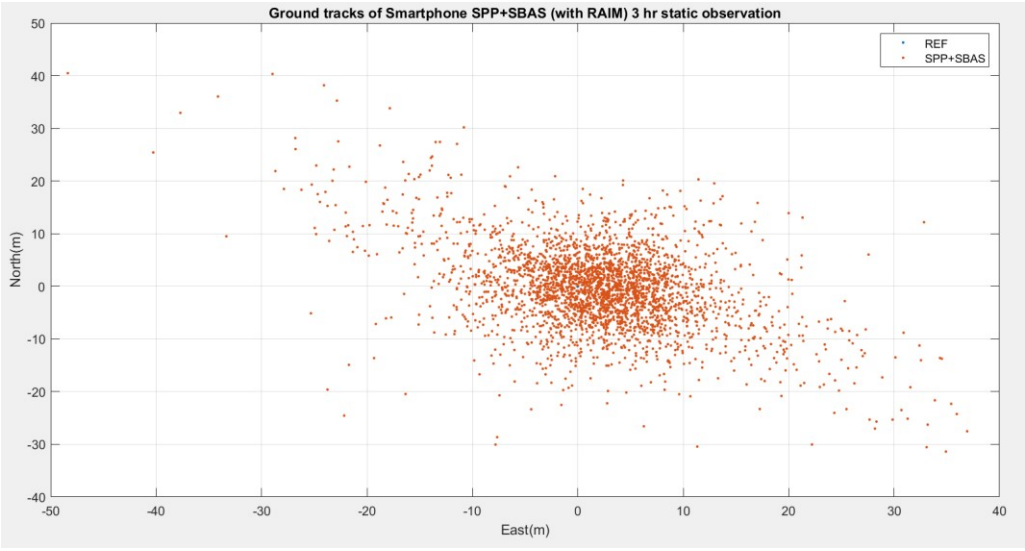

Figure 104. Ground tracks of Smartphone SPP+SBAS (with RAIM-FDE) during 3 hr stationary test.

The figure above shows the SPP (with EGNOS) solution (in red) and estimated true position (in blue).

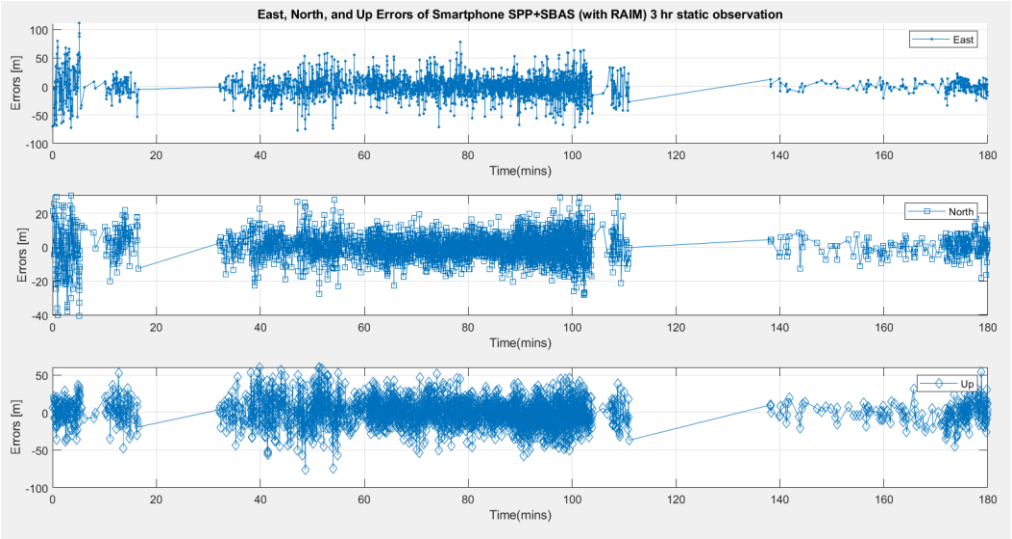

Figure 105. East, North, and Up Errors of Smartphone SPP+SBAS (with RAIM-FDE) during 3 hr stationary test.

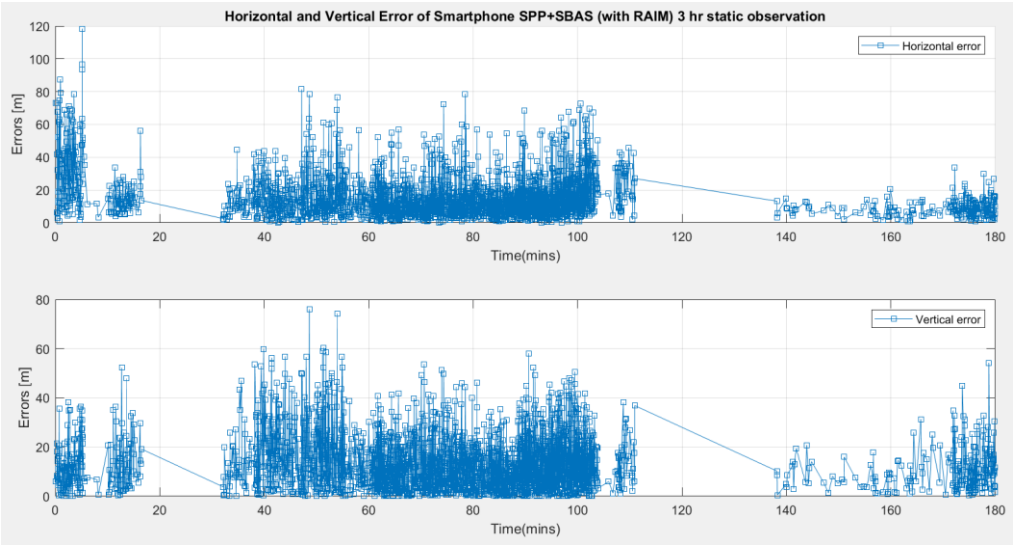

Figure 106. Horizontal and Vertical Error of Smartphone SPP+SBAS (with RAIM-FDE) during 3 hr stationary test.

From figures 104, 105, and 106, signal outage occurs around the 20 minutes (seconds of the day), 110 minutes mark as a result of poor visibility of geo-stationary satellites in northern Europe latitudes. Overall signal availability is diminished when compared to other post-processing modes.

5.6.3.3 PPP plots for smartphone Samsung Galaxy s8 (with RAIM-FDE) during 3 hr stationary test

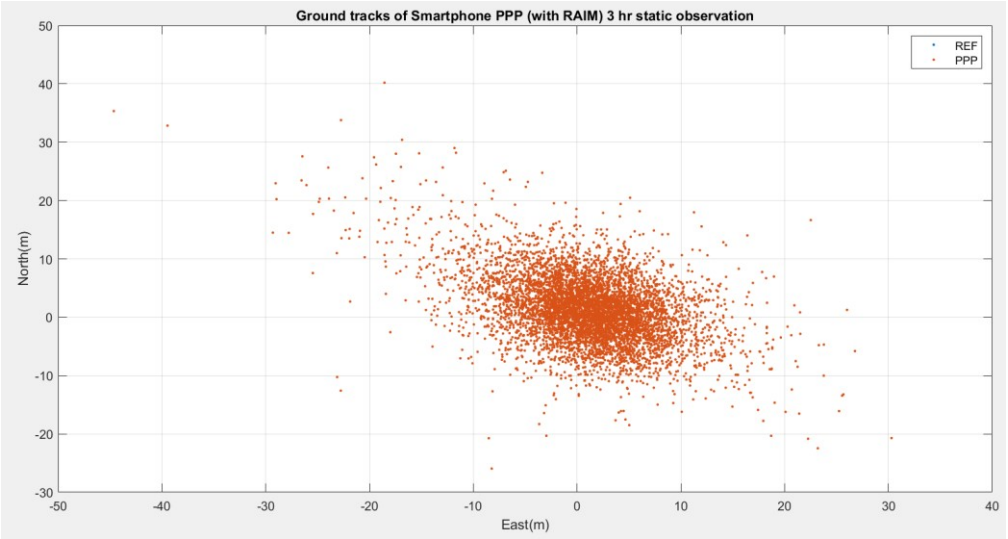

Figure 107. Ground tracks of Smartphone PPP (with RAIM-FDE) during 3 hr stationary test.

The figure above shows the PPP solution (in red) and estimated true position (in blue).

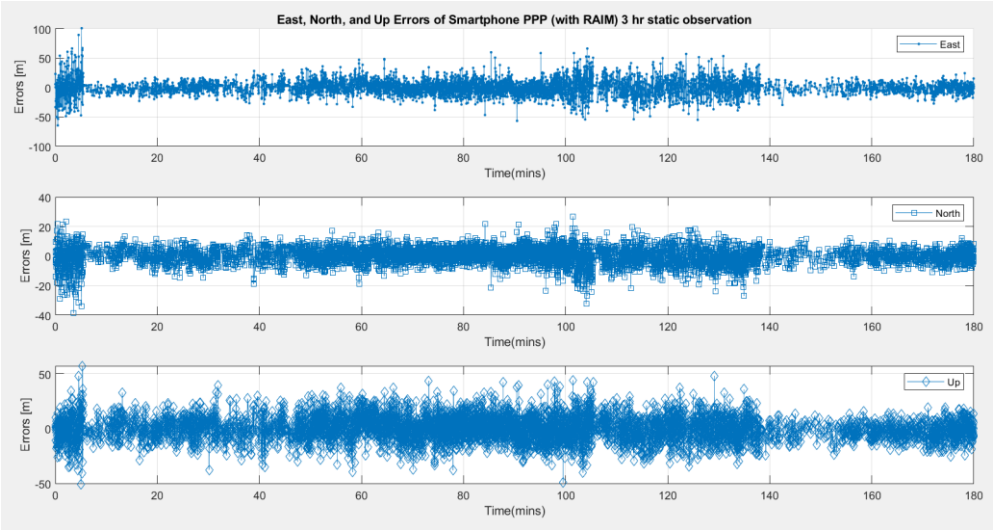

Figure 108. East, North, and Up Errors of Smartphone PPP (with RAIM-FDE) during 3 hr stationary test.

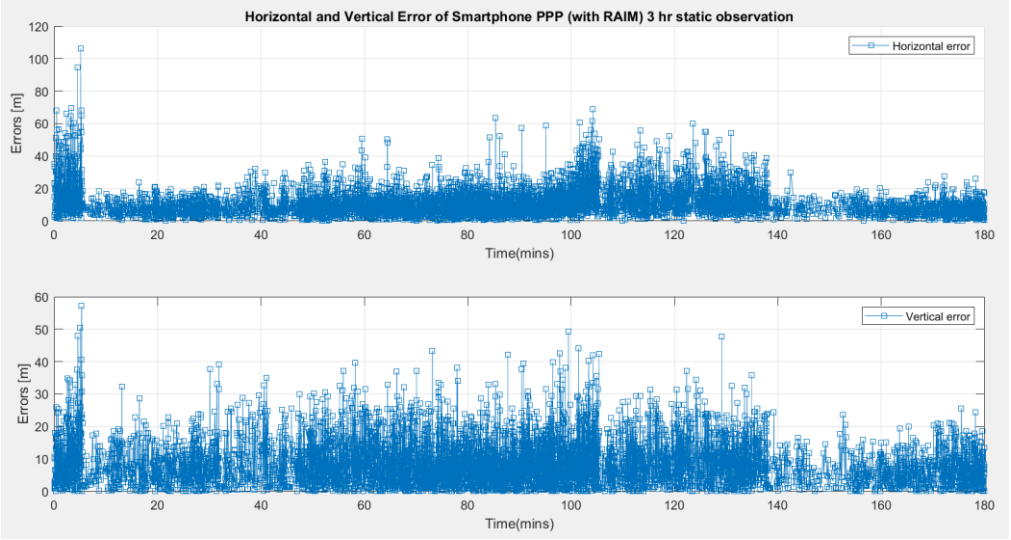

Figure 109. Horizontal and Vertical Error of Smartphone PPP (with RAIM-FDE) during 3 hr stationary test.

5.6.3.4 RTK plots for smartphone Samsung Galaxy s8 (with RAIM-FDE) during 3 hr stationary test

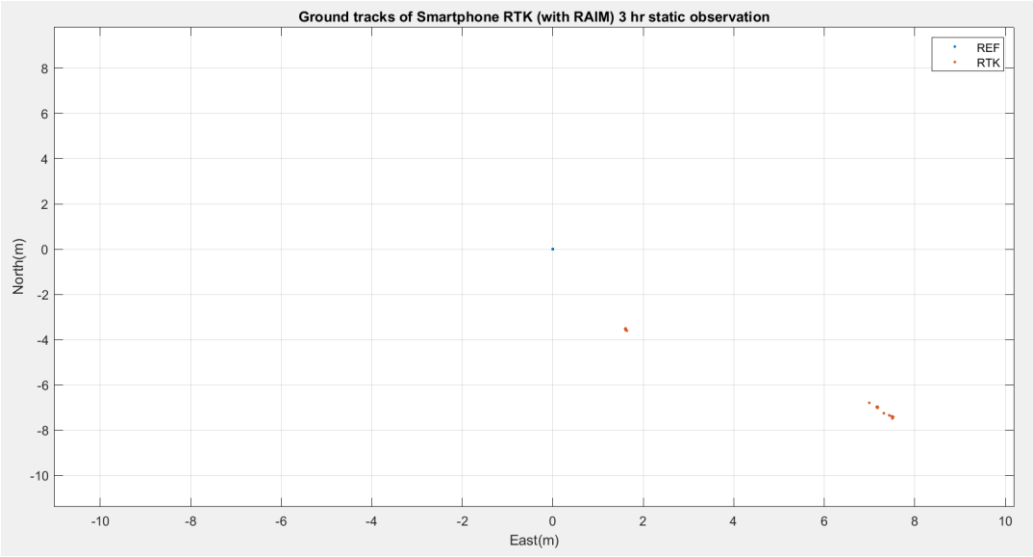

Figure 110. Ground tracks of Smartphone RTK (with RAIM-FDE) during 3 hr stationary test.

The figure above shows the RTK solution (in red) and estimated true position (in blue).

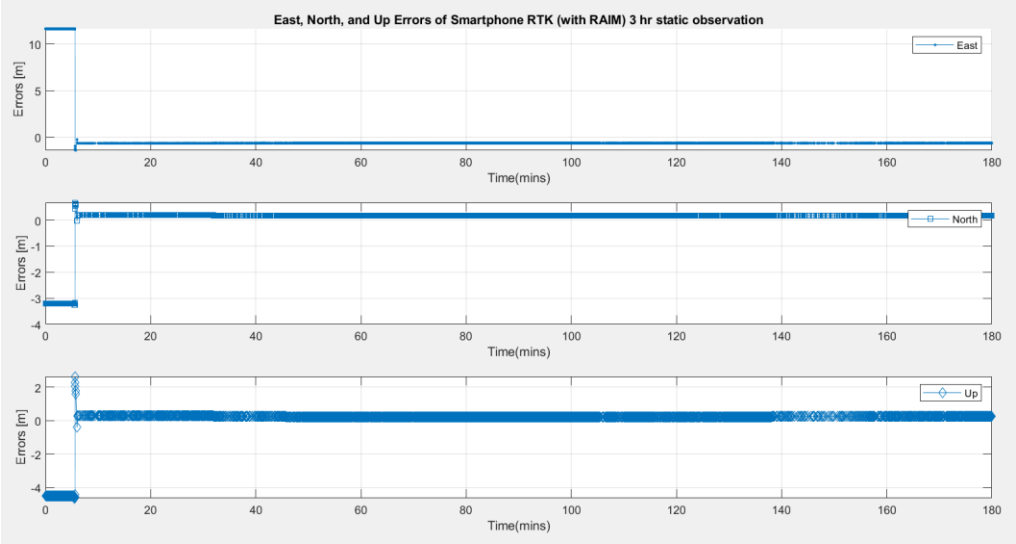

Figure 111. East, North, and Up Errors of Smartphone RTK (with RAIM-FDE) during 3 hr stationary test.

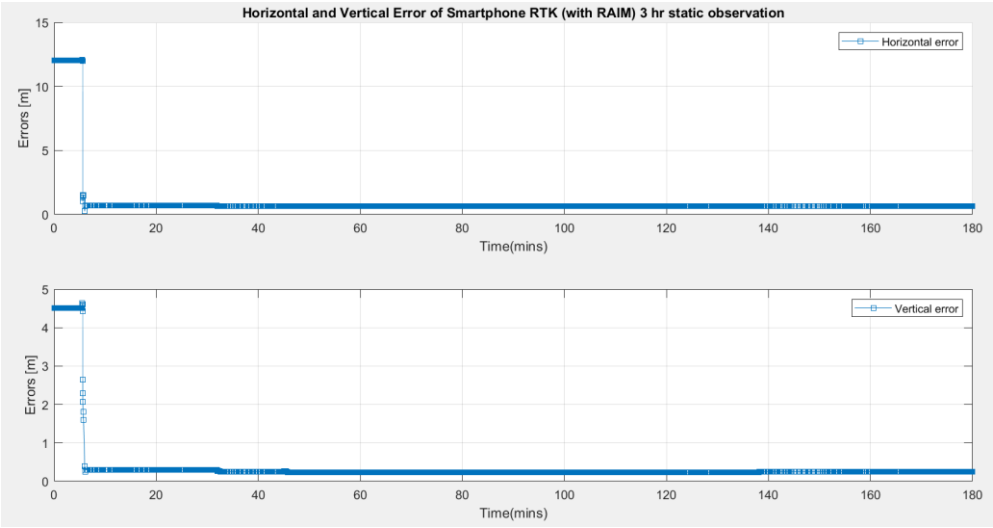

Figure 112. Horizontal and Vertical Error of Smartphone RTK (with RAIM-FDE) during 3 hr stationary test.

From figures 111, and 112, 2D and NEU errors are minimized as a result of carrier-based positioning techniques.

5.7 Ground track, ENU (east, north, up), horizontal and vertical error plots of various GNSS post-processing modes for dynamic tests

For simplicity, only plots for the 32 minutes dynamic test (with RAIM-FDE) will be presented. Plots for the dual frequency-(1) device will not be shown. Dual frequency-(2) will be used as the de-facto, and will be shown.

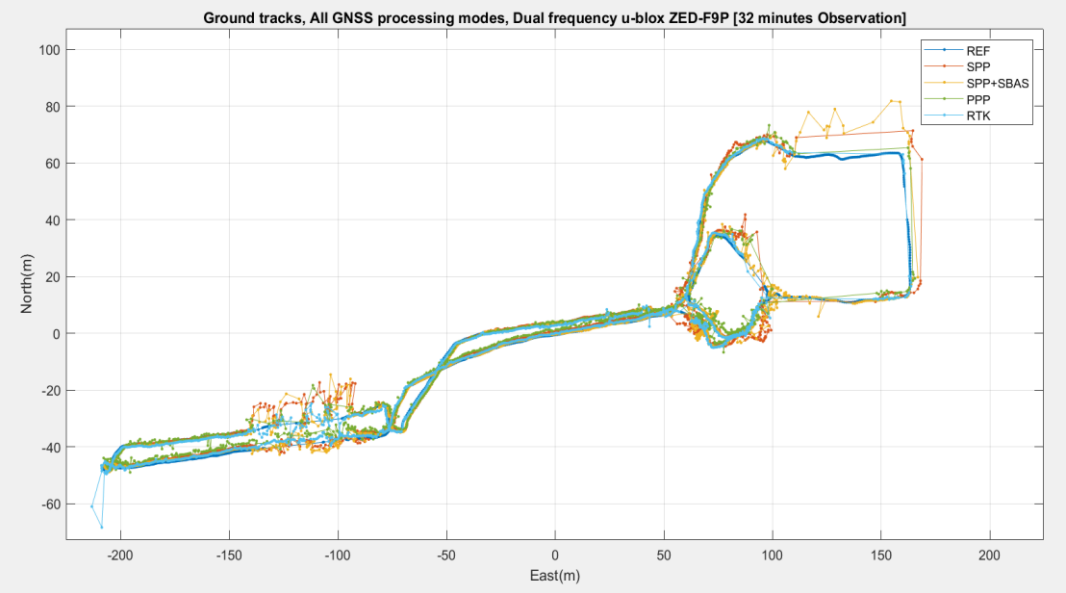

Figure 113. Ground tracks - All GNSS processing modes - for dual frequency u-blox ZED-F9P during 32 min dynamic test.

The figure above shows the ground tracks of various GNSS processing modes (SPP, SPPP+SBAS, PPP and RTK), and Topcon REF (in blue).

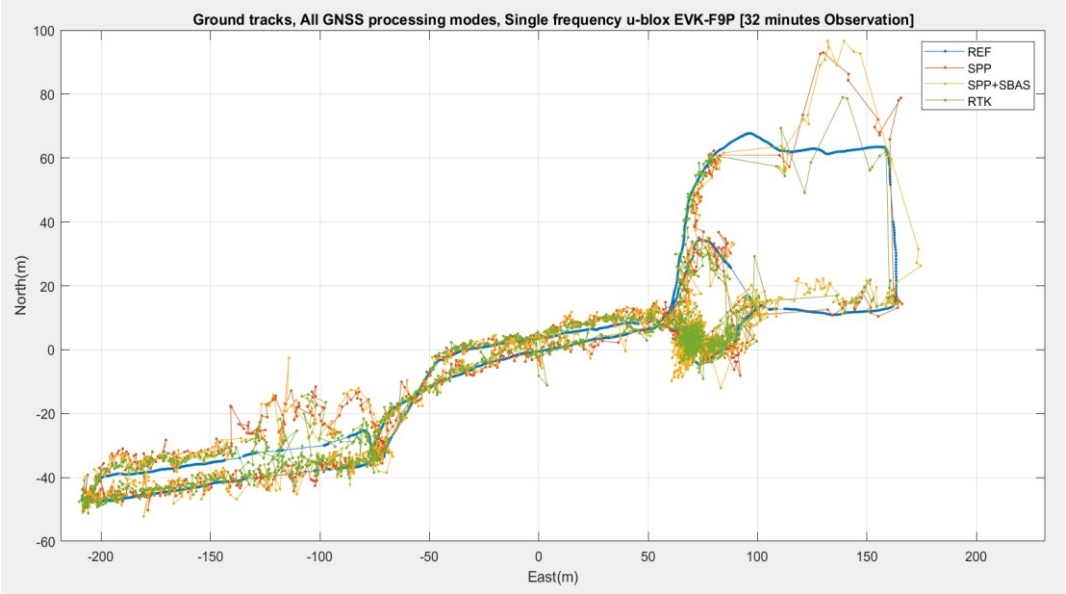

Figure 114. Ground tracks - All GNSS processing modes - for single frequency u-blox EVK-F9P during 32 min dynamic test.

The figure above shows the ground tracks of various GNSS processing modes (SPP, SPPP+SBAS, PPP and RTK), and Topcon REF (in blue).

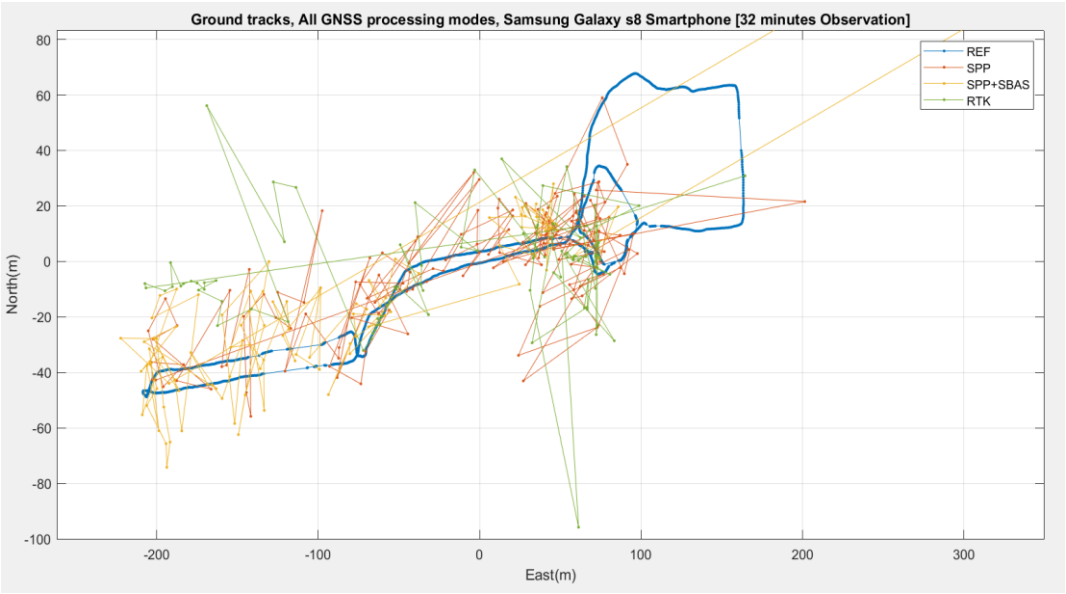

Figure 115. Ground tracks - All GNSS processing modes - for Samsung Galaxy s8 smartphone during 32 min dynamic test.

The figure above shows the ground tracks of various GNSS processing modes (SPP, SPPP+SBAS, PPP and RTK), and Topcon REF (in blue).

From figures 113, 114, and 115, it can be observed that the RTK is the best solution as it matches the reference ground truth more closely. The dual frequency receiver is the best performer as shown in Figure 116.

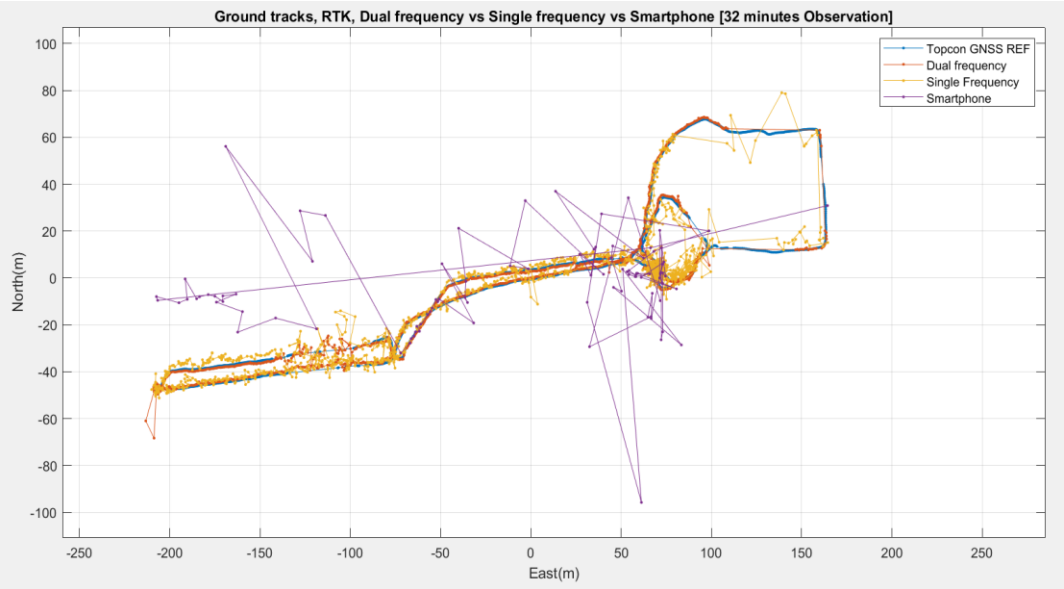

Figure 116. Ground tracks - RTK - for dual frequency vs single frequency vs smartphone during 32 min dynamic test.

The figure above shows the RTK solution ground tracks of various GNSS receivers (dual frequency, single frequency and smartphone), and Topcon GNSS REF (in blue).

5.7.1 GNSS post-processing mode plots for Dual frequency ZED-F9P (with RAIM-FDE) during dynamic test

5.7.1.1 SPP plots for Dual frequency ZED-F9P (with RAIM-FDE) during 32 min dynamic test

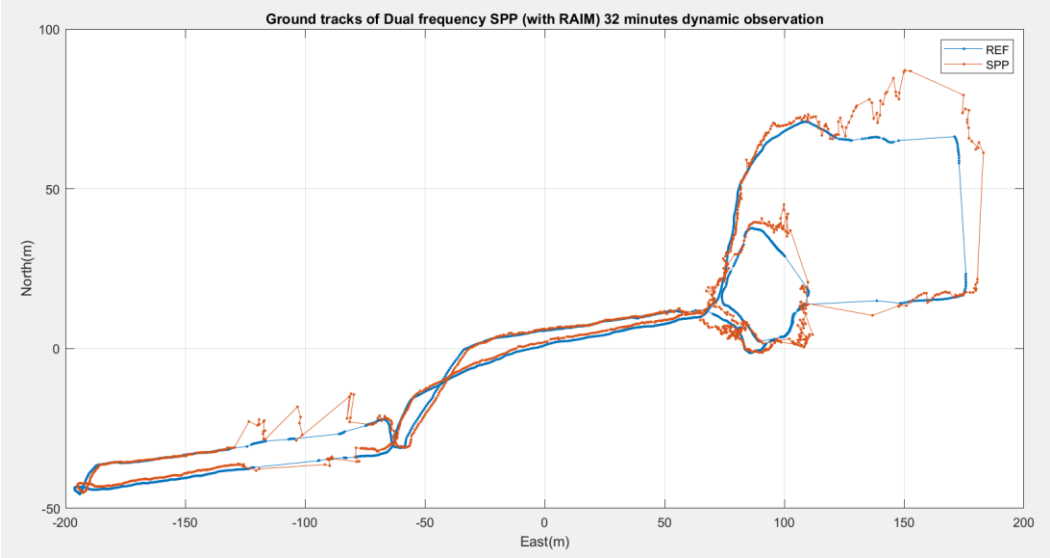

Figure 117. Ground tracks of Dual frequency SPP (with RAIM-FDE) during 32 min dynamic test.

The figure above shows the SPP solution (in red) and Topcon REF (in blue).

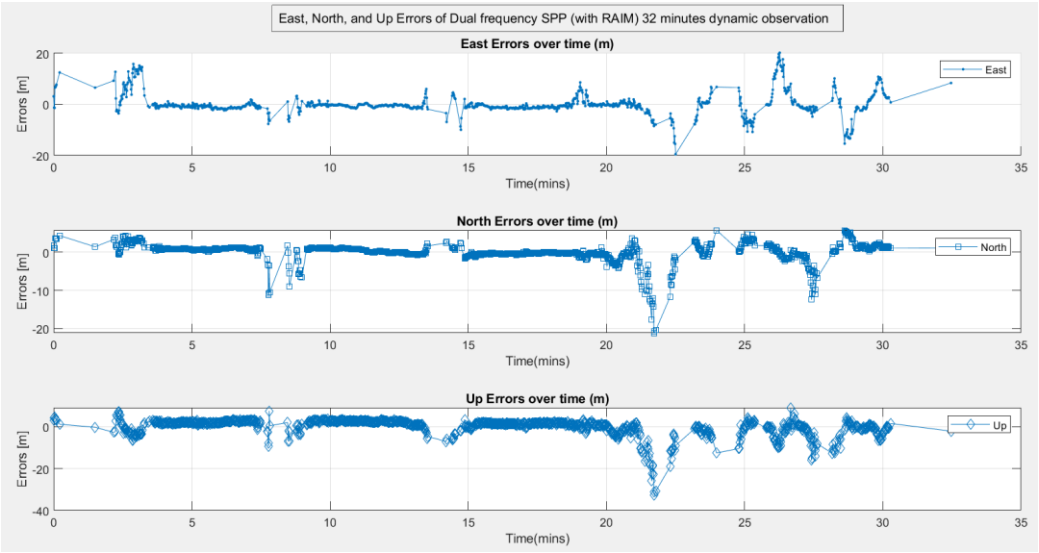

Figure 118. East, North, and Up Errors of Dual frequency SPP (with RAIM-FDE) during 32 min dynamic test.

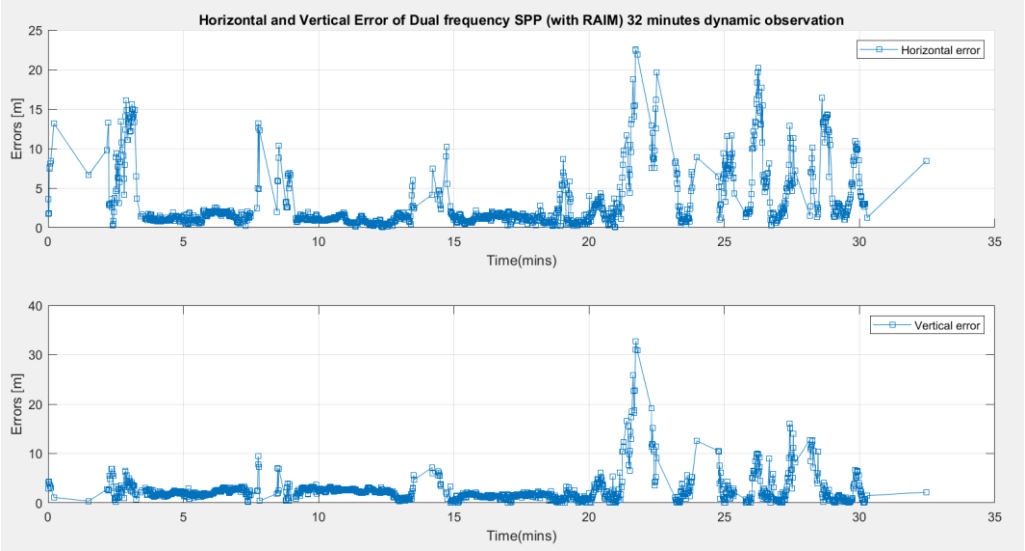

Figure 119. Horizontal and Vertical Error of Dual frequency SPP (with RAIM-FDE) during 32 min dynamic test.

From figures 117, 118, and 119, signal outage and resulting large errors was observed at around 8, 13, and 22 minutes as a result of multipath effects caused by signal obstructions, and shadowing.

5.7.1.2 SPP+SBAS plots for Dual frequency ZED-F9P (with RAIM-FDE) during 32 min dynamic test

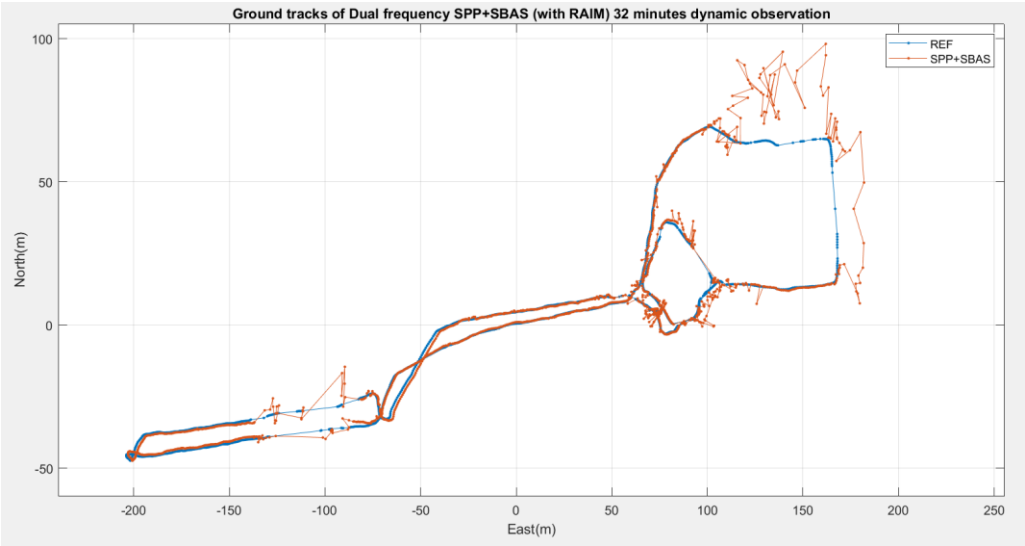

Figure 120. Ground tracks of Dual frequency SPP+SBAS (with RAIM-FDE) during 32 min dynamic test.

The figure above shows the SPP (with EGNOS) solution (in red) and Topcon REF (in blue).

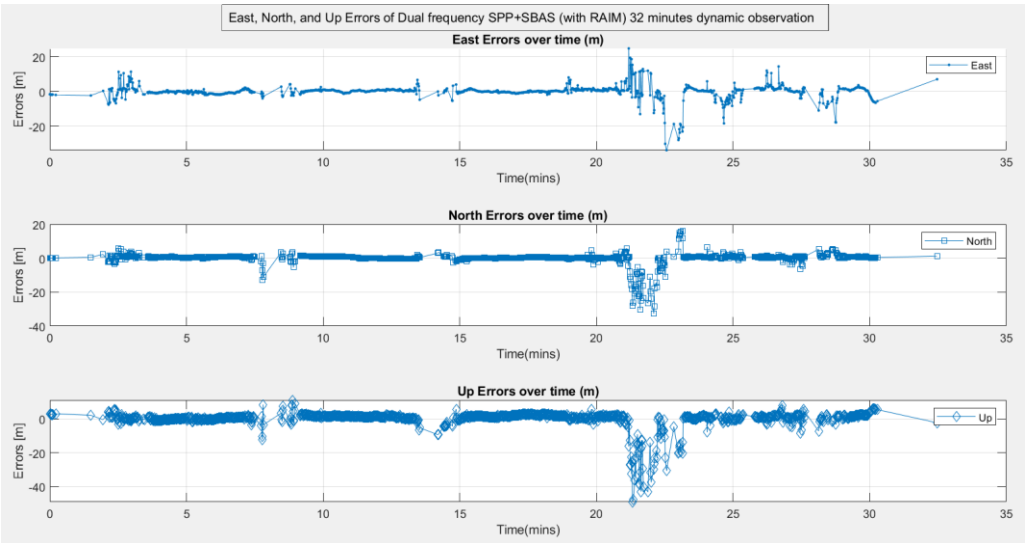

Figure 121. East, North, and Up Errors of Dual frequency SPP+SBAS (with RAIM-FDE) during 32 min dynamic test.

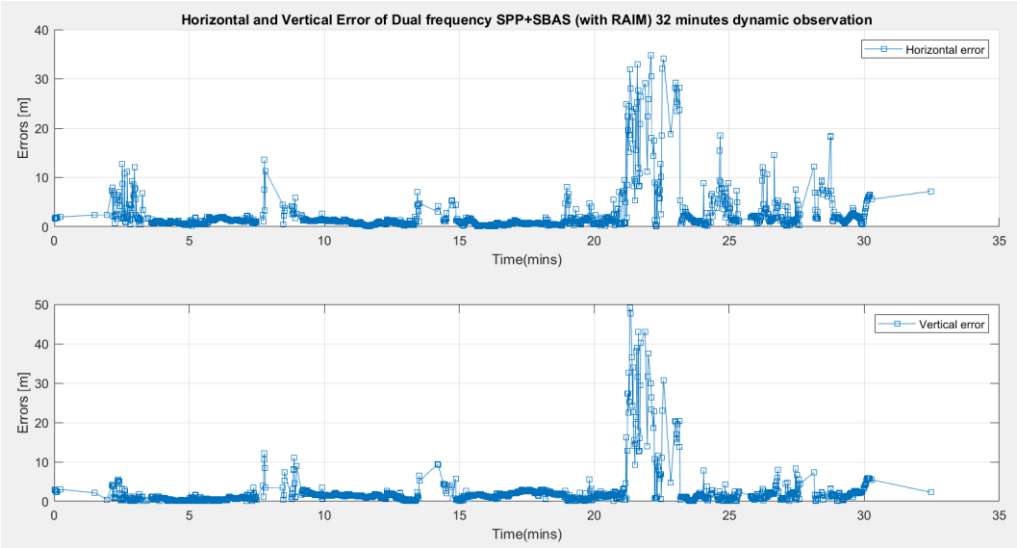

Figure 122. Horizontal and Vertical Error of Dual frequency SPP+SBAS (with RAIM-FDE) during 32 min dynamic test.

From figures 120, 121, and 122, signal outage, and resulting large errors was observed at around 8, 13, and 22 minutes as a result of multipath effects caused by signal obstructions, and shadowing.

5.7.1.3 PPP plots for Dual frequency ZED-F9P (with RAIM-FDE) during 32 min dynamic test

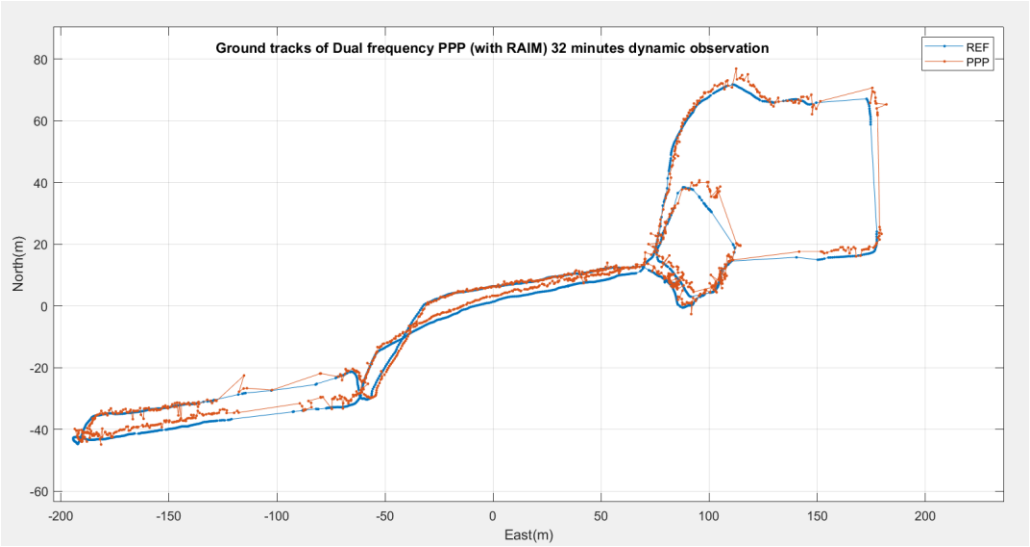

Figure 123. Ground tracks of Dual frequency PPP (with RAIM-FDE) during 32 min dynamic test.

The figure above shows the PPP solution (in red) and Topcon REF (in blue).

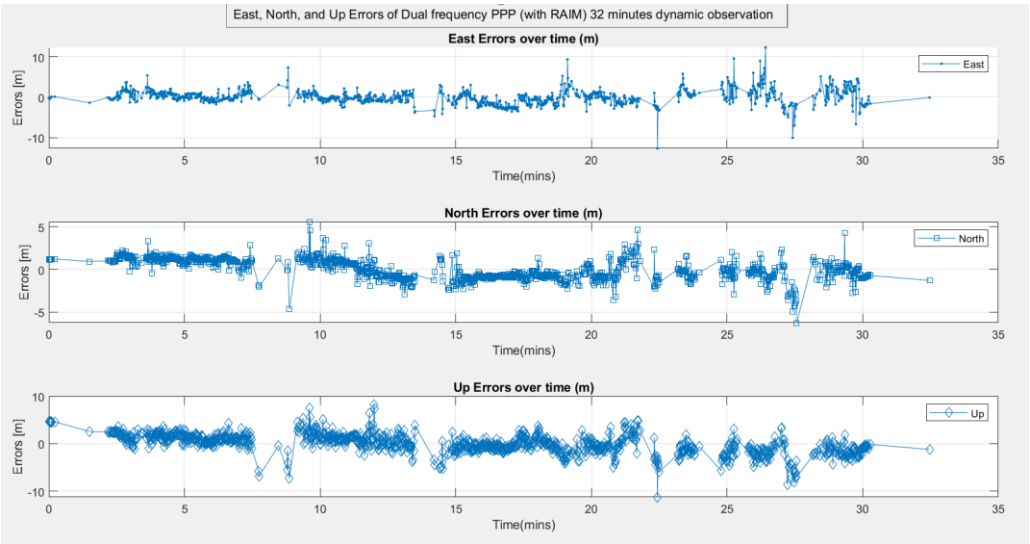

Figure 124. East, North, and Up Errors of Dual frequency PPP (with RAIM-FDE) during 32 min dynamic test.

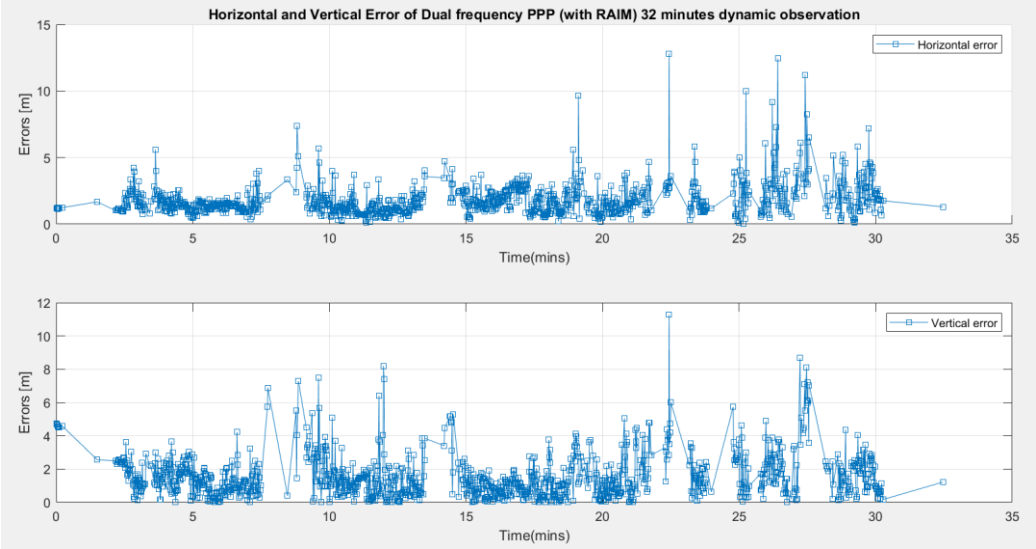

Figure 125. Horizontal and Vertical Error of Dual frequency PPP (with RAIM-FDE) during 32 min dynamic test.

From figures 123, 124, and 125, signal outage and resulting errors was observed at around 8, 13, and 22 minutes as a result of multipath effects caused by signal obstructions, and shadowing.

5.7.1.4 RTK plots for Dual frequency ZED-F9P (with RAIM-FDE) during 32 min dynamic test

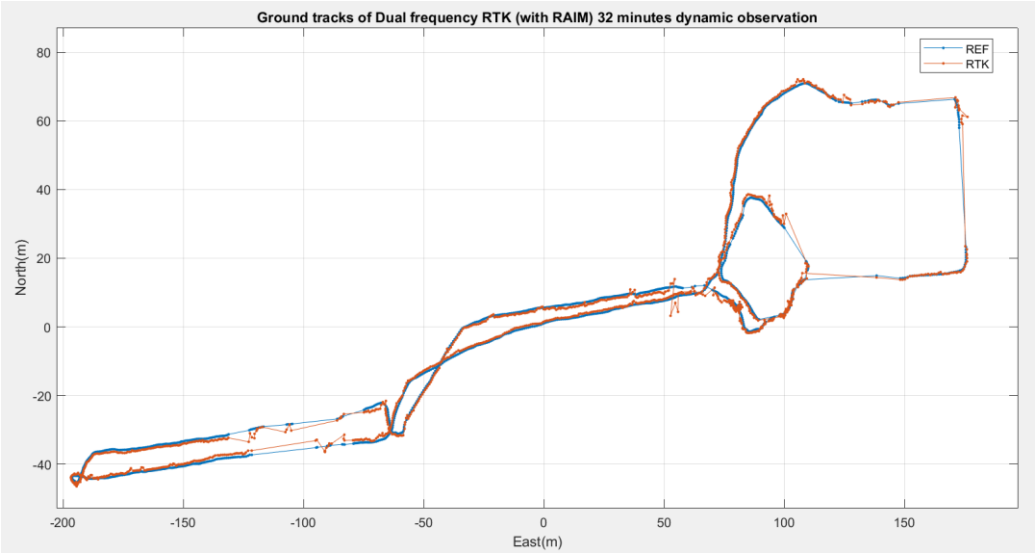

Figure 126. Ground tracks of Dual frequency RTK (with RAIM-FDE) during 32 min dynamic test.

The figure above shows the RTK solution (in red) and Topcon REF (in blue).

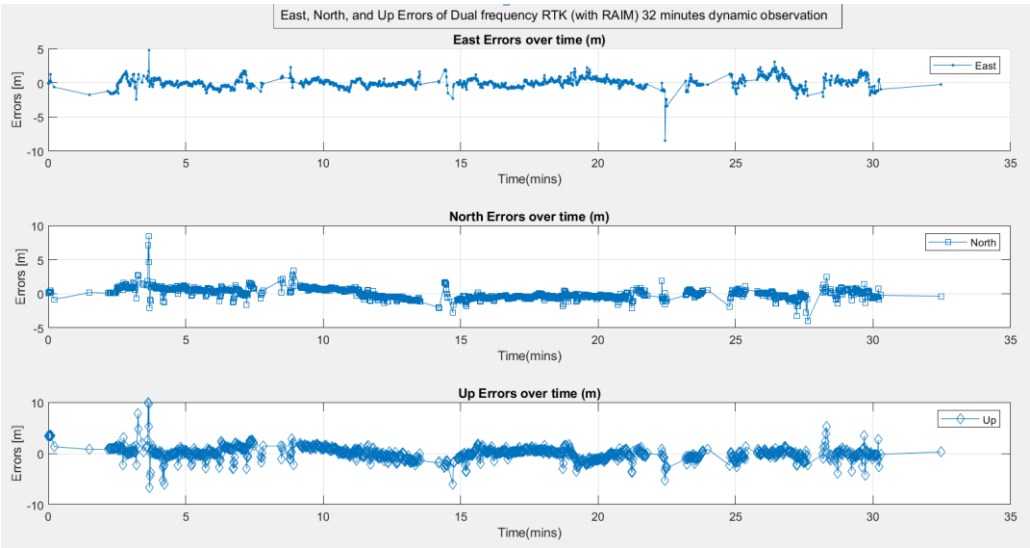

Figure 127. East, North, and Up Errors of Dual frequency RTK (with RAIM-FDE) during 32 min dynamic test.

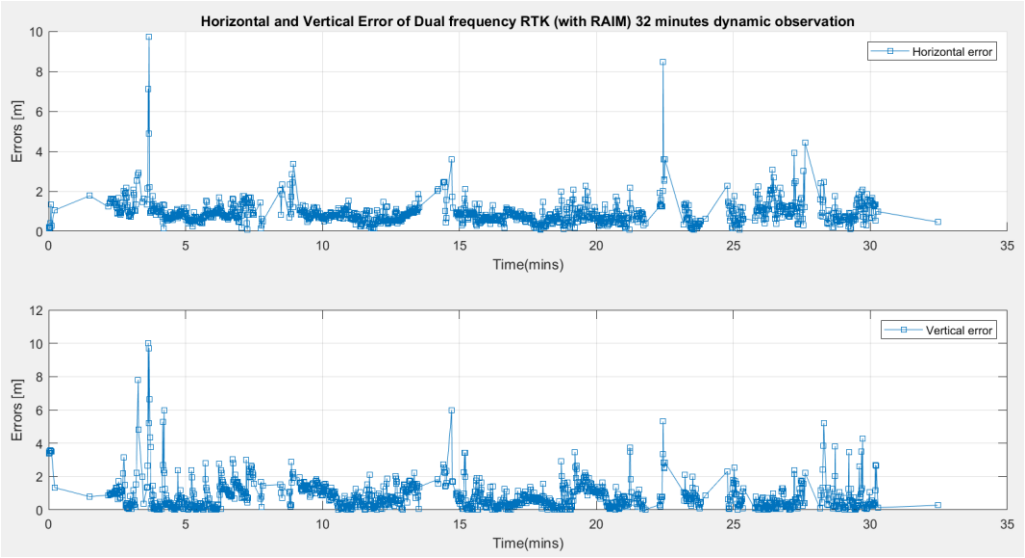

Figure 128. Horizontal and Vertical Error of Dual frequency RTK (with RAIM-FDE) during 32 min dynamic test.

From figures 126, 127, and 128, signal outage was observed at around 8, 13, and 22 minutes as a result of multipath effects caused by signal obstructions, and shadowing.

5.7.2 GNSS post-processing mode plots for Single frequency EVK-M8T (with RAIM-FDE) during dynamic test

5.7.2.1 SPP plots for single frequency EVK-M8T (with RAIM-FDE) during 32 min dynamic test

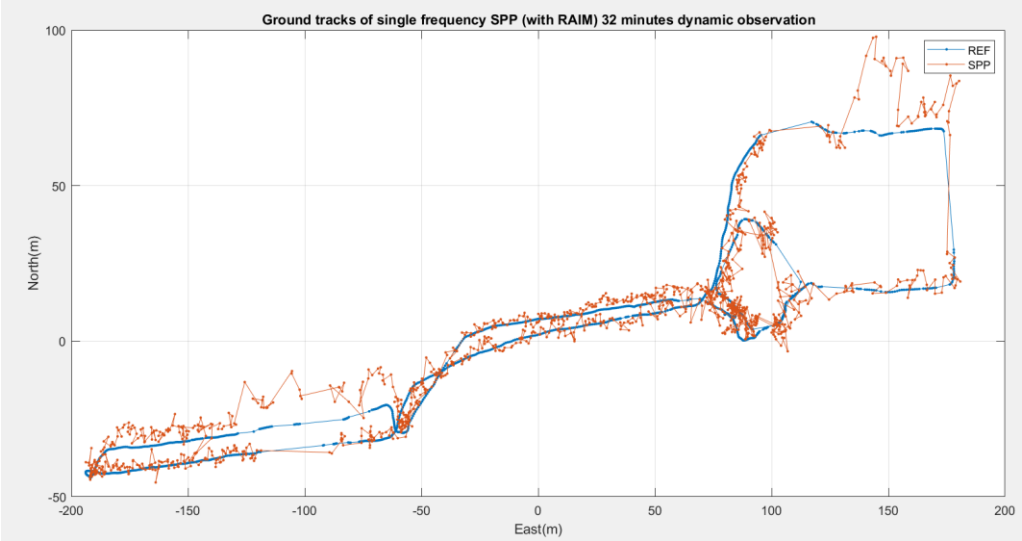

Figure 129. Ground tracks of single frequency SPP (with RAIM-FDE) during 32 min dynamic test.

The figure above shows the SPP solution (in red) and Topcon REF (in blue).

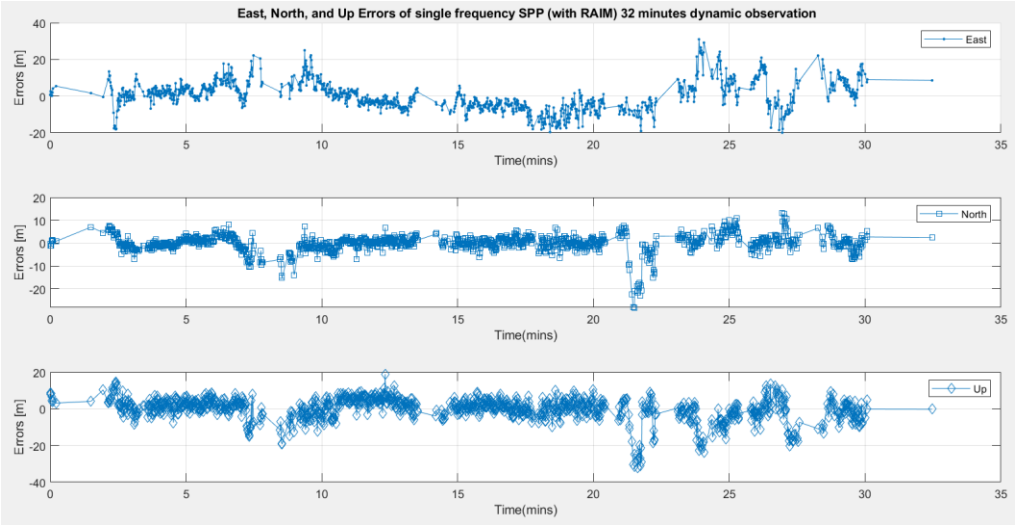

Figure 130. East, North, and Up Errors of single frequency SPP (with RAIM-FDE) during 32 min dynamic test.

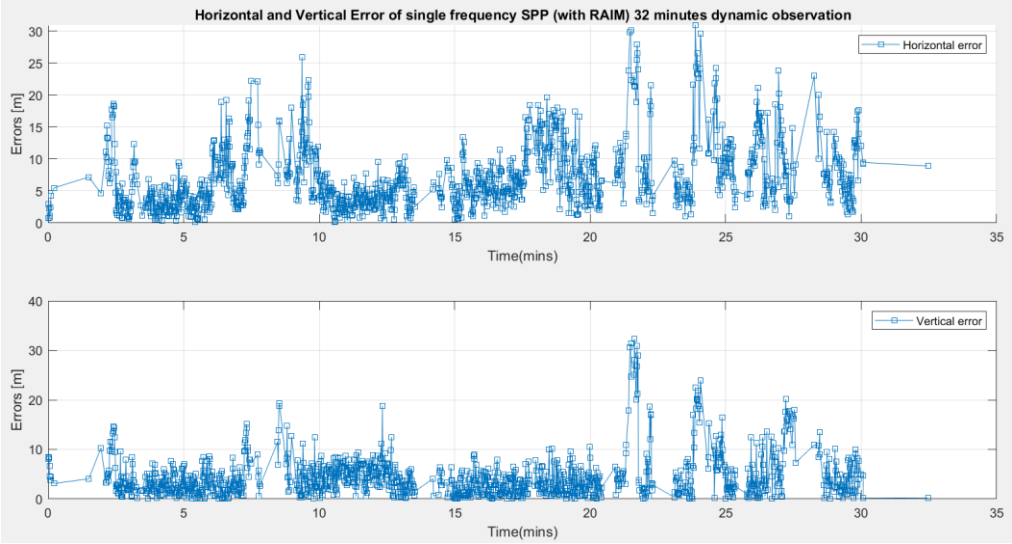

Figure 131. Horizontal and Vertical Error of single frequency SPP (with RAIM-FDE) during 32 min dynamic test.

From figures 129, 130, and 131, large errors was observed at around 8, 13, and 22 minutes as a result of multipath effects caused by signal obstructions, and shadowing.

5.7.2.2 SPP+SBAS plots for single frequency EVK-M8T (with RAIM) during 32 min dynamic test

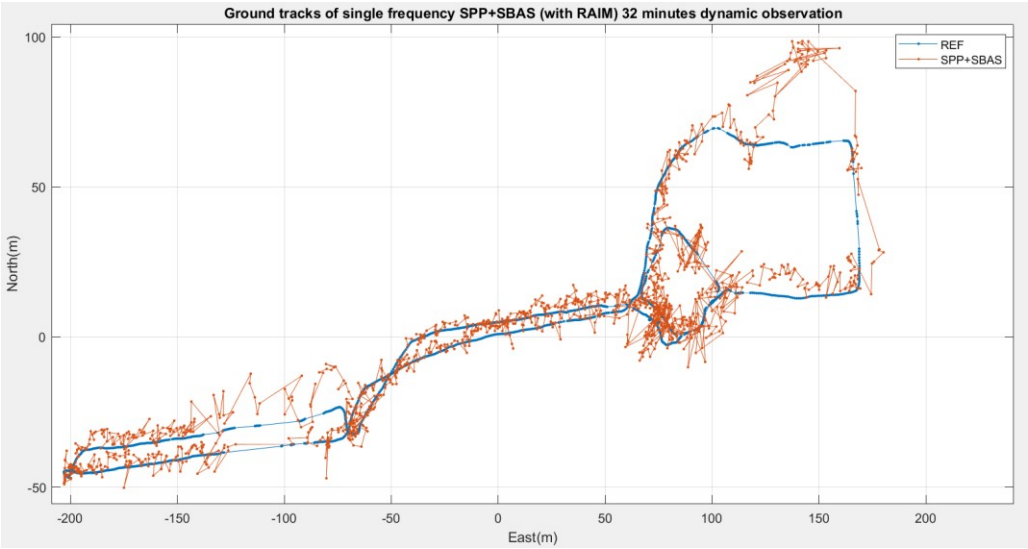

Figure 132. Ground tracks of single frequency SPP+SBAS (with RAIM-FDE) during 32 min dynamic test.

The figure above shows the SPP (with EGNOS) solution (in red) and Topcon REF (in blue).

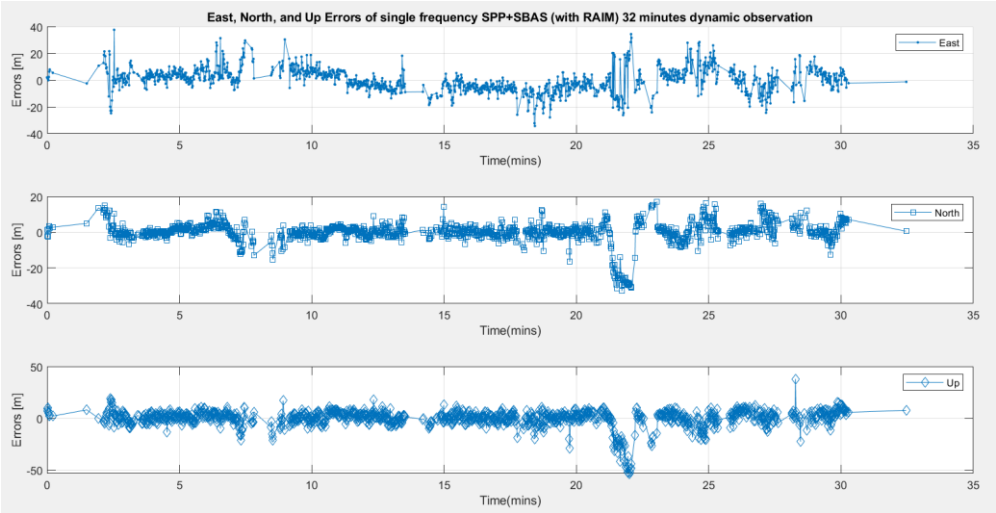

Figure 133. East, North, and Up Errors of single frequency SPP+SBAS (with RAIM-FDE) during 32 min dynamic test.

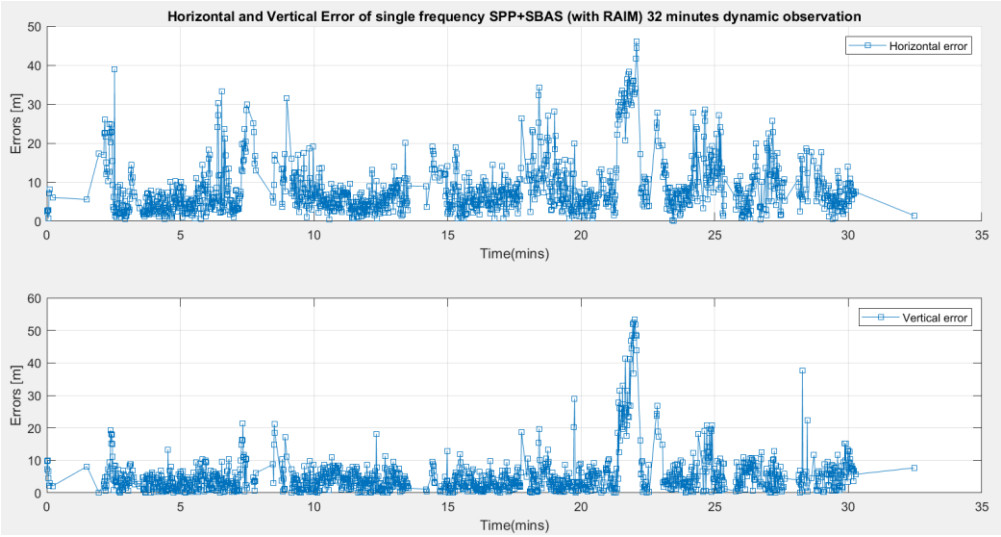

Figure 134. Horizontal and Vertical Error of single frequency SPP+SBAS (with RAIM-FDE) during 32 min dynamic test.

From figures 132, 133, and 134, large errors were observed at around 8, 13, and 22 minutes as a result of multipath effects caused by signal obstructions, and shadowing.

5.7.2.3 RTK plots for single frequency EVK-M8T (with RAIM) during 32 min dynamic test

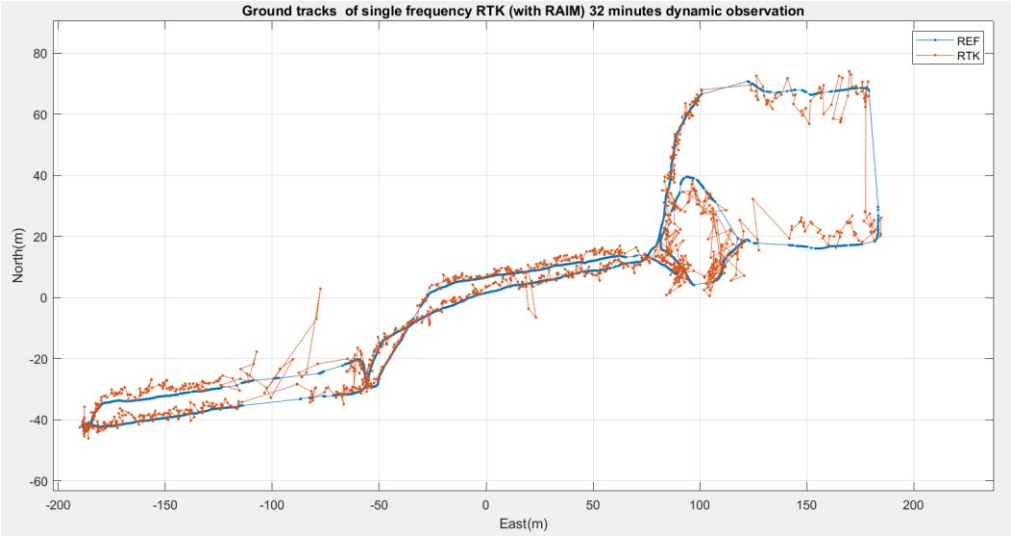

Figure 135. Ground tracks of single frequency RTK (with RAIM-FDE) during 32 min dynamic test.

The figure above shows the RTK solution (in red) and Topcon REF (in blue).

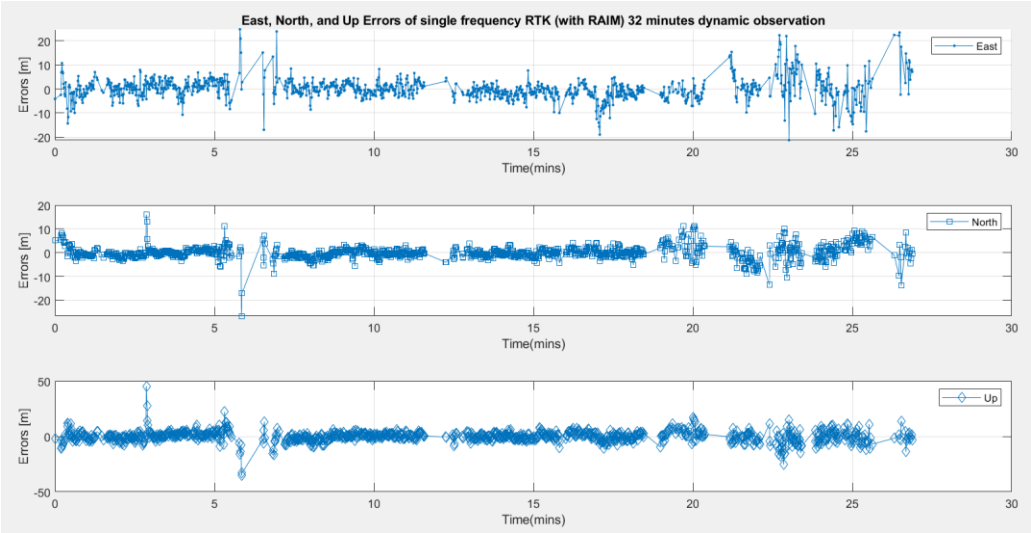

Figure 136. East, North, and Up Errors of single frequency RTK (with RAIM-FDE) during 32 min dynamic test.

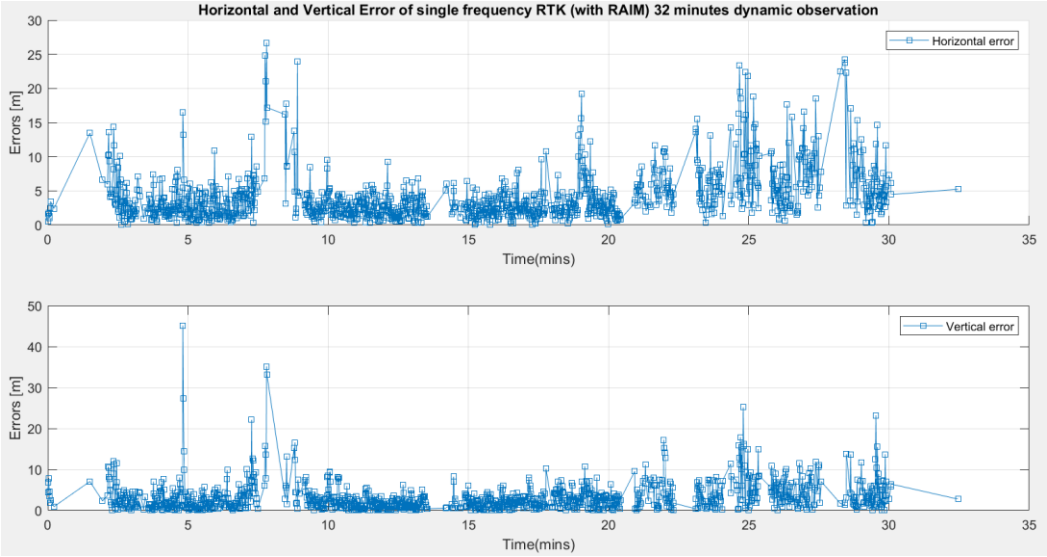

Figure 137. Horizontal and Vertical Error of single frequency RTK (with RAIM-FDE) during 32 min dynamic test.

From figures 135, 136, and 137, signal outage and resulting large errors were observed at around 8, 13, and 22 minutes as a result of multipath effects caused by signal obstructions, and shadowing.

5.7.3 GNSS post-processing mode plots for smartphone Samsung Galaxy s8 (with RAIM-FDE) during dynamic test

5.7.3.1 SPP plots for Smartphone Samsung Galaxy s8 (with RAIM-FDE) during 32 min dynamic test

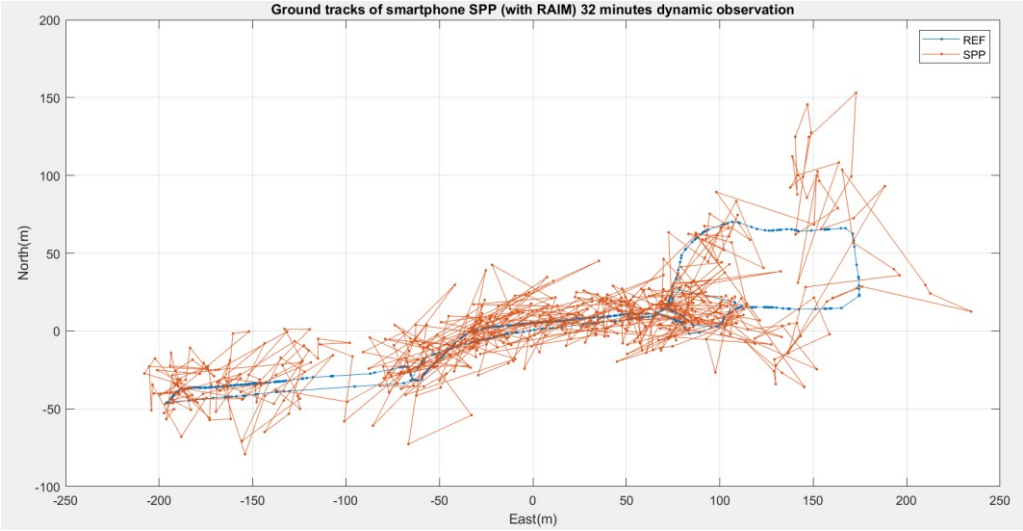

Figure 138. Ground tracks of smartphone SPP (with RAIM-FDE) during 32 min dynamic test.

The figure above shows the SPP solution (in red) and Topcon REF (in blue).

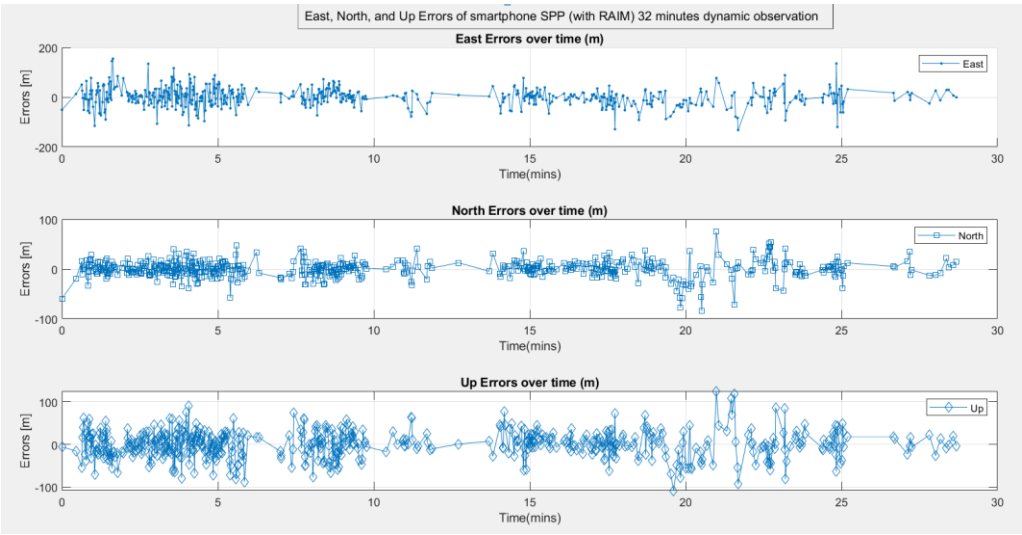

Figure 139. East, North, and Up Errors of smartphone SPP (with RAIM-FDE) during 32 min dynamic test.

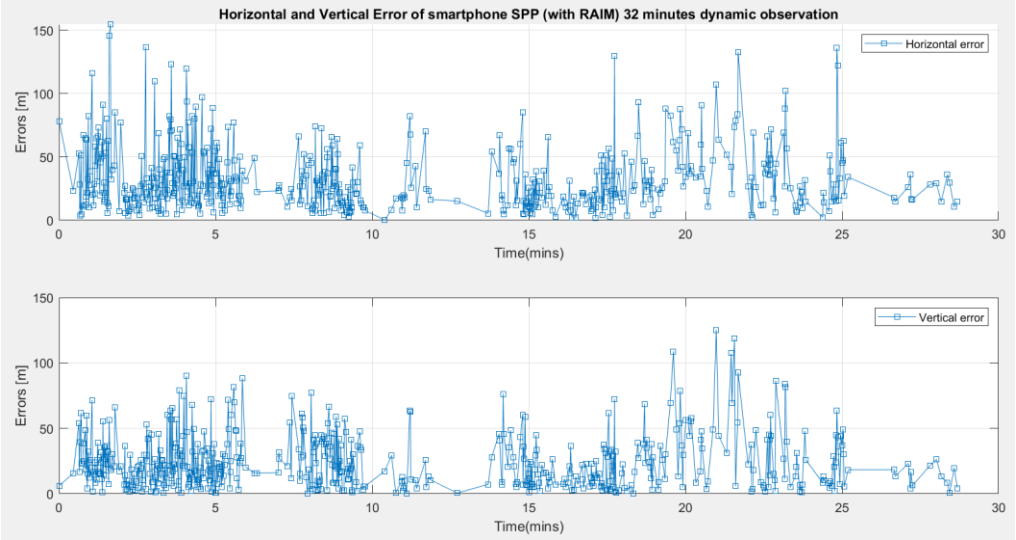

Figure 140. Horizontal and Vertical Error of smartphone SPP (with RAIM-FDE) during 32 min dynamic test.

From figures 138, 139, and 140, signal outage was observed at around 8, 13, and 22 minutes as a result of multipath effects caused by signal obstructions, and shadowing.

5.7.3.2 SPP+SBAS plots smartphone Samsung Galaxy s8 (with RAIM) during 32 min dynamic test

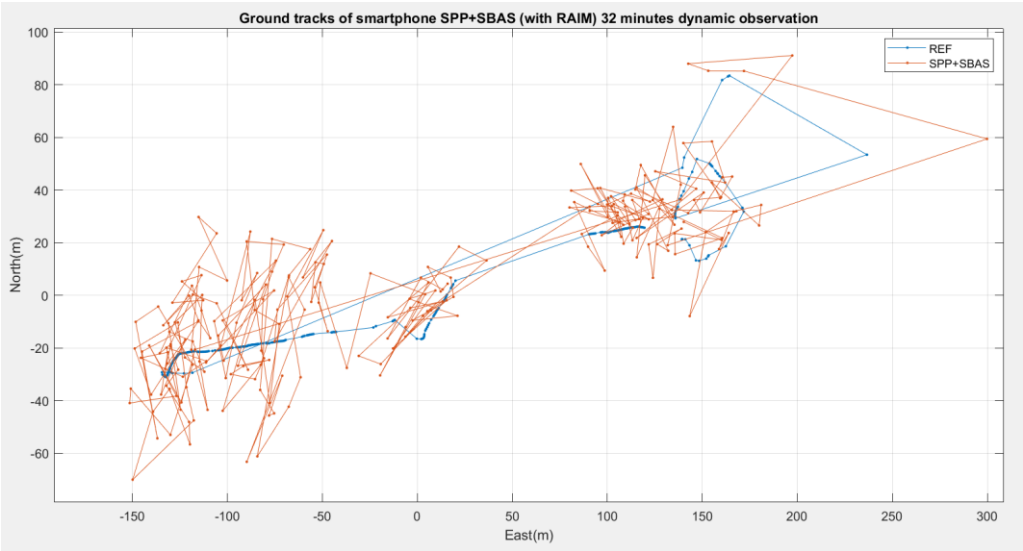

Figure 141. Ground tracks of smartphone SPP+SBAS (with RAIM-FDE) during 32 min dynamic test.

The figure above shows the SPP (with EGNOS) solution (in red) and Topcon REF (in blue).

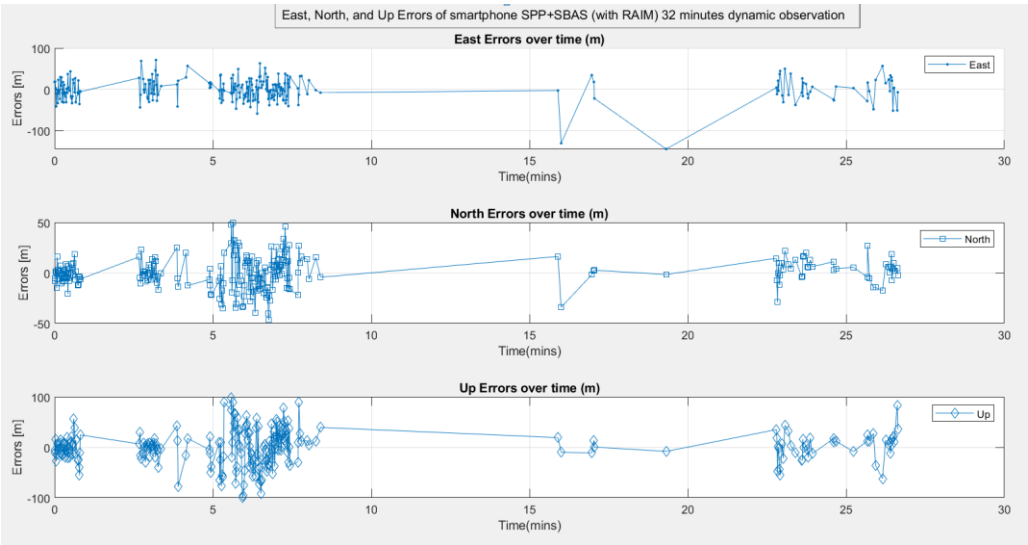

Figure 142. East, North, and Up Errors of smartphone SPP+SBAS (with RAIM-FDE) during 32 min dynamic test.

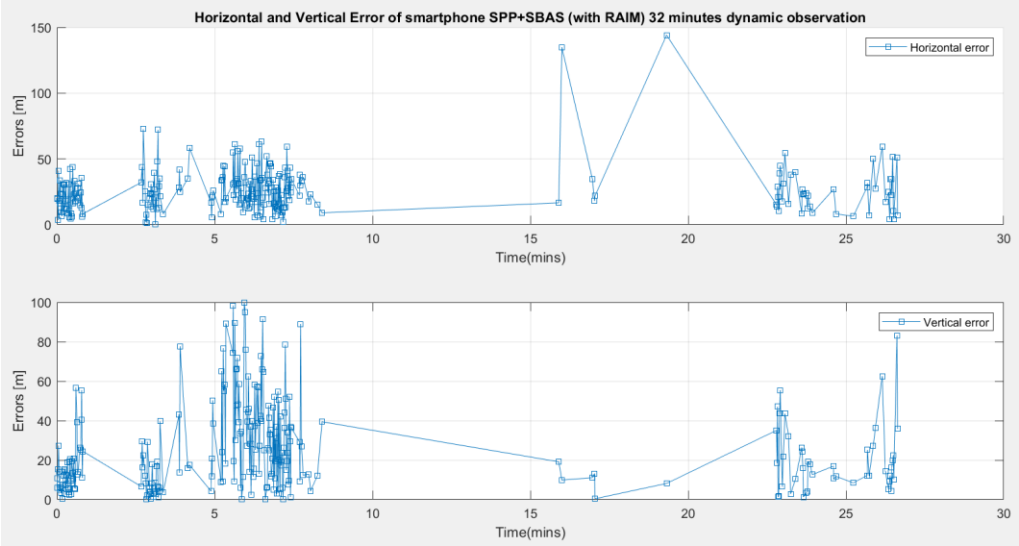

Figure 143. Horizontal and Vertical Error of smartphone SPP+SBAS (with RAIM-FDE) during 32 min dynamic test.

From figures 141, 142, and 143, signal outage was observed at around 8, 13, and 22 minutes as a result of multipath effects caused by signal obstructions, and shadowing. Little signal availability can be notices across the entire observation

set as a result of poor visibility of geo-stationary EGNOS satellites in north-eastern latitudes.

5.7.3.3 RTK plots for smartphone Samsung Galaxy s8 (with RAIM) during 32 min dynamic test

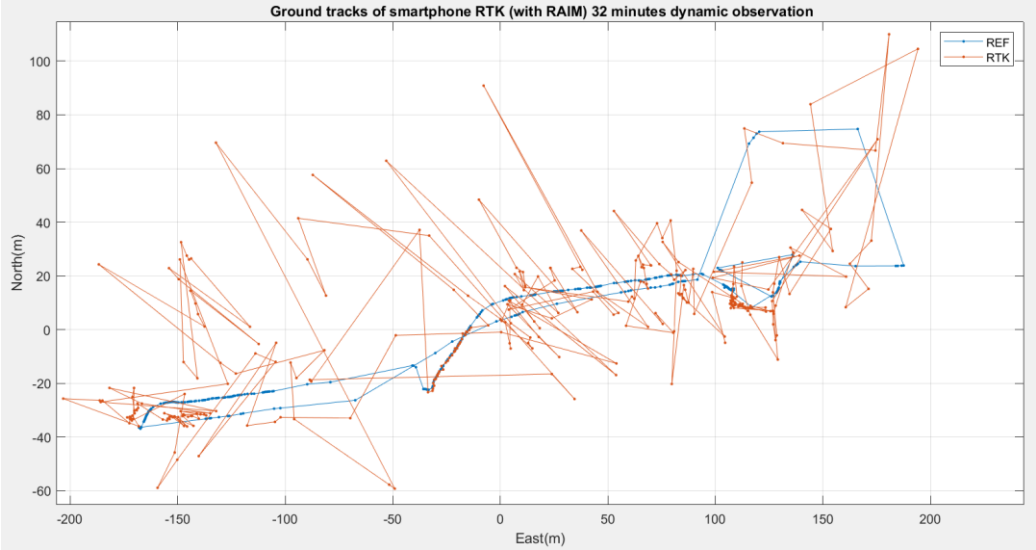

Figure 144. Ground tracks of smartphone RTK (with RAIM-FDE) during 32 min dynamic test.

The figure above shows the RTK solution (in red) and Topcon REF (in blue).

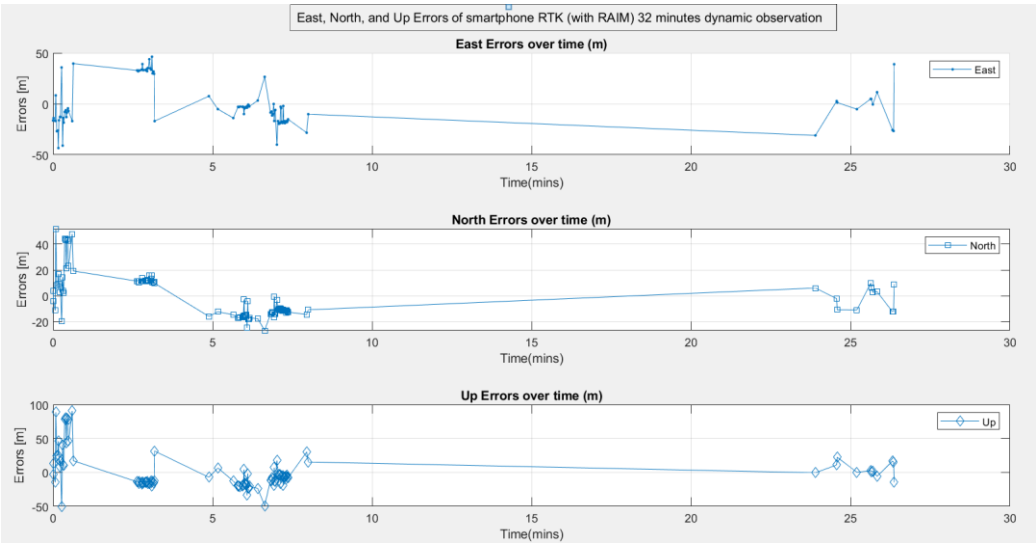

Figure 145. East, North, and Up Errors of smartphone RTK (with RAIM-FDE) during 32 min dynamic test.

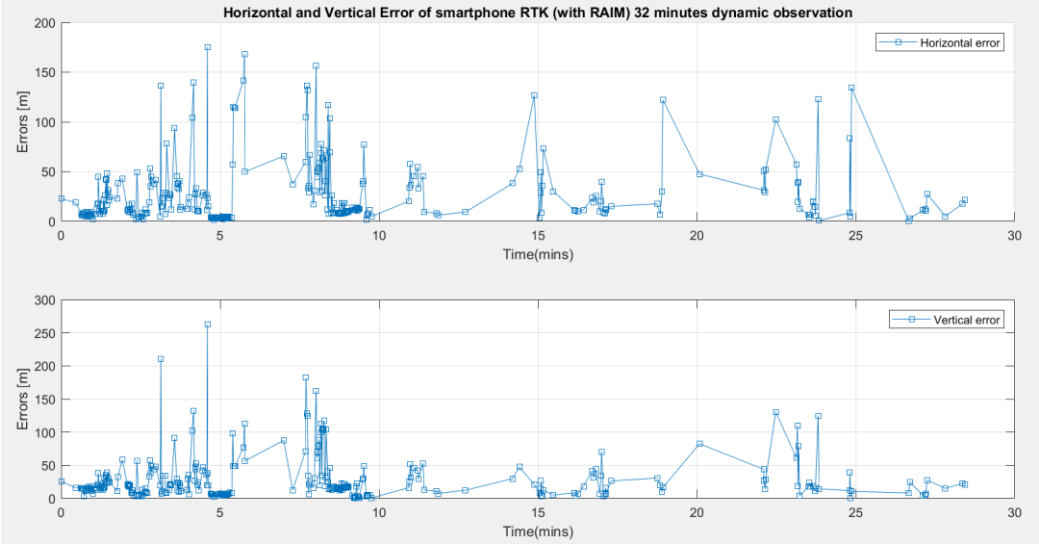

Figure 146. Horizontal and Vertical Error of smartphone RTK (with RAIM-FDE) during 32 min dynamic test.

From figures 144, 145, and 146, signal outage was observed at around 8, 13, and 22 minutes as a result of multipath effects caused by signal obstructions, and shadowing.

6. CONCLUSION AND FUTURE WORK

In this thesis, we have observed that the use of a carrier-phase based GNSS processing modes such as RTK increases the positioning accuracy by higher orders of magnitude. With RAIM-FDE (Receiver Autonomous Integrity Monitoring- Fault detection and Exclusion) availability is improved for dynamic tests.

In these limited set of experiments, RAIM-FDE did not have much impact, but there is a slight improvement in positioning accuracy for various GNSS devices when RAIM-FDE is used in stationary tests.

For stationary tests during a session length of 3 hours, the (RTK) 2D positioning accuracy for the dual frequency receiver was 0.47 cm, while 57.84 cm was observed on the single frequency, and 2.39 m on the smartphone when RAIM-FDE *was not* enabled.

For stationary tests during a session length of 3 hours, the (RTK) 2D positioning accuracy for the dual frequency receiver was 0.43 cm, while 57.58 cm was observed on the single frequency, and 1.45 m on the smartphone when RAIM-FDE *was* enabled.

For dynamic tests, during a session length of 19 minutes, the (RTK) 2D positioning accuracy for the dual frequency receiver was 2.39 m, while 11.5 m was observed on the single frequency, and 58.36 m on the smartphone when RAIM-FDE *was not* enabled.

For dynamic tests, during a session length of 19 minutes, the (RTK) 2D positioning accuracy for the dual frequency receiver was 3.05 m, while 12.73 m was observed on the single frequency, and 58.13 m on the smartphone when RAIM-FDE *was* enabled.

For dynamic tests, during a session length of 32 minutes, the (RTK) 2D positioning accuracy for the dual frequency receiver was 1.75 m, while 10.34 m was observed on the single frequency receiver when RAIM-FDE *was not* enabled.

For dynamic tests, during a session length of 32 minutes, the (RTK) 2D positioning accuracy for the dual frequency receiver was 1.86 m, while 11.35 m was observed on the single frequency receiver when RAIM-FDE *was* enabled.

Dual frequency devices perform better than single frequency devices in both availability and accuracy as a result of the presence of more receiver channels and therefore observables. The use of dual frequency channels aid in ionosphere error mitigation, and improves positioning accuracy via better measurement redundancy. Smartphone devices are the worst performers as result of e.g. antenna design constraints and placements. It is difficult to obtain a PPP solution for single frequency smartphones. The accuracy of SPP with EGNOS corrected ephemeris (SPP+SBAS) depends on the location as reported in this work.

This work recommends the use of dual frequency GNSS receivers for port applications. Our results show that low-cost dual frequency GNSS devices meets some of the category 2 *(2.5m horizontal alert limit)* Maritime and Inland Waterways (IWW) user requirements for port operations shown in Table 2 (see Chapter 1). Further experiments such as using real-time RTK corrections is necessary to achieve improved performance, even towards millimetre level positioning accuracy.

Future work

From the conclusions, it is clear that further experiments are needed to achieve centimetre and towards millimetre level positioning accuracy for dual frequency receivers and continuity. For static tests, the true positions were not estimated with a survey-grade geodetic receiver. This problem will be rectified in future experiments. To ensure experiment reliability, a signal splitter will be used to split signals from a single antenna. Future studies will also investigate why 2D and vertical accuracy of SPP with EGNOS corrections were not consistent and improved across all devices.

REFERENCES

Bhuiyan, Mohammad Zahidul H. & Kuusniemi, Heidi & Soderini, Auryn & Honkala, Salomon & Marila, Simo. (2017). *Performance of EGNOS in North-East European Latitudes*. 10.33012/2017.14881.

Chang, X. -W., Yang, X., & Zhou, T. (2005). MLAMBDA: A modified LAMBDA method for integer least-squares estimation, J. Geodesy, vol.79, 2005.

EUREF Permanent GNSS Network 2020. [Cited 28 April 2020]. Available from Internet <URL: http://www.epncb.oma.be/>

European GNSS Agency (2015). *Expanding Opportunities for Maritime use of GNSS*. [Cited 4 Feb. 2020]. Available from Internet <URL: https://www.gsa.europa.eu/news/expanding-opportunities-maritime-use-gnss>

European GNSS Agency (2019). *Report on Maritime and Inland Waterways User Needs and Requirements.* Outcome of the European GNSS' User Consultation Platform. [Cited 16 Sept. 2020]. Available from Internet <URL: https://www.gsa.europa.eu/gnss-applications/user-needs-and-requirements>

European GNSS Agency (2020a). *EGNOS*. [Cited 28 April 2020]. Available from Internet <URL: https://egnos-user-support.essp-sas.eu/new_egnos_ops/egnos-system/about-egnos>

European GNSS Agency (2020b). *SBAS*. [Cited 28 April 2020]. Available from Internet <URL: https://www.gsa.europa.eu/european-gnss/what-gnss/what-sbas>

European GNSS Agency (2020c). *WARTK-EGAL: WARTK based on EGNOS and Galileo: technical feasibility study.* [Cited 28 April 2020]. Available from Internet <URL: https://www.gsa.europa.eu/wartk-based-egnos-and-galileo-technical-feasibility-study>

Federal Aviation Administration (2020). *Satellite Navigation - Wide Area Augmentation System (WAAS).* [Cited 28 April 2020]. Available from Internet <URL:

https://www.faa.gov/about/office_org/headquarters_offices/ato/service_units/techops/navservices/gnss/waas/>

FinnRef (2020). [Cited 28 April 2020]. Available from Internet <URL: https://www.maanmittauslaitos.fi/en/research/research/other-research-and- measuring-stations/finnref-gnss-stations>

Geotrim Oy (2020a). [Cited 28 April 2020]. Available from Internet <URL: https://geotrim.fi/palvelut/trimnet-vrs/>

Geotrim Oy (2020b). [Cited 28 April 2020]. Available from Internet <URL: https://www.finder.fi/Mittauslaitteet+tutkimuslaitteet/Geotrim+Oy/Vantaa/yhteystiedot/134624>

Gleason, S., Demoz Gebre-Egziabher (2009a). *GNSS Applications and Methods*, ISBN-13: 978-1-59693-329-3, © 2017 Artech House.

Gleason, S., Quigley, M., Abbeel, P. (2009b). *An Open Source AGPS/DGPS Capable C-coded Software Receiver.* Proceedings of the 22nd International Technical Meeting of the Satellite Division of The Institute of Navigation (ION GNSS 2009), Savannah, GA, September 2009, pp. 1926-1931.

GNSS Market Report (2015). [Cited 4 Feb. 2020]. Available from Internet <URL: https://www.gsa.europa.eu/sites/default/files/Maritime_0.pdf >

GNSS Planning Online (2017-2018), Trimble Inc. Version: 1.4.6.0. [Cited 28 April 2020]. Available from Internet <URL: https://www.gnssplanning.com/#/>

Google Earth Engine (2021). Google. All rights reserved.

Government of India (2020), Department of Space, Indian Space Research Organisation. [Cited 28 April 2020]. Available from Internet <URL: https://www.isro.gov.in/applications/step-towards-initial-satellite-based-navigation-services-india-gagan-irnss>

Gurtner, W. (2007). RINEX the Receiver Independent Exchange Format Version 2.10, December 10, 2007.

Hexagon (2021). *GPS & GNSS Correction Services*. [Cited 19 April 2021]. Available from Internet <URL: https://novatel.com/products/correction-services>

IMO Resolution A. 915(22) (2002). *Revised Maritime Policy and Requirements for a Future GNSS*. Adopted on January 22nd, 2002, London.

International GNSS Service (2020). International GNSS Service. [Cited 21 April 2020]. Available from Internet <URL: http://www.igs.org/>

Kaplan, Elliott D., Hegarty, Christopher J. (2009). *Understanding GPS/GNSS Principles and Applications Second Edition*, ISBN-10: 1-58053-894-0, © 2017 Artech House.

Kaplan, Elliott D., Hegarty, Christopher J. (2017). *Understanding GPS/GNSS Principles and Applications Third Edition*, ISBN-13: 978-1-63081-058-0, © 2017 Artech House.

Lachapelle, G., Gratton, P. (2019). *GNSS Precise Point Positioning with Android Smartphones and Comparison with High Performance Receivers*. IEEE International Conference on Signal, Information and Data Processing Chongqing, China, 11-13 Dec 2019. [Cited 4 Feb. 2020]. Available from Internet <URL: https://schulich.ucalgary.ca/labs/position-location-and-navigation/node/1956>

Leandro, R.F., Santos, M.C., & Langley, R.B. (2006). *UNB Neutral Atmosphere Models: Development and Performance.* Proceedings of ION NTM 2006, the 2006 National Technical Meeting of The Institute of Navigation, Monterey, California, 18-20 January 2006; pp. 564-573.

Leica Geosystems (2020a). [Cited 28 April 2020]. Available from Internet <URL: https://leica-geosystems.com/products/gnss-reference-networks/software/leica-gnss-spider>

Leica Geosystems (2020b). [Cited 28 April 2020]. Available from Internet <URL: https://leica-geosystems.com/services-and-support/workflow-services/leica-crosscheck>

Li-Ta Hsu, Yanlei Gu, Shunsuke Kamijo (2016). *Autonomous driving positioning using building model and DGNSS*. European Navigation Conference (ENC) 2016.

Mattias Eriksson (2017). *Status on GNSS Applications in the Nordic Countries*. 57th Meeting of the Civil GPS Service Interface Committee Portland, Oregon. September 25-26, 2017.

NASA's Archive of Space Geodesy Data, CDDIS (2021a). *Broadcast Ephemeris Data*. [Cited 19 April 2021]. Available from Internet <URL: https://cddis.nasa.gov/Data_and_Derived_Products/GNSS/broadcast_ephemeris_data.html>

NASA's Archive of Space Geodesy Data, CDDIS (2021b). *GNSS Orbit Products*. [Cited 19 April 2021]. Available from Internet <URL: https://cddis.nasa.gov/Data_and_Derived_Products/GNSS/orbit_products.html>

National Land Survey of Iceland (2020a). [Cited 28 April 2020]. Available from Internet <URL: https://www.lmi.is/en/icecors-network/>

National Land Survey of Iceland (2020b). [Cited 28 April 2020]. Available from Internet <URL: https://www.sonel.org/spip.php?page=gps&idStation=828>

Navipedia (2020a). *Carrier Phase Ambiguity Fixing.* [Cited 28 April 2020]. Available from Internet <URL: https://gssc.esa.int/navipedia/index.php/Carrier_Phase_Ambiguity_Fixing>

Navipedia (2020b). *Code Based Positioning*. [Cited 21 April 2020]. Available from Internet <URL: https://gssc.esa.int/navipedia/index.php/Code_Based_Positioning_(SPS)>

Navipedia (2020c). *Differential GNSS*. [Cited 21 April 2020]. Available from Internet <URL: https://gssc.esa.int/navipedia/index.php/Differential_GNSS>

Navipedia (2020d). *GNSS Basic Observables*. [Cited 21 April 2020]. Available from Internet <URL: https://gssc.esa.int/navipedia/index.php/GNSS_Basic_Observables>

Navipedia (2020e). *RTK Fundamentals*. [Cited 28 April 2020]. Available from Internet <URL: https://gssc.esa.int/navipedia/index.php/RTK_Fundamentals>

Navipedia (2020f). *WARTK Fundamentals*. [Cited 28 April 2020]. Available from Internet <URL: https://gssc.esa.int/navipedia/index.php/WARTK_Fundamentals>

Navipedia (2020g). *Wide Area RTK*. [Cited 28 April 2020]. Available from Internet <URL: https://gssc.esa.int/navipedia/index.php/Wide_Area_RTK_(WARTK)>

NEC Corporation (2020). *MTSAT Satellite-based Augmentation Navigation System.* [Cited 28 April 2020]. Available from Internet <URL: https://www.nec.com/en/global/solutions/cns-atm/navigation/msas.html>

Norwegian Mapping Authority (2020). [Cited 28 April 2020]. Available from Internet <URL: https://www.kartverket.no/en/Positioning/>

Novatel (2020a). *GNSS Error Sources.* [Cited 22 April 2020]. Available from Internet <URL: https://www.novatel.com/an-introduction-to-gnss/chapter-4-gnss-error-sources/>

Novatel (2020b). *GNSS Measurements.* [Cited 22 April 2020]. Available from Internet <URL: https://www.novatel.com/an-introduction-to-gnss/chapter-5-resolving-errors/gnss-measurements/>

Novatel (2020c). *Precise Point Positioning.* [Cited 22 April 2020]. Available from Internet <URL: https://novatel.com/contactus/an-introduction-to-gnss/chapter-5-resolving-errors/precise-point-positioning-ppp.>

Novatel (2020d). *Real Time Kinematics RTK*. [Cited 28 April 2020]. Available from Internet <URL: https://novatel.com/contactus/an-introduction-to-gnss/chapter-5-resolving-errors/real-time-kinematic-rtk>

Novatel (2020e). *Satellite-based Augmentation Systems*. [Cited 28 April 2020]. Available from Internet <URL: https://www.novatel.com/an-introduction-to-gnss/chapter-5-resolving-errors/satellite-based-augmentation-systems/>

OmniSTAR (2021). [Cited 21 April 2021]. Available from Internet <URL: https://www.omnistar.com/>

Ray, J., & Gurtner, W., (2010). RINEX extensions to handle clock information version 3.02, September 2, 2010.

Russian System of Differential Correction and Monitoring (Russian SDCM) (2020). [Cited 28 April 2020]. Available from Internet <URL: http://www.sdcm.ru/smglo/staticpages?version=eng&site=extern&title=about>

Sergio Magdaleno et al. (2019). *SBAS Guidelines for Shipborne Receiver: EGNOS Performance Based on IMO RES. A.1046 (27).* DOI: 10.1515/aon-2019-0008.

Hilla, S. (2010). *The extended standard product 3 orbit format (SP3-c)*, August 17, 2010.

Swedish Maritime Administration (2020). [Cited 28 April 2020]. Available from Internet <URL: https://www.sjofartsverket.se/en/Maritime-services/Fairways/DGPS--Differential-Global-Positioning-System/>

Takasu, T. (2007-2013). RTKLib ver. 2.4.2 Manual pgs. 1, 140, 141, 149, 165, 166, 169.

TerraStar (2021). *TerraStar Correction Services*. [Cited 19 April 2021]. Available from Internet <URL: https://terrastar.net/>

Teunissen, P. J. G. (2005). *The least-square ambiguity decorrelation adjustment: a method for fast GPS ambiguity estimation.* Journal of Geodesy, vol.70, 1995.

Tim Everett (2021a). RTKLib Explorer, [Cited 19 April 2021]. Available from Internet <URL: https://rtklibexplorer.wordpress.com/2016/03/13/improving-rtklib-solution-fix-and-hold/>

Tim Everett (2021b). RTKLib Explorer, [Cited 19 April 2021]. Available from Internet <URL: https://rtklibexplorer.wordpress.com/2017/08/21/ppk-vs-rtk-a-look-at-rtklib-for-post-processing-solutions/>

VERIPOS (2021). [Cited 19 April 2021]. Available from Internet <URL: https://veripos.com/>

Wikipedia (2020a). *Local tangent plane coordinates*. [Cited 21 April 2020]. Available from Internet <URL: https://en.wikipedia.org/wiki/Local_tangent_plane_coordinates>

Wikipedia (2020b). *Precise Point Positioning*. [Cited 21 April 2020]. Available from Internet <URL: https://en.wikipedia.org/wiki/Precise_Point_Positioning>